Stability of perovskite solar cells

Philippe Holzhey

Trinity College

Condensed Matter Physics

Department of Physics

University of Oxford

This dissertation is submitted for the degree of Doctor of Philosophy

January 2024

1. Acknowledgement

I want to thank Henry Snaith for his guidance, time and passion. Henry allowed me to explore and do what I liked, allowing me to grow in a way I didn't imagine at the start of my PhD. During the pandemic, Henry's infectious energy motivated me and ensured that I had the passion to continue. His never-ending ideas and suggestions kept me thinking when I otherwise would have given up. Thank you, Henry!

I also had the unique opportunity to work in the laboratories of Udo Bach at Monash in Melbourne, Australia. Udo allowed me to visit his laboratories for over a year, which was a wonderful experience. His input was always on point, improving and helping to improve the project. Vielen Dank, Udo!

My deepest gratitude also goes to the people I worked closely with David McMeekin, Benjamin Gallant and Wei-Ting Wang. David's perseverance ensured that everything worked out in the end. He also mentored me and read, for example, parts of this thesis. Working with Benjamin is inspiring; he opened my eyes to the world of chemistry and everything I have yet to understand. Wei-Ting is an incredibly reliable and hard-working collaborator who always surprises me with how she comes up with new experiments. Thank you all!

I also would like to thank all the amazing people I met throughout my scholarship. Thijs, I know you are probably still salty, but please just know that I am a farmer from the bottom of my heart. Vivek, Agus, Christina, Rahul, Nadja, Luigi, Lefteris, Sijo and Rene thank you for making it such a wonderful time during MAESTRO!

During my time in Australia, I met some incredible people I would like to thank. To name some: Josh, Kevin, Sebastian, Jamie, Pria, Amit, Siqi, Juan, Adam, Boer, Manoj, Prof. Sudar, Anu,

Nadja and the others from the Exciton Science Centre. Thank you all for welcoming me and including me in the research group! You all made this year in Australia a very special one. Special thanks also to Kevin for proofreading my thesis.

I am also very grateful to Shien-Ping Feng, a great person to work with. Thanks also to Harry Sansom, who read my thesis and my status transfer. Harry always gave me advice when I needed it. I am also very grateful to Yen and Kelly, who showed me how to make devices in the Snaith lab.

I also would like to thank Clare Moloney for her support and help! Clare often stayed behind only to ensure that everything was organised and in place. Without her, many things wouldn't have worked the way they did.

I also want to thank James for his reliable and accurate advice. Also, big thanks to Grey, Augustin and Mike for the help with all the equipment. Thank you also to all my work colleagues: Akash, Alex, Amit, Andreas, Anna, Ashley, Ben, Bernd, Derek, Elisabeth, Emil, Enrico, Esthy, Flo, Giulia, Heon, Irfan, Jake, Jarla, Jay, Jin, Joel, Jonny (Devices!), Julianna, Laura, Manuel, Ming, Nakita, Nicky, Olivia A., Olivia G., Pascal, Pietro, Robbie, Ruohan, Seongrok, Silvia, Spencer, Suer, Suhas and Tino. Big thanks also to all the others in the group! I very much enjoyed working with all of you.

Last, I would like to thank my mum. She always has the right advice and guidance for me. Her unconditional love gave me the confidence I needed for this journey. She taught me to care. Thank you for all that, Mama!

And finally, thank you for reading this thesis. I hope you find it useful!

2. Declaration

This thesis is a result of my own work and includes nothing that is the result of collaboration except where explicitly stated in the text.

I declare that no part of this work has been submitted for a degree or any other qualification at this or any other university.

Philippe Holzhey, January 2024.

3. Abstract

Metal-halide perovskites have emerged as promising next-generation solar cells and have already achieved high power conversion efficiencies, rivalling current technologies. The chemical stoichiometry of perovskite can be easily varied to tune the material's bandgap to produce a range of photovoltaic devices unrealised by other materials. Halide perovskites can also be easily fabricated from solutions or evaporated at a possibly low cost. However, what use does a solar cell have if it only lasts a few months? Little! So, I choose to explore the material stability of lead-halide perovskites in this thesis. Making stable halide perovskites would allow the fabrication of more efficient and more cost-effective solar cells. Hopefully, that can alleviate some of the possible outcomes of climate change. Even if perovskites are unsuitable for photovoltaic applications, extending the range of possible semiconductors away from only classically inorganic ones to more hybrid materials will hopefully bring an advantage for humanity. And for any semiconductor application, a stable material is needed!

The challenge with improving the stability of halide perovskites lies in the manifold of different factors one has to consider:

- A variety of different environmental conditions in which the device must be stable
- The different materials which are in contact with the perovskite absorber
- The myriad of chemical stoichiometries that constitute lead halide perovskites, each facing different stability issues, to name some:
    - Phase stability
    - Halide segregation
    - Cation segregation

- Evaporation of the organic component
- Sublimation of the halides
- Ion migration

One of the critical findings in this thesis is that instabilities are not inherent for a specific perovskite, e.g., $FAPbI_3$, but strongly depend on how the material is made. I developed two new fabrication routes (the DMA^+ and 2D-3D-route), which, surprisingly, resulted in more stable perovskites compared to the classical routes with, for example, DMF and DMSO. Even though the classical and new routes both deliver a nominal almost identical material. Critical factors for that are the processing solvents and the crystallisation. With the DMA route, I got significantly more stable mixed halide perovskites. At 65 °C and under full-spectrum illumination, the DMF/DMSO devices had a T_{80} (the time until it reaches 80% of its peak median efficiency) of 780 h, while the DMF/DMACl devices had a T_{80} of 1190 h. 32 devices of each were measured. The best DMF/DMSO and DMF/DMACl device had a T_{80} of 1040 h and 1410 h, respectively. At 85 °C and otherwise the same aging conditions, the DMF/DMSO and DMF/DMACl devices had a median T_{80} time of 330 h and 430 h, respectively. 27 devices were measured for each. The most stable DMF/DMSO and DMF/DMACl devices at 85 °C had a median T_{80} time of 380 h and 490 h, respectively. In terms of efficiency, I found that the DMA route produces equally efficient devices as the DMF/DMSO route.

Besides these fabrication methods, I also developed a new passivation type. It is dynamic. It allows for the passivation of defects not only during the fabrication but also to passivate newly evolving defects during the operation. The molecule is called HUBLA (hindered urea/thiocarbamate bond Lewis acid-base). It is inspired by the field of living polymers. I prove the dynamic passivation of HUBLA chemically through X-ray photoelectron spectroscopy (XPS) and physically through photoluminescence maps of aged and not-aged perovskite films. I then

go on to show the stability of perovskite films under various different stressors. HUBLA improves the stability of the thin films under moisture and heat. In devices, HUBLA significantly improves the efficiency and stability. The best-performing n-i-p device with HUBLA reaches 24.7%, while the control reaches 21.7%. In p-i-n devices, the best-performing device with HUBLA reached 25.1% and for the control, 22.7%. Devices under 1 sun illumination at 85 °C retained less than 50% of their initial performance after 431 h. The same devices under the same conditions with HUBLA retained 88% of their initial value over 1000 h. In N_2 at 85 °C and under 1 sun, the control devices have a T_{80} of 866 h, and the HUBLA devices maintain 94% after aging for nearly 1500 h. At 85 °C in N_2, the HUBLA devices retained 90% of their initial efficiency after 21864 hours. Nearly 2.5 years at the highest tested operating temperature for photovoltaics, and the devices still worked well. I believe that this shows the extraordinary potential of dynamic passivations.

4. Contents

5. List of Abbreviations

2PACz - [2-(9H-carbazol-9-yl)ethyl]phosphonic acid

ALD - atomic layer deposition

Al_2O_3 NPs - alumina nanoparticles

ATR-IR - attenuated total reflection fourier transform infrared spectroscopy

BA^+ - $[C_4H_9NH_3]$

BnA^+ - $[PhCH_2NH_3]$

BCP - bathocuproine

C_{60} - buckminsterfullerene

CTL - charge-transport layer

CB - chlorobenzene

CF - chloroform

CH - hydrochloride

CL - compact Layer

CuSCN - copper thiocyanate

D_2O - deuterium oxide

DFT - density functional theory

DCB - dichlorobenzene

DMSO-d_6 - dimethyl sulfoxide-d_6

DMA route – the here introduced fabrication route with excess DMAX

DMACl - dimethylammonium chloride

DMF - N, N-dimethylformamide

DMSO - dimethylsulfoxide

DBTDL - dioctyltin dilaurate

DSSC - dye-sensitised solar cell

DCBs - dynamic covalent bonds

ETL - electron transporting layer

ESI-MS - electrospray ionization mass spectrometry

EA - ethyl acetate

EA^+ - ethylammonium

EDA - ethylenediamine

EQE - external quantum efficiency

F4-TCNQ - 2,3,5,6-Tetrafluoro-7,7,8,8-tetracyanoquinodimethane

FF - fill factor

FK209 - tris(2-(1h-pyrazol-1-yl)-4-tert-butylpyridine)-cobalt(III)tris(bis(trifluoromethylsulfonyl)imide)

FTO - fluorine-doped tin oxide

FA^+ or FA - formamidinium

GBL - γ-butyrolactone

GHGs - greenhouse gases

GA^+ or Gua^+ - guanidinium

$HMTA^+$ - hexamethylenetetramine

HUBLA - hindered urea/thiocarbamate bond Lewis acid-base

HTM - hole transporting material

$Imid^+$ - imidazolium

ITO - Indium tin oxide

IMPS - Intensity-modulated photocurrent spectroscopy

IPA - isopropyl alcohol

J_{SC} - short-circuit current

J-V curve - current-voltage characteristic

Li-TFSI - li-bis(trifluoromethanesulfonyl)imide

LEDs - light-emitting devices

LiBr - lithium bromide

MPP - maximum power point

MPPT - maximum power point tracking

mim^+ - methaniminium

MA^+ or MA - methlyammonium

MDA^{2+} - methylenediammonium

MoO_3 - molybdenum(VI) oxide

NPs - Nanoparticles

NCO-AS - NCO-terminated ammonium salt

NH-AS - NH_2-terminated ammonium salt

NMR - nuclear magnetic resonance

PCBM - [6,6]-phenyl-C_{61}-butyric acid methyl ester

PCE or η - power conversion efficiency

PSCs - perovskite solar cells

PL - photoluminescence

polyTPD - poly(4-butylphenyl-diphenyl-amine)

PTAA - poly[bis(4-phenyl)(2,4,6-trimethylphenyl)amine]

PEIE - polyethylenimine ethoxylated

PVP – polyvinylpyrrolidone

PV - photovoltaic (PV)

QE - quantum efficiency

RT - room temperature

SEM - scanning electron microscopy

SAM - self-assembled monolayer

SPO - stabilized power output

tBEDA - tert-butylethylenediamine

tBP - 4-tert-butyl-pyridine

THTZ-H^+ - tetrahydrotriazinium

TD-GC-MS - thermal desorption-gas chromatography-mass spectrometry

TGA - thermogravimetric analysis

TMXDI - 1,3-bis(2-isocyanato-2-propyl)benzene

TOF-SIMS - time-of-flight secondary ion mass spectrometry

TCO - transparent conductive oxide

TEG - tri(ethylene glycol)

TEA - triethanolamine

TFT - α,α,α-Trifluorotoluene

UV-Vis - ultraviolet-visible spectroscopy

V_{OC} - open circuit voltage

WAXS - wide-angle X-ray scattering

XRD - X-ray diffraction

XRD^2 or 2D XRD - two-dimensional X-ray diffraction

XPS - X-ray photoelectron spectroscopy

Zr(acac) - zirconium acetylacetonate

6. Publications throughout my DPhil

1. D. P. McMeekin*, **P. Holzhey***, S. O. Fürer, S. P. Harvey, L. T. Schelhas, J. M. Ball, S. Mahesh, S. Seo, N. Hawkins, J. Lu, M. B. Johnston, J. J. Berry, U. Bach and H. J. Snaith, Intermediate-phase engineering via dimethylammonium cation additive for stable perovskite solar cells, Nature Materials (2023), DOI: 10.1038/s41563-022-01399-8, *these authors contributed equally
2. WT. Wang*, **P. Holzhey***, N. Zhou*, Q. Zhang*, S. Zhou, E. A. Duijnstee, K. J. Rietwyk, JY. Lin, Y. Mu, Y. Zhang, U. Bach, CG. Wu, HL. Yip, H. J. Snaith, SP. Feng, Water- and heat-activated dynamic passivation for perovskite photovoltaics, Nature (2024), DOI: 10.1038/s41586-024-07705-5 *these authors contributed equally
3. E. A. Duijnstee*, B. M. Gallant*, **P. Holzhey***, D. J. Kubicki, S. Collavini, B. Sturdza, H. C. Sansom, J. Smith, M. J. Gutmann, S. Saha, M. Gedda, M. I. Nugraha, M. Kober-Czerny, C. Xia, A. D. Wright, Y. Lin, A. J. Ramadan, A. Matzen, E. Y.-H. Hung, S. Seo, S. Zhou, J. Lim, T. D. Anthopoulos, M. R. Filip, M. B. Johnston, R. J. Nicholas, J. L. Delgado, H. J. Snaith, Understanding the degradation of methylenediammonium and its role in phase-stabilising formamidinium lead triiodide, Journal of the American Chemical Society (2023); DOI: 10.1021/jacs.3c01531, *these authors contributed equally
4. **P. Holzhey**, M. Prettl, S. Collavini, N. L. Chang, M. Saliba, Toward commercialization with lightweight, flexible perovskite solar cells for residential photovoltaics, Joule (2023), DOI: 10.1016/j.joule.2022.12.012.
5. **P. Holzhey***, M. Prettl*, S. Collavini, C. Mortan, M. Saliba, Understanding the impact of surface roughness: changing from FTO to ITO to PEN/ITO for flexible perovskite solar cells.

Scientific Reports (2023), DOI: 10.1038/s41598-023-33147-6, *these authors contributed equally

6. B. M. Gallant, **P. Holzhey**, J. A. Smith, S. Choudhary, K. A. Elmestekawy, P. Caprioglio, I. Levine, A. Sheader, F. Yang, D. T.W. Toolan, R. C. Kilbride, A. K.A. Zaininger, J. M. Ball, M. G. Christoforo, N. Noel, L. M. Herz, D. J. Kubicki, H. J. Snaith, A green solvent system for precursor phase-engineered sequential deposition of stable formamidinium lead triiodide for perovskite solar cells, https://arxiv.org/abs/2406.08441v1
7. X. Shen, B. M. Gallant, **P. Holzhey**, J. A. Smith, K. A. Elmestekawy, Z. Yuan, P. V. G. M. Rathnayake, S. Bernardi, A. Dasgupta, E. Kasparavicius, T. Malinauskas, P. Caprioglio, O. Shargaieva, Y.-H. Lin, M. M. McCarthy, E. Unger, V. Getautis, A. Widmer-Cooper, L. M. Herz, H. J. Snaith, Chloride-Based Additive Engineering for Efficient and Stable Wide-Bandgap Perovskite Solar Cells, Advanced Materials (2023), DOI: 10.1002/adma.202211742
8. S. G. Motti, M. Kober-Czerny, M. Righetto, **P. Holzhey**, J. Smith, H. Kraus, H. J. Snaith, M. B. Johnston, L. M. Herz, Exciton Formation Dynamics and Band-Like Free Charge-Carrier Transport in 2D Metal Halide Perovskite Semiconductors, Advanced Functional Materials (2023), DOI: 10.1002/adfm.202300363
9. K. J. Rietwyk, X. Lin, B. Tan, T. Warnakula, **P. Holzhey**, B. Zhao, S. Deng, M. A. Surmiak, J. Jasieniak and U. Bach, Ideality Factor Mapping of Back-Contact Perovskite Solar Cells, Advanced Energy Materials (2023), DOI: 10.1002/aenm.202200796
10. K.A. Elmestekawy, B. M. Gallant, A. D. Wright, **P. Holzhey**, N. K. Noel, M. B. Johnston, H. J. Snaith, L. M. Herz, Photovoltaic Performance of $FAPbI_3$ Perovskite Is Hampered by Intrinsic Quantum Confinement, ACS Energy Letters (2023), DOI: 10.1021/acsenergylett.3c00656
11. A. Dasgupta, S. Mahesh, P. Caprioglio, Y.-H. Lin, K.-A. Zaininger, R. D. J. Oliver, **P. Holzhey**, S. Zhou, M. M. McCarthy, J. A. Smith, M. Frenzel, M. G. Christoforo, J. M. Ball, B. Wenger

and H. J. Snaith, Visualizing Macroscopic Inhomogeneities in Perovskite Solar Cells, ACS Energy Letters (2022), DOI: 10.1021/acsenergylett.2c01094

12. M. Kober-Czerny, S. G. Motti, **P. Holzhey**, B. Wenger, J. Lim, L. M. Herz and H. J. Snaith, Excellent Long-Range Charge-Carrier Mobility in 2D Perovskites, Advanced Functional Materials (2022), DOI: 10.1002/adfm.202203064
13. S. Zhou, M. Daskeviciene, M. Steponaitis, G. Bubniene, V. Jankauskas, K. Schutt, **P. Holzhey**, A. R. Marshall, P. Caprioglio, G. Christoforo, J. M. Ball, T. Malinauskas, V. Getautis and H. J. Snaith, Low-Cost Dopant-Free Carbazole Enamine Hole-Transporting Materials for Thermally Stable Perovskite Solar Cells, Solar RRL (2021), DOI: 10.1002/solr.202100984
14. B. K. Sturdza, B. M. Gallant, **P. Holzhey**, E. A. Duijnstee, H. J. Snaith, M. K. Riede, and R. J. Nicholas, Direct Observation of Phase Transitions between delta- and alpha-Phase $FAPbI_3$ via Defocused Raman Spectroscopy, Journal of Materials Chemistry A (2024), DOI: 10.1039/D3TA06411E

6.1. Patents

1. Precursor compounds for perovskite films, 18919, PCT/GB2022/052403, UK priority number: 2113494.5, B. M. Gallant, P. Holzhey, H. J. Snaith
2. HMTA additive for perovskite (OPV), 20598, E. A. Duijnstee, B. M. Gallant, P. Holzhey, S. Collavini, J. L. Delgado, H. J. Snaith

6.2. Grants

- £4000 for my trip to Monash, Melbourne, from the International and Industrial Engagement Fund funded by SuperSolar
- 2x £500 for the S-MRS conference in Hawaii and the 50 PVSC IEEE from SuperSolar

- Wrote part of a successful DFG grant proposal - Perovskite solar cells with Graphite electrodes: Advanced Interfaces for highest performance and stability (PeroGAIN)
- £500 Travel grant for the 50th PVSC IEEE conference in Puerto Rico from Trinity College
- £1500 Write-up grant from Trinity College

6.3. Awarded Merit-Based Beamtimes

- Spectroscopy-ptychography of halide distribution and speciation in perovskites for high-efficiency photovoltaic devices at the X-ray Fluorescence Microscopy beamline at the Australian Synchrotron (AS211/XFM/16899)
- Mapping Phase Decomposition and Elemental Migration During Perovskite Solar Cell Degradation at the X-ray Fluorescence Microscopy beamline at the Australian Synchrotron (AS233/XFM/20450)
- Investigate residual solvents and amorphous phases in formamidinium (FA) based lead halide perovskites for improved stability at PETRA III beamline P02.1 (I-20230468)
- Understanding the Structure-Property Relationship for Formamidinium Lead Halide Perovskites for Stable Perovskite Solar Cells at the Diamond Light Source on I15-1: X-ray Pair Distribution Function (CY34887-1)
- Understanding the Structure-Property Relationship for Formamidinium Lead Halide Perovskites for Stable Perovskite Solar Cells at the Diamond Light Source on I11: High Resolution Powder Diffraction (CY37420)
- Revealing the Cubic- to Delta-Phase Transition of Formamidinium Lead Halide Perovskites for Phase-Stable Perovskite Solar Cells at the Diamond Light Source on I15-1: X-ray Pair Distribution Function (CY36125-1)

6.4. Prizes

- Best Student Presentation Award Finalist at the 50th IEEE PVSC conference
- 3rd place for the poster presentation at the PVSAT-17 & Super Solar Conference
- 2nd best student speaker at the Sunrise conference awarded by Sustainable Energy & Fuels
- Graduate Student prize from Trinity College

7. The need to advance PV: Climate Change

Industrialisation in the last two centuries has significantly increased the emission of greenhouse gases (GHGs). These lower the planet's cooling rate by absorbing outgoing longwave radiation and storing the heat instead of allowing it to escape into space. The result is a continuous rise in global temperature and extreme changes in the climate, which have increased human mortality and the likelihood of extreme weather events.[1]

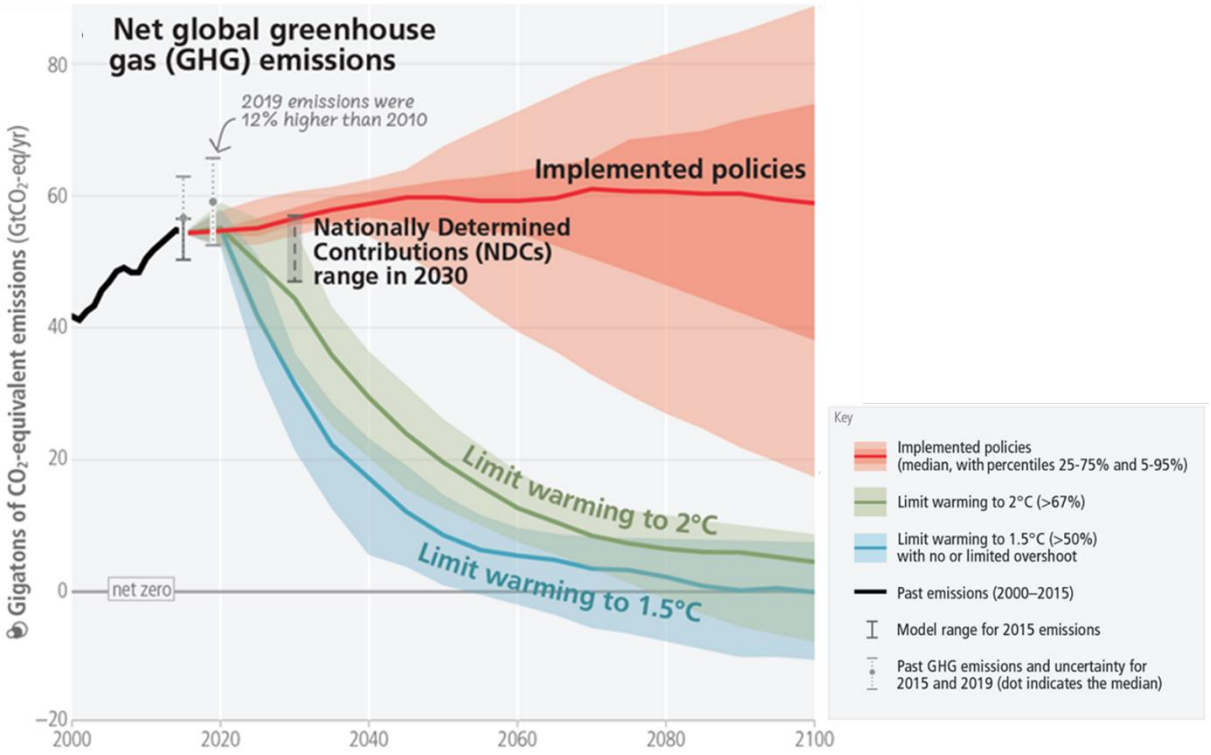

Figure 1 The development of global greenhouse gas emissions and predicted emissions modelled from 2015 onwards. The coloured ranges denote the 5th to 95th percentile across the global modelled pathways. The red ranges depict emissions pathways assuming policies that were implemented by the end of 2020. Ranges of modelled pathways that limit warming to 1.5 °C (>50%) with no or limited overshoot are shown in light blue and pathways that limit warming to 2 °C (>67%) are shown in green. Global emission pathways that would limit warming

to 1.5 °C (>50%) with no or limited overshoot and also reach net zero GHG in the second half of the century do so between 2070–2075. Figure and text adapted from [1].

Strong greenhouse gas emission reductions are needed to limit the warming to 1.5 °C below pre-industrial levels, as shown in **Figure 1**. Photovoltaics (PV) are one of the best ways of mitigating the impact of climate change by changing the way humanity produce energy moving away from fossil fuels towards renewable energies, as shown in **Figure 2**. The more one can lower the environmental footprint, the better. Meaning that further improving PV is a good way of tackling climate change.[2] Especially promising are halide perovskites because as a single-junction device they offer a lower CO_2 footprint compared to already established PV technologies.[3] They can also provide novel functionalities for new applications as, for example, efficient, flexible solar cells, which would extend the possible usage of PV devices.[4] In a tandem stack, they can increase the power conversion efficiency (PCE) of PVs further, which could lower the installation cost and time.

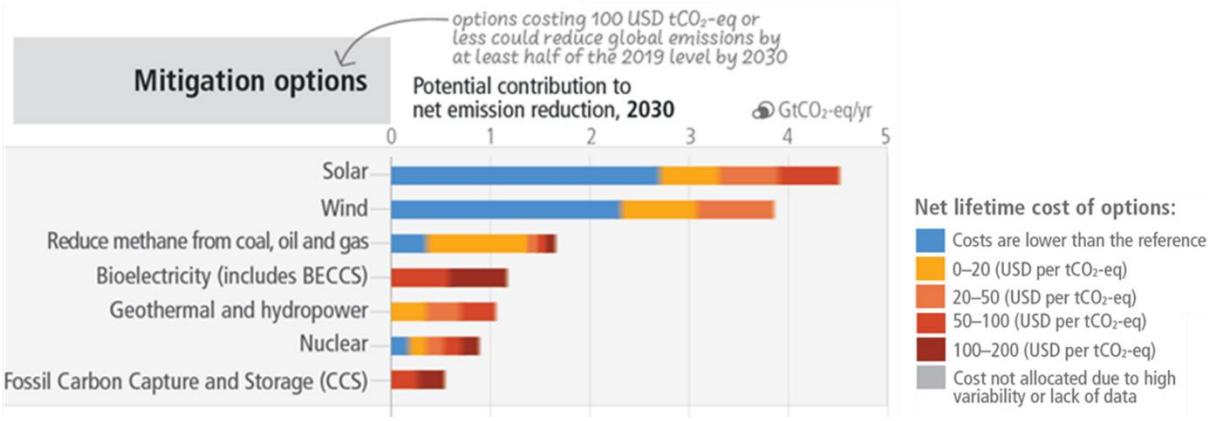

Figure 2 Overview of selected mitigation options and their estimated costs and potentials in 2030. Relative potentials and costs will vary by location, context and time and are likely to change over the longer term beyond 2030. Costs are net lifetime discounted monetary costs of avoided greenhouse gas emissions calculated relative to a reference technology. The unit is

USD tCO2-eq $^{-1}$ which means the cost, in US dollars, of reducing or removing one ton of carbon dioxide equivalent emissions. This unit is commonly used in discussions related to the cost-effectiveness of different strategies for mitigating greenhouse gas emissions. The potential (horizontal axis) is the quantity of net GHG emission reduction that can be achieved by a given mitigation option relative to a specified emission baseline. Net GHG emission reductions are the sum of reduced emissions and/or enhanced sinks. The baseline used consists of current policy (around 2019) reference scenarios from the AR6 (the 2023 IPCC report) scenarios database (25–75 percentile values). The mitigation potentials are assessed independently for each option and are not necessarily additive. Figure and text adapted from [1].

8. General introduction to photovoltaics

Please note that the following text is partly inspired from the book Physics of Solar Cells by Jenny Nelson.[5]

Photovoltaics describes the conversion of light into electricity through the photovoltaic effect. A photovoltaic system consists of solar modules which are made of solar cells. A solar cell produces electricity by absorbing light, as shown in **Figure 3**. Theoretically any radiation can be used to be converted into electricity, even radioactive radiation like beta particles (called betavoltaic).[6] To give some historical introduction, the Bell Labs built the first solar cells out of silicon in 1954 with about 6% efficiency.[7]

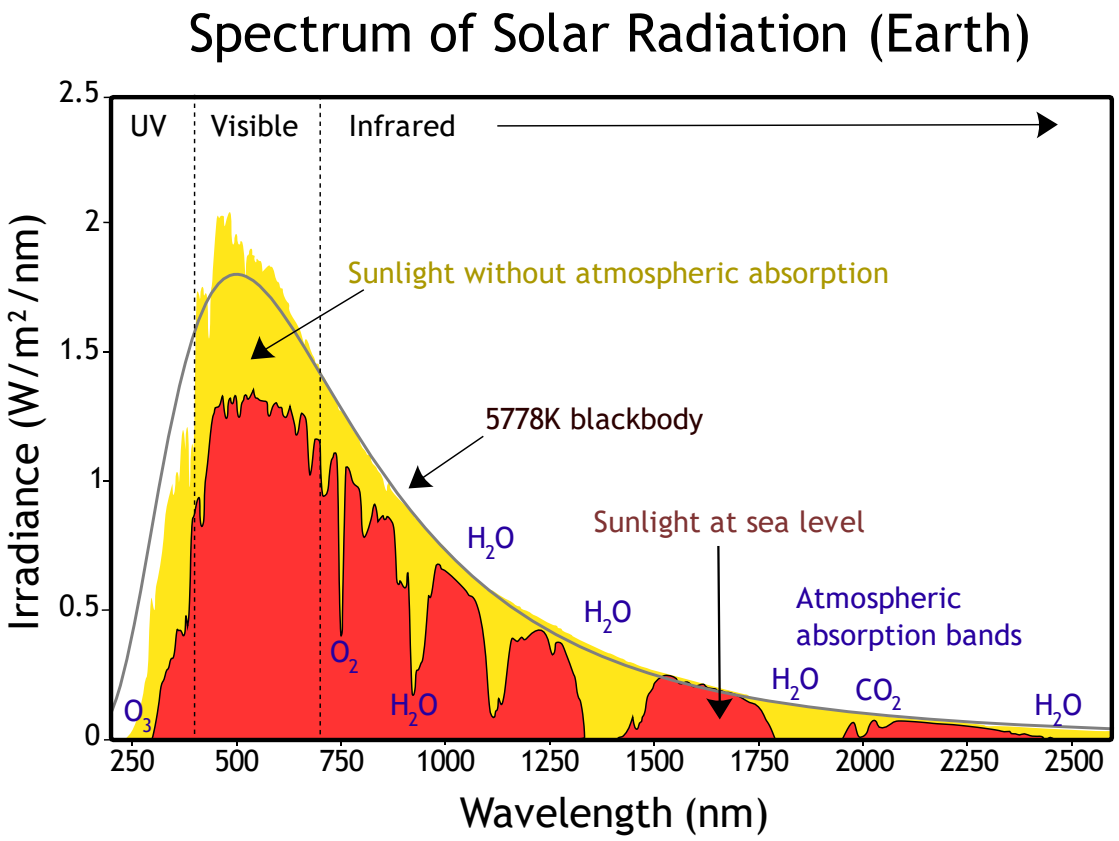

Figure 3 Sun light spectrum and the corresponding ideal black body spectrum for the surface

temperature, the solar spectrum (AM0) and the received solar spectrum at sea level (AM1). Adapted from[8].

The push to develop solar cells further originated from the space industry, where they proved to be the most reliable energy source for space missions. The critical mission was the Vanguard I, launched in 1958, which marked the first use of solar-powered satellites. The Vanguard I demonstrated remarkable longevity, operating for six years, while the concurrently employed battery system failed after just six days.[9] This early success underscored solar cells' reliability and longevity advantages in space applications. Today, PV systems are the typical energy source used in space missions like the international space station, as shown in **Figure 4**. In the following, I will explain how a solar cell works.

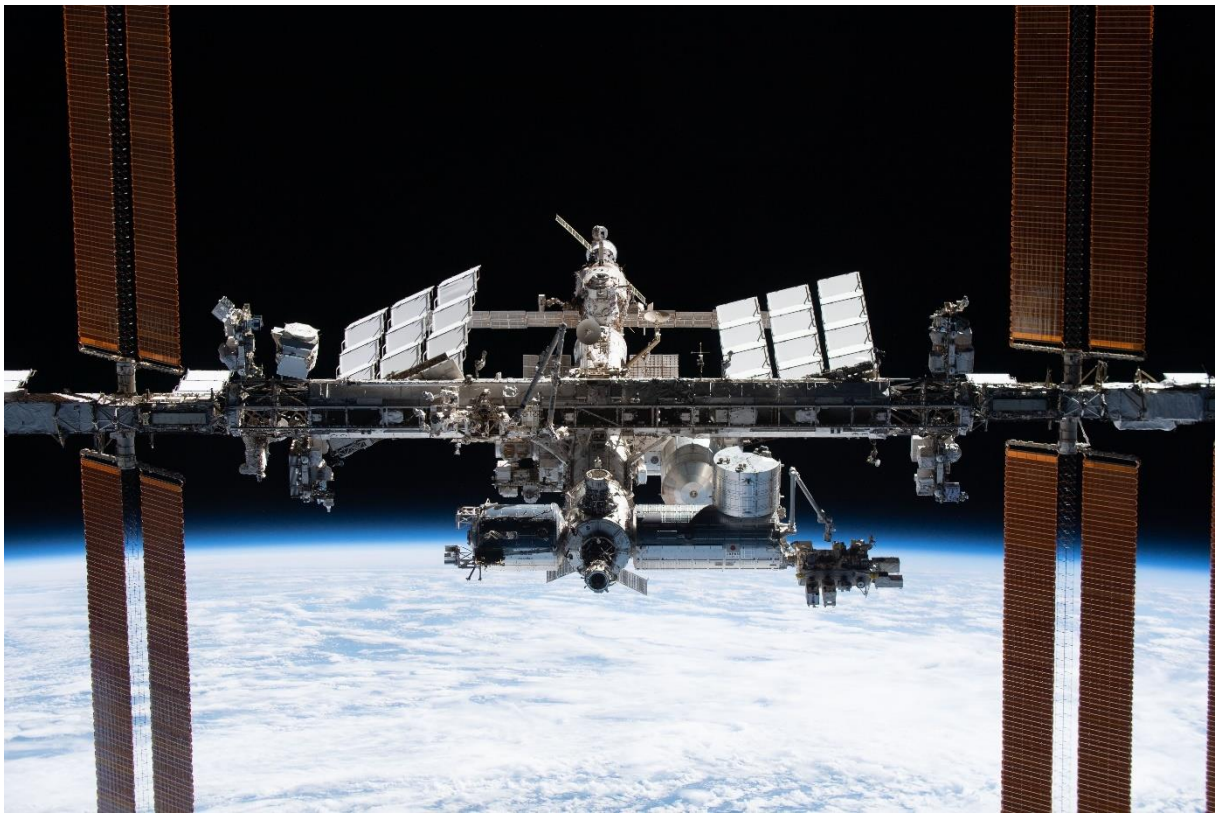

Figure 4 Picture of the International Space Station from the SpaceX Crew Dragon Endeavour on Nov. 8, 2021. The station is 263 miles above the Marshall Islands in the Pacific Ocean at the

moment the picture was taken. The 8 orange/gold panels right and left are PV devices. The picture was taken by NASA.[10]

Light consists of electromagnetic radiation. When absorbed by a semiconductor, the electrons within the material become excited and move to a higher energy band. The electron must be separated from the ground state to harvest this energy. The separation is feasible through the semiconductor bandgap and an asymmetric junction. The electron is excited from the valence into the conduction band. Excess energy is rapidly lost and the electron thermalises to the energy of the conduction band. In the case of metals, the electron could not be extracted because it would recombine through thermalisation with the ground state too quickly to be extracted. For an insulator, the bandgap is too large that the energy of the light is insufficient to excite the electron into the conduction band. Therefore, the semiconductor's bandgap should be significantly larger than the average thermal energy at room temperature (RT) of $k_BT \approx 25.7$ meV.

Upon excitation, the electron leaves behind a quasi-particle in the valence band with opposing polarity, a hole. In an equilibrium, for a solar cell in the dark, the probability of an electron or hole occupying an energetic state is given by the Fermi-Dirac statistic:

$$\bar{n}_i = \frac{1}{e^{(E_i-\mu)/k_BT} + 1}$$

Where $\bar{n}_i$ is the average probability of electrons or holes in a given energetic state E_i. μ is the chemical potential, k_B is the Boltzmann constant, and T is the temperature. At zero Kelvin, the chemical potential would be equal to the Fermi Energy. This equation also describes the Fermi level. It is the energy needed to add one electron to the semiconductor or in other words it is the kinetic energy of the highest occupied state.

Under non-equilibrium conditions, a solar cell under illumination, the Fermi level splits into two quasi-Fermi levels, one for holes and one for electrons. The deviation of each quasi-Fermi level from the equilibrium Fermi-level reflect the local concentration of electrons and holes within their respective bands, in the semiconductor. The difference in the quasi-Fermi levels defines the local chemical potential $\Delta\mu$. If electrons could be collected at one side of the semiconductor and holes the other, the potential difference would simply be $V = \Delta\mu$. Within the light absorbing layer, $\Delta\mu$ reflects the maximum voltage that a solar cell could produce under the current lighting conditions. The total energy increase or electrochemical potential energy is given by the Gibbs free energy, $N\Delta\mu$. N is the number of excited electrons. In the dark, $\Delta\mu=0$.

A gradient in at least one of the quasi-Fermi levels is required to produce power, typically achieved by having spatially varied concentrations of carriers. Two different driving factors can promote that and lead to the separation of the electron-hole pair. (1, drift) A built-in electric field that forms at the interface between two materials with a different work function. (2, diffusion) A charge-carrier gradient is produced through the selective removal of the charge carriers on opposite sides of the device. In perovskite solar cells, charge separation happens primarily via diffusion.[11–13]

In general, the main analysis tool of solar cells is the current-voltage characteristic (the IV-curve). The voltage is varied while measuring the current and the product of both defines the power the solar cell produces. A good solar cell has a J-V curve with the shape shown in **Figure 5**. In the following, the four key parameters which describe a solar cell are explained: The Fill Factor (*FF*), the short-circuit current (J_{SC}), the open circuit voltage (V_{OC}) and the power conversion efficiency (η).

The J_{SC} describes the current produced by the solar cell without an applied load (*V=0* V). It is related to the quantum efficiency (*QE*) of the solar cell. It describes the probability that an incoming photon will produce an outgoing electron for a given energy. It is typically given as a percentage, e.g. 80% of all incoming photons of a given wavelength produced an electron hole pair:

$$J_{SC} = q \int b_S(E)\, QE(E)\, dE$$

q is the elementary charge and b_S describes the incident light spectrum. It is the incoming photon flux density for a given energy, as shown in **Figure 3**. The current-voltage characteristic (J-V curve) for an ideal diode is given by:

$$J(V) = J_{SC} - J_{dark}(V)$$

Where $J_{dark}(V)$ is given with:

$$J_{dark}(V) = J_0(e^{\frac{qV}{k_B T}} - 1)$$

With that one can derrive the V_{OC} with:

$$V_{OC} = \frac{kT}{q} \ln\left(\frac{J_{SC}}{J_0} + 1\right)$$

With *T* being the temperature, *k* or k_B the Boltzmann constant and J_0 is a material property. The FF describes the "squareness" of the current-voltage characteristic. It is given by the ratio of the maximum power and the product of J_{SC} and V_{OC}:

$$FF = \frac{P_{MPP}}{J_{SC} V_{SC}} = \frac{J_{MPP} V_{MPP}}{J_{SC} V_{SC}}$$

The efficiency η is the ratio of the produced power divided by the incoming power of the light. It is given by:

$$\eta = \frac{P_{MPP}}{P_{Light}} = \frac{J_{MPP}V_{MPP}}{P_{Light}} = \frac{J_{SC}V_{SC}FF}{P_{Light}}$$

The dark current represents the potential from the load applied through the electrical circuit. In the dark the J-V curve would have the same shape only shifted to zero current at zero voltage. In **Figure 5**, a typical J-V curve under illumination is shown.

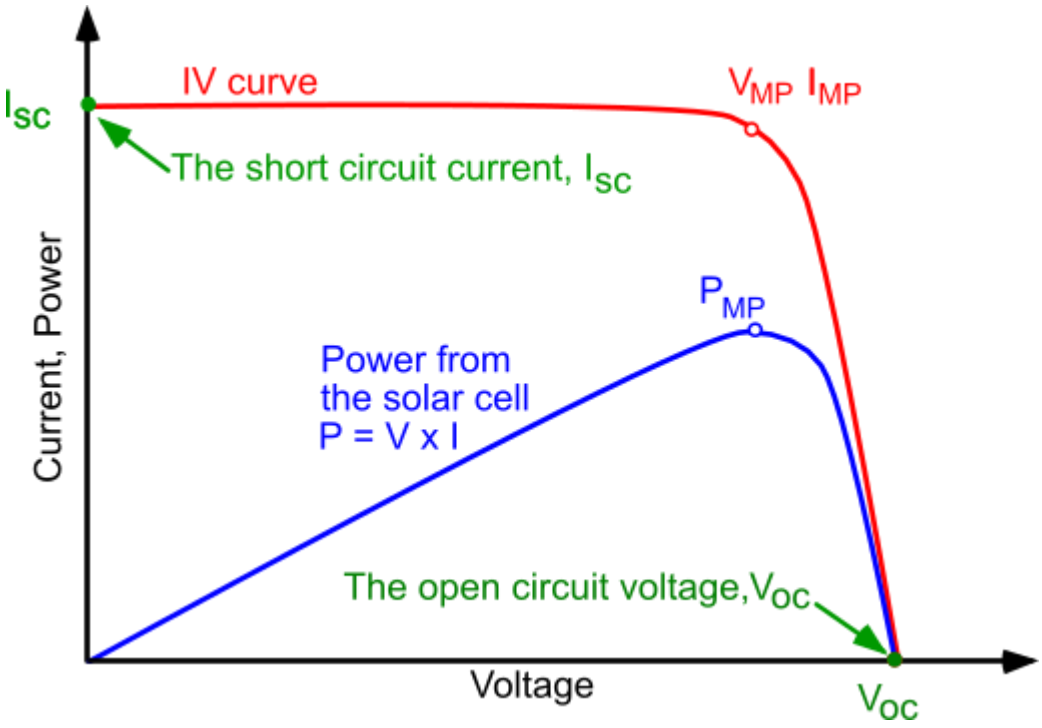

Figure 5 Typical IV-curve and the corresponding power. Adapted from [14].

9. Introduction to halide perovskites

Halide perovskites offer applications ranging from single photon detection[15] to light-emitting diodes (LEDs).[16] Especially prominent are the PV applications, which took off in 2012.[17,18] To give a brief historical introduction, halide perovskites were first used in a PV device by Miyasaka and co-workers in a dye-sensitised solar cell (DSSC) as nanocrystals in 2006[19] and 2009.[20] They synthesized the nanocrystals by combining lead iodide or lead bromide with the corresponding methylammonium halide salts. The dispersion was then spin-coated into the TiO_2 scaffold. They used an iodide-triiodide (I^-/I_3^-) liquid electrolyte redox couple to facilitate hole extraction.[20,21] However, the performance of the device often would last only for up to a few hours. Three years later, Snaith and co-workers[17] showed that it forms a solid at higher molarities and reached surprisingly high power conversion efficiencies (PCE) of 10.9%. At the time, most new emerging PV materials rarely got above 10% and typically only after decades of research. Snaith and co-workers also realised that the commonly used TiO_2 layer wasn't necessary since they could also use an insulating scaffold of AlO_x. The perovskite layer had good enough charge transport that the charge extraction scaffold, the TiO_2, became obsolete or at least could be significantly reduced in size. At the same time as Snaith, Park *et al.*[22] found that using a solid hole transporting material significantly improved the lifetime of their used methylammonium (MA^+) lead iodide nanoparticles (NPs). They reached 9.7% by optimising the thickness of the mesoporous TiO_2 layer. Interestingly, Kanatzidis and co-workers, around the same time, used a halide perovskite as a hole conductor in a solid state DSSC and observed an enhancement in the external quantum efficiency (EQE). However, it was unnoticed that the caesium tin iodide perovskite was photo-absorbing as well.[23] That set the start of an exciting development of solid-state halide perovskites used in photovoltaic devices.

Halide perovskite here describes the typical structure in which three or more elements, of which one is a halide form corner-sharing-octahedrons with one of the elements filling the space between the octahedrons as shown in **Figure 6**. They are described by $A^+B^{2+}(X^-)_3$ with A^+ being an inorganic cation like Cs^+ or an organic molecule like methylammonium (MA^+) or formamidinium (FA^+). B^{2+} is Pb^{2+} or Sn^{2+} (in rare cases also Ge^{2+}) and X^- is a halide as I^-, Br^- or Cl^-. The halides fill the corner positions of the octahedrons, with the metal filling the space in the octahedron, and the A-site filling the space between the octahedrons.

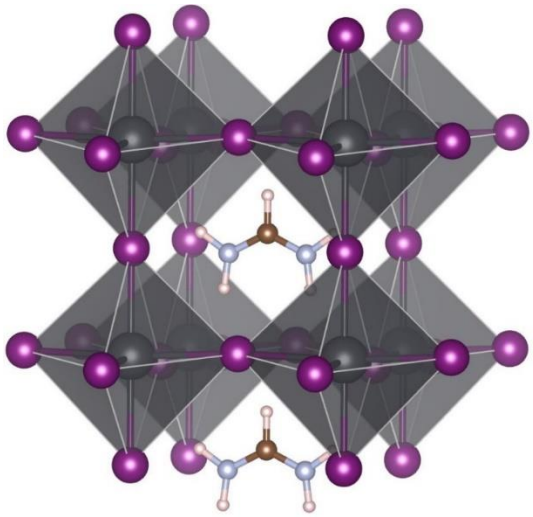

Figure 6 Crystal structure of $FAPbI_3$. The crystal structure was taken from [24]. Formamidinium is shown in the middle with carbon being brown, nitrogen is light blue and hydrogen is white. I^- is purple and Pb^{2+} is grey.

After the initial discovery in 2012, PSCs quickly improved and reached efficiencies of conventional and already established PV technologies like CIGS and silicon (Si). In the following, some critical findings for the rapid increase in efficiency are outlined in chronological order. Please note that often the highest efficiencies are achieved with

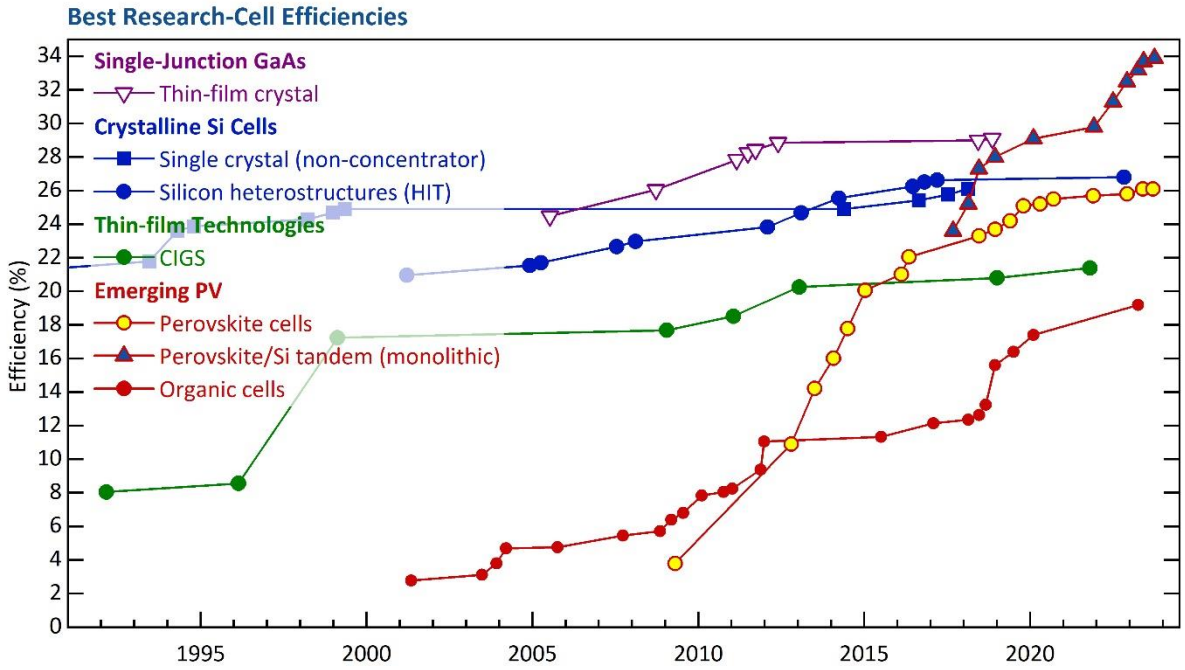

Figure 7 Best research cell efficiencies from National Renewable Energy Laboratory (NREL). Adapted from [25]. Accessed on the 03.01.2024.

solution-processed PSCs meaning that all precursor salts are dissolved in a solvent, mixed, deposited and dried producing a solid thin film. After the initial discoveries as already outlined, Bach and co-workers used a solvent (also called anti-solvent) to rapidly reduce the solubility of the precursor solution on the spinning substrate to rapidly form a dense and solid perovskite film.[26] Seok and co-workers changed the commonly used solvent system to coordinating and high-boiling point solvents like dimethyl-sulfoxide (DMSO) to dissolve the perovskite precursor materials.[27] That changed the crystallisation of the material, an intermediate phase formed with MAI–PbI_2–DMSO. Only by annealing the films at higher temperatures a full 3D perovskite phase would form. Further progress was achieved by mixing of different A-site cations, MA^+ and FA^+ [28] or later even three cations with Cs^+.[29] Pinning down the direct advantage of that is difficult but essentially all three cations have advantages and disadvantages and by combining all three cations the disadvantages (e.g. phase stability) can

be balanced. Also the net tolerance factor is within the stable region, more about that later in this chapter. More progress has been achieved by using a 2D perovskite as a passivator on top, mixed within or below the 3D perovskite layer.[30] This resulted in lower non-radiative recombination losses which are induced at the interface towards charge-transport layers. Finally, the change away from a mesoporous TiO_2 layer towards planar structures with for example SnO_2 or self-assembled monolayers (SAMs) as charge transport layers.[31,32] Through these advances PSCs managed to obtain certified 26.1%, approaching the efficiency of the market leader silicon solar cells of 26.8%, as shown also in **Figure 7**. In a stack with Si they surpassed any other tandem technology even III-V element solar cells as GAAs with certified 33.9%.[25] The first practical Si solar cell was presented in 1954.[7] Silicon has 70 years of research. Within only 12 years perovskite solar cells managed to almost close the gap at least in terms of efficiency.

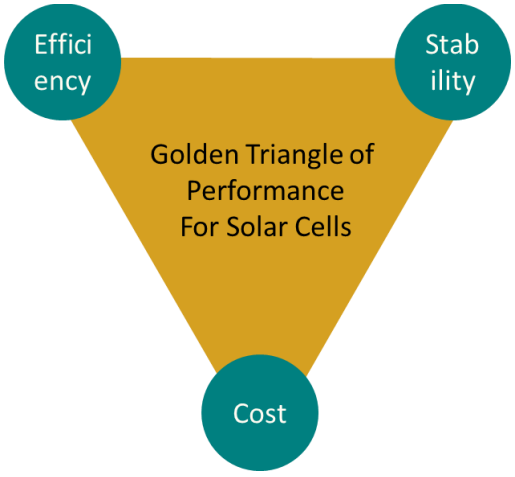

Figure 8 Golden Triangle of performance for solar cells.[33]

While the push towards higher-efficiencies is important, it is equally important that the solar cell retains most of its performance during the usage as device and that the cost of the device is low. That is summarised in the golden triangle of performance for solar cells as shown in

Figure 8. One can relate those three parameters through the levelised cost of electricity (LCOE). The LCOE is simplified the cost of the whole PV installation divided by the total produced energy of the system. In a previous work I used that to derive a parameter space which is defined through the LCOE of silicon solar cells. Meaning that to achieve the same price as silicon solar, the current PV market leader, perovskite solar cells have to achieve these parameters. Or in other words that is what halide perovskites have to achieve to improve PV and help tackle climate change. In **Figure 9,** I show that for scenario representative of 2021 in which the silicon solar cells last 25 years, has an efficiency of 19.9% (the US median value for 2021) and a LCOE of 11.9 US¢/kWh. All these values are based on the NREL PV Benchmark report.[34] The lifetime is given as T_{80} meaning the time until the devices reaches 80% of its initial PCE. Please note that the manufacturing cost are uncertain as they strongly depend on the materials which are used in the commercialised product. The shown manufacturing cost values are based on literature which model a low-cost architecture if it would be scaled-up and produced in large scales.[35–37]

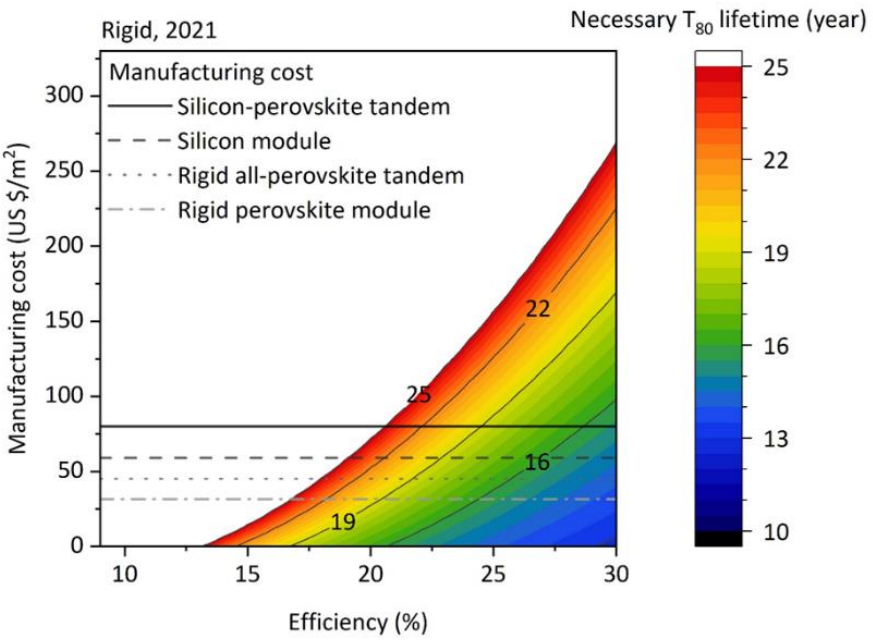

Figure 9 Cost analysis of silicon/perovskite tandems, perovskite/perovskite tandems, single-junction PSCs and a silicon module.[4] Please note that I made this figure. The indicated manufacturing cost are calculated low-cost manufacturing cost for all-perovskite tandem, a perovskite module and a silicon-perovskite module based on literature values. The line for the silicon module cost is the actual cost of a current module. The graph shows how long the modules would have to last depending on the efficiency and manufacturing cost to reach the same cost as silicon in 2021.

As shown in **Figure 9**, PSCs are likely required to last for at least a decade and likely even two. However, so far, most devices only last for days, months or a year. A key reasons for that is that high performance is often achieved by compromising stability. For example, Spiro-OMeTAD, a hole transporting material (HTM), is used in many record efficiencies PSCs even though it is fairly established that the material and the necessary dopings with it cause instabilities.[38] In other words, there is a temptation to use materials which lower the stability in the push for higher efficiencies. Another challenge with improving the stability further lies

in the variety of different conditions it has to be stable under heat, light, moisture, air, electric fields and mechanical pressure.[39] However, assessing if a change to the device improves the stability under all conditions is challenging and takes often significant time. For example, light-stability measurements can take up to 6 weeks or longer, especially if tested under different temperatures and humidity the time-frame can be several months. A third challenge comes from the difficulty in understanding the origins of degradation in a PSC. Multiple layers and materials are used together and it is difficult to disentangle the influence of each layer and material. Given these challenges the focus of this work is on studying the change of the perovskite layer itself first and then later understanding how that change impacted the stability in the full device.

10. Stability of lead halide perovskites

In the following, the major stability challenges of lead halide perovskites are outlined. One of the key challenges is the decomposition of the organic cations and the subsequent degassing of their degradation products and the formation of the wide-bandgap PbI_2. Especially MA^+ is susceptible to deprotonation and consequently reacts with neighbouring atoms, such as iodide, forming HI and CH_3NH_2 which evaporate.[40] Consequently, compositions without MA+ have been becoming the focus for a more stable perovskite. However, even the more thermally stable MA^+ free perovskites suffer from instabilities. The other two binary lead perovskites, $CsPbI_3$ and $FAPbI_3$, are phase-unstable. So, at RT and especially at lower temperatures they are thermodynamically prone to change from a perovskite structure to a non-perovskite structure, called δ-phase. The common solution for that is mixing FA^+ and Cs^+. The resulting $FA_{1-x}Cs_xPb(I_{1-y}Br_y)$ perovskite with $0 < x < 1$ and $0 \leq y \leq 1$ is phase stable at RT. However, under different stress, for example, moisture exposure it is possible that the ions, FA^+ and Cs^+, segregate to form individual phases which are subsequently again phase-unstable. Overall, it seems more likely that it is possible to improve the phase instability of $FAPbI_3$, $CsPbI_3$ or a mixture of both compared to creating stable $MAPbI_3$.[41] Given that MA^+ is inherently more susceptible to heat and more likely to deprotonate than FA^+.[42]

Further stability challenges arise from the halides. In particular, Iodide is prone to degas as I_2 or HI and leave the perovskites structure.[43] Additionally ion migration under light or an electric field might cause detrimental reactions at the interfaces or might worsen the charge extraction.[44] Further other elements from adjacent layers like the metal contact layer might migrate into the perovskite layer and cause the formation of recombination centres or react with the halides.[45] Equally the halides can migrate to the metal electrodes and react with

them.[46] If water is present the perovskite might also hydrate and finally further go into the hexagonal phases from which it then further decomposes.[47] Further there are mechanical adhesion issues especially happening in planar n-i-p structures, meaning the layers can break apart and voids are forming.[48] In summary, there is a variety of different decomposition pathways which are depending on the exact perovskite compositions, the conditions under which the perovskite is aged and in a solar cell the exact device stack. See **Figure 10** for a comprehensive summary.

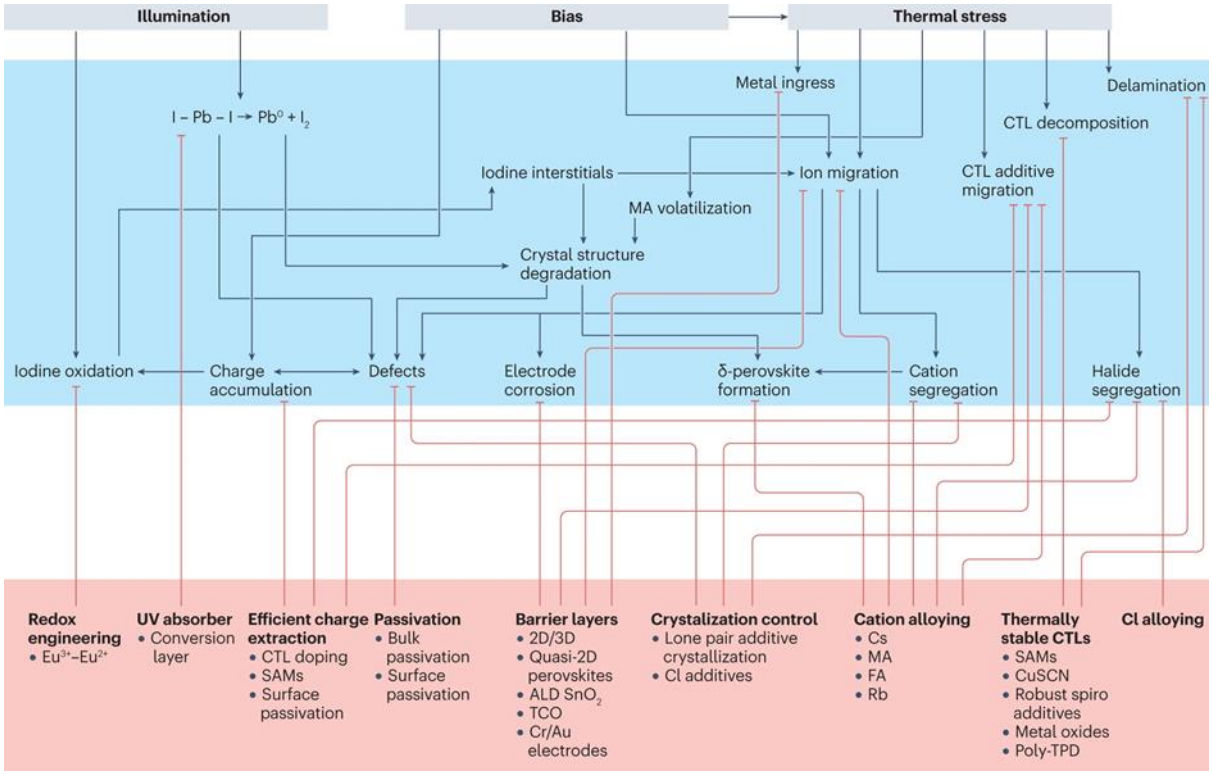

Figure 10 Grey boxes are causes, the blue box are effects and the red box are mitigation strategies and specific implementations. Adapted from [49].

In the following I will outline some of the major progresses for more stable perovskite solar cells which have been reported so far. The first one was changing from a solution to a solid perovskite absorber.[17] That MA^+ is especially volatile and leaves the structure easily.[50] A few

years later it became clear that there are significant influences of the adjacent layer and that for a stable perovskite cell also a stable architecture is needed.[51] Good advancements were also made by improving the encapsulation.[52] Furthermore, the addition or usage of a 2D perovskite was found to improve the stability especially in the presence of moisture.[53]

Some of the recent noticeable device stability achievements are mentioned below. An especially challenging target is the stability under light at 85 °C - the likely highest operating temperature PSCs would encounter.[54] Recently, two research groups reported especially promising results for that. The group around Alex K.-Y. Jen used a 2D conjugated metal–organic framework as an electron transporting layer (ETL) at the perovskite/metal interface and reported 90% after 1000 hrs under maximum power point (MPP) at 85 °C under continuous light exposure.[55] The group around Yanfa Yan reported a passivation of the perovskite with a phosphorus-containing molecule which apparently binds to lead.[56] Their devices retained more than their initial efficiency at 85 °C under light at open circuit (OC) for more than 1500 hrs. In summary there was a continuous and significant progress in the stability of PSCs but it is not yet enough for a successful commercialisation. Perovskite solar cells will have to last for decades to reach the same price as silicon.

Besides that there seem to be some general trends in the stability of halide perovskite as recently analysed by Jacobsson and co-workers.[57] They analysed stability data of over 7000 devices and found that especially a carbon electrode is important for a stable PSC. That is consistent with reported stability records, for example, by Grancini et al.[58] for over 1-year stable devices under continuous light at 55 °C, which also used a carbon electrode in a HTM free, fully printable mesoscopic architecture.[59] However, so far PSCs with carbon electrodes are lacking significantly behind in efficiency. Similar electrode designs, however, reached

higher efficiencies. Liyuan Han and co-workers fabricated a composite of copper–nickel (Cu–Ni) alloy which was covered by an in situ grown bifacial graphene which they hot-pressed onto the device.[60] They reached 24.34% and an impressive light stability at RT of over 5000 hours with only 5% loss of the initial performance. In summary, it is fairly established that for a more stable halide perovskite device a not-metal electrode will be needed[46,61] or at least a dense and continuous layer which prevents the halides from reaching the metal. Boyd et al.[62] showed that this is can be challenging since the halides can also migrate lateral and even a uniform and impermeable ITO layer is not necessarily enough to prevent them from reaching the metal contact.

Jacobsson and co-workers[57] also found that $CsPbI_3$ is more stable than $FAPbI_3$ which again is more stable than $MAPbI_3$. $CsPbI_3$ is general described as an inorganic perovskite since only Cs^+ is used as A-site cation. However, often organic materials like DMA^+ are used to phase-stabilise the perovskite. So, one has to be cautious in assuming that the photo-absorber is inorganic – it likely is not. In general, it also has to be noticed that the phase instability of the $CsPbI_3$ is more severe than for $FAPbI_3$. Under ambient air exposure at RT pure $CsPbI_3$ will degrade within seconds to minutes while pure $FAPbI_3$ will last hours to days. The exact duration till both perovskites are fully degraded depends strongly on the exact fabrication, especially the temperature at which the perovskite layer was annealed and how it was cooled are important. A noticeable work about $CsPbI_3$ was recently published by Yueh-Lin Loo and co-workers.[63] They used large amount of polyvinylpyrrolidone (PVP) as addition to the perovskite precursor which was later removed by soaking the perovskite layer in IPA afterwards. The novelty of their work was the usage of a CsCl treatment after the fabrication to create a 2D $Cs_2PbI_2Cl_2$ perovskite layer on top of the inorganic perovskite. Additionally, they observed a temperature dependent degradation behaviour which fitted to an Arhenius reaction rate behaviour. From

that they estimated that their $CsPbI_3$ devices with a 2D capping layer would last more than 5 years at 35 °C. However, at 110 °C in air without encapsulation their 2D capped $CsPbI_3$ devices degrade within a few hours. In the following, I will go into more detail what describes the phase stability of perovskites.

10.1. Tolerance Factor

The tolerance factor describes the size which the three or more different ions need to have to form a 3D perovskite structure. It is supposed to be a guidance to predict novel 3D perovskite structures, but it can fall short of accurately predicting the formation especially for hybrid materials. However, regardless of its accuracy understanding the limits of the tolerance factor is surprisingly useful in also understanding the challenges of creating phase-stable perovskites. In the following, I will outline various models for the tolerance factor starting with the first and most fundamental model the Goldschmidt tolerance factor. Novel tolerance factor models are described as well.

10.1.1. Goldschmidt tolerance factor

This tolerance factor is based on a mathematical model derived by Goldschmidt in 1926.[64] It is based on the idea that the ions in the cubic perovskite lattice are solid spheres which are not moving. Meaning each ion is only occupying one lattice site, also called non-rattling principle. It is important to keep these assumptions in mind given that they are for example not fulfilled for $CsPbI_3$.[65] The tolerance factor t is given by:

$$t = \frac{r_A + r_X}{\sqrt{2}\,(r_B + r_X)}$$

Where r_A, r_B and r_X are the ionic radii of the cation, metal and halide, respectively. To understand the valid range of the tolerance it is necessary to introduce the octahedral factor μ.

$$\mu = \frac{r_B}{r_X}$$

Filip et al.[66] further expanded the model and introduced guidelines for the tolerance factor. In **Figure 11** the limits of the tolerance factor are shown. It is solely based on geometrical principles. So, assuming one expands the size of an element further how long can the perovskite lattice still form. Based on the calculations one can derive various limits the stretch limit (SL, **Figure 11B**), octahedral tilt (OL, **Figure 11C**), tilt limit (TL, **Figure 11D**), chemical and secondary stretch limit (CL and SSL, respectively). The combinations of different limits give the region (**Figure 11E**) in which a 3D perovskite would form. Please note that $\bar{\mu}$ is for the $APbI_3$ perovskites the same as μ.

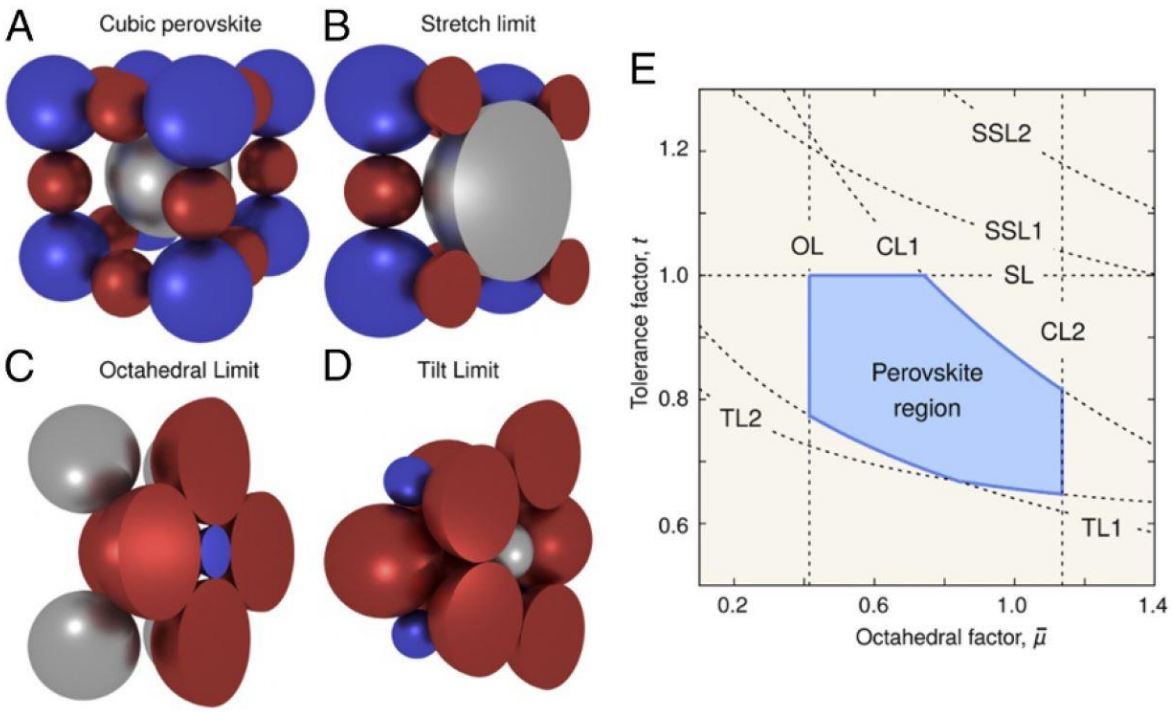

Figure 11 Goldschmidt tolerance factor limits: (**A**) cubic perovskite, (**B**) stretch limit, (**C**) octahedral limit, (**D**) tilt limit and (**E**) the resulting perovskite region. Adapted from [66]

For lead halide perovskites, one can plot this for $APbI_3$, with A being a monovalent cation. Commonly used ionic radii are taken from Shannon's work.[67] For lead halide perovskites, values are also typically taken from Kieslich et al.[68] However, determining the exact ionic radii is difficult given the strong dependence on the individual lattice. I show the tolerance factor for various reported radii in **Figure 12**. The molecules were selected based on their size, and because they were typically used in 2D and 3D halide perovskites. The calculated radii of each molecule are based on [69].

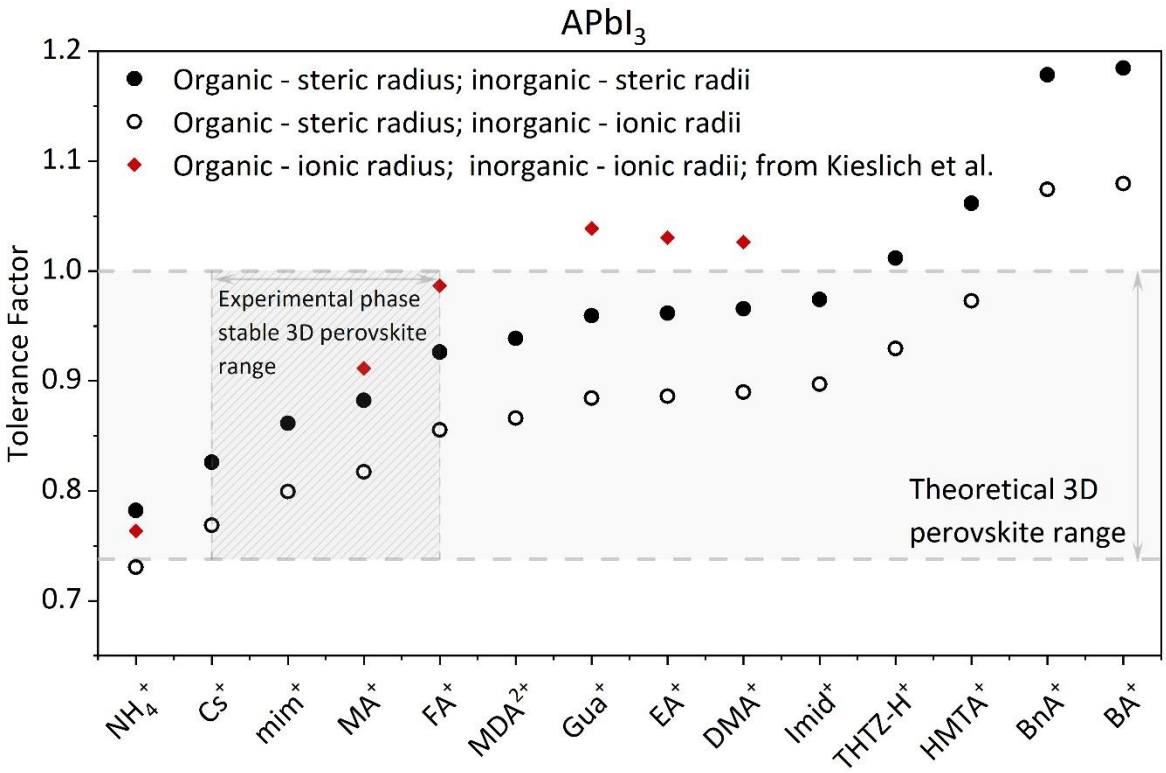

Figure 12 Goldschmidt tolerance factor for monovalent cations which are used in $APbI_3$ perovskites for different possible radii. The steric radii are based on DFT calculations by Santanu Saha and Marina R. Filip or Shannon radii. Ionic radii are based on Shannon radii or by Kieslich et al.[68] The grey shaded area represents the region in which perovskites should form according to the Goldschmidt tolerance factor. Here μ is 0.54 and so the lower limit of the tolerance factor is 0.74. The higher limit is for any cubic perovskite structure always 1. The experimentally-reported phase stable region is between Cs^+ (lower) and FA^+ (upper), as highlighted. Both $CsPbI_3$ and $FAPbI_3$, have a metastable 3D cubic perovskite phase under ambient conditions. NH_4^+ is ammonium, mim is methaniminium, MDA^{2+} is methylenediammonium, Gua^+ is guanidinium, EA^+ is ethylammonium, DMA^+ is dimethylammonium, $Imid^+$ is imidazolium, tetrahydrotriazinium is $THTZ\text{-}H^+$, $HMTA^+$ is hexamethylenetetramine, BnA^+ is $[PhCH_2NH_3^+]$ and BA^+ is $[C_4H_9NH_3^+]$. Adapted from [69]. Please note that I made this graph.

The strength of the tolerance factor lies in its ease of application, and one is free of typical concerns associated with experimental work. However, as shown in **Figure 12,** the accuracy of the tolerance factor is limited. Below are some of the challenges with it elaborated:

- Hard sphere assumption

The Goldschmidt tolerance factor assumes that the elements are solid spheres which don't change their size depending on the surroundings. This assumption is accurate primarily for perovskites with O^- or F^- where the electronegativity is large and the bonding is largely ionic.[70] However, for heavier halides the electronegativity is lower and especially iodide is softer chemically. So, this assumption is less valid. Also, for organic molecules the shape might change. For example, Kubicki et al.[71] showed that the organic molecule guanidinium can re-orientate once it is incorporated in the lattice.

- Non-rattling principle

Further, it is assumed that each ion only occupies one lattice site in the perovskite structure; in other words, it does not vibrate (rattle) and leaves its spot between the Pb-halide scaffold. However, as already mentioned, that is not valid for $CsPbI_3$. Cs^+ rattles in its cage, and together with the low number of iodide contacts and the distortion of the octahedrons, it causes the material to decompose at RT.[65]

- Cubic lattice

All calculations assume that the lattice is cubic. However, recent research by Doherty et al. suggests that for at least $FAPbI_3$, the lattice is possibly more accurately described with a tetragonal structure.[72] That would have interesting implications given that $FAPbI_3$ is at the higher end of the tolerance factor close to the stretch limit. However, this limit is only valid for cubic structures.[66]

- Estimating accurately ionic radii

Ionic radii are typically extracted from crystallographic data. However, the definition of ionic radii varies, and even in the same definition, there are variations depending on the

coordination and local chemistry.[66] Therefore, Palgrave et al.[70] suggested a revised ionic radii system which is more suitable for halide perovskites. It is further outlined below.

- Molecules are not a sphere

The fundamental assumption of the tolerance factor is that one can fit each ion with a sphere. While that is accurate for atoms, it is challenging for molecules, which can have complicated structures. Saliba and co-workers[73], therefore, introduced the globularity model. They fit the molecule surface and give a number of how close the shape is to a sphere.

There are further challenges which are more related to the experimental conditions. Typically, halide perovskites are fabricated at lower temperatures around 100 to 150 °C. So, the lattice can still include other low-temperature phases or solvents.[69] Given all these challenges further efforts have been dedicated to developing improved tolerance factor calculations. An important one is outlined below.

10.1.2. Revised radii for an improved tolerance factor

Palgrave et al.[70] also revisited the tolerance factor of Goldschmidt and found that especially the assumption that the ionic radius of the halide is not accurate. They found that the commonly used halide radii derived by Shannon[67] is accurate for oxides and fluorides but not for heavier anions especially iodide. They compared the ionic radii derived by Shannon with other measured radii for MX_6 octahedra and derived revised ionic radii $r_{B(x)}$ for the metal depending on the halide *X*. For chloride that $r_{Pb(Cl)}$ is 0.99, for bromide it is $r_{Pb(Br)}$ 0.98 and iodide is $r_{Pb(I)}$ is 1.03.

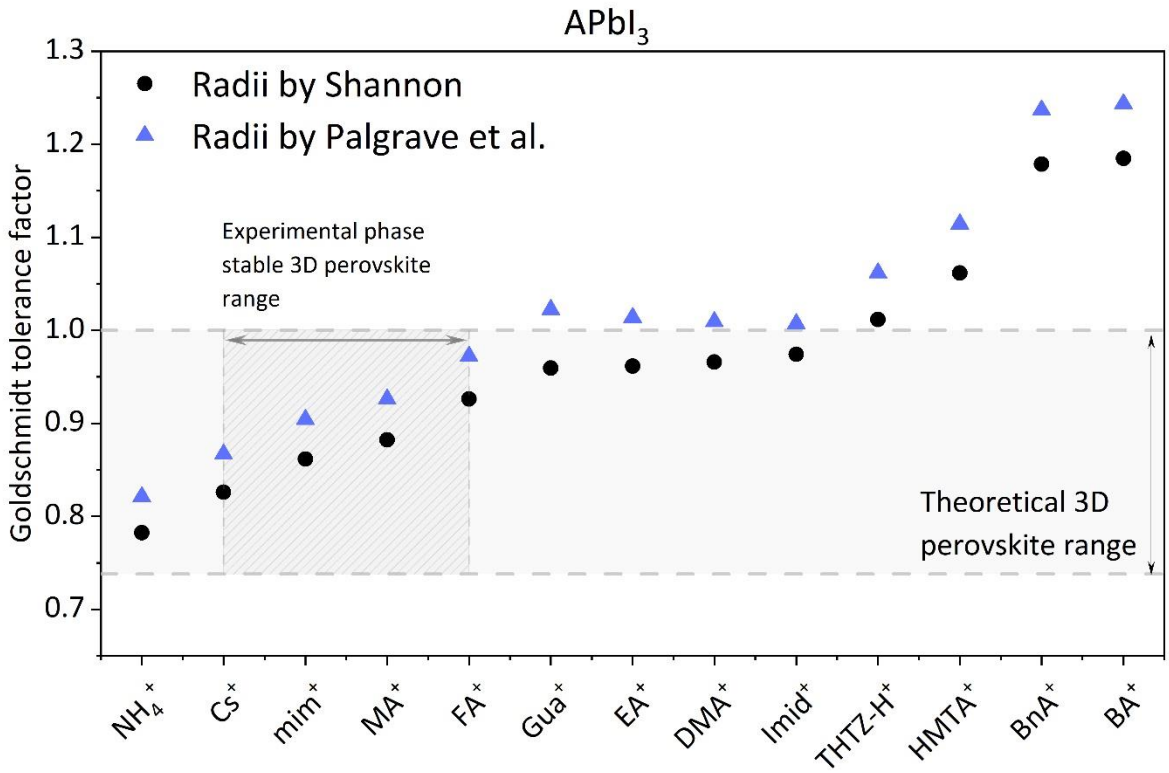

Figure 13 Goldschmidt tolerance factor with revised radii for the B-site by Palgrave et al.[70] compared to the ones by Shannon et al.[67]

As shown in **Figure 13** the Goldschmidt tolerance factor fits well with the experimental data with the revised radii for the B-site. Please note that for the A-site I and also Palgrave et al.[70] used the approach of Kieslich et al.[74] to estimate the radius of the organic which is based on:

$$r_{Aeff} = r_{mass} + r_{ion}$$

With r_{Aeff} being the effective radius of the A-site cation. r_{mass} is the distance from the centre of mass of the molecule to the furthest distant atom which is not hydrogen and r_{ion} is the corresponding radius of this atom.[68]

In summary, the tolerance factor is a useful tool to understand the impact of the individual cations, metals and halides have on the phase-stability of halide perovskites. For $FAPbI_3$ it is close to the stretch limit meaning the A-site is slightly too large. For $CsPbI_3$ the Cs^+ atom does

not fulfil the non-rattling principle. In Chapter 1 and 2, I will be using DMA^+ as excess cation and find that it is residual in the material. As shown in **Figure 13**, it seems likely that it could at least be partly incorporated into the perovskite lattice. In the following, the phase-stability of halide perovskites is further elaborated and explained.

10.2. Phase-stability of $FAPbI_3$ and other lead halide perovskites

$FAPbI_3$ is a polymorph meaning it is crystalline material which exists over a broad range of different phases. The cubic photoactive phase of $FAPbI_3$ is called α-phase and at RT it tends to degrade into a hexagonal δ-phase, also called 2H. Additionally, there is also a β- and γ-phase. The β-phase is similar to the α-phase only with slightly tilted octahedrons and not anymore cubic but a tetragonal structure. The β-phase is the intermediate phase between the α- and γ-phase. The low-temperature black phase is the γ-phase. All phases are shown in **Figure 14**.

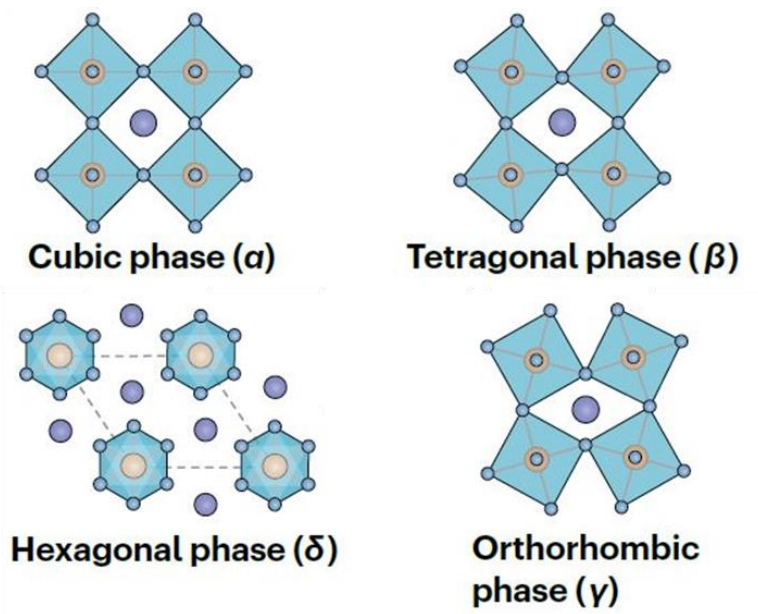

Figure 14 Different possible phases of the halide perovskites. With the FA^+ being a dark blue sphere, lead being beige and iodide being light blue. Adapted from [75].

The exact structure of $FAPbI_3$ at RT matters as Doherty et al.[72] found that the degradation of the perovskite starts at the cubic phase and then propagates further into the material. In comparison the tetragonal structure frustrates the phase transition and stabilises the perovskite phase. There are different reports for the crystal structure of the black α-phase of $FAPbI_3$ at RT. The main difference lies in the orientation of the FA^+ molecule. Chen et al.[76] solved the structure as cubic with $Pm\bar{3}m$ symmetry and lattice constant of a_c = 6.3855(2) Å. In there they found that the FA molecules have isotropic orientation meaning there is no preferred alignment. Stoumpos et al.[77] have fitted $FAPbI_3$ with a trigonal structure with a well-defined FA molecule position. Overall, the cubic structure seems to be the one commonly reported for single crystals of $FAPbI_3$, as various reports, as described in the following, also found a cubic structure. Weller et al.[78] found in two reports that it adopts a cubic structure with a = 6.3620(8) Å, in which the FA^+ molecule is located in the central mirror plane. They found that the FA molecule also very quickly rotates at RT. Kieslich et al.[78,79] also found that $FAPbI_3$ single crystal adopt a cubic $Pm\bar{3}m$ structure at RT with a = 6.3566(2) Å. Seshadri et al.[80] fitted $FAPbI_3$ single crystals also with a cubic $Pm\bar{3}m$ structure with a = 6.35788 Å at 299 K.

Interestingly, the work by Kieslich et al.[74] and Weller et al.[79] also showed that $FAPbI_3$ single crystals have a phase transition from the cubic $Pm\bar{3}m$ structure to a tetragonal *P4/mbm* phase between 300 and 250 K. This tetragonal phase has slightly tilted octahedrons and a checker board alignment with the FA^+ molecule following the alignment and stretching them out as well. This checker board alignment was also reported for the tetragonal phase of $FAPbBr_3$ by Franz et al.[81] Šimėnas et al.[82] developed on the results by Franz also a general model describing the phase transition from the cubic to the tetragonal phase. They find that the quadrupole moment of the FA^+ cations causes the checkerboard alignment of the molecules.

Meaning that the electric field of the molecules matters since it changes the orientation of other aligning molecules.

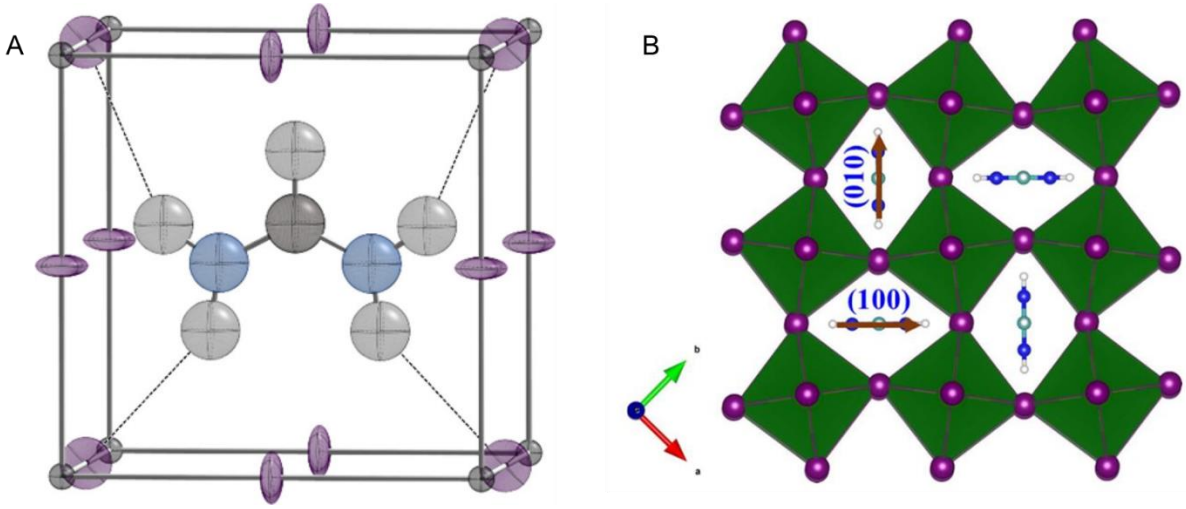

Figure 15 (**A**) The cubic unit cell of α-$H_2N–CH–NH_2PbI_3$ ($FAPbI_3$) single crystal according to Weller et al.[78] The ellipsoids are indicated at 30% probability. Blue is nitrogen, grey is hydrogen, dark grey is carbon, lead is dark grey, iodide is purple and NH-I bonds are dotted lines. Please note that this is one of 12 different possible arrangements the FA^+ molecule can take in the cavity between the octahedrons. These results are in agreement with the reports of Seshadri et al.[80] and Kieslich et al.[74] Adapted from [78]. (**B**) The tetragonal phase of $FAPbI_3$ from Weller et al.[79] The cubo-octahedral cages stretch out in the [100] or [010] lattice directions. The FA^+ cations align themselves in the same elongated direction, as indicated by the brown arrow. This checker board alignment is consistent with their ab initio molecular dynamics simulations which also demonstrates a similar tilting pattern of octahedra and the orientation of FA cations within the cages. These results are also consistent with the reports by Franz et al. for $FAPbBr_3$.[82] Adapted from [79].

Regardless of what the initial crystal structure of $FAPbI_3$ is, it is already surprising that $FAPbI_3$ is meta-stable at RT and that this meta-stability depends strongly on the fabrication process.

To understand that further, it is helpful to understand the phase transition between the cubic and hexagonal phases, which will be discussed in the following. Since it is not a direct group/subgroup transition between the two different phases, there must be a complex combination of sliding and twisting among the organic molecules, lead, and iodide atoms, leading to the breaking and forming of Pb-I bonds. Meaning that several atoms and molecules have to move for the transition to occur. From an energy landscape perspective, this complex transition does not occur spontaneously, but rather requires to overcome an energy barrier between the two final states.[76]

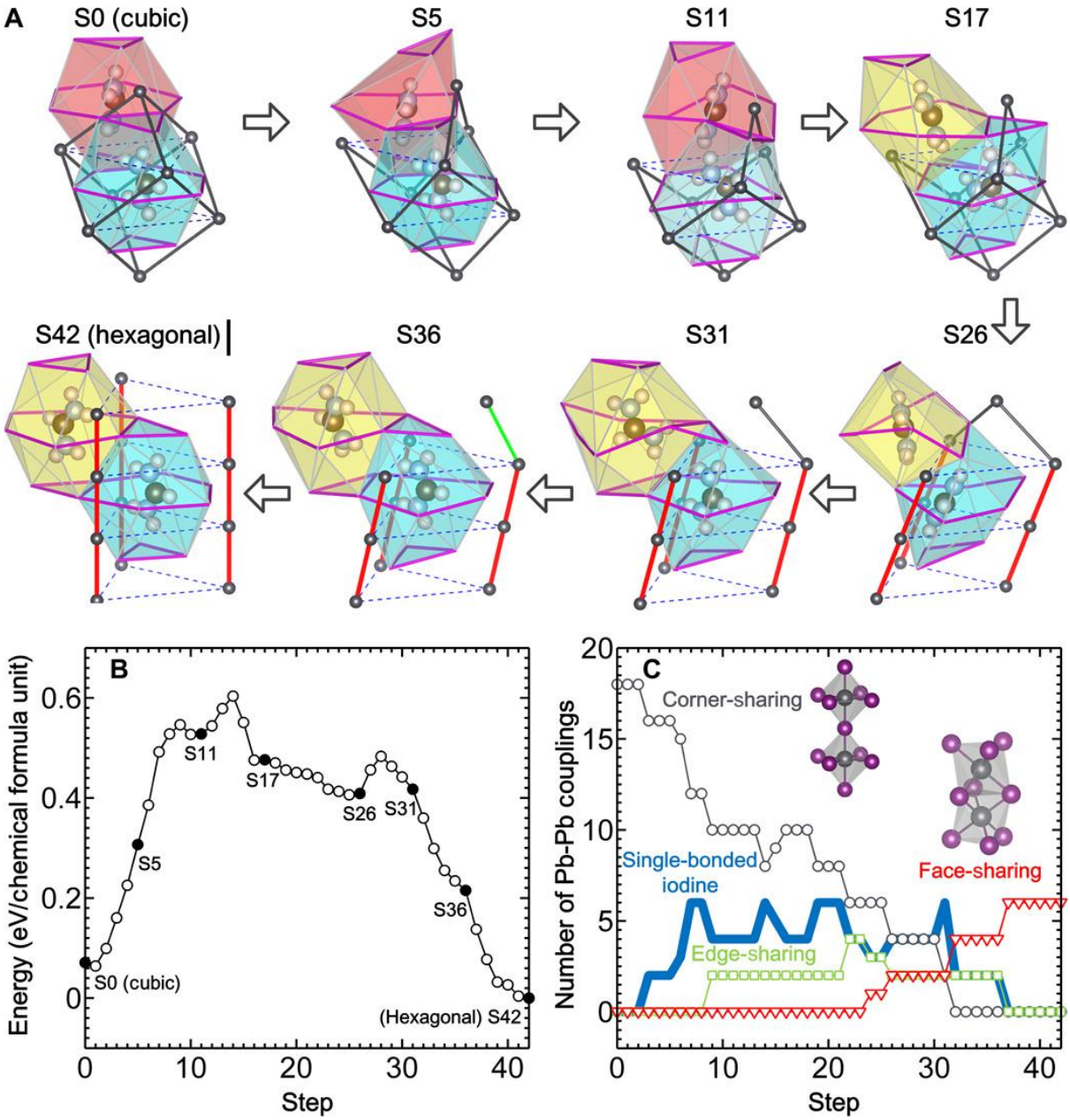

Figure 16 (**A**) This illustration shows a possible pathway for transitioning from a cubic structure to a hexagonal structure. The colored polygons represent cages formed by iodine atoms. Purple lines indicate the movement of iodine atoms and the distortion of cages during each step. The eight spheres inside each polygon represent the FA^+ cation, while the dark gray spheres represent lead atoms. Each lead atom is surrounded by six iodine atoms. The dark gray, green, and red solid lines connect neighboring lead atoms that share one, two, and three iodine atoms, respectively. The dark gray lines in the initial cubic structure depict the unit cell's cube, while the dashed blue lines in the final hexagonal structure connect lead atoms in different unit cells in the hexagonal ab plane. (**B**) Calculated energies of

the structures along the pathway from the cubic to the hexagonal phase. (**C**) The number of corner-sharing (dark gray symbol), edge-sharing (green symbol), and face-sharing (red symbol) PbI_3 octahedra, as well as single-bonded iodine atoms (blue symbol), per six cubic unit cells along the pathway. Adapted from [76].

In **Figure 16A** a possible pathway from the cubic to the hexagonal phase is illustrated showing some of the 43 phase transition intermediates. Please note that this is only one of many possible pathways and the height of the final energy barrier between the two states depends on the exact pathway between them. In other words, the phase transition can also happen through a different pathway in which different combinations of movements occur. In **Figure 16B** the energies derived from density functional theory (DFT) calculations are shown for each phase transition intermediate. In **Figure 16C** an overview is given of the different arrangements during the pathway. Please note that the hexagonal phase is face-sharing and the cubic phase is corner-sharing. Any change from the shown cubic structure would change the total barrier height and length towards the hexagonal phase. Showing again why understanding and characterising the initial crystal structure matters. Because possible a solution towards a phase-stable $FAPbI_3$ under typical solar cells operating temperatures lies in changing its initial phase so that the energy barrier is high enough to keep $FAPbI_3$ in its photoactive phase. **Figure 17** shows from a thermodynamic perspective how the delta and alpha phase relate energetically. An ideal solution would be to make the black phase the thermodynamically favoured phase. However, as an anecdotal note to that, even diamonds have at 25 °C atmospheric pressure a negative Gibbs free energy to change to graphite.[83] The necessary activation energy, however, is too large so that it is not observed. In other words, ΔG (the difference in Gibbs free energy) is no measure of the rate of the reaction which might matter.

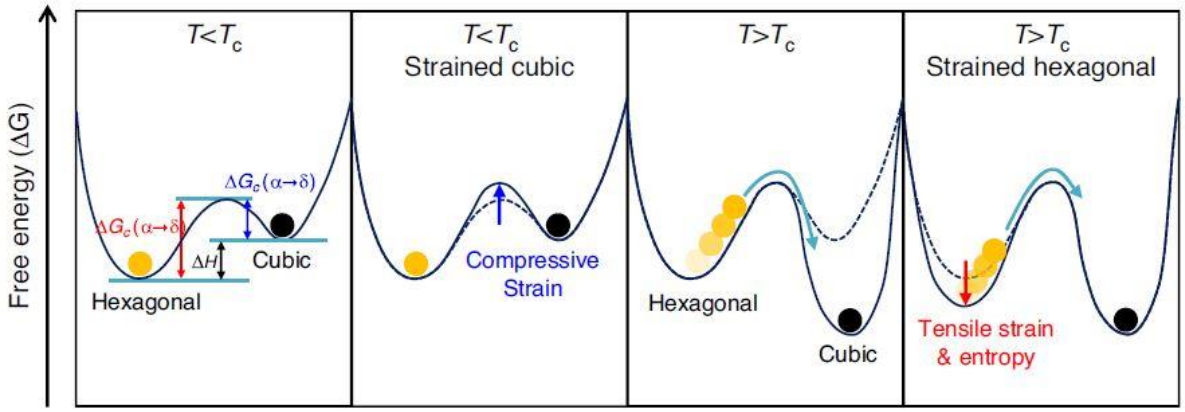

Figure 17 Change of Gibbs free energy (G_C) depending on the temperature and applied strain. T_c is the critical temperature at the which the cubic phase is more favored than the hexagonal phase. H is the enthalpy. Adapted from [84]. Please note that this is a simplification, as shown in **Figure 16** the energy barrier between the α- and δ-delta phase is not a single peak but rather a series of peaks.

In the following, I will discuss how solvents impact the phase stability of lead halide perovskites.

10.3. Residual solvents

It is possible that solvents like γ-butyrolactone (GBL) are remnant in the single crystal and thin film structure, which might have an impact on the size of the crystal structure and other properties.[69] Seok et al.[85], for example, showed that residual GBL is the reason for a significant faster phase transformation of $FAPbI_3$ single crystals from the α-phase into the δ-phase. As shown in **Figure 17A**, they dissolved an equal amount of FAI and PbI_2 and added enough GBL that the precursors material didn't dissolve visible as yellow precipitate in the solution. They added then enough solvent until the precipitate vanished. Afterwards, they increased the temperature which caused the precursor again to precipitate because of the inverse solubility

in GBL.[86] They then added again more solvent to measure a solubility curve. Interestingly, from 90 °C the precipitate isn't any more yellow (indicative of the hexagonal phase) but now forms in the black phase. That, indicates that the interaction of the solvent with the precursors might change the energy barrier height between the two different phases, as shown in **Figure 18B.** Meaning that residual solvents have likely a strong impact on the phase stability on the lead halide perovskite. That is also what I find in Chapter 2 of this thesis. In the next section I will talk more about the different perovskite solar cell architectures and the fabrication of the halide perovskite layer.

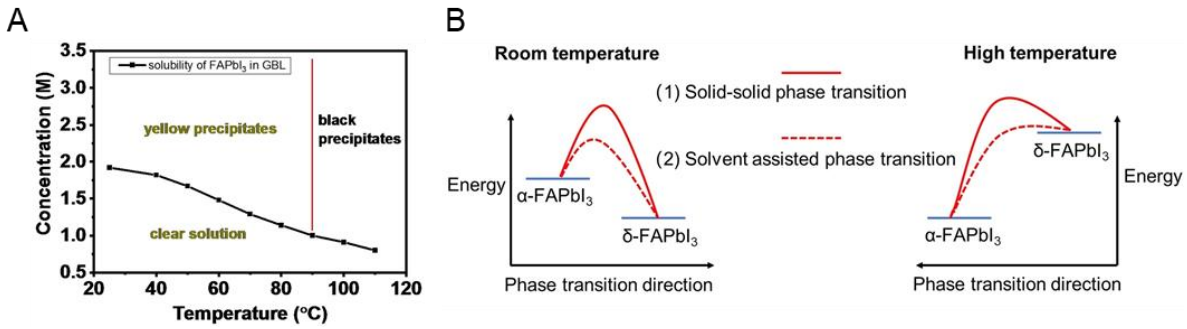

Figure 18 (A) Solubility curve of $FAPbI_3$ in GBL. (B) Change in energetics for the δ- to α-phase transition. Adapted from [86].

11. Perovskite solar cell architectures

There are three commonly used architectures for perovskite solar cells, as shown in **Figure 19**. While there are also other used architectures[21], like, for example, the triple mesoscopic architecture[59], most of them have never achieved efficiencies above 20% or have been used by other research groups frequently. The mesoporous n-i-p structure originally came from DSSC, where the mesoporous TiO_2 layer was necessary to help with efficient charge transport. Often, FTO is used as TCO since ITO is not stable under the high temperatures needed to make

the TiO_2 layer.[87] Then, a spray-coated compact TiO_2 layer is deposited, followed by a spin-coated mesoporous TiO_2 layer. On top, a perovskite layer is deposited with a small capping layer.[88] A 2D passivation follows that. Afterwards, the hole transporting layer is deposited, which is often spiro-OMeTAD, PTAA or P3HT. For the top electrode, Au or Ag are often used. Au is generally more stable, and Ag allows a lower temperature deposition, which can benefit the PCE. However, the mesoporous architecture has been lacking in terms of efficiency in recent years. The highest achieved efficiency for a mesoporous device is 24.9%[89], while planar devices reach efficiencies of 25% and above.[90] The planar n-i-p architecture is similar, except that the mesoporous TiO_2 layer is commonly replaced with a SnO_2 layer. Often, a chemical bath deposition or spin-coated nanoparticles are used to deposit the SnO_2.[31,91] For p-i-n devices, the HTL and the ETL layer order were swapped. So, the HTL is deposited before the perovskite layer and the ETL afterwards. That changes the possible choice of charge transport layers because of the solvent combability. PTAA, NiOx, or SAMs are often used for the bottom substrate. The SAMs are often based on carbazole and have different functional groups, such as Me-4PACz ([4-(3,6-dimethyl-9H-carbazol-9-yl)butyl]phosphonic acid).[32] While for years, the p-i-n devices were lacking behind the n-i-p devices, in recent years, that trend changed. The key was the discovery of the SAMs.[32,92] For the ETL in p-i-n devices often fullerene are used like evaporated C_{60} or solution processed PCBM and BCP.

In general, I was able to achieve better stabilities with p-i-n devices and higher efficiencies with n-i-p devices.[93] Because of that, I use both architectures in this thesis.

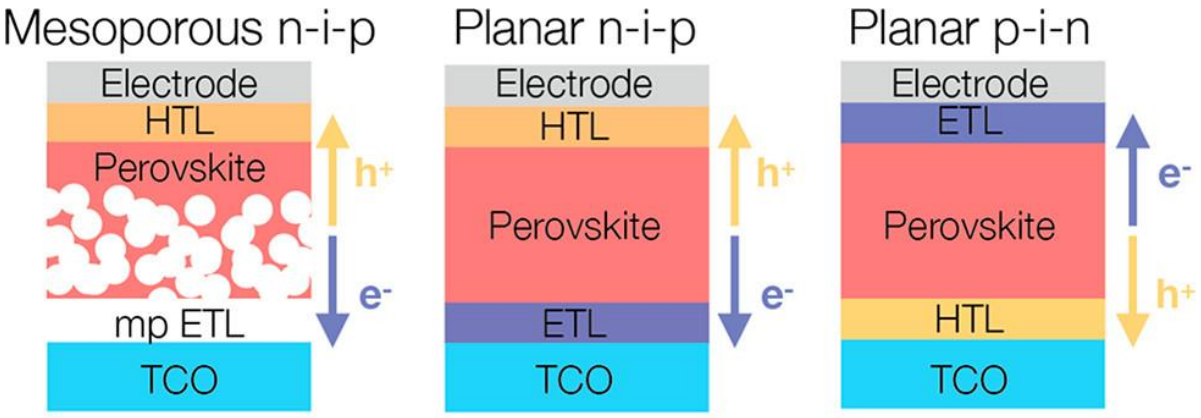

Figure 19 Different perovskite solar cell architectures. Adapted from [94]. TCO means transparent conductive oxide. ETL means electron transport layer and HTL means hole transporting layer. MP means mesoporous. P-i-n means positive-intrinsic-negative and n-i-p means negative-intrinsic-positive. That refers to the order of charge transport layers. E.g. for a p-i-n device the HTL is below the perovskite layer. Please note that in this example the sunlight comes from the bottom.

11.1. Perovskite deposition: Solvent quenching

Various fabrication and deposition methods have been developed for PSCs.[95] The solvent quenching method, as already mentioned, has been especially successful and reproducible since it is easy to adapt and produces highly efficient devices. A schematic of it is shown in **Figure 20A.** Vaynzof and co-workers[96] studied 14 different antisolvents; they found two key factors that impacted the resulting perovskite film quality: the solubility of the organic precursors in the antisolvent and its miscibility with the host solvent(s) of the precursor solution. They were able to produce efficient devices with a variety of different antisolvents by using a fast and slow deposition method by varying the pipette tip size. They categorised the antisolvent into three groups, as shown in **Figure 20B**. In this thesis, I mostly use Anisole and TFT for the perovskite fabrication.

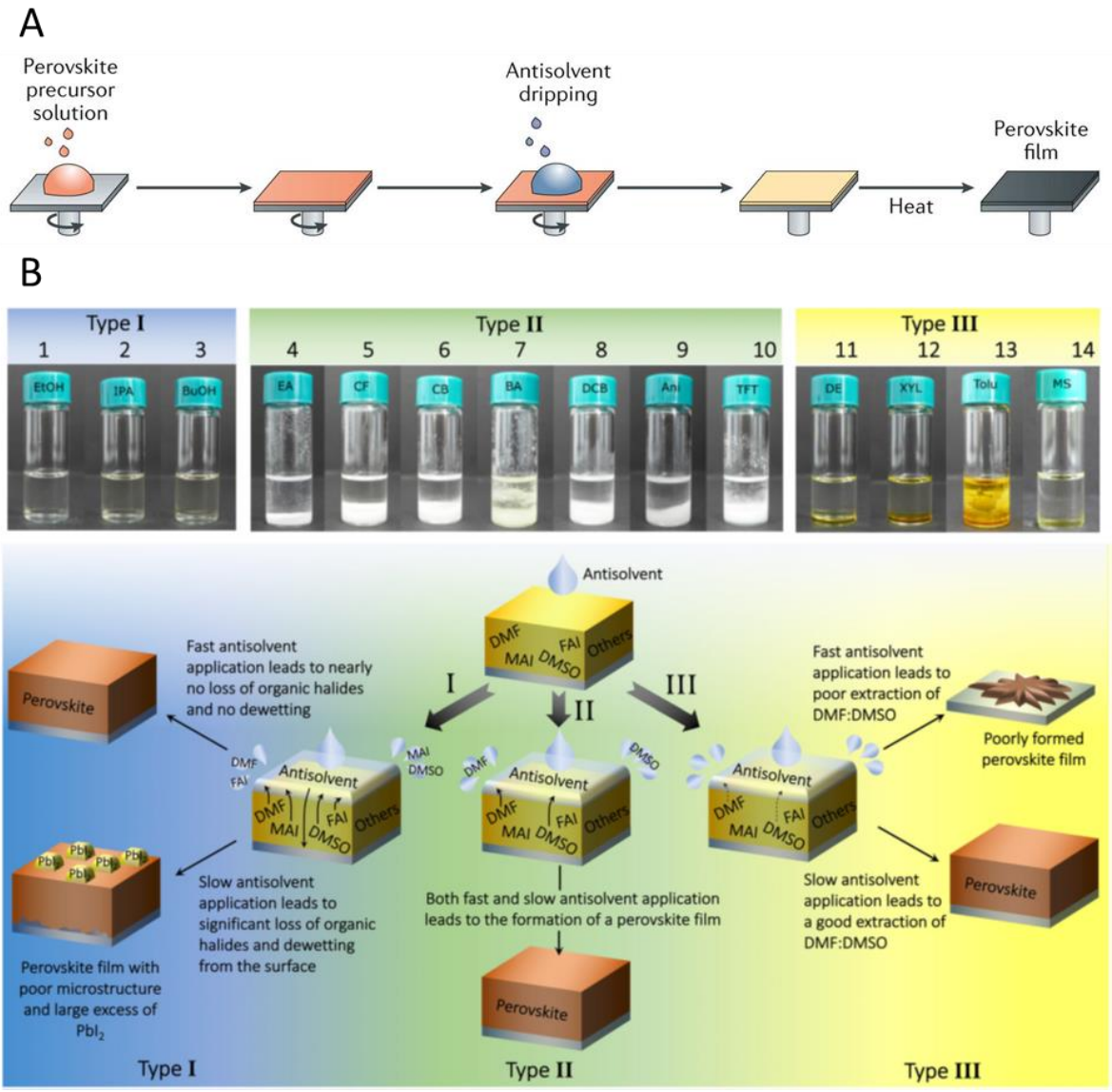

Figure 20 (A) Schematic for the antisolvent treatment. Based on [97]. (B) Understanding of the impact of different antisolvents. The various antisolvents are categorized depending on their impact on the crystallization. The top shows the solubility of MAI in the corresponding antisolvents. The bottom is a summary of the various proposed film formation mechanisms. The solvents are: 1: ethanol (EtOH), 2: isopropanol (IPA), 3: butyl alcohol (BuOH), 4: ethyl acetate (EA, only here EA), 5: chloroform (CF), 6: chlorobenzene (CB), 7: butyl acetate (BA), 8: 1,2-dichlorobenzene (DCB), 9: anisole (Ani), 10: trifluorotoluene (TFT), 11: diethyl ether (DEE), 12: m-xylene (Xyl), 13: toluene (Tol), are 14: mesitylene (Mesit). Text and pictures are adapted from [96].

11.2. Crystallisation of lead halide perovskites

Applying the anti-solvent induces rapid super-saturation in the precursor solution on the substrate, and the perovskite starts nucleating. Depending on the desired bandgap, different amounts of halides are used. The larger the bandgap, the more bromide or chloride salts are used. However, often, the larger bandgap materials suffer from larger non-radiative recombination losses.[98] I recently found that the halides Cl^-, Br^-, and I^- have different crystallisation times.[99] First, a chloride-rich phase forms, than bromide and finally iodide ($Cl^- > Br^- > I^-$). Other reports also support that.[100,101] As shown in **Figure 21A**, adding the antisolvent, here Anisole, to the precursor solution of a $FA_{0.83}Cs_{0.17}Pb(I_{0.6}Br_{0.4})_3$ leads to forming an intermediate phase. The colour of the intermediate shows the predominant halide species, with orange being more bromide-rich and white/yellow being chloride-rich when MACl is added.[102] In **Figure 21B,** one can see that after a mild heat treatment (60 °C for 1 s), the control shows a PL indicative of an iodide-rich region while the sample with MACl has a more homogenous PL, which is also shifted towards higher energies. In **Figure 21C**, the in-situ annealing of an antisolvent-quenched but not annealed thin film is shown. One can observe that already at 25 °C, the film with MACl shows a crystalline peak, which is shifted towards smaller lattice parameters compared to the control, which shows a significantly less crystalline initial peak.

In summary, the usage of different halides changes the crystallisation. The chloride phase has the lowest needed heat of formation (standard enthalpy of formation), followed by bromide, and iodide.[103,104] These differences cause different formation times. Then, during the growth stage, a halide homogenisation process happens. The other halides are gradually incorporated into the expanding perovskite lattice through diffusion. Chloride seems to help with overall

having a more homogenous halide distribution of iodide and bromide compared to composition with only bromide and iodide. This might explain why I find in Chapters 1 and 2 that DMACl works better than DMAI and DMABr.

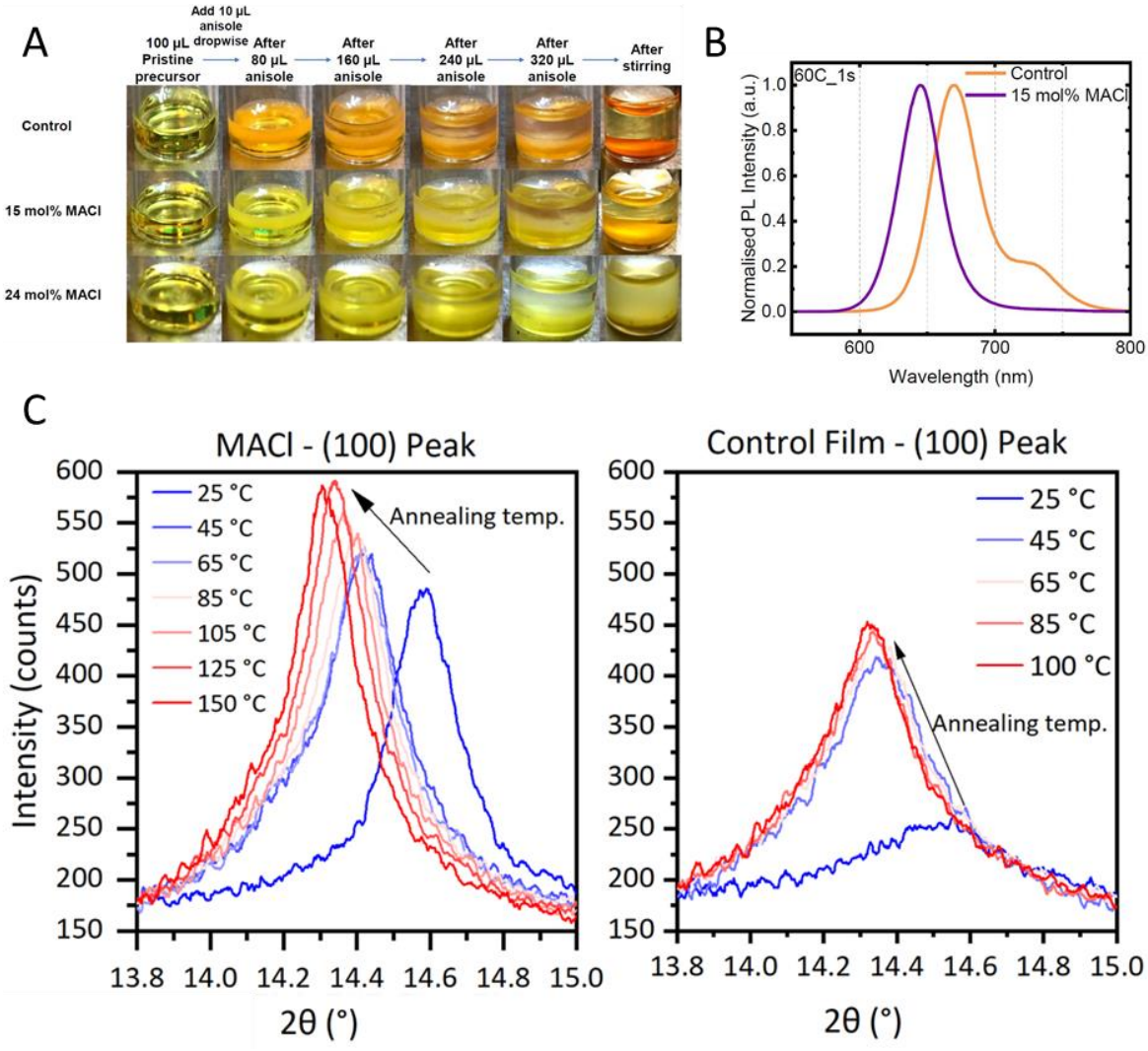

Figure 21 (**A**) Solvent quenching of the $FA_{0.83}Cs_{0.17}Pb(I_{0.6}Br_{0.4})_3$ without or with 15 mol% or with 24 mol% MACl under N_2 atmosphere by antisolvent dripping with anisole. 320 µL of anisole is added dropwise (10 µL each time) into 100 µL of perovskite precursors. Please note that the same amount of anisole is used during the device fabrication. (**B**) Normalised PL spectra of intermediates formed for $FA_{0.83}Cs_{0.17}Pb(I_{0.6}Br_{0.4})_3$ and 15 mol% MACl-processed $FA_{0.83}Cs_{0.17}Pb(I_{0.6}Br_{0.4})_3$ after 1 seconds of thermal annealing at 60 °C. (**C**) XRD patterns tracking

the evolution of cubic perovskite *(100)* peak during step-wise annealing of 15 mol% MACl and control perovskite films. The control film, with no MACl additive, is annealed at 100 °C in a N_2 atmosphere, whereas the perovskites fabricated with 15 mol% MACl additives is annealed at 150 °C in air with ≈30% RH. Text and figures are adapted from [98]. Please note that I measured (A) and (C).

12. Methods

The following text is adapted from two of my first-author publications.[105,106]

12.1. Device fabrication for the DMA route

12.1.1. p-i-n devices

I used a stack of glass/FTO/PTAA/Al_2O_3 NPs/perovskite/LiBr/C_{70}/Zr(acac)/Au. The devices were prepared by David McMeekin. They were measured by David McMeekin and me.

Substrate Preparation: Devices were fabricated on fluorine-doped tin oxide (FTO) coated glass (Pilkington, 15 Ω/sq). Initially, FTO was removed at specific regions where the anode contact will be deposited. This FTO etching was done using a 2M HCl and zinc powder. Substrates were then cleaned with Hellmanex detergent and rinsed with water. Finally, the substrates were then cleaned sequentially in acetone and isopropyl alcohol (IPA) and dried with a compressed air gun.

PTAA layer fabrication: A Poly[bis(4-phenyl)(2,4,6-trimethylphenyl)amine] (PTAA) precursor solution was prepared by dissolving a 1.5 mg ml^{-1} PTAA (Xi'an Polymer) in a 1:1 anhydrous chloroform (CF): chlorobenzene (CB). I spin-coated this solution dynamically in a nitrogen-filled glovebox at 2000 rpm for 20s and annealed the substrate at 150 °C for 10 min in air.

Al_2O_3 Nanoparticles (NPs) layer fabrication: Alumina nanoparticles (Al_2O_3 NPs) (< 50 nm) precursor solution was prepared by dispersing an IPA in 1:150 v/v ratio (Al_2O_3 NPs: IPA). 50 µL of this dispersion was then dynamically spin-coated onto the PTAA layer at 4000 rpm for 30 s. A subsequent annealing of at least 5 minutes at 85 °C was done.

The "DMF/DMSO" $FA_{0.83}Cs_{0.17}Pb(Br_{0.2}I_{0.8})_3$ – perovskite precursor solution preparation: The FA/Cs (formamidinium/Cs) perovskite solutions were prepared by dissolving the precursor salts: 171.3 mg FAI (99.99%, GreatCellSolar), 53.0 mg CsI (99.9%, Alfa Aesar), 132.1 mg $PbBr_2$ (98%, Alfa Aesar), 387.2 mg PbI_2 (99.99% trace metals and purity of > 98.0%, TCI), in 1 mL of anhydrous N, N-dimethylformamide (DMF): dimethylsulfoxide (DMSO) in a 4:1 v/v ratio to obtain a stoichiometric solution with the desired composition.

The "DMF/DMSO" $FA_{0.83}Cs_{0.17}Pb(Br_{0.2}I_{0.8})_3$ – perovskite layer preparation: The perovskite precursor perovskite solution was spin-coated in a nitrogen-filled glovebox using a two-step program. After spreading 50 µL of the perovskite solution onto the substrate, the first step is programmed to spin at 1000 rpm for 10 s, and the second step is programmed at 6000 rpm for 20 s. 10 s prior to the end of the second step, 100 µL of ethyl acetate solvent was dropped on the film to quench the growth of perovskite. The films were immediately placed on a hotplate in N_2 at 100 °C for 20 m.

The "DMF/DMACl" $DMA_xFA_{0.83}Cs_{0.17}Pb(Br_{0.12}I_{0.88})_3Cl_x$ – perovskite precursor solution preparation: The perovskite solutions were prepared by dissolving the precursor salts: 199.8 mg FAI, 61.8 mg CsI, with x mol% DMACl (e.g. 34.2 mg for x=0.3), 92.5 mg $PbBr_2$, 529.2 mg PbI_2, in 1 mL of anhydrous DMF. The precursor solution was prepared using the following precursor salts: FAI (99.99%, GreatCellSolar), CsI (99.9%, Alfa Aesar), PbI_2 (99.99% trace metals and purity of > 98.0%, TCI), $PbBr_2$ (98%, Alfa Aesar), Dimethylammonium Chloride (DMACl) (≥ 98.0 %, Alfa Aesar).

The "DMF/DMACl" – $DMA_xFA_{0.83}Cs_{0.17}Pb(Br_{0.12}I_{0.88})_3Cl_x$ – perovskite layer deposition: The perovskite precursor solution was spin-coated in a nitrogen-filled glovebox using a two-step program. After spreading 50 µL of the perovskite solution onto the substrate, the first step is

programmed to spin at 1000 rpm for 7 s, and the second step is programmed at 4000 rpm for 20 s. 5 s after the start of the second step, 100 µL of a 3:1 trifluorotoluene (TFT): EA solvent mixture was dropped on the film. The films were immediately placed on a hotplate in N_2 at 100 °C for 5 m. This step is designed to remove the solvent, however, at this point, the perovskite remains in its yellow intermediate phase. A subsequent annealing step on a 170 °C preheated hotplate in air for 10 m allows for the 2H to 3C sequence to take place, where the films turn from a yellow to a black colour. The last annealed step takes place in a 175 °C preheated oven in the air for 90 m to fully crystallize the perovskite. In the oven, a large glass cover lid is placed over the samples to prevent dust particles and air flow from affecting the annealing.

FABr layer deposition: A FABr precursor solution was prepared by dissolving a 2 mg ml^{-1} of FABr (99.99%, GreatCellSolar) in IPA. After the full crystallization of the perovskite, I spin-coated this solution dynamically in a nitrogen-filled glovebox at 4000 rpm for 20s and annealed the substrate at 100 °C for 5 min in N_2.

LiBr layer deposition: A lithium bromide (LiBr) precursor solution was prepared by dissolving 0.15 mg ml^{-1} of LiBr (Sigma) in IPA. I spin-coated this solution dynamically in a nitrogen-filled glovebox at 4000 rpm for 20s and annealed the substrate at 85 °C for 10 min in N_2.

C_{70} layer fabrication: A C_{70} fullerene precursor solution was prepared by dissolving a 24 mg ml^{-1} of C_{70} (Solenne) in dichlorobenzene (DCB). I spin-coated this solution statically in a nitrogen-filled glovebox at 800 rpm for 40s on a pre-heating substrate at 85 °C. I annealed the substrate at 85 °C for 10 min in N_2.

Zr(acac)/PEIE layer fabrication: A zirconium acetylacetonate/polyethylenimine ethoxylated (Zr(acac)/PEIE) precursor solution was prepared by dissolving a 2 mg ml^{-1} of Zr(acac) (sigma,

97%) in IPA and adding a 0.1% (v/v) of PEIE (80% ethoxylated solution, 37 wt. % in H_2O, Sigma) to this solution. I spin-coated this solution dynamically in a nitrogen-filled glovebox at 4000 rpm for 20s.

Metal electrode layer fabrication: 80 nm silver or gold electrodes were thermally evaporated under a vacuum of ≈10^{-6} mbar at a rate of ≈0.2 nm·s^{-1} or 0.01 to 0.04 nm/s, respectively. I used gold electrodes for stability measurements and silver electrodes for efficiency measurements.

12.1.2. n-i-p devices

For n-i-p devices, I employed two slightly different architectures using a compact layer (CL) of SnO_2 combined with a chemical bath (CB) deposited SnO_2 and SnO_2 nanoparticles. Otherwise, all layers are the same of glass/FTO/SnO_2 CL/SnO_2 CB/perovskite/Spiro/Au and glass/FTO/SnO_2 NPs/perovskite/Spiro/Au. These devices were made by me, only the champion device (**Figure 46**) with a KCl surface treatment was made by Seongrok Seo.

Substrate Preparation: Devices were fabricated using FTO Tec7 coated glass (Pilkington) as the transparent electrode. FTO was etched with 2 M HCl and zinc powder to obtain the required electrode pattern. Following a cleaning procedure consisting of a series of sonication steps was applied. First, 10 min in Decon mixed with DI water (5% in DI), followed by 10 min of sonication in acetone and finally isopropanol.

SnO_2 Layer for DMF/DMSO Controls, SnO_2 Compact Layer (CL): The substrates were plasma cleaned (Pico, Diener electronic) for 10 min. In the meantime, a $SnCl_4{\cdot}5H_2O$ (Sigma-Aldrich, 244678-100G, 98% lumps) of 17.5 mg/ml solution in IPA was prepared. Statically, 200 ml of the $SnCl_4$ solution was deposited at 3000 rpm (200 acc.) for 25 s in an ambient atmosphere (30 to 50% RH, 20 to 25 °C). Until all substrates were finished, they were annealed at 100 °C

and brought onto a sintering hotplate. They were heated with the lid closed and no gas flow attached for 1 h at 180 °C. In the meantime, the CB solution was prepared. After adding each component, the solution was stirred with a stir bar for a few minutes. For 32 substrates (28 x 28 mm), the following solution was prepared:

- 200 ml of deionised water
- 2.5 g Urea (Sigma-Aldrich)
- 50 µl Thioglycolic acid (Sigma-Aldrich, 98%)
- 2.5 ml HCl (99.999%, Alfa Aesar, 087617.AK, CAS 7647-01-0)
- 540 mg $SnCl_2$ (≥ 99.99%, Sigma-Aldrich, 43508-50g, CAS 10025-69-1)

I first added the substrates into a glass baker, filled it carefully with the CB solution, and covered it with a glass cover. Consequently, the substrates were heated in a ventilated oven at 90 °C for 4 h. Afterwards, the CB was drained, and the glass baker was quickly filled with DI water. Consequently, the substrates were sonicated for 5 minutes in deionised water, blown and dried and then IPA for 5 minutes, respectively. Finally, the substrates were heated at 180 °C on a sintering hotplate for 1 h again. The substrates were subjected to UV ozone for 15 min before usage.

SnO_2 Layer for DMF/DMACl, SnO_2 Nanoparticles (NPs) solution: A 2% diluted SnO_2 nanoparticle solution (Alfa Aesar) diluted in H_2O (UltraPure Water, Cambridge Bioscience). The solution was spin-coated statically onto FTO Tec7 at a spin rate of 4000 rpm (1000 rpm acc.) for 30 sec. Substrates were annealed at 150°C for 30 min. Before spinning the perovskite layer, the substrates were treated with UV-ozone for 10 minutes.

KCl Treatment: 20 mM of KCl (Sigma-Aldrich) were dissolved in DI water. It was then spin-coated onto the SnO_2 CB layer. Statically 200 ul of the solution were dropped at 3000 rpm

(2000 acc.) for 30 s in an ambient atmosphere and then dried it on a hotplate at 100 °C for 10 minutes.

The "DMF/acid" - $FA_{0.83}Cs_{0.17}Pb(Br_{0.2}I_{0.8})_3$ perovskite precursor solution preparation: The FA/Cs perovskite solutions were prepared by dissolving the precursor salts: 171.3 mg FAI (99.99%, GreatCellSolar), 53.0 mg CsI (99.9%, Alfa Aesar), 132.1 mg $PbBr_2$ (98%, Alfa Aesar), 387.2 mg PbI_2 (99.99% trace metals and purity of > 98.0%, TCI), in 1 mL of DMF to obtain a stoichiometric solution with the desired composition. 85.6 µl of hydroiodic acid (HI) (57 wt.% in H_2O, distilled, stabilized, 99.95%, Sigma-Aldrich) and 18.4 µl/ml of hydrobromic (HBr) (48 wt. % in H_2O) was added for every 1 ml of DMF. After the addition of the acids, the perovskite precursor solution was aged for 48 h in a nitrogen atmosphere. The DMF/acid films were made by David McMeekin and me.

DMF/DMSO perovskite preparation: $FA_{0.83}Cs_{0.17}Pb(I_{0.9}Br_{0.1})_3$ perovskite 827.86 mg of FAI (99.999%, Dyenamo), 256.17 mg CsI (99.998% Alfa Aesar), 2272.78 mg of PbI_2 (99.999% Alfa Aesar) and 319.30 mg $PbBr_2$ (98%, Alfa Aesar) are dissolved in 4 ml of 4:1 DMF: DMSO. They were stirred at room temperature in the glovebox for 1 to 3 hours before deposition. 70 µl of the solution are spread onto the substrate statically and spin-coated at 10 s at 1000 rpm (200 rpm acc.) and 35 s at 6000 rpm (2000 rpm acc.) and solvent quenched with 150 µl anisole 10 s before the end. The layers were annealed at 100 °C for 15 min. Spinning and heating for the control device were done in a N_2 glovebox.

DMF/DMACl perovskite preparation: $DMACl_{0.3}FA_{0.83}Cs_{0.17}Pb(I_{0.85}Br_{0.15})_3$ perovskite 136.99 mg DMACl (Sigma-Aldrich), 799.32 mg of FAI (99.999%, Dyenamo), 247.34 mg CsI (99.998% Alfa Aesar), 2000.78 mg of PbI_2 (99.999% Alfa Aesar) and 462.43 mg $PbBr_2$ (98%, Alfa Aesar) are dissolved in 4 ml DMF. They are stirred at room temperature in the glovebox for 1 to 3 hours

before deposition. 70 µl of the solution are spread onto the substrate statically and spin-coated at 10 s at 1000 rpm (1000 rpm acc.) and 30 s at 4000 rpm (4000 rpm acceleration) and is quenched with 150 µl of TFT 17 s into the program. The layers were annealed at 100 °C for 10 min and directly afterwards at 170 °C. The 30 mol% DMACl: $FA_{0.83}Cs_{0.17}Pb(I_{0.85}Br_{0.15})_3$ perovskite was spun in a drybox at 20% RH at around 23 to 25 °C. The heating for the 170 °C step was performed in ambient (30 to 55% RH).

Spiro-OMeTAD preparation: The hole transfer materials were deposited by preparing a spiro-OMeTAD in chlorobenzene (90 mg/mL, Lumtech) and mixing with 35.5 uL 4-tert-butyl-pyridine (tBP), 23 uL Li-bis(trifluoromethanesulfonyl)imide (Li-TFSI) (520 mg/mLacetonitrile), and 5uL tris(2-(1h-pyrazol-1-yl)-4-tert-butylpyridine)-cobalt(III)tris(bis(trifluoromethylsulfonyl)imide) (FK209, Lumtech) (180 mg/mL acetonitrile). The spiro-OMeTAD layer was deposited at 4000 rpm for 25 s with 2000 acceleration in a N_2 glovebox. Afterwards, 75 nm of Ag was deposited under a vacuum (10^{-6} mbar).

12.2. Device fabrication for the HUBLA chapter

N-i-p and p-i-n devices were used. The n-i-p devices were made by Wei-Ting Wang. The p-i-n devices were made Wei-Ting Wang, Ning Zhou, Hin-Lap Yip and me. For simplicity, all materials are first mentioned here.

12.2.1. Materials for Chapter 3

Tin(IV) oxide (SnO_2, 15% in H_2O colloidal dispersion), lead iodide (PbI_2, 99.999%) and molybdenum(VI) oxide (MoO_3) were purchased from Alfa Aesar. Triethanolamine (TEA, 98%), tri(ethylene glycol) (TEG, 98%), *tert*-butylethylenediamine (tBEDA, 98%), 1,3-bis(2-isocyanato-2-propyl)benzene (TMXDI, 97%), cysteamine hydrochloride (98%), LiTFSI (99%), tBP (98%), anisole (anhydrous, 99.7%), dimethyl sulfoxide-d_6 (DMSO-d_6), ethylenediamine (EDA) and

deuterium oxide (D_2O) were obtained from Sigma-Aldrich. Dioctyltin dilaurate (DBTDL, 96%) was purchased from Merck. IPA (99.8%), dried diethyl ether (99%), DMF (99.8%), DMSO (99.8%), chlorobenzene (CB, 99%), acetonitrile (ACN, 99.8%), and γ-butyrolactone (GBL, 99%) were obtained from Acros Organics. Formamidinium iodide (FAI) and methylammonium iodide (MAI) were purchased from Greatcell Solar Materials. Cesium iodide (CsI) (>99.999%) was purchased from Alfa Aesar. $PbBr_2$ was purchased from TCI. Spiro-OMeTAD (>99.5%) was obtained from Lumtech. Au and Ag pellets were purchased from Kurt J. Lesker. PTAA was purchased from Flexink. Poly(4-butylphenyl-diphenyl-amine) (polyTPD) was purchased from 1-Material. 2,3,5,6-Tetrafluoro-7,7,8,8-tetracyanoquinodimethane (F4-TCNQ), [6,6]-phenyl-C61-butyric acid methyl ester (PCBM), buckminsterfullerene (C_{60}) and bathocuproine (BCP) were bought from Lumtec; [2-(9H-carbazol-9-yl)ethyl]phosphonic acid (2PACz) was purchased from Xi'an Baolaite Photoelectric Technology Co., Ltd. CbzPh was prepared according to the previous literature.[107] HelioSeal PVS 101 Tape was obtained from Koemmerling (Nanjing) Advanced Material Co., Ltd. UV curable resin (TB3035B) was purchased from Three-Bond.

12.2.2. Fabrication of FAMA ($FA_{0.72}MA_{0.28}PbI_3$) composition n-i-p perovskite solar cells

Substrate preparation: Indium tin oxide (ITO)-coated glass substrate was sequentially sonicated in deionized water, acetone, and IPA, then treated with ultraviolet ozone for 10 min after being dried with an air gun.

SnO_2 layer preparation: SnO_2 nanoparticles (2.67%, diluted by deionized water) were spun onto the above ITO substrate at 5,000 rpm for 30 s, and annealed in ambient air at 150 °C for 30 minutes.

FAMA ($FA_{0.72}MA_{0.28}PbI_3$) composition: 1.3 M perovskite precursor solution (1ml) was constructed by mixing FAI, PbI_2, MAI in DMF: DMSO mixed solvent (9:1, v: v) with the chemical

formula $FA_{0.72}MA_{0.28}PbI_3$, and 27 mg $PbCl_2$ was also added as additive. The perovskite precursor solution was deposited onto the prepared substrate with 1000 rpm for 10 s and 5,000 rpm for 20 s. During the spin coating step, 100 µl CB was poured on the precursor film at 10 s prior to the end of spin and the film was then annealed at 100 °C for 30 minutes in a nitrogen-filled glove box.[108] For the HUBLA device, HUBLA (0.03 - 0.2 mg ml^{-1} in IPA) was spun onto the perovskite film.

Hole transport layer and electrode deposition: Spiro-OMeTAD was dissolved in 1 ml of CB solution which contains 72.3 mg Spiro-OMeTAD, 18 µL LiTFSI solution (520 mg ml^{-1} in ACN) and 30 µl tBP. HTM was deposited onto perovskite film at a spin rate of 4000 rpm for 30 s. The above film was then left overnight under controlled ambient conditions. Finally, MoO_3 was evaporated on to the samples under vacuum of $<10^{-5}$ torr at a rate of 0.1-0.2 Å s^{-1}, and then 100 nm Ag were evaporated under vacuum of $<10^{-5}$ torr at a rate of 1-2 Å s^{-1}. Evaporation masks of 0.1 cm^2 device areas were used.

12.2.3. Fabrication of FAMACs ($FA_{0.72}MA_{0.18}Cs_{0.1}PbI_3$) composition p-i-n perovskite solar cells

Substrate preparation: ITO-coated glass substrate was sequentially sonicated in deionized water, acetone, and IPA, then treated with ultraviolet ozone for 10 minutes after being dried with an air gun.

Self-assembled monolayer (SAM) layer preparation: 2PACz solution (70 µl 2PACz in 1.2 ml IPA) was spin-coated on ITO substrate at 4000 rpm for 30 s and then annealed at 120 °C for 10 minutes.[32]

FAMACs ($FA_{0.72}MA_{0.18}Cs_{0.1}PbI_3$) composition: 1.3 M perovskite precursor solution (1ml) was constructed by mixing FAI, PbI_2, MAI, CsI in DMF: DMSO mixed solvent (9:1, v: v) with the

chemical formula $FA_{0.72}MA_{0.18}Cs_{0.1}PbI_3$, and 27 mg $PbCl_2$ was also added as additive. The perovskite precursor solution was deposited onto the prepared substrate with 1000 rpm for 10 s and 5000 rpm for 20 s. During the spin coating step, 100 µL CB was poured on the precursor film at 10 s prior to the end of spin and the film was then annealed at 100 °C for 30 min in a nitrogen-filled glove box.[108] For the HUBLA device, HUBLA (0.03-0.2 mg mL^{-1} in IPA) was spun onto the perovskite film.

Electron transport layer and electrode deposition: Afterward, 30 nm C_{60} and 5 nm BCP were evaporated onto the samples under vacuum of $<5\times10^{-6}$ torr at a rate of 0.1-0.3 Å s^{-1}. Finally, 100 nm Au electrode was deposited by a thermal evaporator at the rate of 1-2 Å s^{-1}. Evaporation masks of 0.1 cm^2 device areas were used.

12.2.4. Fabrication of $FA_{0.92}Cs_{0.08}PbI_3$ composition in p-i-n perovskite solar cells

SAM layer preparation: Cleaned ITO substrates were subjected to ultraviolet-ozone for 25 min and transformed in a N_2-filled glovebox for film fabrication. SAM (0.5 mg mL^{-1} in IPA) was dynamically spin coated onto the cleaned ITO at 3000 rpm for 30 s, followed by annealing at 100 ℃ for 15 min. The substrates were cooled down to room temperature and washed with pure IPA and then annealed at 100 °C for 5 min.[32]

$FA_{0.92}Cs_{0.08}PbI_3$ composition: Then, 1.7 M perovskite precursor solution was dissolved in DMF: DMSO mixed solvent (4:1, v:v) with the chemical formula $FA_{0.92}Cs_{0.08}PbI_3$. Then, 50 µl of the prepared precursor solution was spin-coated at 1,000 rpm for 10 s and 5,000 rpm for 30 s onto the SAM-based ITO substrate; 180 µl CB as the antisolvent was dripped on the film at 10 s before the end of the last procedure and then annealed at 100 °C for 30 min. After deposition of the perovskite active layer, 50 µl HUBLA (dissolved in IPA) solution was spin-coated onto the film.

Electron transport layer and electrode deposition: PCBM (5 mg/ml) was spin coated onto the perovskite film and annealed at 70 °C for 10 min. The films were then cooled down to room temperature and readied for thermal evaporation. 25 nm C_{60}, 8 nm bathocuproine (BCP) and 100 nm Au electrode were sequentially evaporated under a high vacuum.

12.2.5. Fabrication of $FA_{0.83}Cs_{0.17}Pb(I_{0.9}Br_{0.1})_3$ composition in p-i-n perovskite solar cells

Substrate Cleaning: The FTO substrates (30 × 30 mm) were brushed with a detergent (fairy liquid with a toothbrush) and consequently sonicated for at least 10 minutes in a 4% v/v solution of Decon 90, acetone and IPA.

Poly-TPD layer preparation and deposition: 1 mg ml^{-1} Poly-TPD were dissolved in an amber vial in toluene with 0.2 mg ml^{-1} of F4-TCNQ. The solution was stirred overnight at 80 °C in a nitrogen glovebox. Before usage the solution was filtered a 0.22 µm PTFE filter. The FTO substrates were treated with UV-ozone for 10 minutes directly before use. In ambient (30 to 55% RH), 80 µL of poly-TPD were dynamically deposited onto the FTO substrate (2000 rpm, 2000 acc. for 20 s). Afterwards, the substrates were heated for 5 min at 130 °C in ambient.

$FA_{0.83}Cs_{0.17}Pb(I_{0.9}Br_{0.1})_3$ perovskite and deposition: To prepare the 1.45 M $FA_{0.83}Cs_{0.17}Pb(I_{0.9}Br_{0.1})_3$ perovskite precursor, 827.86 mg FAI, 256.17 mg CsI, 2272.78 mg PbI_2 and 319.30 mg $PbBr_2$ are dissolved in 4 ml of 4:1 DMF: DMSO (Sigma-Alderich). They are stirred at room temperature in the glovebox over night before deposition. Before the deposition the solution was filtered with a 0.4 µm PTFE filter. 200 µl solution was dynamically applied onto the substrate 7 to 8 s into the first step of the spin-coating. The spin-coating program is 10 s at 1000 rpm (200 rpm acc.) and 35 s at 5000 rpm (2000 rpm acc.). 10 s before the end of the second spin-coating step, 400 µl anisole was applied. The perovskite layer was annealed at 100 °C. Spinning and heating for the devices was done in a nitrogen glovebox.

PCBM, BCP layer and electrode deposition: 20 mg ml^{-1} PCBM were dissolved in a mixed solvent of 3:1 CB: DCB overnight. Before usage the solution was filtered with a 0.22 µm PTFE filter. In a nitrogen glovebox, 50 µl PCBM were dynamically deposited onto the substrate at 2000 rpm (2000 acc.) for 20 s. The substrates were annealed afterwards for 4 minutes at 100 °C. 0.5 mg ml^{-1} BCP was dissolved in IPA and stirred overnight at 80 °C. Before usage the solution was filtered with a 0.22 µm PTFE filter. 70 µl BCP was deposited dynamically at 5000 rpm (2000 acc. for 30 s). The substrates were finally annealed for 1 minute at 100 °C. 75 to 100 nm Au were deposited through a shadow mask at ($<3 \times 10^{-6}$ torr) using a thermal evaporator (Nano 36, Kurt J. Lesker).

12.3. Measurements

12.3.1. X-ray diffraction (XRD) characterization

The 1D-XRD patterns were obtained with a Panalytical X'Pert Pro or an X-Ray diffractometer or a Bruker D8 Advance with a Cu K_α X-ray tube at 40 kV and 40 mA. For Chapter 3, the XRD diffraction patterns of FAMA and $FAPbI_3$ films were carried on an D8 Discover, Brucker with Cu K_α (λ=1.54059 Å) radiation. The XRD measurements for Chapter 1 and 2 were done by me or David McMeekin. The XRD measurements for Chapter 3 were done by me or Qiang Zhang. XRD analysis in Chapter 1 was partly done by Harry Sansom.

12.3.2. Wide-angle X-ray scattering (WAXS) measurement:

Wide-angle X-ray scattering (WAXS) measurement was performed using the Stanford Synchrotron Radiation Lightsource (SSRL) Beamline 11–3 with an X-ray wavelength of 0.9744 Å. Two-dimensional scattering data were collected using a Rayonex MX225 detector in a grazing incidence geometry with the X-ray beam held at an incident angle of 3°. Images are calibrated using a LaB_6 standard and integrated between $10° < \chi < 170°$ (χ is the polar angle) using GSAS-II.[109] WAXS was measured by Laura Schade.

12.3.3. Two-dimensional (2D) X-ray diffraction (XRD^2):

2D-XRD pattern were conducted in ambient air at room temperature using a Rigaku SmartLab X-ray diffractometer with $CuK_{\alpha1}$ (1.54060 Å) and a HyPix-3000 2D hybrid pixel array detector, operated at 40 kV. XRD^2 was measured by me. For the in-situ measurements I measured roughly every minute a XRD^2 of a thin film sample which is deposited on a heating stage at different temperature. With XRD^2 not only the 2θ direction is measured but also the conic section of a poly-crystalline sample. As I show in **Figure 22**, the diffraction compared to a normal single crystal (**Figure 22A**) is not an individual peak but a diffraction cone (**Figure 22B**).

Measuring it with a 2D detector results in the appearance of characteristic diffraction rings showing the spread of the diffraction peak in γ-direction. More information about XRD[2] can be found in the work of He *et al*. (*Powder Diffr.* 18, 71-85 (2003))[110].

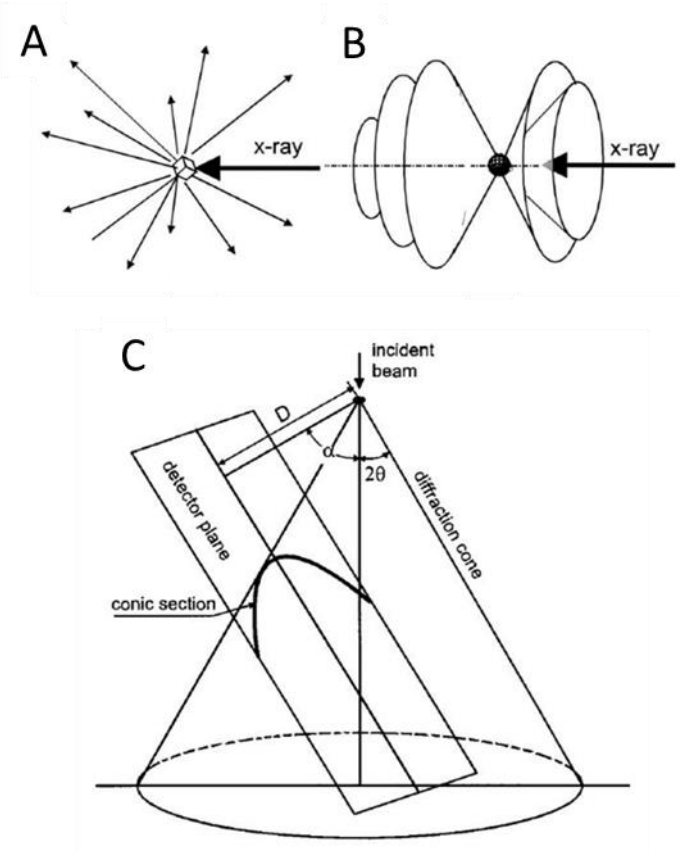

Figure 22 (A) Single crystal XRD, show typically sharp and defined peaks. (B) X-ray diffraction of poly-crystalline samples show typically cones. (C) Measurement of a diffraction cone with a 2D detector. Figure is adapted from [110].

12.3.4. Nuclear magnetic resonance (NMR)

^{1}H-NMR spectra were recorded on a Bruker Avance III 400 MHz or 600 MHz spectrometer. For each measurement, 16 perovskite films (2.5 x 2.5 cm) were scratched off the substrates. The perovskite material was then suspended in deuterated acetonitrile (CD_3CN) and the suspension decanted. All spectra are referenced versus residual solvent peaks with respect to

δ(TMS) = 0 ppm. For Chapter 3, the HUBLA sample was tested by dissolving in DMSO-d_6 solvent. For the hydrolysis of HUBLA, the HUBLA sample was prepared by dissolving in DMSO-d_6 first, and then D_2O was added with a volume ratio 15% after the spectrum at 0 minute was tested. The NMR tube was heated at 65 ℃ after 1 hour. To record the generation of disulfide bond, cysteamine hydrochloride and iodine (I_2) pellets were added into 10 mL D_2O solution and stirred. NMR was measured by Sebastian Fürer in Chapter 1 and 2. For Chapter 3 it was measured by Qiang Zhang.

12.3.5. Scanning electron microscopy (SEM)

The morphology of perovskite films was investigated using a SEM (Hitachi S-4300) at an accelerating voltage of 3-5 kV. The SEM images in Chapter 3 of the FAMA films were performed with a Hitachi S-4800 operated at 15 kV and measured by Qiang Zhang.

12.3.6. Solar cell characterization

For chapters 13 and 14 the current density–voltage (J-V) curves were measured (2400 Series SourceMeter, Keithley Instruments) under simulated AM 1.5 sunlight at approximately 100 mW cm^{-2} irradiance generated by an Abet Class AAB sun 2000 simulator, with the intensity calibrated with an NREL calibrated KG5 filtered Si reference cell. The mismatch factor was calculated to be less than 1%. The active area of the solar cell is 0.0919 cm^{-2}, by employing an opaque mask with an aperture. The forward J–V scans were measured from forward bias (FB) to short circuit (SC) and the backward scans were from short circuit to forward bias, both at a scan rate of 0.25 V s^{-1}. A stabilization time of 5 seconds under 1 sun illumination and forward bias of 0.2 V above the expected V_{OC} was done prior to scanning. The devices were measured by David McMeekin and me.

For Chapter 3 the FAMA n-i-p devices and FAMACs p-i-n devices were measured with a Keithley 2400 source meter under a simulated AM 1.5 G spectrum and the active area was 0.1 cm^2. With a solar simulator (Enli Technology Co., Ltd., Taiwan), the light intensity was calibrated using a KG5 reference cell before each measurement and the scan rate was 200 mV s^{-1}. For the $FA_{0.83}Cs_{0.17}Pb(I_{0.9}Br_{0.1})_3$ p-i-n devices in Chapter 3, they were characterized in ambient condition with the room temperature around 20-24 ℃ and 45% relative humidity under AM1.5G simulated sunlight generated by a class AAA WaveLabs Sinus-220 solar simulator, using a Keithley 2400 source meter. The intensity of the solar simulator was set to produce 100 mW cm^{-2} equivalent irradiance using a certified KG3-filtered Si reference photodiode (Fraunhofer ISE). The voltage was swept at a rate of 0.61 V s^{-1} first from forward bias to reverse bias (forward sweep) followed by a reverse sweep in the opposite scan direction. The minimum voltage was -0.1 V and the maximum voltage was 1.2 V. The areas were defined using black anodized aluminum shadow masks in direct contact with the glass side of the substrates within enclosed sample holders. For chapter 3 the devices were measured by Wei-Ting Wang, Suer Zhou and me.

12.3.7. Thermogravimetric analysis (TGA)

The TGA was directly performed on a perovskite coated glass substrate. A thin microscope glass cover slip was used as substrate. The choice of a low-weight substrate allowed for an acceptable signal-to-noise ratio for the TGA measurement. A TA Instruments Q500 Thermogravimetric Analyser was used for the measurements of the coatings. This instrument allows the measurement of weight change as a function of temperature/time in a controlled environment. Instrument control was performed using TA Instruments Thermal Advantage software. Subsequent data analysis was performed using TA Instruments Universal Analysis data analysis program. The sample was cut to size and placed inside a 100 ul Platinum crucible

(Coated side up) and heated at a rate of 10 °C per minute in a controlled atmosphere (Nitrogen) at a flow rate of 100 ml per minute. Precise gas flow control was maintained via a Mass Flow Controller built into the instrument. The mass of the sample was recorded as a function of temperature during the experiment. Data has been plotted to show the relationship between weight and temperature and also included are the first derivative profiles for the weight losses observed which give a clear indication of the onset and range of decomposition. The TGA was measured by Nicholas Hawkins. The films were prepared by David McMeekin.

12.3.8. Time-of-flight secondary ion mass spectrometry (ToF-SIMS) measurements

An ION-TOF TOF-SIMS V TOF SIMS spectrometer was utilized for depth profiling and chemical imaging of the perovskite utilizing methods outlined in detail by Harvey *et.al.*[111] Analysis was completed utilizing a 3-lens 30kV BiMn primary ion gun. 3-D tomography was completed with 100nm lateral resolution using a Bi_3^{++} primary ion-beam cluster (100 ns pulse width, 0.1 pA pulsed beam current), a 50 x 50 µm area was sampled with a 1024: 1024 primary beam raster. Depth Profiling was accomplished with a 1kV oxygen ion sputter beam (5-10 nA sputter current) with a raster of 150×150 microns. After completion of the SIMS measurements the depth of the craters was determined by optical interference light microscopy, in order to convert the SIMS sputter time scale to a sputter depth scale. The TOF-SIMS measurements were done by Steven P. Harvey.

12.3.9. Stability test

For the stability measurements in Chapter 2 a glass/glass encapsulation was sealed with a UV-cured epoxy (LT-U001 UV-Glue, Lumtec). The UV glue was cured for 30m with a UV lamp containing 4 x 9W bulbs under N_2 atmosphere. All the devices were aged under full spectrum

simulated AM1.5G, 76 mW cm^{-2} irradiance at V_{oc} using an Atlas SUNTEST XLS+ (1700W air-cooled Xenon lamp). The chamber temperature was set to 65 or 85 °C. The aging test is in correspondence to ISOS-L-2 aging condition. Please note that the light source is pulsed at 100Hz frequency. The devices were measured by David McMeekin and me.

For the stability measurements in Chapter 3, I used p-i-n devices with a $FA_{0.83}Cs_{0.17}Pb(I_{0.9}Br_{0.1})_3$ composition and poly-tPD as p-type layer and PCBM/BCP as n-type layer. The recipe is based on [112]. I measured the stability of the $FA_{0.83}Cs_{0.17}Pb(I_{0.9}Br_{0.1})_3$ p-i-n devices at 85 °C in N_2 in the dark, and chose to compare device performance to the most efficient HUBLA device after 1 day of aging as it induced the most significant increase in performance. The devices were put inside a home-built oven with a temperature control set to 85 °C (±4 °C) and removed periodically to measure device performance under ambient conditions (45% RH).

The other stability tests in Chapter 3 were done as following:

A MPPT test of encapsulated FAMACs p-i-n devices were performed and measured under 1 sun, 85 °C and 30% RH. The light source for the MPPT test was a BBZM-III xenon lamp with filter. The FAMACs p-i-n devices were sealed with encapsulation adhesives, including HelioSeal PVS 101 Tape and UV Curable resin (TB3035B). The devices were measured by Wei-Ting Wang. The MPPT test of unencapsulated p-i-n devices based on $FA_{0.92}Cs_{0.08}PbI_3$ composition were subjected to testing within the high-throughput solar-cell lifetime test system developed by CRYSCO under 1 sun and 85 °C in N_2. This system incorporates MPPT while operating under a light-emitting-diode-simulated AM 1.5 G spectrum. Ning Zhou and Hin-Lap Yip fabricated and measured the $FA_{0.92}Cs_{0.08}PbI_3$ devices.

12.3.10. Intensity-modulated photocurrent spectroscopy (IMPS) mapping

Impedance techniques, such as IMPS imaging, involve the measurement of a device's response to a small alternating current (AC) perturbation while simultaneously being illuminated with a constant direct current (DC) level, typically set at 1 sun intensity.[113] IMPS imaging operates in the frequency domain and quantifies the current (j_e) at each pixel in response to modulated light intensity (current density, j_φ), as depicted in **Figure 23A**.[114] The modulation frequency is systematically varied, resulting in a dispersion relationship or transfer function denoted as Q. When one possess knowledge of the equivalent circuit, one can fit the data in the form of arcs plotted in polar coordinates, as illustrated in **Figure 23B**. This fitting process enables the extraction of valuable information such as recombination lifetimes, shunts (low resistance paths between electrodes), interfacial trapping parameters, ionic and carrier mobilities, and more, all of which are related to specific transport and charge storage characteristics of the cell.

Here, however, the device area is too large and the RC attenuation did not allow the extraction of most parameters besides the series resistance. All photocurrent data is nevertheless preserved in vector format for subsequent impedance-based analyses. In contrast to previous IMPS imaging data, this study benefits from an integrated IV measurement system and a multiplexer system, allowing for the seamless execution of both IMPS imaging and subsequent IV measurements as a streamlined batch process for monitoring cell degradation over time. Jamie Laird and I both measured the devices together at the University of Melbourne. Jamie analysed and plotted the data.

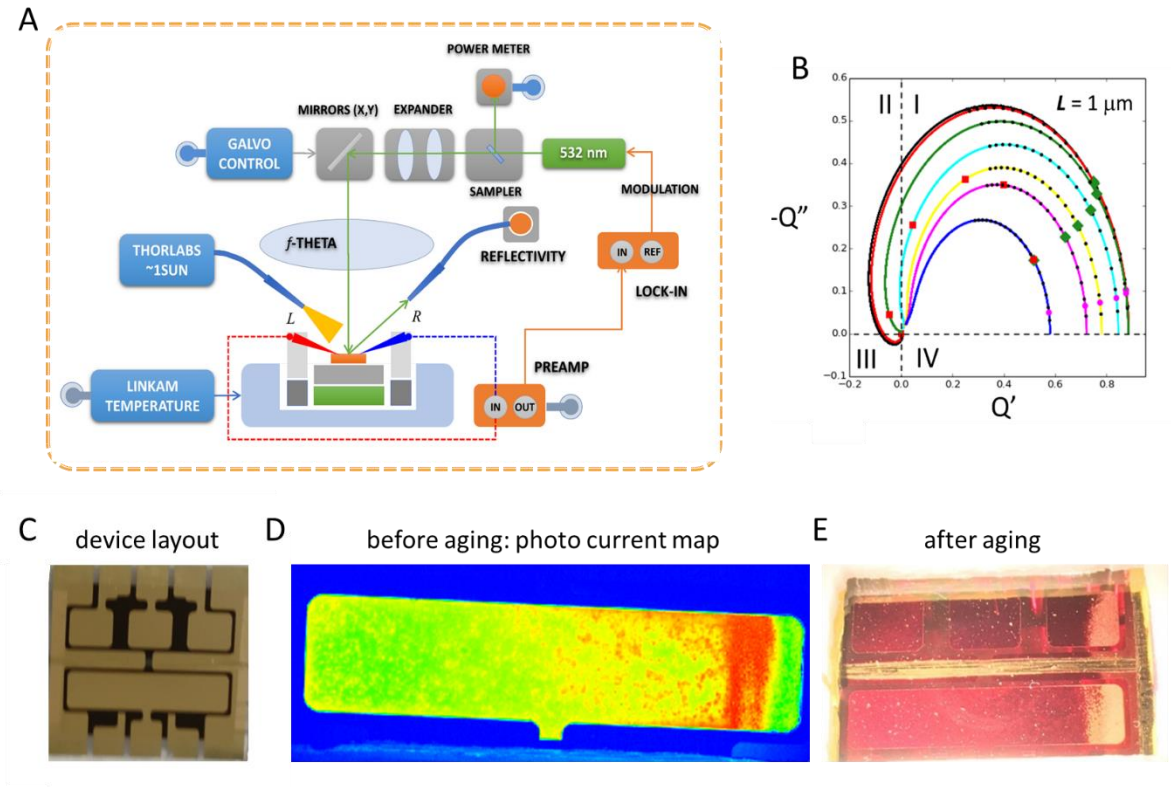

Figure 23 (**A**) Simplified schematic of the protype IMPS microscope.[114] (**B**) Typical arcs measured in an RC unlimited device where useful parameters can be extracted. Figure (**A**) and (**B**) were adapted from [114]. (**C**) 4-pixel device layout which was used for the IMPS mapping setup. Each of the 3 smaller squares (upper row) has an active area of 0.25 cm^2 when masked and the large rectangle below has an active area of 1 cm^2 when masked. (**D**) Photocurrent (j_e) map of ~1 cm^2 device before aging showing a large inhomogeneity on the right side of the device. (**E**) Same device after aging at around 0.75 suns in ambient air (~50% RH) for around 400 h without encapsulation showing a large discoloring on the right side. The spot on the right is likely transparent and only the gold metal electrode below is still visible.

12.3.11. In-situ photoluminescene (PL) map spectra

For the PL map measurements, the thin film samples were prepared by the precursor solution using 1.6 M $FAPbI_3$: MACl in 4:1 (v/v) DMF: DMSO (e.g., 633 mg of $FAPbI_3$ and 23.6 mg of MACl in 500 µL DMF and 125 µL DMSO) and deposited on FTO glass. I statically spread 160 µL perovskite precursor solution on the FTO substrate and start the spin coating program (6000 rpm, 3000 rpm/s acceleration) for 50 s. At 10-12 s I quench with 250 µL of anisole. Afterwards I anneal the films at 150 °C for 15 minutes. All of the perovskite layer fabrication was performed in a N_2 filled glovebox. The thin film sample was mounted in a Nikon Ti2 microscope base with a 130 W mercury lamp, Kymera 328i spectrometer, and Zylar 4.2 PLUS sCMOS. The light was monochromated using a Semrock brightline filter cube to provide 488 nm excitation. The light intensity was 9.65 W/cm^2 at 60x magnifications. The illuminated area was 4.91x10^{-4} cm^2. The PL signal were normalized by the exposure time to ensure comparability between the images of different films. The samples were mounted with the perovskite surface towards the objective. All films and measurements were done by me. Analysis of the data was done by Kevin J. Rietwyk.

12.3.12. Optical Microscope

Optical microscope images were taken on a Nikon Eclipse LV100ND microscope with Nikon TU Plan Fluor lenses (10x/0.30 A, 20x/0.45 A, 50x/0.60 B, 100x/0.90 A). The images are taken with an attached Nikon Digital Camera D6.10. All measurements were done by me.

12.3.13. UV-Vis absorption spectroscopy (UV-Vis)

Absorbance spectra of $FA_{0.83}Cs_{0.17}Pb(I_{0.9}Br_{0.1})_3$ films were measured with a Varian Cary 300 Bio UV-visible spectrophotometer with 50×50 mm reflective neutral density filters with an optical

density of 3.0 (made out of UV fused silica). All UV-Vic measurements in Chapter 1 and 2 were done by David McMeekin and in Chapter 3 by me.

12.3.14. X-ray photoelectron spectroscopy (XPS)

XPS spectra were taken on a Thermo Fisher K-Alpha system (X-ray source: Al Kα; pressure: 1×10^{-8} Pa). To obtain the N 1*s* and Pb 4*f* spectra of $FAPbI_3$/HUBLA film under humid condition (30% or 65% RH at 25 ℃), $FAPbI_3$/HUBLA films were aged in a Xenon Arc Test Chamber (Xi'an LIB Environmental Simulation Industry). To obtain the S 2*p* and Pb 4*f* spectra of $FAPbI_3$/HUBLA film under heating condition (85 ℃ in N_2), $FAPbI_3$/HUBLA films were aged in a N_2 glovebox at elevated temperature. To obtain the binding energies of each monomer, TMXDI, TMXDI hydrolysate, tBEDA, CH and CDH were coated on the $FAPbI_3$ films, respectively, and their N 1*s* and S 2*p* XPS spectra were performed. Here, N 1*s* and S 2*p* XPS spectra were used to evaluate the hydrolysis and redox reactions of HUBLA itself coated on perovskite under humid and heating conditions, respectively, while Pb 4*f* spectra were used to evaluate whether HUBLA and its evolving agents could effectively passivate defects on perovskite. XPS measurements were done by Qiang Zhang.

12.3.15. Thermal Desorption-Gas Chromatography-Mass Spectrometry (TD-GC-MS)

The following text was adapted from our publication [115].

The thin films with different perovskite compositions were loaded into a thermal extractor unit (Micro-Chamber/Thermal Extractor M-CTE250 from Markes International). The films were heated at 165 °C for 60 minutes under a flow of N_2 gas (50 ml min^{-1}). The volatile components which were released during the extraction were collected onto a sorbent-packed collection tube. The tube is then loaded into a thermal desorption unit. It is heated to release the volatiles concentrated in the tube. The volatiles are then passed into the gas

chromatography-mass spectrometry instrument (Agilent 5977B GC/MSD). The volatile components were identified by comparing it to the NIST 17 Mass 20 Spectral Library. The reported components had at least 85 % match with the database compound. The measurements were done by Shuan Reeksting. The analysis was done by Benjamin M. Gallant with advice from Shuan Reeksting.

12.3.16. Attenuated total reflection-infrared spectroscopy (ATR-IR) characterization

The ATR-IR spectra were taken using a Thermo Scientific Nicolet 6700 FTIR spectrometer, equipped with a diamond attenuated total reflection (ATR) crystal. The ITO/SnO_2/perovskite and ITO/SnO_2/perovskite/HUBLA samples were measured in ATR mode using spectral range from 4000 cm^{-1} to 400 cm^{-1} and signal average over 32 scans. ATR-IR spectroscopy was done by Qiang Zhang.

12.3.17. Steady-state photoluminescence (PL) and time-resolved photoluminescence (TRPL) characterizations

The PL was recorded with an optical microscope system from UniRAM, Protrustech (excitation wavelength 532 nm). TRPL spectra were measured with an Edinburgh FLSPP20 Spectrofluorometer (excitation wavelength 405 nm). To coat the single-crystals they were dipped into 0.125 mg ml^{-1} of HUBLA solution and afterwards dried with nitrogen. PL and TRPL were measured by Elisabeth A. Duijnstee.

12.3.18. External quantum efficiency

External quantum efficiency (EQE) measurements were carried out with a QE-R system (Enli Technology Co., Ltd., Taiwan) under 25 °C, 30-45% RH. EQE was measured by Wei-Ting Wang.

12.3.19. Preparation of hindered urea/thiocarbamate bond Lewis acid-base (HUBLA)

1.72 g tBEDA (10 mmol), 10 ml DMF were charged in 250 ml three-necked flask under inert nitrogen atmosphere and kept in ice bath. And then 4.89 g TMXDI (20 mmol) was dropped into the solution and stirred for 2 h. Afterward, 2.27 g cysteamine hydrochloride (20 mmol) and three drops of DBTDL were dissolved in 20 ml DMF and then dropped in the reaction system. The reaction was carried for 3 days and then poured into dried diethyl ether. The precipitates were collected and purified by precipitation at dried diethyl ether for three times. Finally, the white solid was dried under vacuum overnight. The material was prepared by Wei-Ting Wang, Qiang Zhang and Yanfeng Zhang.

12.3.20. Preparation of poly(urea-urethane) elastomer and self-healing experiment

In a 50 ml three-necked flask, 3.71 g TMXDI (15.2 mmol) was dissolved in 5 ml DMF and cooled to 4 °C. And then 0.86 g tBEDA (5 mmol) was slowly dropped into the above solution to form oligo-urea. Afterward, 0.188 g TEA (1.26 mmol), 1.282 g TEG (8.54 mmol) and two drops of dibutyltin dilaurate were added and the solution was vigorously homogenized. Finally, the polymer solution was charged to a 5×5×0.5 cm^3 mold followed by curing at room temperature for 24 h under vacuum to remove the DMF. For the self-healing test of elastomer, 14 black cubes and 13 white cubes were stuck together and self-healed for 24 hours at 25 °C. The material was prepared by Wei-Ting Wang, Qiang Zhang and Yanfeng Zhang.

12.3.21. Preparation of single crystals

Single crystals were grown according to a previously published protocol.[116,117] An equimolar amount of FAI and PbI_2 were dissolved in GBL. The solution was stirred at 60 °C for one hour and then filtered with a 0.45 µm GMF filter (25 mm diameter). 4 ml of the filtered solution was added to a $FAPbI_3$ seed crystal and annealed for 8 h at 95 °C in an oil bath. For the HUBLA

treatment, the crystals were dipped into the HUBLA solution. Single crystals were fabricated by Elisabeth A. Duijnstee.

12.3.22. Preparation of poly(urea-urethane) and its self-healing behavior

To show the self-healing ability of HUB, a HUB-based poly(urea-urethane) elastomer was prepared; TEA, TMXDI, TEG, and tBEDA were mixed and cured at room temperature to form the elastomer.[118] Here, the sixteen elastomer cubes (5×5×5 mm^3; poly(urethane-urea)) were dyed with black color while another sixteen cubes were white. As seen, after being placed at room temperature for 24 h, the elastomer cubes can be reconnected through the cross-linked interfaces to build a Rubik's Cube. This self-healing property can be attributed to the dynamic reaction of HUBs with a dissociation-association reaction (the equilibrium reaction between HUB) at the interface.[118] Initially, the HUB dissociated on the surface of the white and black cubes, and the isocyanate and hindered amine groups at the interfaces will then react again to form HUB when the two surfaces were attached. The material was prepared by Wei-Ting Wang, Qiang Zhang and Yanfeng Zhang.

13. Intermediate phase engineering with DMAX

The work in this chapter has been adapted and reproduced in part from D. P. McMeekin*, **P. Holzhey***, S. O. Fürer, S. P. Harvey, L. T. Schelhas, J. M. Ball, S. Mahesh, S. Seo, N. Hawkins, J. Lu, M. B. Johnston, J. J. Berry, U. Bach and H. J. Snaith, Intermediate-phase engineering via dimethylammonium cation additive for stable perovskite solar cells, Nature Materials, 22 (2023) 73–83.; DOI:10.1038/s41563-022-01399-8, *these authors contributed equally

13.1. Context and Summary

The pursuit of the perfect perovskite composition, one that balances long-term stability and efficiency, remains an ongoing challenge. The focus in this thesis shifts from the typical emphasis on perovskite chemical composition to an often-overlooked facet: the quality of its crystalline structure.

In recent years, the metal-halide perovskite field has gravitated towards a straightforward fabrication process, initially introduced by Jeon et al.[119] This process involves employing a solvent system consisting of DMF and DMSO, along with an "antisolvent" such as chlorobenzene, toluene, diethyl ether, or anisole, which is used to induce a rapid perovskite growth.[26] Although this method may not be readily adaptable for industrial use, it allows for the effortless creation of laboratory-scale prototypes, offering a satisfactory degree of film consistency and uniformity across various perovskite compositions.

Throughout the spin-coating procedure, the introduction of the antisolvent prompts rapid nucleation, giving rise to a series of intermediate phases and expelling a significant portion of the initial high-boiling-point solvents.[120] Subsequent annealing creates the necessary thermodynamic conditions for a fully formed 3D corner-sharing perovskite structure.

However, DMSO-PbX_2 complexes (e.g., DMSO·PbX_2 and $(DMSO)_2$·PbX_2, where X = I, Br or Cl) can lead to residual DMSO solvent being trapped within the film, owing to their strong molecular interaction with perovskite/PbX_2 and their high boiling points. This represents only one of numerous precursor phase pathways that could be explored to yield higher-quality perovskite structures.[121–124]

The anti-solvent quenching approach accelerates heterogeneous nucleation with a high concentration of nucleation centres, resulting in a brief crystal growth period. This method yields materials with relatively small grain sizes and polycrystalline films characterised by a higher degree of structural and energetic disorder. These defects typically translate into an increased density of trap states and shorter carrier diffusion lengths when compared to lengthier, more homogeneous nucleation and growth methods, such as single crystal growth techniques.[125–127]

Additionally, the smaller grain sizes result in a greater abundance of grain boundaries, which, in turn, cause more surface defects. These defects and boundaries have been implicated in promoting pathways leading to moisture-induced degradation.[128] While these films may perform admirably initially in photovoltaic devices, enhancing the crystal quality towards a "single-crystal-like" perovskite film is a significant stride toward bolstering the long-term stability of perovskite materials and devices. In the following chapter I compare the commonly used solvent-quenching method with DMF/DMSO to the acid-route. The acid route is a different fabrication method in which an acid is added to the precursor solution and only DMF is used and there is no need to use an “anti-solvent” to quench the perovskite. I analyse both methods and try to understand key differences. I find that the acid-route produces more stable films but also has some drawbacks. Finally, I analyse what is a key difference in the acid

route and combine it with the solvent quenching method to derive a novel and better fabrication method: the DMA route.

13.2. Background – the Acid route

In Henry's group the lead halide perovskites were initially fabricated by adding an acid to the perovskite precursor. However, this method is limited to using DMF exclusively, as DMSO tends to form an adduct with the introduced HI and HBr.[129] After the addition of the acid the solution was left for several days.[130] Please note that no antisolvent was used here. The acid films were only placed on a hotplate. These aged precursor solution with the addition of hydrohalic acids resulted in apparent larger, highly crystalline and oriented perovskite grains as shown in **Figure 24**.

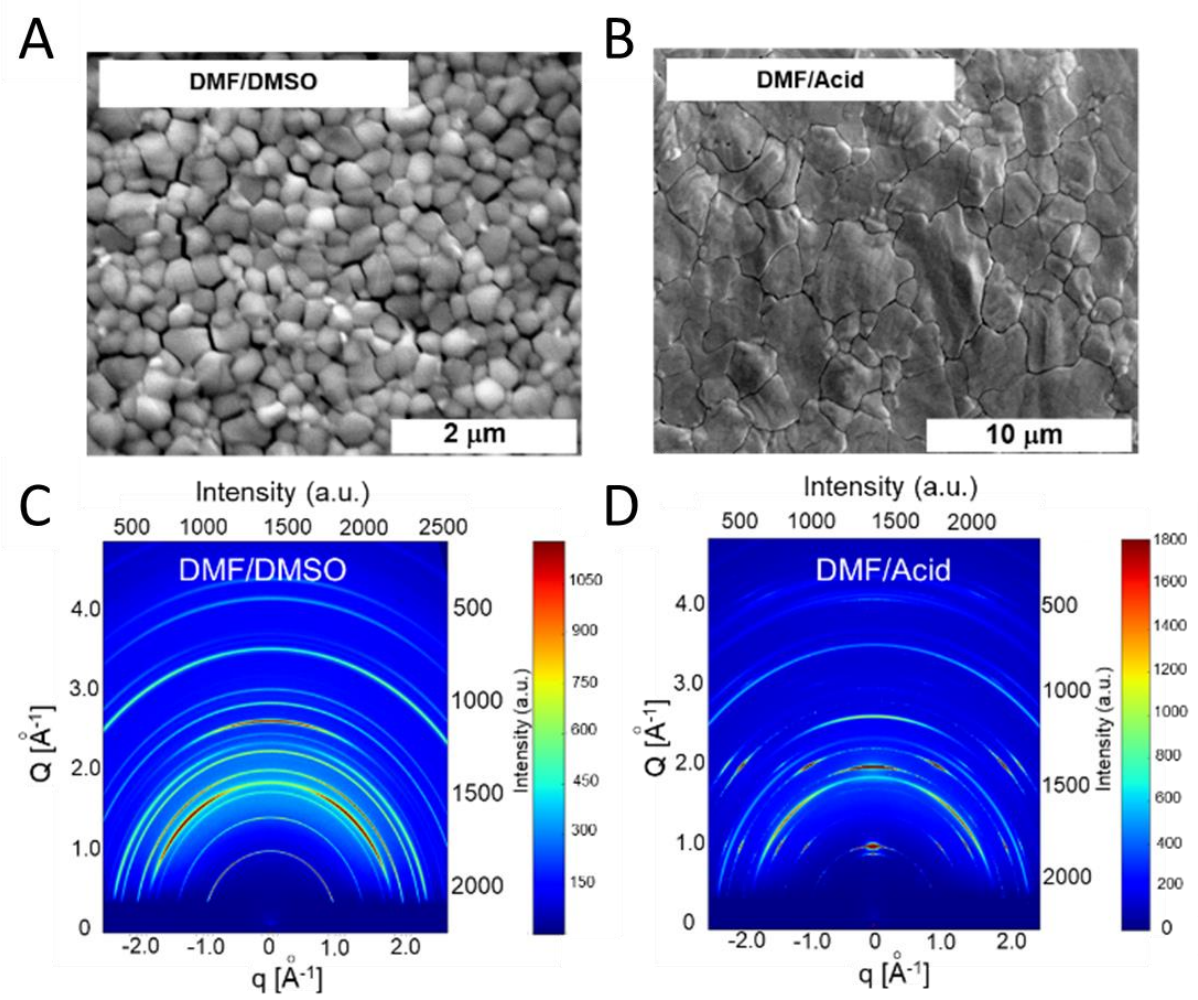

Figure 24 Impact of hydrohalic acids on the morphology and crystal quality of the $FA_{0.83}Cs_{0.17}Pb(I_{0.6}Br_{0.4})_3$ perovskite film. (**A**) A scanning electron microscope (SEM) image of a $FA_{0.83}Cs_{0.17}Pb(I_{0.6}Br_{0.4})_3$ perovskite film prepared with a DMF/DMSO solvent mixture and (**B**) with hydrohalic acid (HI/HBr) additives. (**C, D**) Wide-angle X-ray scattering (WAXS) image of $FA_{0.83}Cs_{0.17}Pb(I_{0.6}Br_{0.4})_3$ perovskite films deposited on a fluorine doped tin oxide (FTO) substrate with both methods. Text and figure adapted from [105].

I see a change in the morphology of the films with the domains/apparent grains observed in SEM changing in size from a few hundred nanometres to several microns (**Figure 24A and B**) commensurate with the scattering measurements.[131] Please note that the larger gaps in **Figure 24A** are a result of the longer beam exposure during the SEM measurement. Fresh films

are hard to focus on and only after some exposure it is possible to focus on the surface. That, however, damages the films as well. In **Figure 24C** and **D**, I display wide-angle X-ray scattering (WAXS) measurements, where I observe that the control "DMF/DMSO" route results in concentric Debye–Scherrer rings indicative of polycrystalline thin films with a low degree of texture. They show two points of maxima around the rings indicative of slight preferred orientation along the *(110)* plane. For the acid route, I observe a significant variation in intensity across the Debye–Scherrer rings, indicative of a highly textured film which has a high degree of preferred orientation vertical to the substrate plane. In **Figure 25**, I present the in-situ crystallization WAXS measurements for both fabrication methods during heating, plotting scattering intensity versus time, revealing that the DMF/acid films crystallize at a significantly slower rate compared to the DMF/DMSO films, even though they crystallize at a higher temperature (185 °C vs 100 °C). Further, the acid route shows additional peaks which are likely polytypes (2H, 4H, 6H and PbI_2) showing that the acid route goes through a series of different intermediates until it forms the perovskite structures. The fast and rapid crystallisation of the DMF/DMSO route likely indicates that most of the perovskite phase already formed during the solvent quenching step. In the next part I study the device and light stability of the two different routes.

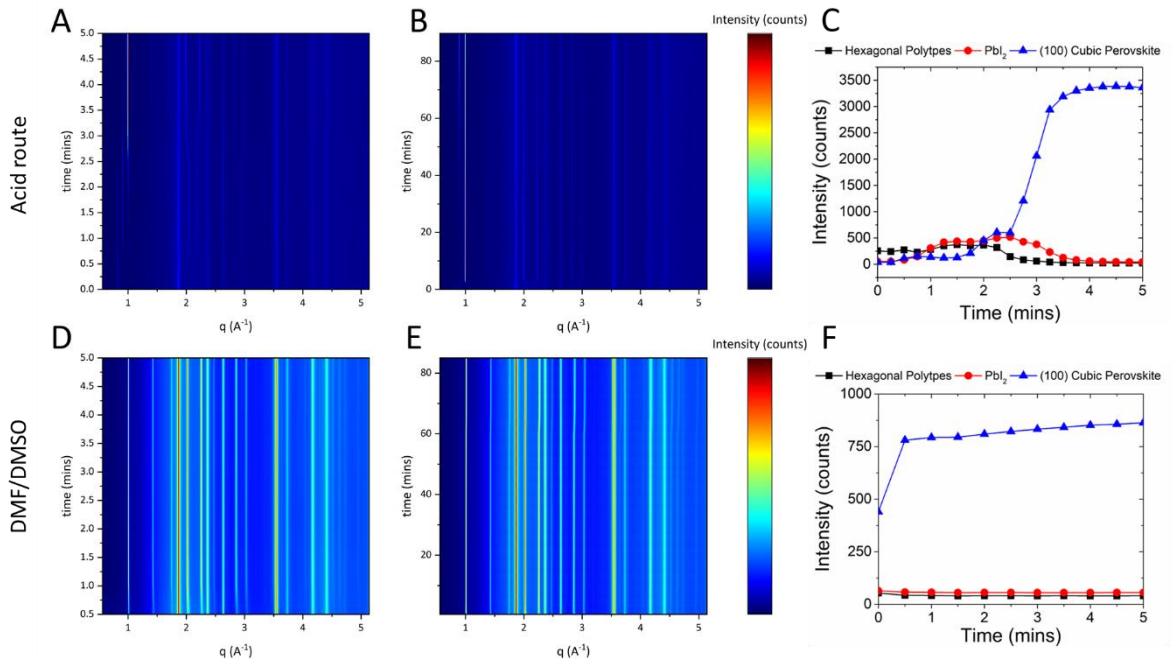

Figure 25 WAXS 2D plot of a $FA_{0.83}Cs_{0.17}Pb(I_{0.6}Br_{0.4})_3$ perovskite film fabricated with a low-temperature DMF/DMSO and a high-temperature DMF/Acid fabrication method. The data shows the first 5 and 90 min of a $FA_{0.83}Cs_{0.17}Pb(I_{0.6}Br_{0.4})_3$ perovskite film fabricated with the (**A, B**) acid route annealed at 185 ° C. An overview of the evolution of the relevant phases in the first 5 mins for the acid route is shown in (**C**). The data shows the (**D, E**) DMF/DMSO fabrication method annealed at 100 ° C and the corresponding overview in (**F**). The DMF/Acid method was prepared with a "fully-aged" solution, which was aged for more than 72h after adding the HI/HBr additive. Annealing was done in a helium atmosphere with slight water/oxygen contamination. Text and figure adapted from [105].

The devices were aged under AM 1.5G sunlight at maximum power point (MPP) in ambient air for 24 hours without encapsulation. All devices were fabricated with a $FTO/SnO_2/PC_{61}BM/FA_{0.83}Cs_{0.17}Pb(I_{0.6}Br_{0.4})_3$/ 2,20,7,70-tetrakis(N, N-di-p-methoxyphenyl-amine)-9,90-spirobi-fluorene (spiro-OMeTAD)/Au architecture. In **Figure 26**, I show the TOF-SIMS tomography of pristine and aged perovskite devices with the DMF/DMSO and DMF/acid

perovskite films. This measurement allowed me to assess the inhomogeneities of the FA/Cs A-site cations and the I/Br halides. After aging, I observed a stronger compositional variation of the A-site for the DMF/DMSO perovskite films than the DMF/acid films, consistent with improved compositional stability of the DMF/acid processed films.

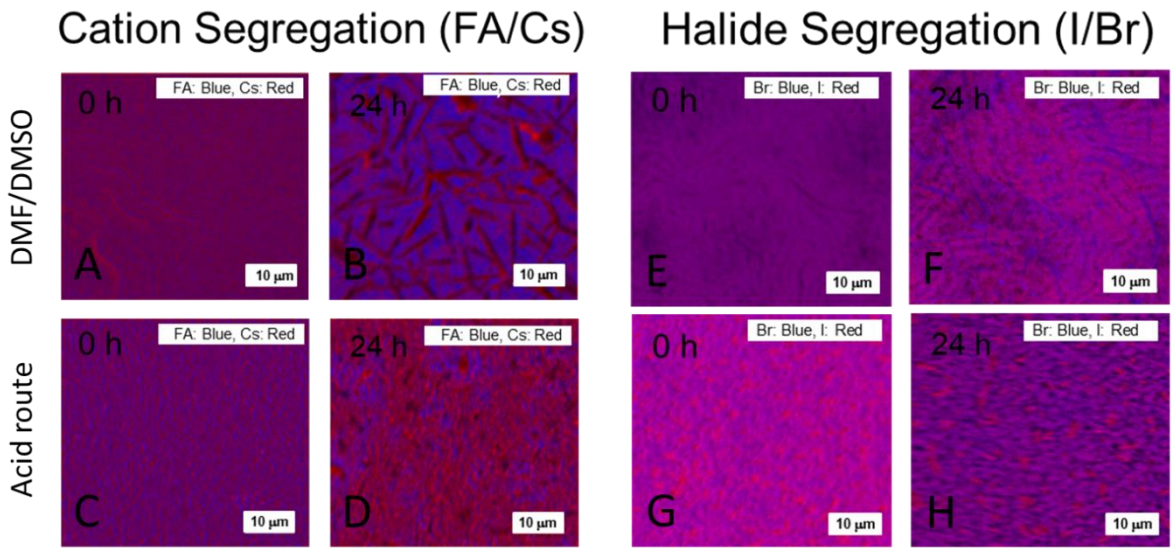

Figure 26 FA^+/Cs^+ A-site cation and halide segregation. TOF-SIMS 2D mapping of FA^+ (blue) and Cs^+ (red) overlays for the (**A**) DMF/DMSO, (**B**) DMF/acid devices aged for 0 hours, and (**C**) DMF/DMSO, (**D**) DMF/acid devices aged for 24 hours. 2D maps for Br^- (blue) and I^- (red) overlays for the (**E**) DMF/DMSO, (**F**) DMF/acid devices aged for 0 hours, and (**G**) DMF/DMSO, (**H**) DMF/acid devices aged for 24 hours. The data was reconstructed to include data only from the perovskite absorber layer from a 3D tomography dataset of the entire device stack. The images are based on a relative intensity scale for each species, which is shown for each individual image in the appendix in **Figure A 1** and **Figure A 2**. Text and figure adapted from [105].

Interesting is that the dominant decomposition pathway is the segregation of the A-cations and not the halides as commonly assumed for FACs compositions with high Br^- content.[98,132–134] Recent work by Knight et al. showed similar results.[135] That might be related to the ambient

aging given that CsI is hygroscopic and FAI is also likely very sensitive to moisture at least according to the material safety datasheet (MSDS). E.g. it could be that the moisture decomposition which is typically accompanied with the formation of a orthorhombic $CsPb(I_{1-x}Br_x)_3$ phase[47] is faster than the halide segregation. Further tests without moisture present would be necessary to entangle the origin of the effect. While the acid route has some advantages it also has some downfalls. An "under-aged" solution leads to lower crystallinity, smaller grain sizes, and lower charge-carrier mobilities and an "over-aged" solution suffers from poor perovskite coverage across the substrate. Further it has been challenging to use them in p-i-n structures which I believe originates from their higher surface roughness.

Ideally, I would like to combine both the acid-route with the solvent quenching route to produce a new more stable solvent quenching route. I realised over time that one of the key components of the acid-route is the decomposition of the DMF. Over time dimethylamine ($(CH_3)_2NH$) and formic acid (HCOOH) are formed in the solution via the hydrolysis of dimethylformamide.[136,137] This degradation process can also happen alone or be accelerated through the exposure of the solution to air or water (**Figure 27A**).[136,138] Through TOF-SIMS measurements residual amounts of DMA^+ in the perovskite film are found. The film was annealed at 185 °C for 90 mins in an oven and prepared from a DMF precursor solution aged for 48h with hydrohalic acids additives (**Figure 27B**). Hence, I can confirm that these hydrohalic acids in water (HI 57 wt. % H_2O and HBr 48 wt. % H_2O) cause fast hydrolysis of DMF while simultaneously providing a source of halide, causing an unintended and uncontrolled addition of dimethylammonium halide salt $(CH_3)_2NH_2^+X^-$ into the perovskite solution. With this insight, I introduce a new controllable method of precursor phase engineering with the addition of dimethylammonium halide, and specifically dimethylammonium chloride (DMACl).

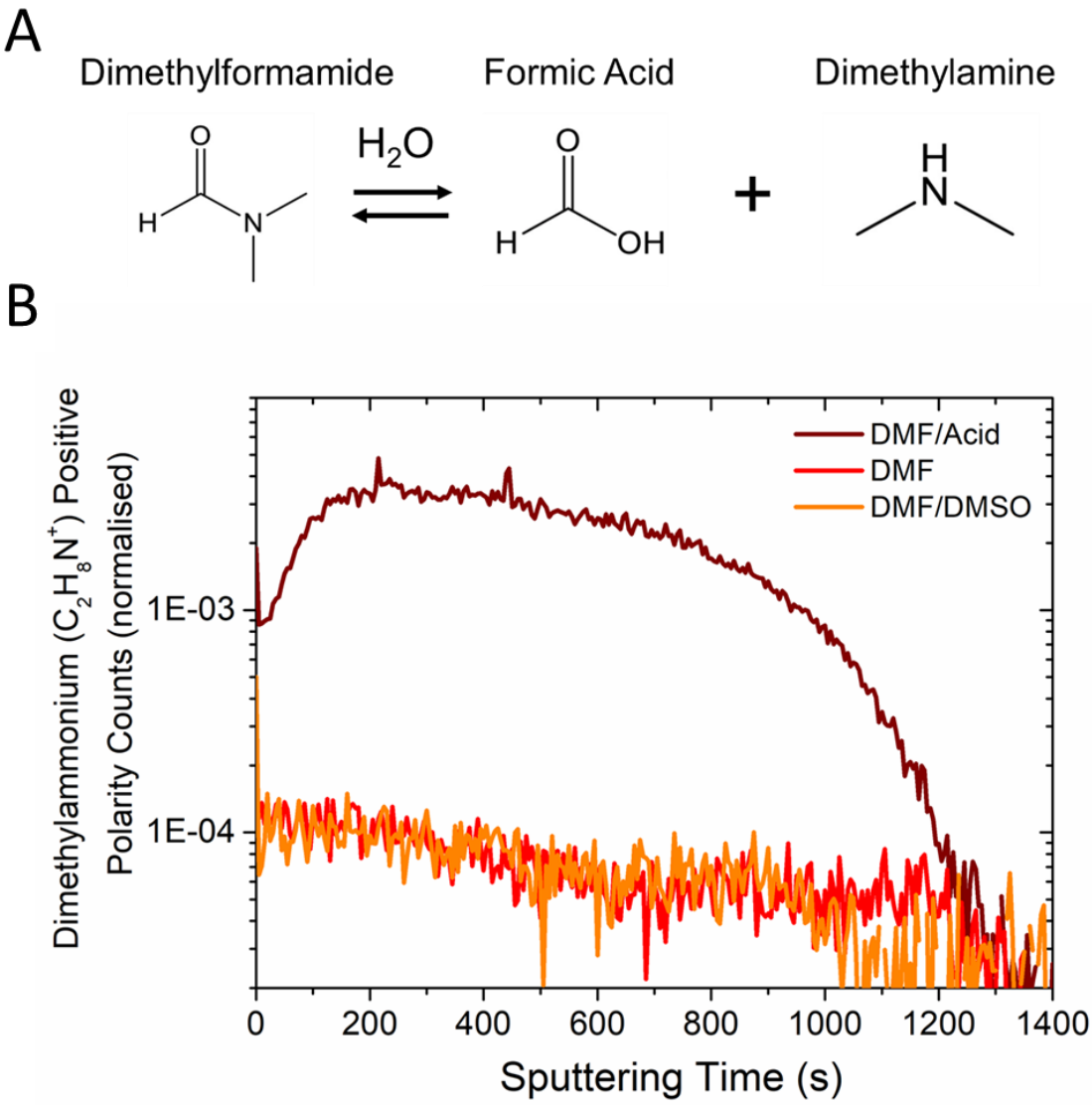

Figure 27 (A) Schematic showing the degradation of dimethylformamide (DMF) into dimethylamine and formic acid in the presence of water. The chemical equation of the DMF hydrolysis reaction, where DMF is the reactant, while dimethylamine and formic acid are the products. $(CH_3)_2NC(O)H \rightleftharpoons HCOOH + (CH_3)_2NH.$ (B) Positive Polarity Time-of-flight secondary ion mass spectrometry (TOF-SIMS) detecting dimethylammonium $C_2H_8N^+$ ions of (FA, Cs)Pb(Br, I)$_3$ films prepared using various fabrication methods after a 185 °C 90 m annealing step. Text and figure adapted from [105].

13.3. Intermediate phase of the DMA route

Intermediate, or precursor phases commonly occur during the formation of polycrystalline metal-halide perovskite thin-films.[139] Although influential, they are often an overlooked aspect of the complex crystallization process driven by thermodynamics. I observed that films prepared with a precursor solution aged with hydrohalic acids crystallized via distinct intermediate phases. I postulate that the source of these specific intermediate phases and thus control the formation process, is the unintentional presence of DMA^+. To test this theory, I prepared perovskite thin-films from precursor solutions which contained increasing concentrations of dimethylammonium halide salts (DMAX). Consistent with my hypothesis, I observed that this addition of the DMAX induces the formation of perovskite precursor phases, which allows for crystallisation to proceed via the formation of hexagonal perovskite polytype (2H, 4H and 6H) intermediate phases, which I illustrate in **Figure 28**. This class of perovskite polytypes is comprised of a mixture of corner-sharing (cubic) and face-sharing (hexagonal) octahedral connections assembled in various ratios. This family of perovskites are commonly found in perovskite oxides but have also been reported to occur in metal-halide perovskites.[140–142] Here, I identify the $DMA_zFA_yCs_{1-y}Pb(I_xBr_{1-x})_3Cl_z$ perovskite system as part of this polymorphism class of material, where the proportion of cubic to hexagonal octahedral connections increases when exposed to high-temperatures (> 140 °C) (**Figure 28A**); resulting in a phase transition from 2H, 4H or 6H face-sharing hexagonal frameworks, to a 3C corner sharing cubic perovskite.[143]

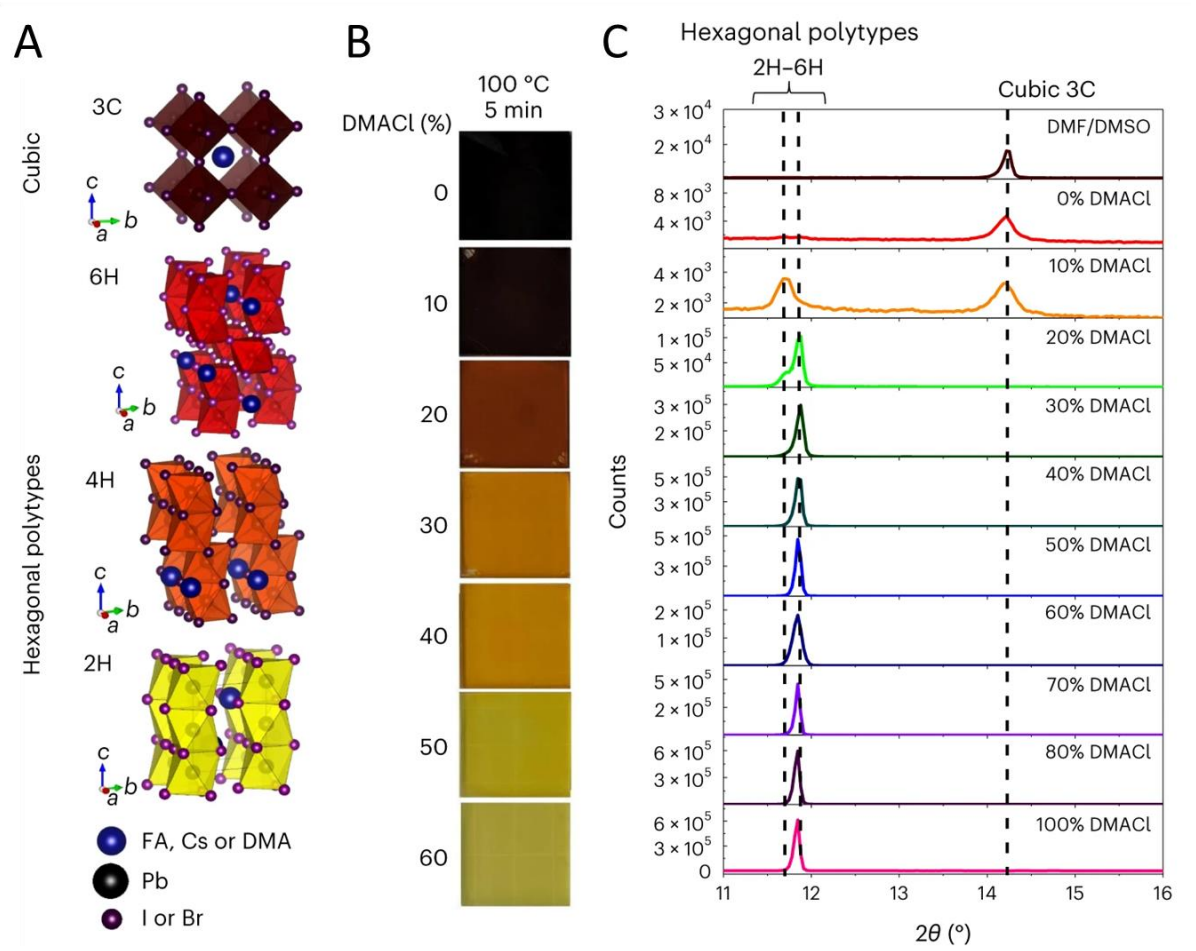

Figure 28 (**A**) Crystal structure of a unit cell of the hexagonal lead halide perovskite polytypes—2H, 4H and 6H—showing PbI_6 octahedra connectivity, along with a 3C cubic perovskite structure. (**B**) A series of photographs of $DMA_x(FA_{0.83}Cs_{0.17})_{1-x}Pb(Br_{0.2}I_{0.8})_3Cl_x$ perovskite films spin-coated with various amounts of DMACl additive, where percentages are expressed in excess amounts with respect to the lead content. (**C**) A series of X-ray diffraction patterns of the corresponding thin films showing the intermediate precursor phases in the form of hexagonal polytypes. Text and figure adapted from [105].

As Mancini et al.[144] and García-Fernández et al.[145] have independently reported that $DMAPbX_3$, where X is I^-, Br^- or Cl^- anions, forms in various hexagonal face-sharing crystal arrangements. For example, $DMAPbI_3$ crystallizes in a 2H-hexagonal polytype with a space-

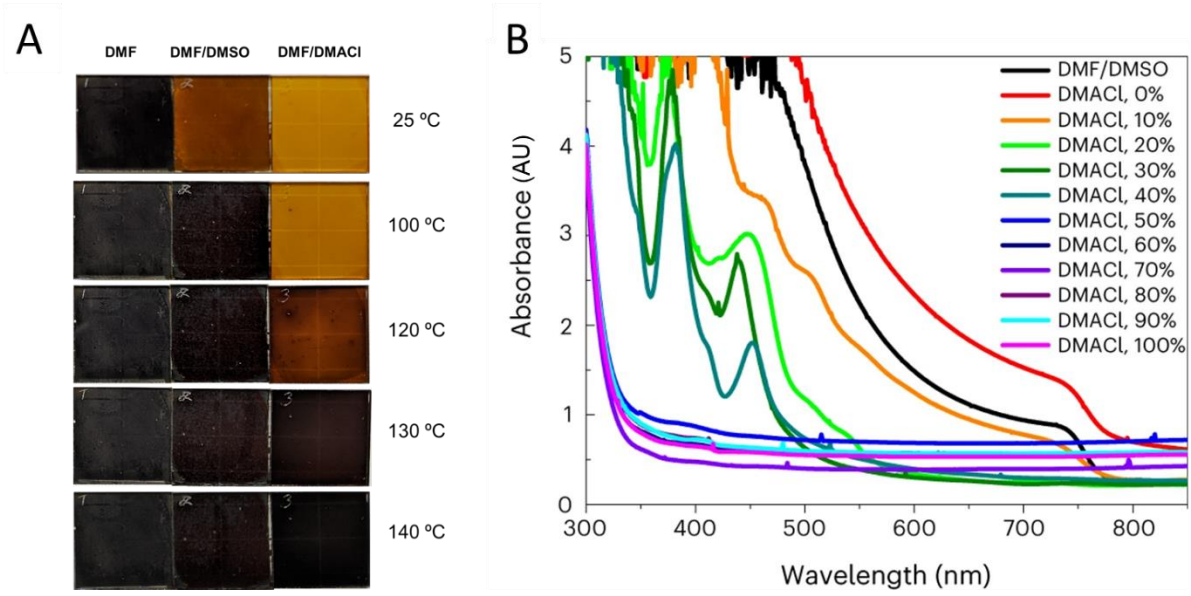

Figure 29 (**A**) Impact of temperature on the various film preparation methods DMF, DMF/DMSO and DMF/DMACl. The films were heated at 25 °C, 100 °C, 120 °C, 130 °C and 140 °C for 1 minute in an air atmosphere. The neat DMF film appeared black immediately after spin coating, while the DMF/DMSO and DMF/DMACl had a translucent appearance after spin coating and only at a temperature above 100 °C and 140 °C that these films appeared black. All images were captured on the FTO glass side. (**B**) A series of Ultraviolet-visible (UV-Vis) absorbance spectra of $DMA_x(FA_{0.83}Cs_{0.17})_{1-x}Pb(Br_{0.2}I_{0.8})_3Cl_x$ perovskite films spin-coated with various amounts of DMACl additive, where percentages are expressed in excess amounts with respect to lead. Text and figure adapted from [105].

group $P6_3/mmc$ comprising chains of face-sharing $[PbI_6]^{4-}$ octahedra separated by chains of DMA^+ cations,[146] whereas $DMAPbCl_3$ and $DMAPbBr_3$ both crystalize in a 4H-hexagonal perovskite polytype. These 4H perovskite polytypes are formed with Pb_2X_9 dimers of face-sharing octahedra, which are then connected to one another via corner-sharing octahedra.[145] **Figure 28** shows the intermediate phases occurring in the solvent-dried films before the conversion to fully crystalline 3C perovskite form. After a 5 minute 100 °C anneal, I observe a

colour change, along with the appearance of the 2H to 6H hexagonal polytypes phase, identified by peaks between $2\theta \sim 11.6° – 11.8°$. Moreover, I observe that with $\geq$ 20% excess DMACl (with respect to the Pb or combined $FA^+ + Cs^+$ content) I fully suppress the formation of the 3C cubic $FA_yCs_{1-y}Pb(I_xBr_{1-x})_3$ perovskite when heated at or below 100 °C. As it also becomes evident from the UV-Vis absorbance spectra in **Figure 29B**. I assume that most of the solvent (DMF) has been removed from the film during this 100 °C annealing process, but most of the DMACl remains incorporated within the crystalline polymorphs. With a subsequent anneal at higher temperatures, I assume that most of the DMACl (the most volatile remaining component) is driven out of the film until only the 3C cubic $FA_yCs_{1-y}Pb(I_xBr_{1-x})_3$ perovskite predominantly remains. However, I am aware from further characterisation described later that some of the DMA^+ and potentially also some fraction of Cl^- remains in the lattice.

When adding DMACl in excess with respect to lead to the $FA_yCs_{1-y}Pb(I_xBr_{1-x})_3$ perovskite system, it appears to act as a "crystallizing agent" which controls the speed at which the 2H, 4H, 6H to 3C crystallization sequence takes place. In turn, this directly impacts the nucleation dynamics, crystallization rate and final crystal quality of the perovskite film. These hexagonal polytypes may template the perovskite orientation due to their similar hexagonal crystal structure to the 2H δ-$FAPbI_3$ "yellow" phase, which also exhibits a strong diffraction peak at $2\theta \sim 11.8°$. This template offers a unique perovskite crystallization strategy, where the 2H to 3C crystallization sequence is controlled in a minute rather than seconds for the standard DMF/DMSO solvent system. Furthermore, I highlight that intermediate phases, induced with the additions of DMSO or DMAX, are indispensable for avoiding large macroscopic cracks, which are otherwise found in films processed from neat-DMF (**Figure 30**).

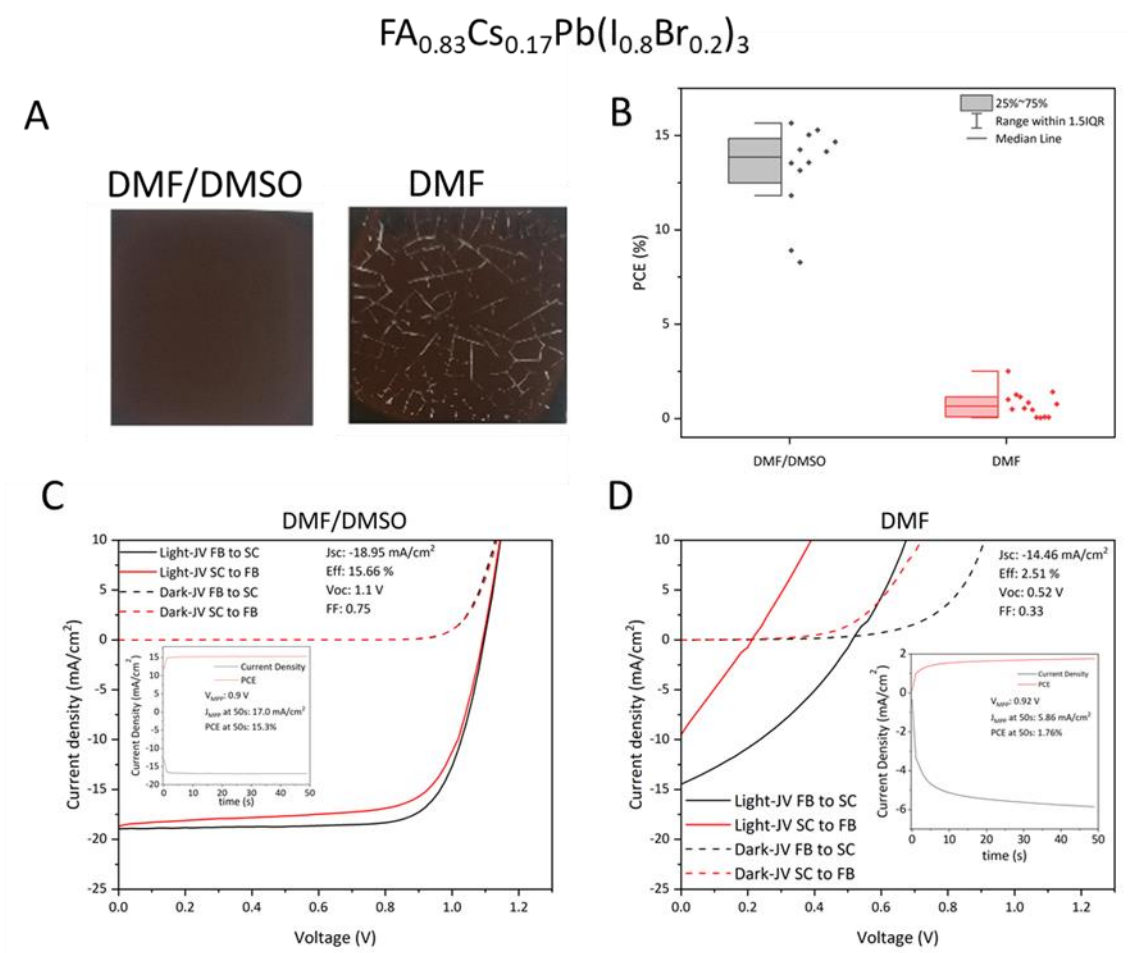

Figure 30 Comparison between a DMF/DMSO and a neat DMF solvent mixture for perovskite devices. (A) Images of backlit perovskite films prepared with a DMF/DMSO and a neat DMF solvent mixture. (B) PCE comparison between both methods. (C) J-V characteristics and steady-state photocurrent at a fixed voltage of a DMF/DMSO device. (D) J-V characteristics of a neat DMF device. Text and figure adapted from [105].

The intermediate phases induced by the DMSO·PbI_2 and/or $(DMSO)_2$·PbI_2 complexes disappear within the first few seconds of the annealing process, leading to rapid crystal formation. For the DMF/DMACl route, I observe that little to no hexagonal face-sharing $DMAPbX_3$ crystal structure remains when DMAX is added in excess, and the films are annealed at elevated temperatures (> 185 °C) (**Figure A 3**). Films with higher DMACl content do require

longer annealing time or higher temperatures to fully or at least mostly remove the $DMAPbX_3$ crystal structure, which is consistent with the postulation that the excess DMACl needs to be volatilized from the film, for crystallisation to occur. A further in-depth discussion of the $DMAPbX_3$ and the ideal DMACl content is given in the next chapter. Please note that this is a similar requirement to when processing perovskite films from non-halide lead salts, such as lead acetate or lead chloride with an excess of A-halide cations.[147]

Eperon et al. have previously investigated substituting FA^+/Cs^+ for DMA^+ in lead-halide perovskites[148] as opposed to the excess addition that I have undertaken here. To investigate the similarities and differences of these two approaches, in **Figure A 4**, I show photographs, XRD and UV-Vis absorption data of a series of films that were prepared using a cation substitution method, where A-site FA/Cs cations were replaced by DMA^+ cations targeting a $DMA_y(FA_{0.83}Cs_{0.17})_{1-y}Pb(Br_xI_{1-x})_3$ perovskite system. Similarly to Eperon et al.,[148] I observed a slight blue shift in absorption onset with substitution. However, this was accompanied by lower preferred crystal orientation along the (100) plane. More importantly, I observe the presence of the formation of two separate phases, a 2H face-sharing located at 2θ = 11.8° associated with δ-$FAPbI_3$ (11.78° and 11.81°) and/or $DMAPbI_3$ (11.72° and 11.75°), along with a 3C corner-sharing perovskite (**Figure A 4**). I also observe a lowering of the steepness of optical absorption onset, indicative of an increased electronic disorder.[149] **Figure A 5** shows films of the identical $DMA_y(FA_{0.83}Cs_{0.17})_{1-y}Pb(Br_xI_{1-x})_3$ perovskite system after a 185 °C annealing step. This high-temperature annealing step resulted in the removal of the 2H δ-$FAPbI_3$ and/or $DMAPbI_3$ peak; however, significant PbI_2 peaks located at $2\theta \sim 12.7°$ appeared. In contrast, when DMAX is added in excess amounts with respect to the $FA_{0.83}Cs_{0.17}Pb(Br_xI_{1-x})_3$, I obtain film morphology and crystal quality similar to the "acid

method", where hydrohalic acids would hydrolyse the DMF over time to introduce DMA^+ into the precursor solution. This "excess cation" method is therefore different to the DMA^+ substitution explored previously and consists of a $DMA_y(FA_{0.83}Cs_{0.17})Pb(Br_xI_{1-x})_3X_y$, where X is I^-, Br^- or Cl^- anions, in a perovskite precursor solution, that serves to control the intermediate phases during the crystallization process. As shown in **Figure A 3**, this results in highly textured perovskite films without any additional hexagonal polytypes remaining in the fully annealed films. Incidentally, if I add 50% excess $DMABr_xI_{1-x}$, as opposed to DMACl, I observed a 25 nm redshift in bandgap for films fully crystallised into the 3C perovskite, compared to neat $FA_{0.83}Cs_{0.17}Pb(Br_xI_{1-x})_3$ films, potentially due to a preferential loss of bromide (in DMABr) during the crystallization processing. Lastly, I have investigated the use of all DMAX and dimethylamine as an additive and have observed that all of these compounds can form hexagonal polytype intermediate phases (**Figure 31**). However, I found that in order to achieve an efficient device with a smooth perovskite morphology, DMACl was the most suitable additive, resulting in $DMA_x(FA_{0.83}Cs_{0.17})Pb(Br_{0.2}I_{0.8})_3Cl_x$ precursor phases. Notably, DMACl allowed for faster removal of excess compounds at lower temperatures and did not significantly narrow the band gap of the perovskite, which is the case when adding DMAI/DMABr or HI/HBr in excess.

As reported by García-Fernández et al.,[146] due to the low dimensionality of the $DMAPbI_3$ crystal structure, this compound appears to behave as an ionic conductor but suffers from poor electronic conductivity. These insulating properties may be the reason why the optimum annealing requires high temperatures along with long durations in order to drive out the face-sharing $DMAPbX_3$ perovskite. However, I note that a small portion of DMA^+ could potentially be incorporated into the cubic $(FA_{0.83}Cs_{0.17})Pb(Br_yI_{1-y})_3$ structure, as I measure some residual DMA^+ using TOF-SIMS. Ke et al. recently reported that up to 30% of the caesium in $CsPbI_3$ can

be substituted with DMA^+, thus forming $Cs_{0.7}DMA_{0.3}PbI_3$ in a 3C corner-sharing cubic crystal structure.[150] Similarly, Marshall et al. recently showed that the $Cs_xDMA_{1-x}PbI_3$ perovskite only forms a pure-phase material with up to ≈ 25% DMA^+ substitution; above this point, the A-site cations begin to phase segregate.[151] Hence, assuming similar incorporation fractions, 4-5% (i.e. 25 to 30% of the 17% Cs) DMA^+ cations may be incorporated into the final perovskite structure.

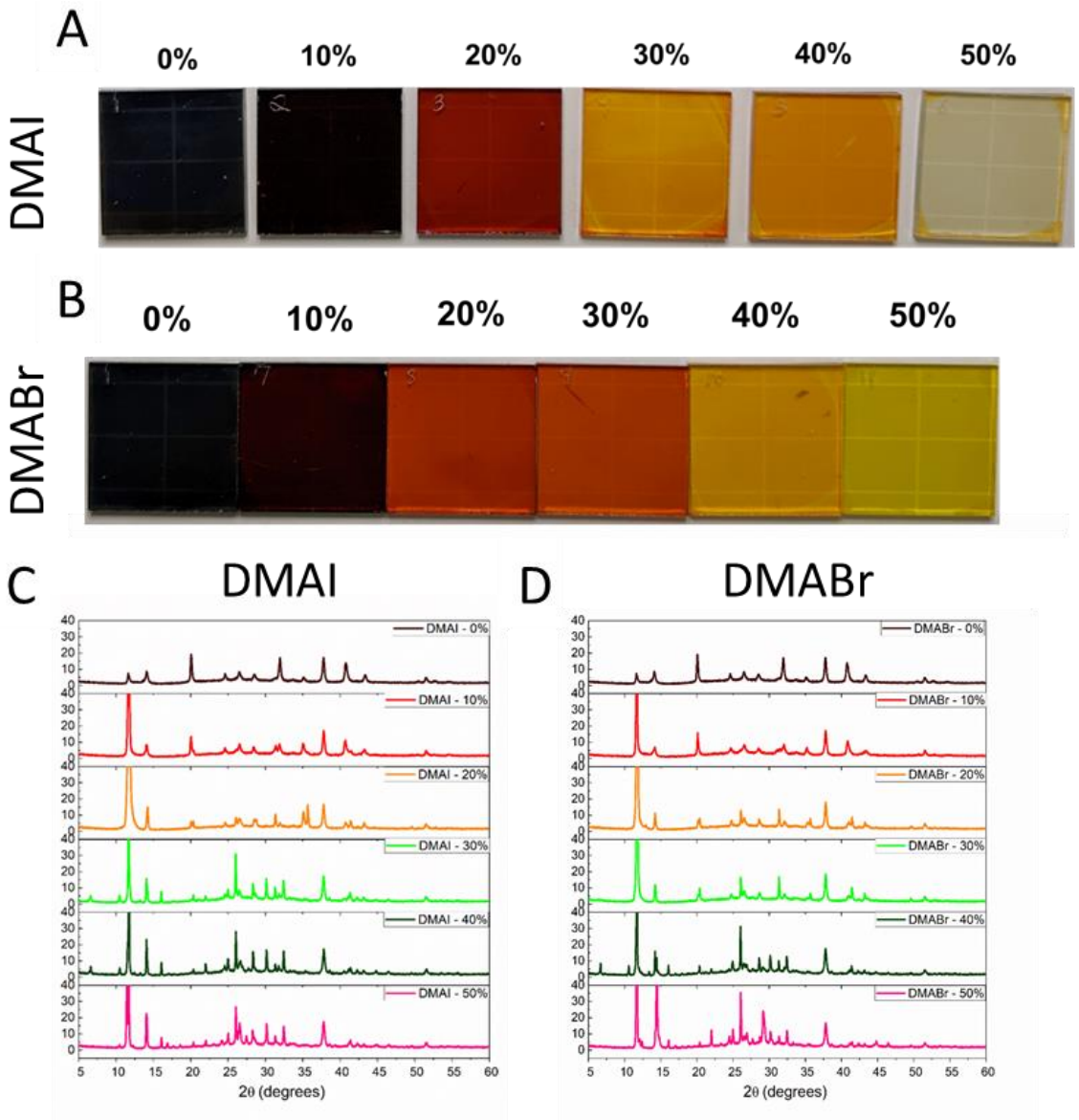

Figure 31 Impact of DMAI and DMABr on the intermediate phases of the $FA_{0.83}Cs_{0.17}Pb(Br_{0.8}I_{0.2})_3$.

(A, B) A series of photographs of $DMA_xFA_{0.83}Cs_{0.17}Pb(Br_{0.8}I_{0.2})_3I_x$ and $DMA_xFA_{0.83}Cs_{0.17}Pb(Br_{0.8}I_{0.2})_3Br_x$ perovskite films spin-coated heated at 100 °C for 1 m, with various amounts of DMAI and DMABr additive, where percentages are expressed in excess amounts with respect to lead. (C, D) A series of X-Ray diffraction patterns of the corresponding thin film showing the intermediate precursor phases in the form of hexagonal polytypes. Text and figure adapted from [105].

However, I did not observe a significant change in absorption onset between the "DMF/DMSO" and DMF/DMAX fabrication methods after fully annealing the neat iodide perovskite film at high temperature (**Figure 32**). However, for larger Br^- contents I find that there is a slight shift in bandgap as discussed in the next chapter.

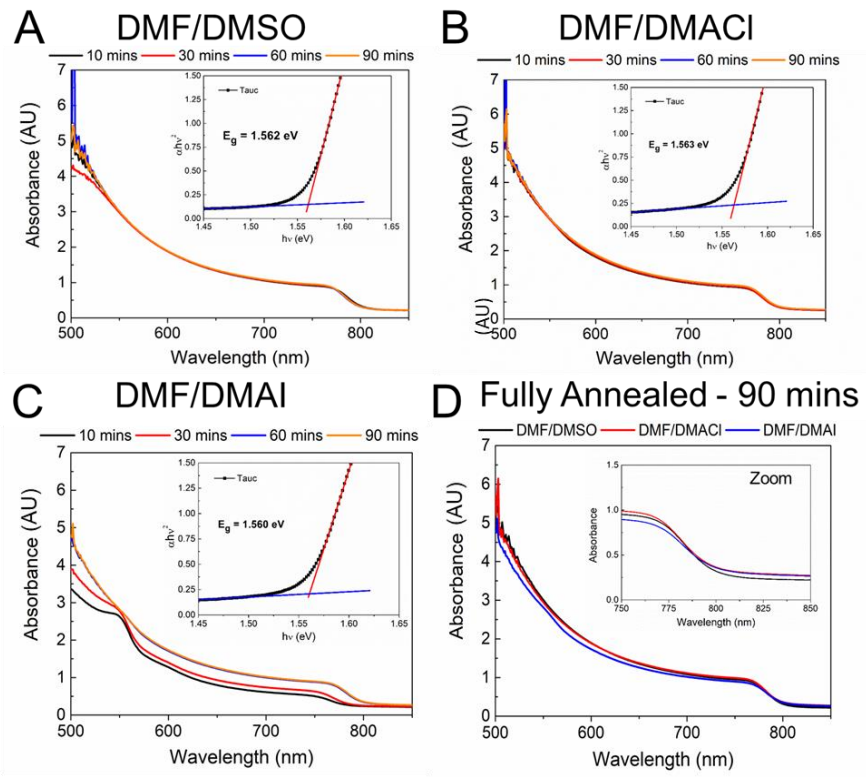

Figure 32 Optical band gap comparison between the perovskite films prepared with three different precursor solutions: $FA_{0.83}Cs_{0.17}PbI_3$ (DMF/DMSO), $DMA_{0.3}FA_{0.83}Cs_{0.17}PbI_3Cl_{0.3}$

(DMF/DMACl), $DMA_{0.3}FA_{0.83}Cs_{0.17}PbI_{3.3}$ (DMF/DMAI). All films were characterised throughout the annealing process after 10 mins of annealing at 170 °C on a hotplate and subsequent annealing in an oven at 175 °C after 30, 60 and 90 mins. A series of UV-Vis absorbance spectra measured throughout the annealing process of a film prepared with a precursor solution composed of (**A**) $FA_{0.83}Cs_{0.17}PbI_3$ (DMF/DMSO) (**B**) $DMA_{0.3}FA_{0.83}Cs_{0.17}PbI_3Cl_{0.3}$ (DMF/DMACl) (**C**) $DMA_{0.3}FA_{0.83}Cs_{0.17}PbI_{3.3}$ (DMF/DMAI). (**D**) A UV-Vis comparison spectrum of a series of fully annealed films. Text and figure adapted from [105].

13.4. Properties of the DMA route

In the next section, I compare the crystallographic and photophysical properties of $FA_yCs_{1-y}Pb(I_xBr_{1-x})_3$ perovskite films prepared with the "DMF/DMSO" and the "DMF/DMACl" route. A series of XRD pattern of 0-100% excess DMA are shown in **Figure 33**. The peaks are labelled in **Figure 33**. Interestingly, the crystal orientation (**Figure 34**) is not linearly correlated with the used DMA content but rather shows a peak at around 20% and then goes down again for 40% and increases again towards higher amounts. Further from 40% DMA a new peak appears at around 10.9° as analysed in **Figure 34B**. This could indicate that potentially undesired phases form inside the FACs perovskite. This peak fits the hydrated $FA_{0.83}Cs_{0.17}Pb(I_{0.85}Br_{0.15})_3 \cdot H_2O$ perovskite phase.[47] The DMACl salt is relatively wet as it is delivered so it might contain trace quantities of H_2O. That would agree with the findings using the DMACl route for Pb-Sn where Michael Farrar found similar evidence for a hydrated perovskite phase in the DMACl Pb-Sn thin films.[152] However, the films for pure Pb were annealed at 180 °C for 1h in an oven which should remove any residual water.

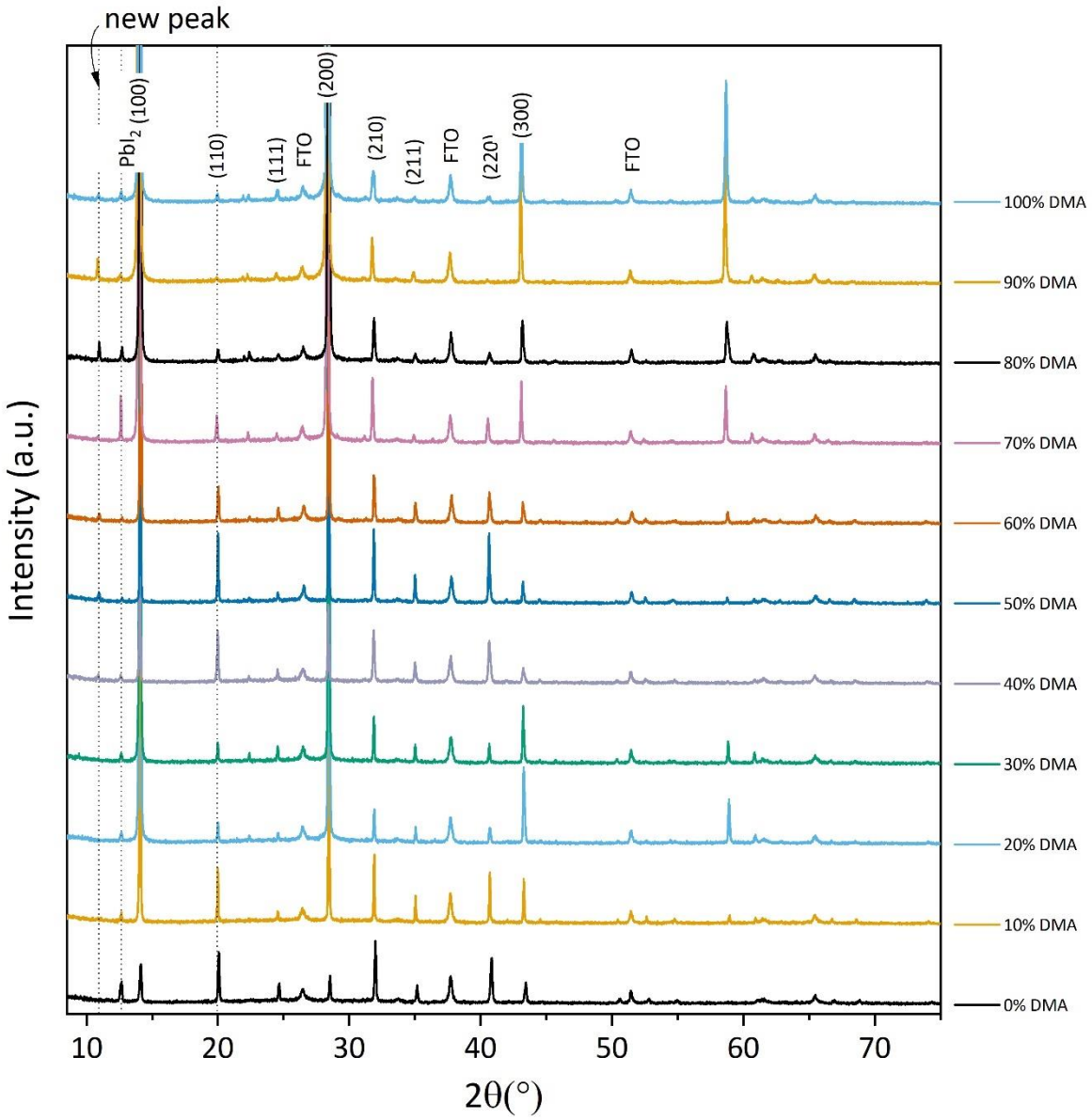

Figure 33 XRD of FACs thin films with excess DMA content from 0 to 100% (in mol% regarding the Pb content), peaks are labelled accordingly.

Further one would expect a linear increase in the hydrated perovskite phase with increasing amount of DMACl amount but that is not the case. To double-check the reproducibility of the peaks I repeated the same series as shown in **Figure A 8** and an in-depth analysis in **Figure A 9** and **Figure A 10**. All three series (the third one is made by David P. McMeekin) show a new peak appearing at around 10.9° which increases around 40 mol% DMACl added in excess and

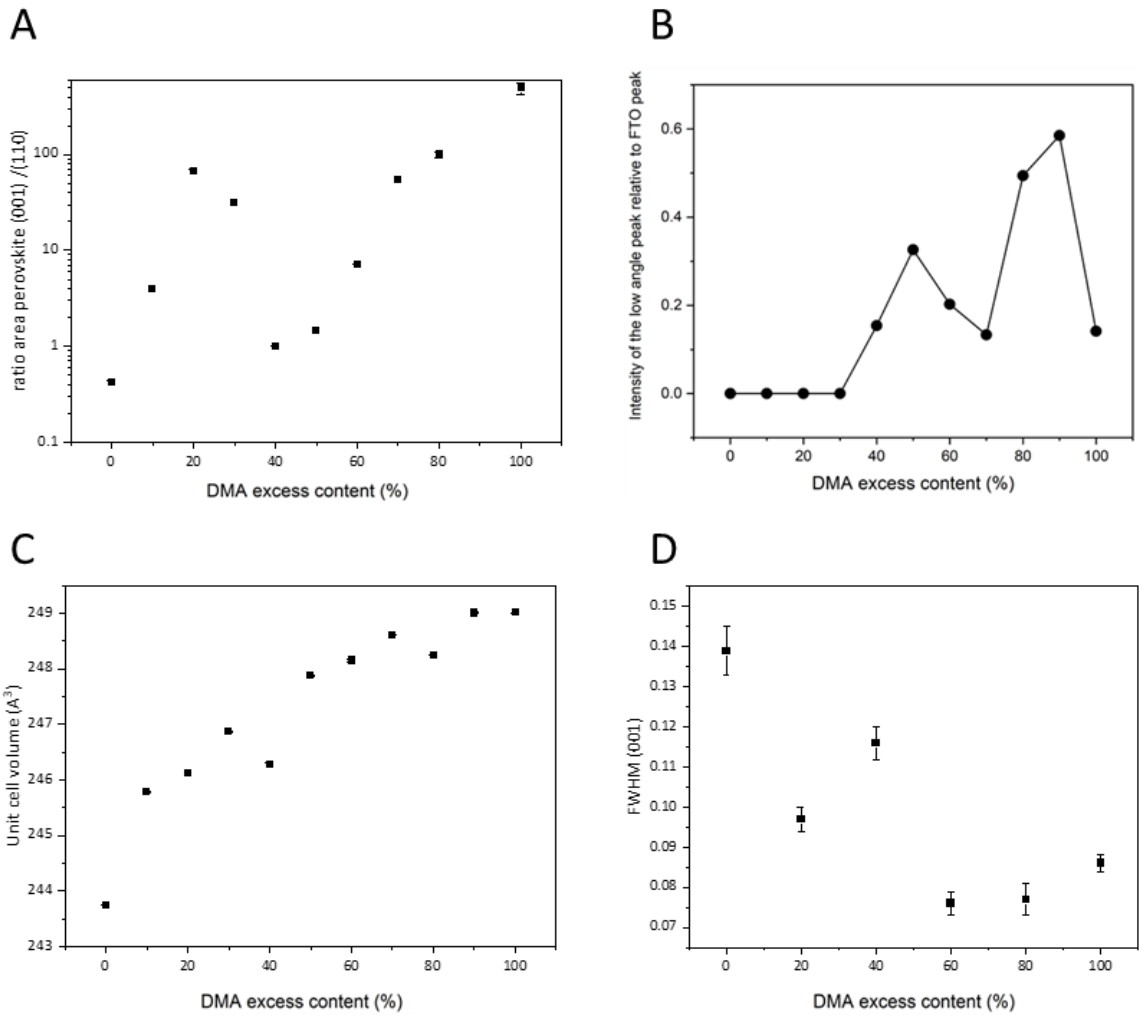

Figure 34 Analysis of XRD of FACs thin films with excess DMA content from 0 to 100% (in mol% regarding the Pb content), peaks are labelled accordingly. (**A**) The orientation of the crystals is measured by the relative peak intensity of the *(100)* to the *(110)* peak. (**B**) Peak intensity of the new unknown peak, which appears at around 10.9° relative to the FTO *(100)* peak. (**C**) Unit cell volume (A^{-3}) of the lattice fitted with a $Pm\bar{3}m$ structure. (**D**) Full-width half maximum (FWHM) of the *(100)* peak. Measurements were done by me and the analysis was done by Harry Sansom.

goes down in intensity around 60 to 70 mol% and increase again with more DMACl. The peak does not fit the reported crystal structure of DMA^+ structures[144,145,153] and also does not fit with any measured XRD pattern for the fabricated films as for example $DMAPbI_3$ spin-coated onto a

FTO substrate (**Figure A 6** and **Figure A 7**). It is not clear what this peak might be and with only one new peak a XRD fitting of this structure is impossible. By fitting each XRD structure with the $Pm\bar{3}m$ crystal structure one can determine the given unit cell volume which is plotted in **Figure 34C**. I see a linear increase in volume indicative of a possible incorporation of DMA^+. In **Figure 34D,** I plot the full width half maximum (FWHM) of the corresponding peaks. To further understand the materials quality I measured XRD^2 to understand not only the out-of-plane orientation (1D XRD) but also the in-plane orientation of a new series of $DMA_z(FA_yCs_{1-y})Pb(Br_xI_{1-x})_3Cl_z$ perovskite films. As shown in **Figure 35**, the in-plane orientation seems to correlate with the same trend as for the 1D XRD. There is an increase in orientation towards 20% to 30% DMA and then it decreases again for higher DMA content.

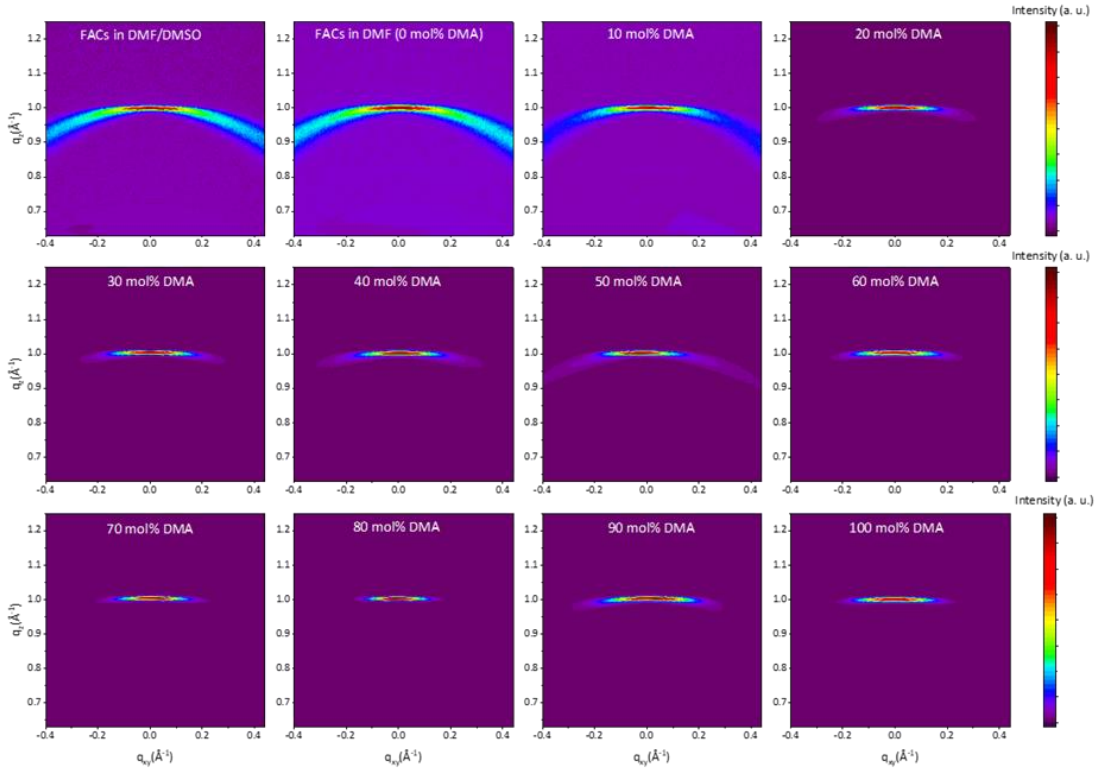

Figure 35 XRD^2 of the (100) peak of a $FA_{0.83}Cs_{0.17}Pb(I_{0.85}Br_{0.15})_3$ perovskite film prepared using DMF/DMSO and a series of $DMA_xFA_{0.83}Cs_{0.17}Pb(I_{0.85}Br_{0.15})_3Cl_x$ dissolved in DMF only. Text and figure adapted from [105].

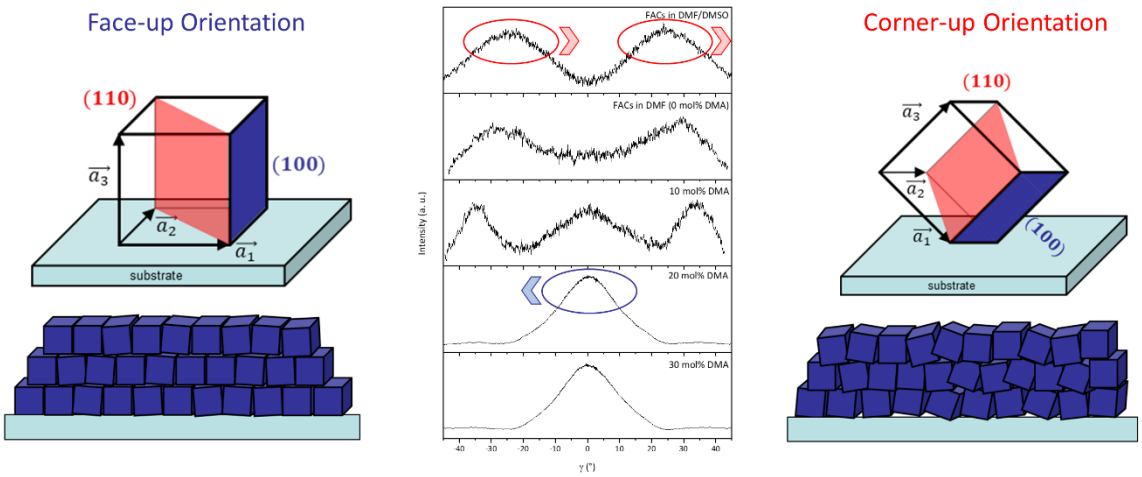

Figure 36 XRD^2 gamma peak analysis, showing the distribution of the *(100)* peak along the in-plane direction as a function of the azimuth angle (γ) for a series of DMACl and DMF/DMSO control films. Left and right are the graphical depictions of the corresponding orientation of the grains. The same analysis for 0 to 100% DMACl is shown in **Figure A 11**. Text and figure adapted from [105].

For 40% and 50% DMACl it shows a slight increase in broadening. The peak then increases again towards 100% DMA content. Oesinghaus et al.[154] outlined a potential interpretation of the XRD^2 which would translate to the graphical depicted interpretation of crystal grains as show in **Figure 36**. The FACs film made with DMF/DMSO shows two peaks along the cone section of the (100) peak which corresponds to a slight corner-up orientation meaning an average maximum of 30° between the FTO surface and the (100). That becomes slight less pronounced with the removal of DMSO. With the addition of DMA^+ the orientation changes towards a face-up orientation as it becomes apparent with the addition of 10% DMACl and the emergence of a third peak. That peak becomes dominant with 20% and more DMACl corresponding to a face-up orientation of the perovskite lattice. These findings coincide with the previous XRD^2 analysis of the DMF/acid method, where films prepared with an aged

solution with the addition of hydrohalic acids tend to orient their (100) peak to $\chi = 0°$.[131] Films with a high DMA^+ content have slower crystallization rates, allowing for face-up orientation to occur, while films with low or no DMA^+ content, such as the conventional DMF/DMSO films, crystallize at a much quicker rate, resulting in a significant portion of crystallite with a corner-up orientation. I hypothesize that crystallites may preferentially orient with their *(100)* plane parallel to the substrate if enough time and thermal energy is available. Similarly, Oesinghaus et al. established links between different $MAPbI_3$ perovskite fabrication methods prepared via various lead precursors (e.g. PbI_2, $PbCl_2$, or $Pb(CH_3COO)_2$) and their crystalline orientation.[154] Here, I expand on this knowledge by establishing links between the DMA^+ induced 2H-3C precursor phases, which govern the crystallisation kinetics of the $FA_yCs_{1-y}Pb(I_xBr_{1-x})_3$ perovskite system in order to template the growth of the highly ordered face-up domains. As shown in **Figure 37A**, by comparing XRD patterns of perovskite thin films with roughly identical thicknesses and scan parameters, I observe an increase of almost two orders of magnitude (77x) in the number of counts between the DMF processed neat $FA_{0.83}Cs_{0.17}Pb(Br_{0.2}I_{0.8})_3$ film and the $DMA_{0.5}(FA_{0.83}Cs_{0.17})Pb(Br_{0.2}I_{0.8})_3Cl_{0.5}$ processed film. Concurrently, I observe the disappearance of the XRD peak associated with the *(110)* orientation located at $\sim 20.1°$ for precursor solutions with over 40% DMACl. Lastly, the full-width-half-maxima (FWHM) for the *(100)* peak was lowered by roughly a factor of two compared to the DMF/DMSO control, indicative of an increase in the crystal grain size and reduction in micro strain of the perovskite material (**Figure 37B**).

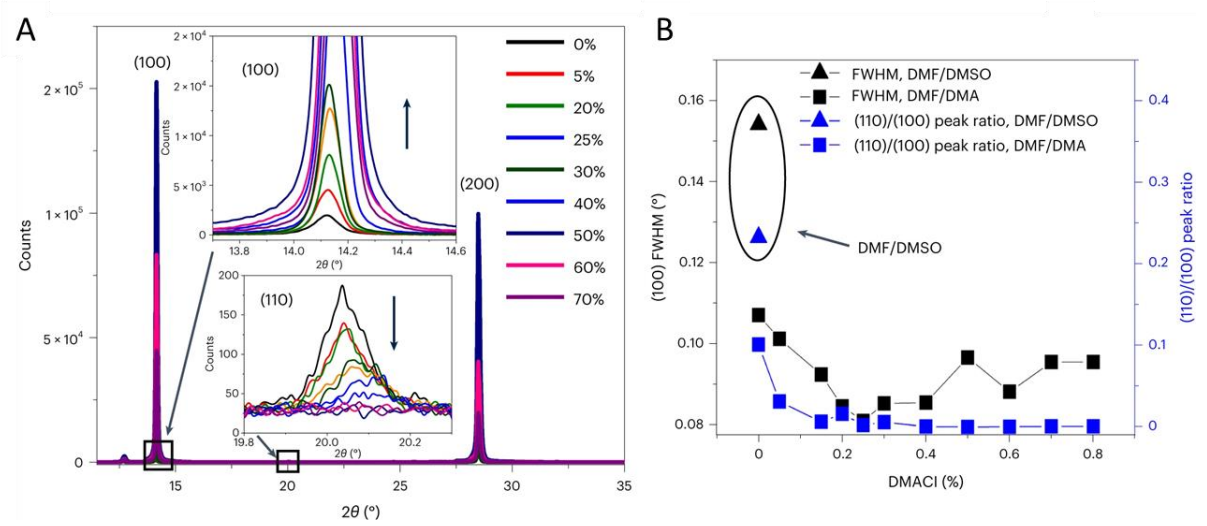

Figure 37 (**A**) One-dimensional XRD patterns of $DMA_x(FA_{0.83}Cs_{0.17})Pb(I_{0.8}Br_{0.2})_3Cl_x$ perovskite thin films with various amounts of excess DMACl after a full annealing step. The inset figures show enlarged regions of the *(100)* and *(110)* XRD peaks. (**B**) FWHM of the *(100)* peak, and a *(110)* to *(100)* peak ratio for films with various DMA^+ contents, compared to a control film with DMF/DMSO as solvents. Text and figure adapted from [105].

Lastly, I also show a series of scanning electron microscope (SEM) of the DMACl series from 0 to 100 mol% excess compared to the control with DMF/DMSO (**Figure 38**). There is a significant increase in apparent grain size until 20% mol excess. At 30% mol excess of DMACl the grain structure changes towards larger grains which are surround by several smaller grains. With 40% mol excess the apparent grains are again smaller and more convoluted. The convolution continues to increase and smaller holes appear in the films. With 100% mol excess the FTO substrate below even becomes visible.

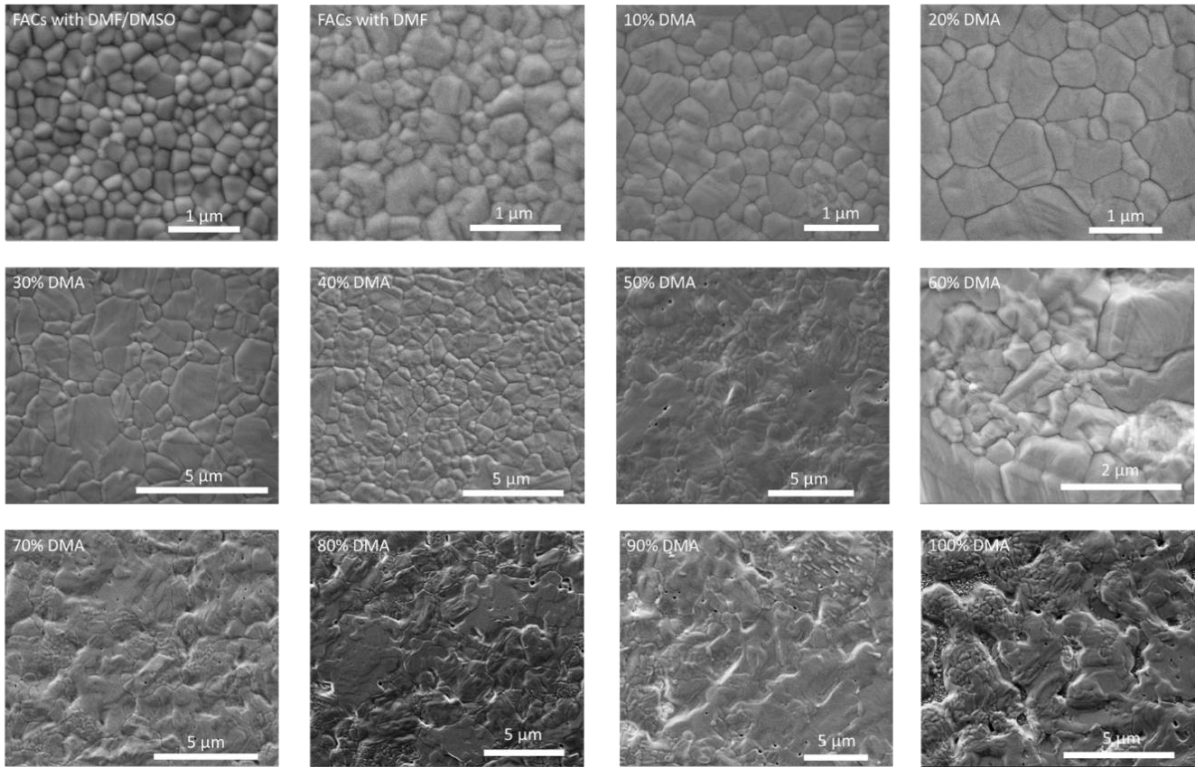

Figure 38 SEMs of $DMA_x(FA_{0.83}Cs_{0.17})Pb(I_{0.8}Br_{0.2})_3Cl_x$ perovskite thin films with 0 to 100 %mol amounts of excess DMACl after a full annealing step and a control film with DMF/DMSO.

13.5. Discussion and summary

On the pursuit of the perfect crystallisation route for lead halide perovskites for photovoltaics I found that the acid route has distinct advantage compared to the commonly employed solvent quenched fabrication route with DMF/DMSO. The acid route produced FACs thin films with larger apparent grains, stronger orientation and better light and device stability. One of the key differences during the formation is the crystallisation sequence of going through the hexagonal polytypes 2H, 4H and 6H before forming the final 3C perovskite phase.

Through the analysis of the acid route it became clear that dimethlyamine is a crucial component and might be the origin of the enhanced stability. To utilise also the advantages of the solvent quenching route with DMF/DMSO both methods were combined to a new

fabrication route called DMA route. For that the commonly used DMSO was replaced with a dimethylammonium halide which is added in excess to the perovskite precursor solution. For the quenching solvent we used TFT or a mixture of TFT with EA. Because of the large amount of excess organic cation, we also changed the heating treatment to three steps annealing at 100 °C in the N_2 glovebox, 170 °C on a hotplate in ambient air and finally 180 °C in a dry oven. The DMA route is a novel fabrication route which hasn't been reported so far. Previous publications used DMA but only by replacing other A-sites and still with DMSO.[148,155]

This new DMA route already has been adapted to other perovskite systems. Michael Farrar and I have been using the DMA route for the Pb-Sn perovskite.[152] James Drysdale and I also used the DMA route successfully for larger bandgaps of 2eV (with 60 to 70% Br^-). For both perovskite systems the DMA route has led to more stable and reproducible halide perovskites. I am hopeful that the field will adapt this method and use it.

In the next chapter I will investigate the performance and stability of the DMA route in films and devices. Interesting further research would be to understand the new peak arising in the XRD at around 10.9 ° with ≥40 mol% excess. Do new secondary phases form as result of the DMA route with ≥40 mol% excess? Might these phases also play a role for less excess DMA even though they are not visible in XRD?

This effect mainly originates from the decomposition of the DMF through the acid which lead also to the formation of Dimethylamine. By just adding the DMAX halide salt with I^-, Br^- or Cl^- one is able to reproduce this change in intermediate phases while not having to use an acid. The resulting and new fabrication method, the DMA route, results in films which also have larger apparent grains, enhanced crystallinity, a face-up orientation and allow for the removal of DMSO as solvent. DMACl worked the best of the three salts likely given that the excess

halide is easier to remove. Amounts of 20 to 30% mol of DMACl as excess worked the best in giving good FACs perovskite thin films. In the next chapter I will study the stability of these films and also fabricate devices.

14. Stability and performance of the DMA route

The work in this chapter has been adapted and reproduced in part from D. P. McMeekin*, P. Holzhey*, S. O. Fürer, S. P. Harvey, L. T. Schelhas, J. M. Ball, S. Mahesh, S. Seo, N. Hawkins, J. Lu, M. B. Johnston, J. J. Berry, U. Bach and H. J. Snaith, Intermediate-phase engineering via dimethylammonium cation additive for stable perovskite solar cells, Nature Materials, 22 (2023) 73–83.; DOI:10.1038/s41563-022-01399-8, *these authors contributed equally

14.1. Ambient thin film stability

In the previous chapter, I showed that the acid route produces significantly more stable perovskite solar cells. By understanding that dimethylamine, one of the degradation products of DMF, was a crucial component in the acid route and responsible for many properties, I was able to develop a new DMA route. In this chapter, I will study the stability of thin films and full devices. In **Figure 39**, the impact of the perovskite processing solvent composition on the stability of perovskite thin films in a humid environment is shown. A series of films prepared with various DMF to DMSO ratios were continually exposed to humid air with a relative humidity (RH) of approximately 85% at room temperature. These films are compared to the optimised, highly orientated and crystalline DMF/DMACl processed $FA_{0.83}Cs_{0.17}Pb(I_{0.8}Br_{0.2})_3$ perovskite films. I observe improved stability with reducing DMSO content in the solvent and significantly improved stability for the DMF/DMACl processed films.

DMSO is a common Lewis-base solvent known to complex and coordinate with lead halide (PbX_2). This ability allows intermediate precursor phases to occur, slowing the perovskite crystallisation process and increasing its processing window.[120,156–158] However, the combination of strong molecular interaction with perovskite/PbX_2 and a high boiling point

results in residual DMSO solvent remaining in the final perovskite film. With NMR spectroscopy powders from perovskite thin films dispersed in deuterated-acetonitrile (ACN-d_3) were analysed and residual DMF or DMSO was detected. **Figure 39B** shows residual solvent peaks for both DMF (7.93, 2.89 and 2.77 ppm)[159] and DMSO (2.51 ppm) for a thin film fabricated with a 50 μL drop-casted perovskite film, indicative that 1 hour 100 °C anneal is not sufficient to remove all solvents from a thick drop-casted film. Although a control DMF/DMSO solvent-quenched approach with ~ 500 nm thick films did show no residual DMF, a DMSO

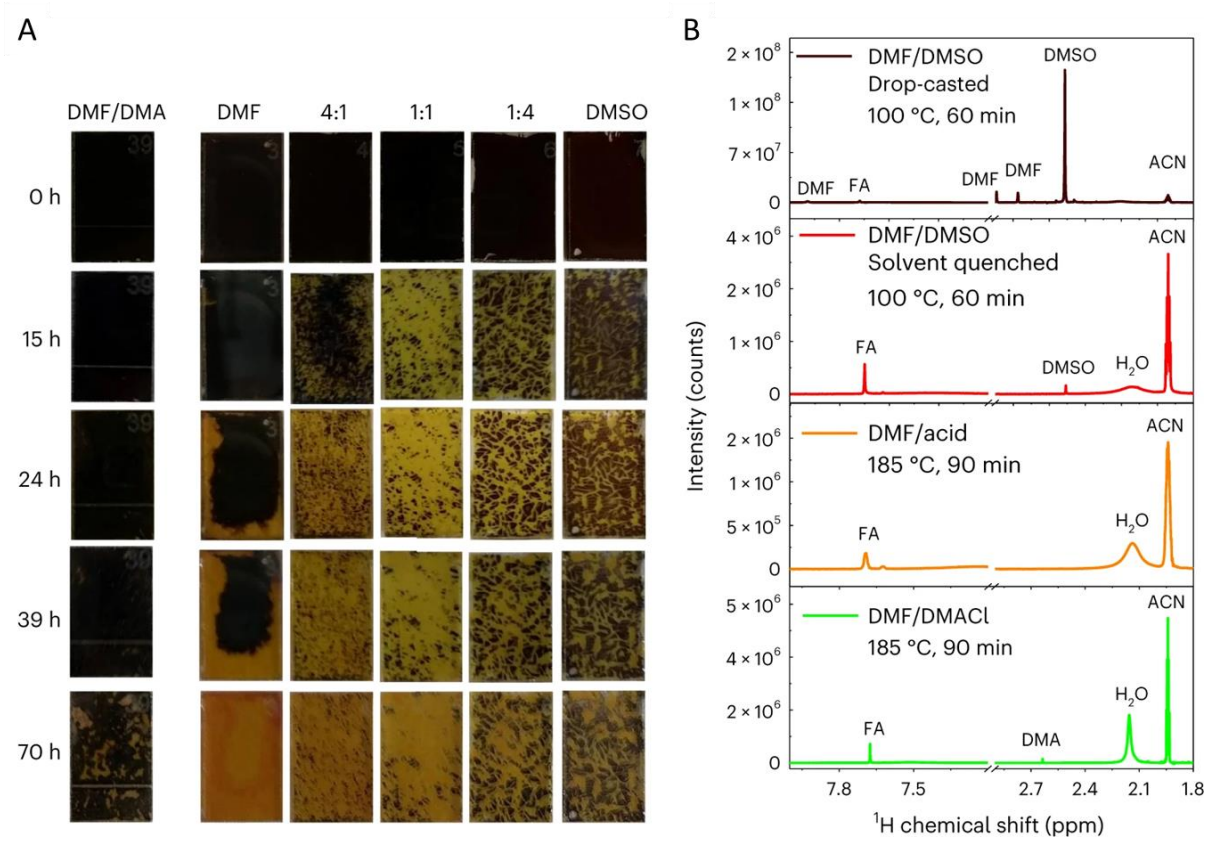

Figure 39 Impact of solvent and fabrication method on thin film humidity stability. (A) A series of photographs of thin films spin-coated fabricated with different ratios of DMF to DMSO, along with a comparison of the DMF/DMACl method. (B) ^{1}H Nuclear Magnetic Resonance (NMR) spectra of perovskite thin films dispersed in ACN-d_3. NMR spectra of a perovskite thin film prepared with a (Top) DMF/DMSO drop-casted method, (Middle) DMF/DMSO solvent-

quenched method, and (Middle) DMF/Acid method, (Bottom) DMF/DMACl method. Text and figure adapted from [105].

peak could still be detected after the standard 1 hour 100 °C annealing step. On the other hand, the DMF-only perovskite film prepared with an excess amount of DMACl is compatible with high-temperature annealing processing (> 170 °C), enabling the film to drive out most of the processing solvents from the films, while the 2H, 4H, 6H to 3C crystallization sequence takes place. While I cannot measure any DMF with solution NMR, I was able to measure residual solvent with thermal desorption gas chromatography mass spectrometry

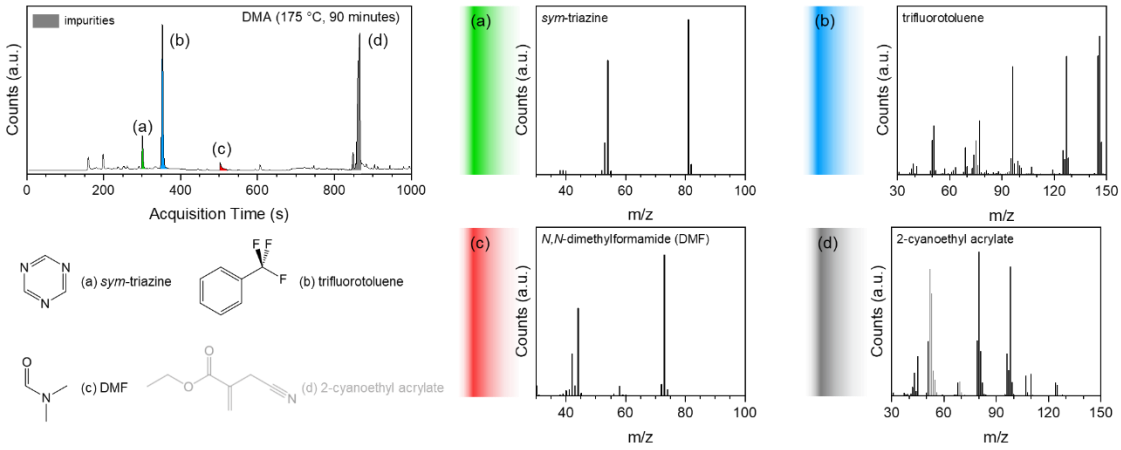

Figure 40 Thermal Desorption-Gas Chromatography-Mass Spectrometry. The chromatograms correspond to the release of different compounds during the thermal desorption of a $DMA_{0.3}FA_{0.83}Cs_{0.17}Pb(I_{0.85}Br_{0.15})_3Cl_{0.3}$ thin film annealed for 100 °C, 170 °C each for 10 min followed by 175 °C in an oven in air for 90 min. Mass spectra were used to identify the desorption products. All identified compounds were matched with the National Institute of Standards and Technology (NIST) 17 database and scored at least 85% for identification accuracy. Unlabeled signals represent compounds for which no satisfactory match was found in the NIST 17 database. 2-cyanoethyl acrylate is a common contaminant associated with plastics and plastic manufacturing processes. They were likely introduced in trace amounts

through contact between the sharp-edged glass substrates and the plastic containers used to transport samples before measurements.

(TD-GC-MS). TD-GC-MS has a significantly higher resolution limit than solution NMR, which might explain the difference. Further, for the solution NMR measurements, the thin films were scraped off the substrate with a razor blade, meaning that residual material at the bottom close to the TCO substrate might not be measured. The material at the bottom interface is the one which most likely contains residual solvents like DMSO.[160] Interestingly, I also found that the solvent used for quenching the perovskite fabrication (α,α,α-trifluorotoluene (TFT)) residual in the perovskite thin film. However, I nevertheless observed a significant difference in the stability. It seems that residual DMSO is more harmful than other residual solvents, which could be related to the stronger coordination of the solvent. Equally, the amount of residual solvent might be relevant. The performed TD-GC-MS measurements were not quantitative. In **Figure A 12**, I show the TD-GC-MS for a $DMA_{0.30}FA_{0.83}Cs_{0.17}Pb(I_{0.8}Br_{0.2})_3Cl_{0.3}$ thin film, which was only annealed for 100 °C and 170 °C for 10 mins each. Surprisingly, I observed the same residual solvents. The higher temperature (+ 10 °C) and longer annealing time (+1 hr in the oven in air) do not help remove residual solvents. Given that the boiling point of DMF is 153 °C and of TFT at 103 °C, one might expect that the annealing condition in both cases would be enough to remove both solvents. However, boiling point values are given for a solvent in itself, meaning that the boiling point is not necessarily an accurate guideline for when one would expect a solvent to leave, especially if a solvent like DMF is still coordinating.

In summary, I hypothesize that the entrapped DMSO causes the reduced humidity stability of the DMF/DMSO processed films. However, further investigation into residual solvents is needed to fully understand their impact on the stability of lead halide perovskite. Recent

research by Seok and co-workers,[85] suggests that residual solvents lower the energetic barrier to transition from the α- to the δ-phase for $FAPbI_3$, which correlates with these results here.

14.2. Thermal stability

Another advantage of the DMACl route is the high-temperature processing without significant degradation of the $FA_{0.83}Cs_{0.17}Pb(I_{0.8}Br_{0.2})_3$ film. There is no significant PbI_2 XRD peak appearing for temperatures below 200 °C for 7 minutes, as shown in **Figure 41**. PbI_2 is the degradation product of the lead halide perovskite.[161] Showing that the DMACl route gives rise to a thermally robust lead halide perovskite.

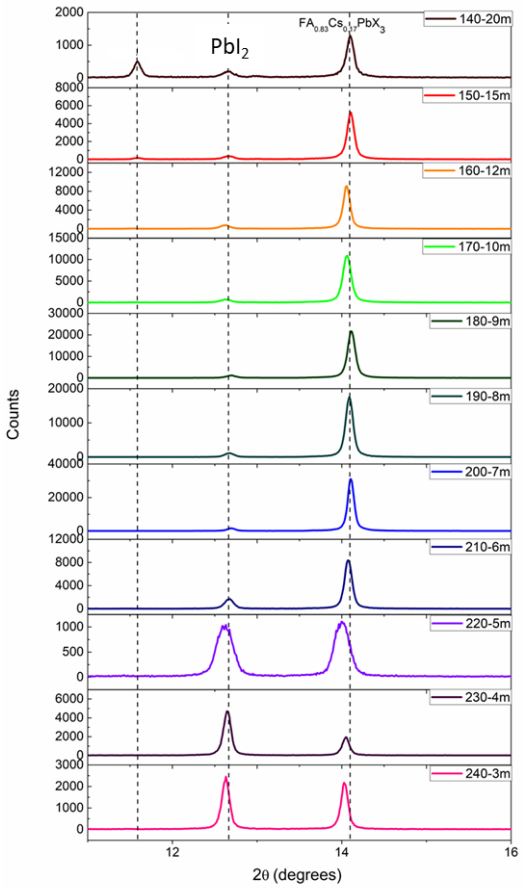

Figure 41 $DMA_{0.3}(FA_{0.83}Cs_{0.17})Pb(I_{0.8}Br_{0.2})_3Cl_{0.3}$ perovskite films after various annealing conditions varying time and temperature. Text and figure adapted from [105].

In **Figure 42**, I show the thermal degradation of various perovskite films prepared with different deposition techniques when heated at 150 °C in an N_2 atmosphere.[128,162] I present in **Figure 42B - D** the UV-Vis absorption spectra and the XRD pattern in **Figure 42E-G** zoomed in the 11-15° 2θ region of the corresponding $FA_{0.83}Cs_{0.17}Pb(I_{0.8}Br_{0.2})_3$ perovskite films. The DMF/DMSO perovskite film shows a significantly faster rate of "yellowing", which occurred within the first 24 hours of 150 °C heating, compared to both DMF/acid or DMF/DMACl processed films, which remained dark until 50 h. Neat $FAPbI_3$ or $CsPbI_3$ perovskite compositions are prone to revert from their black perovskite phase to a yellow non-corner-sharing phase when cooled down to room temperature or exposed to moisture.[76,163–166] However, excess heat can also create a similar colour change, where thermal decomposition occurs when the more-volatile organic matter is removed from the crystal lattice when exposed to heat, creating a $Pb(Br_xI_{1-x})_2$ film associated with an XRD peak located at $2\theta \sim 12.7°$. In **Figure 42B**, I observe that the DMF/DMSO processed perovskite films show a gradual decrease in the sharpness of the perovskite absorption onset and complete disappearance of absorption onset after only 24 hours of heating at 150 °C. On the other hand, the DMF/acid and/or DMF/DMACl fabrication routes showed roughly half the degradation rate, where the perovskite absorption onset fully disappeared after 40-50 h. Similarly, I observe the complete loss of the perovskite *(100)* peak, located at 2θ = ~14°, after 18 hours of heating for the DMF/DMSO route and 50 hours for both the DMF/acid and DMF/DMACl route films. Correspondingly, I observe a rise of the $Pb(Br_xI_{1-x})_2$ peak located around $2\theta \approx 12.7°$. In **Figure A 13**, I present the evolution of the normalised intensity ratio between lead halide and perovskite *(100)* XRD peak versus thermal aging time.

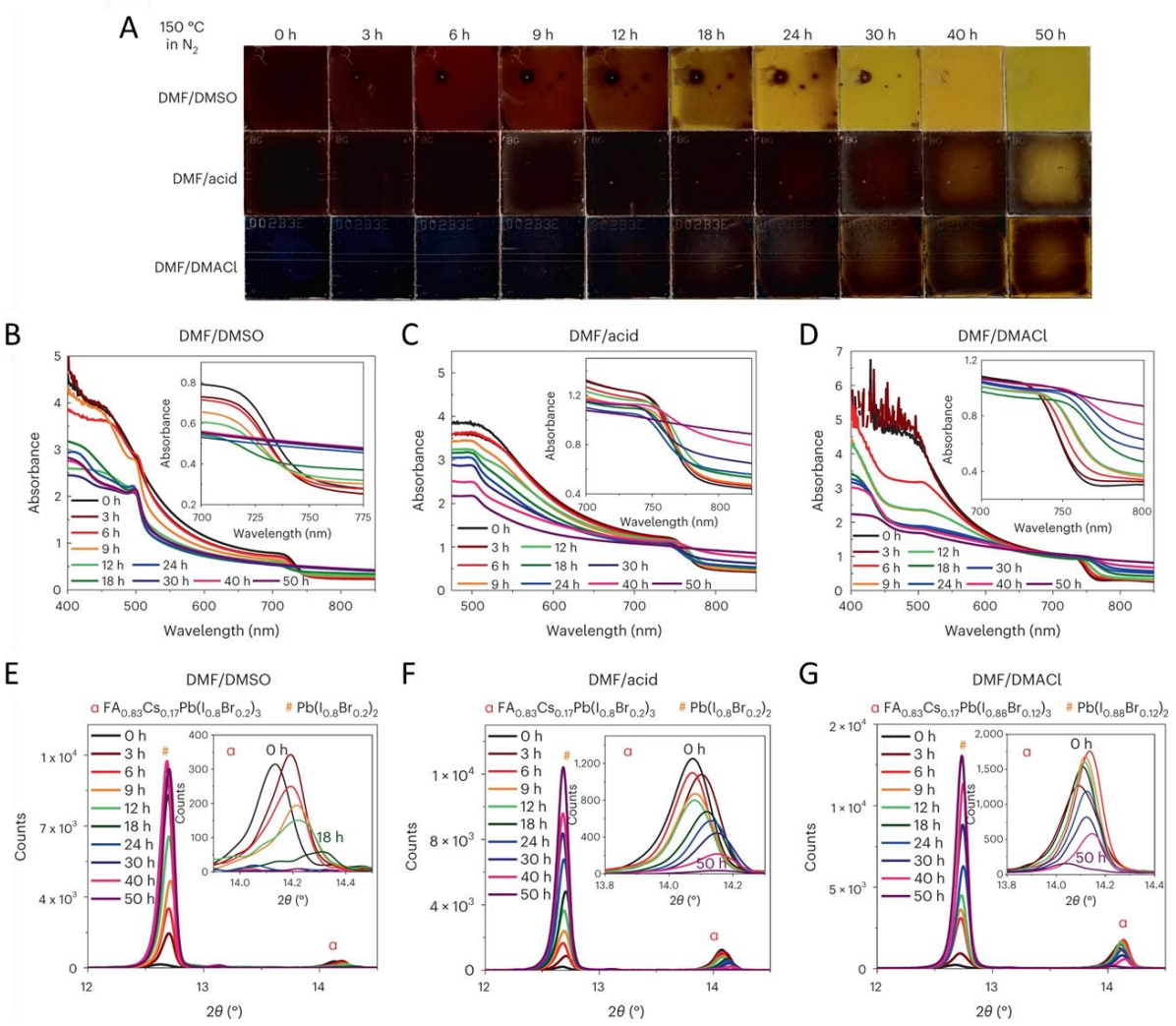

Figure 42 Thin film thermal stability. (**A**) Photographs of perovskite thin films when heated at 150 °C in an N_2 atmosphere. The top row shows $FA_{0.83}Cs_{0.17}Pb(I_{0.8}Br_{0.2})_3$ films fabricated with the standard DMF/DMSO fabrication method, the middle row shows $FA_{0.83}Cs_{0.17}Pb(I_{0.8}Br_{0.2})_3$ films fabricated with the DMF/acid fabrication method, and the bottom row shows and $DMA_xFA_{0.83}Cs_{0.17}Pb(I_{0.8}Br_{0.2})_3Cl_x$ films fabricated with the DMF/DMACl fabrication method. (**B, C, D**) UV-Vis absorbance spectra of films of corresponding films. (**E, F, G**) XRD pattern of corresponding films, where # and α stand for the reflections originated from the PbX_2 (X is a mixture of I, Br and Cl) and cubic perovskite phase, respectively. The insets in (**E, F, G**) show the enlarged XRD patterns, highlighting the evolution of the cubic perovskite phase during the thermal stressing course. Text and figure adapted from [105].

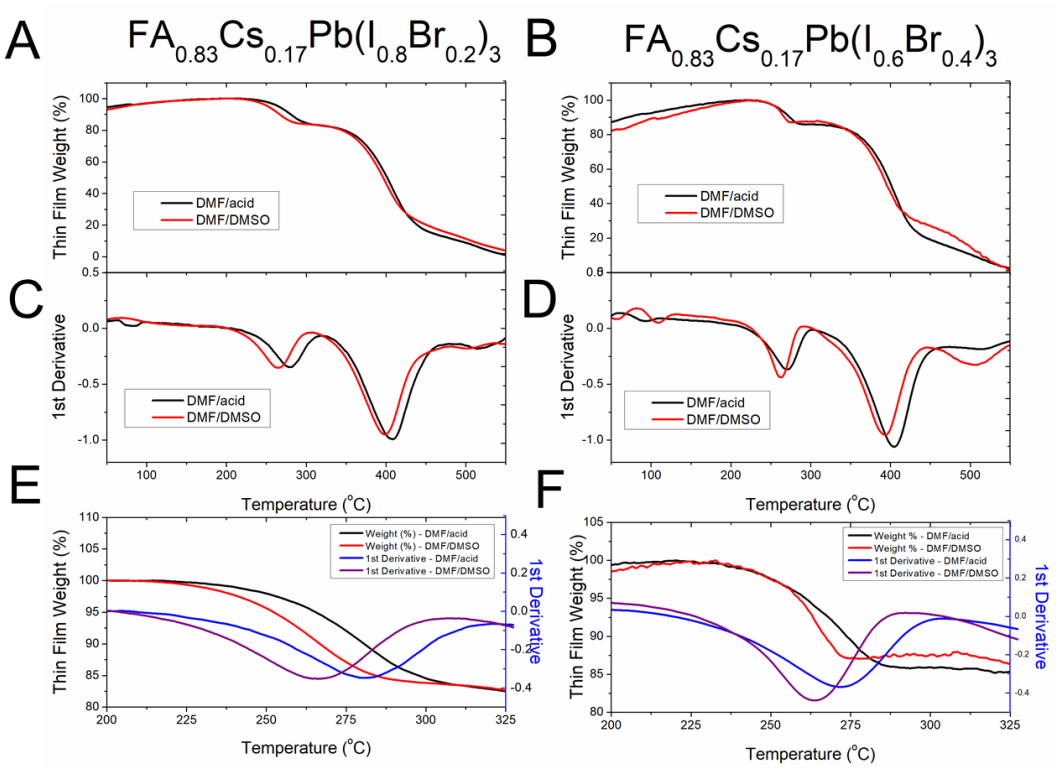

Figure 43 TGA of formamidinium-caesium lead mixed-halide perovskite $FA_{0.83}Cs_{0.17}Pb(Br_xI_{(1-x)})_3$ thin films prepared with different preparation techniques. (**A**) TGA heating curves. (**B**) Corresponding first derivatives for the perovskite thin films. (**C**) Magnification showing both heating curve and first derivatives of the temperature region where organic mass loss is prominent. Adapted from [105].

To further assess and quantify the thermal stability of these films, TGA was measured directly on the perovskite-coated glass substrates to account for the variation in morphology, topography, and crystal orientation of films produced via these different fabrication methods. In **Figure 43**, I show a 14 °C difference, from 265 to 279 °C, between the peaks of first derivative of DMF/DMSO and the DMF/acid films. This difference may appear quite small; however, as shown in **Figure A 14**, the TGA differential for the first derivatives between $MAPbI_3$ and $FAPbI_3$ is 50 °C. Hence, one can expect that a 14 °C represents a significant impact

in overall thermal stability, considering that the MA-based perovskite fully degrades within the first hour when heated at 150 °C (**Figure A 15**). Therefore, the TGA study shows that the highly textured DMF/acid method perovskite film exhibits increased thermal stability, beyond the susceptibility to degradation in oxygen and sunlight, in contrast to the isotropic DMF/DMSO perovskite films, which is in good agreement with the thermal stressing results of the thin films. Please note that TGA performed on the thin films shows a significant buoyancy effect[167,168] where the measured mass at an early time exceeds the original mass. This buoyancy phenomenon is caused by the density of the surrounding gas decreasing upon heating, which creates the appearance of the sample gaining weight. The most significant variation in air density occurs at lower-temperature, hence at the beginning of the experiment. Lastly, I conducted an in-situ thermal degradation XRD study of a series of films, with/without DMSO and/or DMACl, stressed at 130 °C in an air atmosphere with ~33% RH. (**Figure 44**). That shows that the removal of DMSO is helpful but less crucial than the usage of DMACl in case of heat and ambient moisture. Please note that the difference in stability between DMF/DMSO and only DMF films is different under different aging conditions e.g. only ambient moisture aging.

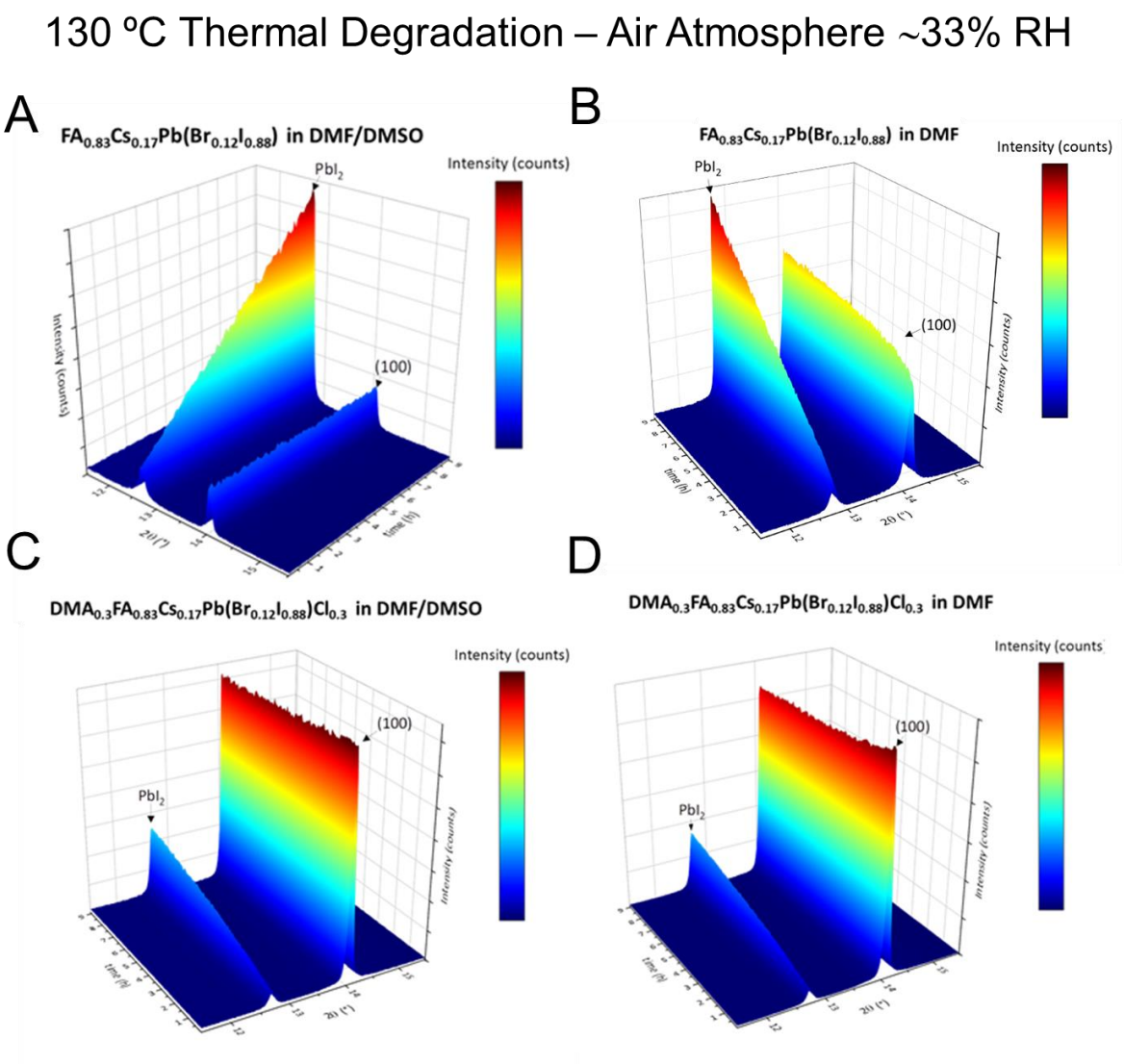

Figure 44 Evolution of XRD during the thermal degradation of perovskite films at 130 °C in an air atmosphere with ~ 33% relative humidity. The perovskite films were prepared using (**A**) $FA_{0.83}Cs_{0.17}Pb(Br_{0.12}I_{0.88})_3$ with a DMF/DMSO solvent mixture (**B**) $FA_{0.83}Cs_{0.17}Pb(Br_{0.12}I_{0.88})_3$ with a neat DMF (**C**) $DMA_{0.3}FA_{0.83}Cs_{0.17}Pb(Br_{0.12}I_{0.88})_3Cl_{0.3}$ with a DMF/DMSO solvent mixture (**D**) $DMA_{0.3}FA_{0.83}Cs_{0.17}Pb(Br_{0.12}I_{0.88})_3Cl_{0.3}$ with a neat DMF solvent. Text and figure adapted from [105].

14.3. Device performance and stability

To assess the performance of these different processed perovskite absorber layers in complete solar cells, negative-intrinsic-positive (n-i-p) and p-i-n devices were fabricated. The device structures were FTO/SnO_2/perovskite/Spiro-OMeTAD/Au for the n-i-p cells and FTO/PTAA/Al_2O_3 nanoparticles/perovskite/LiBr/C_{70}/Zr(Acac)/PEIE/Au for the p-i-n cells. The devices fabricated via the DMF/DMACl route, reaching 18.8% (18.2% steady-state) PCE in an n-i-p configuration and 16.7% (16.1% stabilized) in a p-i-n architecture, which is comparable to the DMF/DMSO processed devices, which achieved 18.3% PCE (18.3% stabilized) in an n-i-p configuration and 16.2 % (14.8% stabilized) in the p-i-n configuration (**Figure 45**).

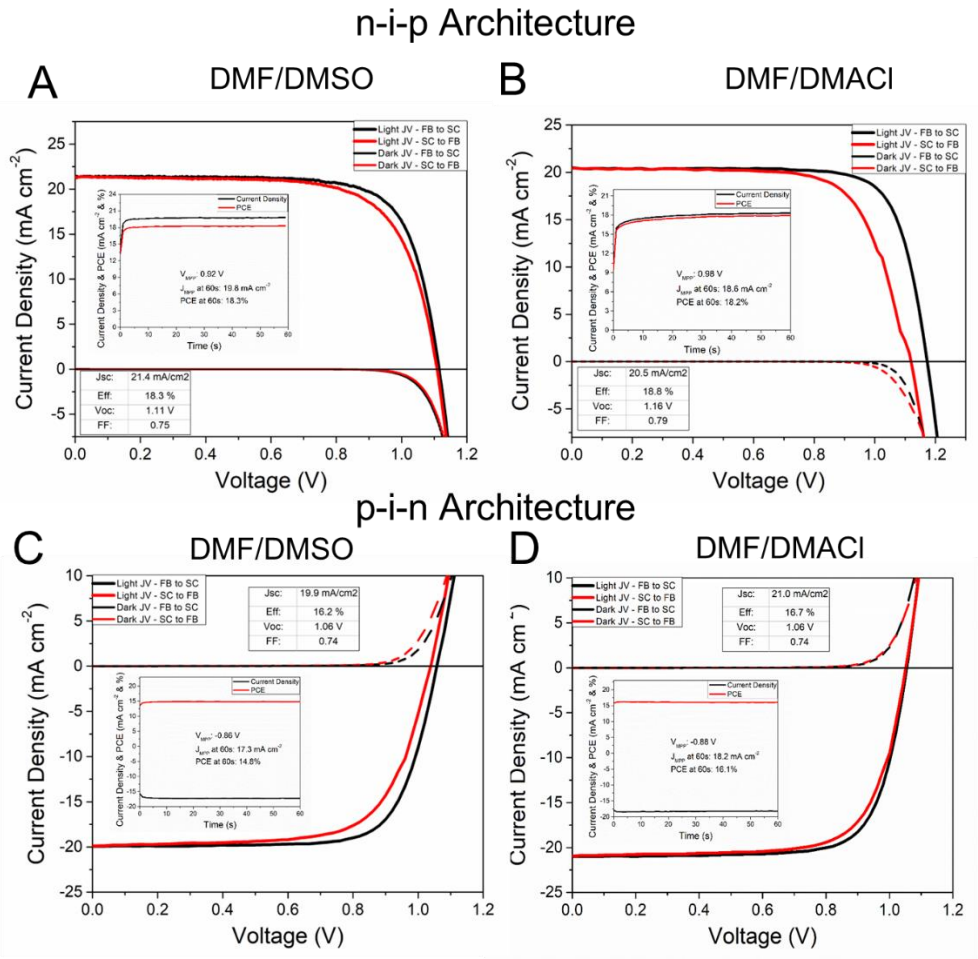

Figure 45 Performance comparison of perovskite solar cells prepared with DMF/DMSO or the DMF/DMACl fabrication method. (**A, B**) J-V characteristics for the champion n-i-p device of DMF/DMSO and DMF/DMACl designs. (Inset) corresponding stabilised PCE and current density measured at the maximum power point. (**C, D**) J-V characteristics for the champion p-i-n devices of DMF/DMSO and DMF/DMACl designs, measured at its peak efficiency. Text and figure adapted from [105]. An EQE for a DMF/DMACl device is shown in **Figure A 16**.

By further optimizing the compact SnO_2 electron transport layer processed via chemical bath deposition and introducing a KCl treatment to this layer, a champion device for the DMF/DMACl n-i-p device was achieved, reaching a PCE of 20.2% (J-V) and 19.9% (steady-state) (**Figure 46**). Please note, that the DMF/DMACl devices and the DMF/DMSO device have a

slightly different bandgap which might come from the used Cl^- or the residual DMA^+.

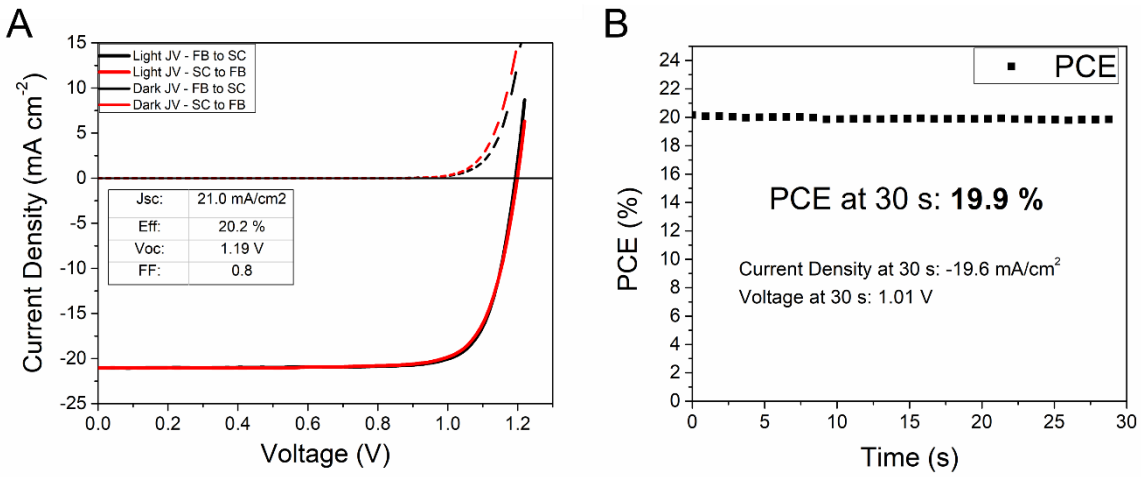

Figure 46 n-i-p performance of the champion perovskite solar cells devices prepared with DMF/DMACl fabrication method with KCl treatment post-treatment of the SnO_2 CB. (**A**) J V characteristics for the champion n-i-p device. (**B**) Corresponding stabilised PCE measured at the maximum power point. Text and figure adapted from [105].

Although the n-i-p, spiro-OMeTAD-based devices tend to outperform the p-i-n in terms of PCE, their operational stability suffers due to HTM instabilities linked to hygroscopic and volatile dopants.[169–176] In order to assess the long-term stability of these two distinct crystallization routes in complete PV devices, two populations of the p-i-n device design for the DMF/DMSO and DMF/DMACl processed devices were aged under simulated sunlight at 65 °C for over 2000 hours and a separate population at 85 °C for over 1000 hours (**Figure 47** and **Figure 48**). A glass/glass encapsulation technique was employed, sealed under an N_2 atmosphere with a UV-cured epoxy resin.

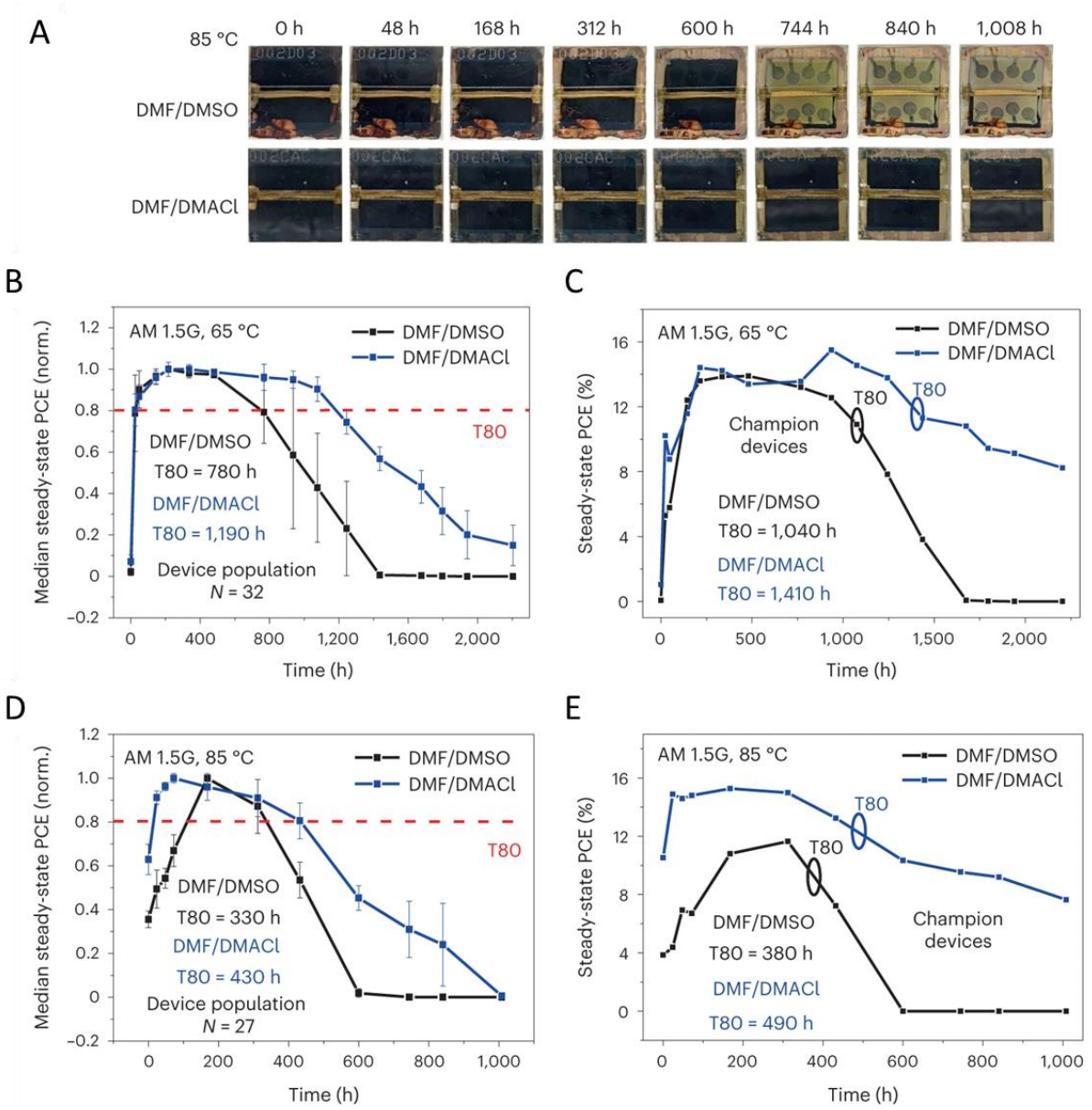

Figure 47 (**A**) Photographs of encapsulated DMF/DMSO (control) and DMF/DMACl p-i-n devices taken at various aging times under full spectrum simulated AM 1.5, 76 mW cm^{-2} average irradiance at VOC in air without a UV filter at 85 °C, using a Suntest XLS+ aging box which irradiates pulsed light. (**B, C**) Evolution of stabilized PCE, measured at its peak efficiency, between two statistical populations and champions devices of encapsulated devices of DMF/DMSO and DMF/DMACl designs aged under simulated sunlight at 65 °C. (**D, E**) Evolution of steady-state PCE, measured at its peak efficiency, between two statistical populations and champions devices of encapsulated devices of DMF/DMSO and DMF/DMACl designs aged

under simulated sunlight at 85 °C. The error bars were calculated using the median absolute deviation (MAD) as a measure of statistical dispersion. Text and figure adapted from [105].

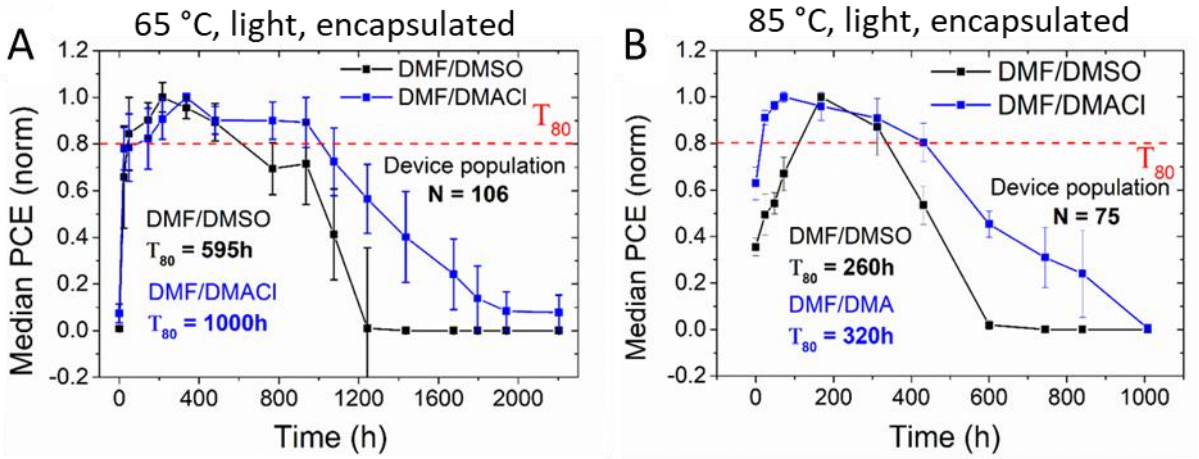

Figure 48 Evolution of the PCE (J-V-scan) between DMF/DMSO and DMF/DMACl fabrication methods under full spectrum simulated AM 1.5, 76 mW cm^{-2} average irradiance at V_{OC} in air without a UV filter at (A) 65 and (B) 85 °C, using a Suntest XLS+ aging box which irradiates pulsed light. All devices are encapsulated p-i-n devices comprised of an FTO/PTAA/Al_2O_3 NPs/perovskite/LiBr/C_{70}/Zr(Acac)/PEIE/Au structure. The error bars were calculated using the median absolute deviation (MAD) as a measure of statistical dispersion. Text and figure adapted from [105].

In contrast to the n-i-p cells, these p-i-n cells (FTO/PTAA/Al_2O_3 NPs/perovskite/LiBr/C_{70}/Zr(Acac)/PEIE/Au) do not exhibit a sharp early degradation, known as the burn-in period.[177] In contrast, a significant gain in PCE over the first 200 hours of light and temperature exposure is observed. This peak PCE to estimate the T_{80} lifetime of encapsulated cells, under full spectrum sunlight illumination, at 65 °C and open-circuit conditions, resulting in a T_{80} lifetime of 1040 (780) hours for the champion (median) control DMF/DMSO device and 1410 (1190) hours for the champion (median) DMF/DMACl

device.[177] Furthermore, for aging past 1600 hours, the control devices have all completely died, consistent with their bleached visual appearance. In contrast, the DMF/DMACl processed devices sustain, on average, 50% of their peak performance at 1600 hours, with the most stable cell sustaining >70% of its peak performance. A sizeable device population of 32 devices was aged for which the steady-state efficiency is shown in Figure 47. For 106 devices the J-V curves during the aging are shown in Figure 48. Such a large number of devices was aged to establish a statistical significance between these two designs. The same full illumination degradation study was also conducted at a higher temperature of 85 °C, where the DMF/DMSO devices obtained a champion (median) T_{80} of 380 (330) hours, while the DMF/DMACl devices obtained a champion (median) T_{80} of 490 (430) hours for a population size of N=27 (steady-state, **Figure 47D**) and N=72 (J-V, **Figure 48B**). All photovoltaic parameters are shown in **Figure A 17**. The improved stability of the perovskite absorber layer processed via the DMF/DMACl route has resulted in a significant increase in the overall PV device stability under elevated temperature light soaking. Incidentally, from these results, I can estimate a thermal degradation "acceleration factor" of roughly 1.7-fold per 10 °C increment for these devices. This can be useful for comparing the relative stability of different materials and devices stressed at different temperatures and is close to the 2-fold acceleration in degradation per 10 °C increment, which is expected for the degradation of silicon PV cells.[178] Please note that the devices were aged at open-circuit conditions, which is expected to accelerate the degradation compared to measuring it at the maximum power point.[38]

14.4. Further investigation into the device stability

In the next part, I try to understand more about the enhancement in device stability and how one could further enhance the stability. In a collaboration with Akash Dasgupta, we found a

strong macroscopic variation in the perovskite absorber and in each charge transport layer.[179] These spatial variations on the millimetre scale lead to substantial charge extraction heterogeneity and efficiency. These spatial variations may also impact the stability. Based on that, I employed a spatial IMPS mapping technique, which allows to measure the current extraction locally resolved during the aging. I age a FACs device with 40% Br and the corresponding DMACl device under continuous light (~0.75 suns) and ambient without encapsulation (~50% RH) (**Figure 49**).

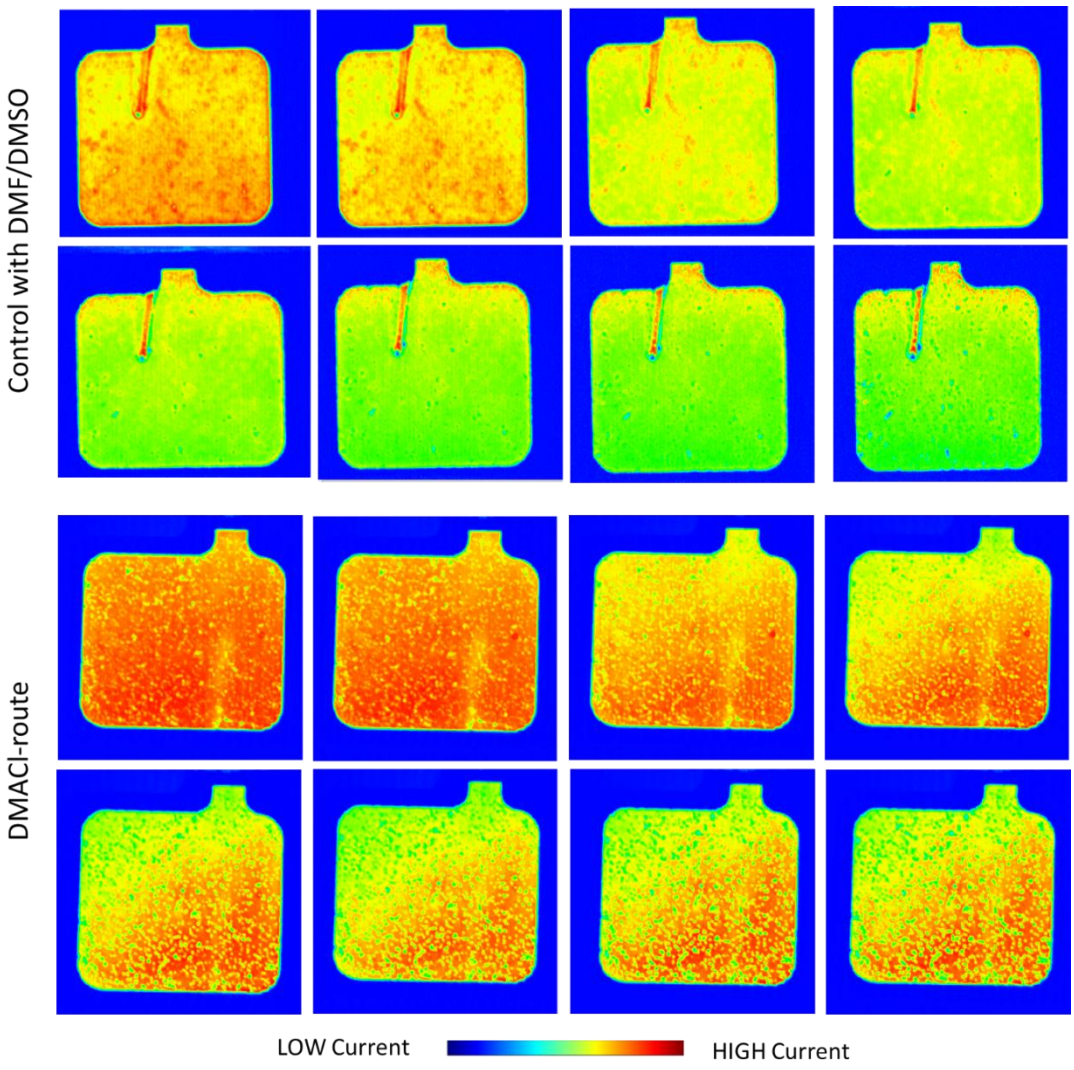

Figure 49 IMPS maps at 4kHz of $FA_{0.83}Cs_{0.17}Pb(I_{0.6}Br_{0.4})_3$ and $DMA_{0.3}FA_{0.83}Cs_{0.17}Pb(I_{0.6}Br_{0.4})_3Cl_{0.3}$ devices with ITO/Me-4PACz/AlO_x/perovskite/PCBM/BCP/Au under light (~0.75 suns) in air

without encapsulation (~50% RH) during the aging. The first and last images are each at the beginning and end of the aging. Please note that each image is scaled individually. The stability aging data is shown in Figure A 18.

Figure A 18 shows the J-V parameter evolution throughout the ageing. The control device has an estimated T80 (time until the device reaches 80% of its initial performance) of 50 h, and the DMACl device has around 300 h. The control device shows a relatively quick exponential degradation behaviour, which varies across the device area. To understand more about the evolution of the different areas, I picked four different areas in the control device and showed the evolution of each area in **Figure A 19**. Some areas, such as the meteor trail, initially increase in photocurrent while others, like the bottom quarter, degrade significantly faster. In general, one can separate the heterogeneity of the current extraction into two parts (named for clearance: **#**) local variations (small points, strips like the meteor, and other forms) and (**&**) gradual regional variations (bottom, top and neck). Local variations (**#**) could derive from small particles like dust or macroscopic variations of the perovskite layer (further discussion in the next chapter). A meteor, as visible in the control, often derives from small particles in the perovskite absorber layer and the subsequent coating of a layer on top of it. The solution is applied in the middle of the substrate and spreads radially outwards from the centre. The solution cannot pass the larger particle sticking out of the surface, and the liquid spreads around the particle, causing a thicker layer in front and around the particle in a streak. Please note that I chose this device to understand more about the correlation between initial heterogeneity and decay.

Different areas (**&**) are a result of the device geometry but also of the fabrication technique. Since I use spin-coating for most of the fabrication, the solution is often applied in the middle

of the spinning substrate and then gets thinner towards the edges of the TCO substrate. Interestingly, one can see that both local variations (**#**) and the different areas (**&**) impact the degradation of the device.

Figure 50 shows an overlay of the first and last IMPS map. Highlighted in green are regions of lower charge extraction from the initial first IMPS image, which overlap well with regions of lower charge extraction in the final IMPS image. This means regions with lower charge extraction are also more likely to degrade and degrade regions around them. I also show that in **Figure A 20** for the control device. Initial local variations (#) are visible in both devices and the areas that are the fastest degrading. Larger regional differences in areas (**&**) also cause differential degradation. In the DMACl device (see

Figure 50 C) the bottom right area degrades less than the top left area. The pixel is at the outer corner of the 3x3 cm substrate (see Methods section for IMPS mapping for a picture of the device layout), with the neck pointing away from the middle. So, the top left corner gets less solution than the bottom right, giving rise to likely slight differences in thickness or other factors like possible differences in crystallisation, which likely impact the degradation. For the control device, there is a difference in degradation between the bottom and the top of the area (&). The pixel is in the middle of the substrate, so it fits well with the observation for the DMACl that differences coming from the spin-coating process also impact the stability of the device.

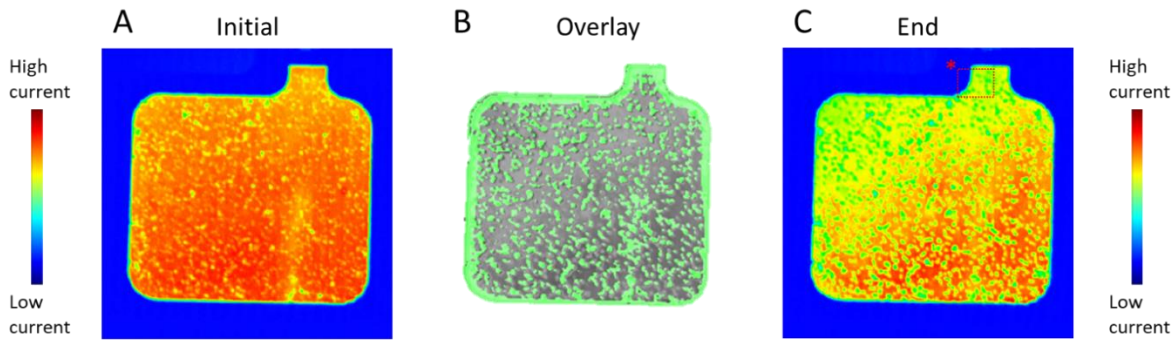

Figure 50 IMPS maps at 4kHz of the $DMA_{0.3}FA_{0.83}Cs_{0.17}Pb(I_{0.63}Br_{0.37})_3Cl_{0.3}$ at the beginning of the aging (t=0) (A) and overlay (B) of the initial (in green) and the final IMPS curves (in grey) which is also shown in (C) as comparison.

14.5. Discussion and summary

I further explored the acid and DMA route and compared their stability to the typically employed DMF/DMSO solvent quenched route. I found that both methods improve the stability and that especially the DMA route with DMACl is promising since it enhances the durability of the lead halide perovskite absorber under ambient, heat and light exposure. The enhancement stems partially from the removal of DMSO, which helps with the ambient stability. Likely because DMSO is hygroscopic. Consequently, encapsulated DMF/DMACl devices reached a T_{80} lifetime of 1410 hours at 65 °C and 490 hours at 85 °C, even when subjected to full spectrum sunlight and open-circuit conditions. In the following I will discuss the results and put them into context in the field of perovskite solar cells.

The stability of halide perovskites is currently their biggest bottleneck towards their commercialisation. Especially for the usage in multi-junctions like a perovskite/silicon tandem, a stable mixed halide perovskite is needed. The DMA route is crucial step towards that. However, it is clear that the DMA route is not perfect yet. The heterogeneity from the photo-current maps showed that there are different regions in the device (see **Figure 49**). These regions might be different materials. One material which degrades faster and one which degrades slower. Ideally the device would be homogenous and only consist of the stable material. The XRD peak at around 10.9 ° in the XRD from chapter 13 is likely a result of that. While I do not see this new peak for the concentrations which I use as standard (30% mol excess) it might still play a role. Future research could try to focus on optimizing the fabrication route further to suppress the formation of these unwanted secondary phases. Another open question is if the residual DMA^+ is part of the more or less stable region?

Besides the DMA^+ cation another important facet was the removal of the DMSO. It is one of the most commonly employed solvents for perovskite solar cells. It allows for an easy fabrication of efficient devices. However, as I showed it is residual in the perovskite films even after a high temperature annealing above the boiling point of DMSO. That posses a significant challenge for the generally used solvent quenched DMF/DMSO route. DMSO removal is needed for a stable device.

Another exciting aspect was that with the TD-GC-MS measurements, I found that all solvents employed were residual in the films — not only DMSO but also the antisolvent and DMF. Benjamin Gallant and I also studied this for his work[115] and found the same results. While removing the solvent for FAPbI3 was possible, it did not work for compositions with Cs^+ or Br^-. Also, removing the solvent for $FAPbI_3$ through heating (180 °C for an hour) led to the formation of a significant amount of PbI_2. I am unsure how detrimental the impact of residual solvents other than DMSO is. However, the significant improvement Benjamin and I measured for the new $FAPbI_3$ route, which has no residual solvents, indicates that removing solvents other than DMSO might be necessary to make stable perovskite solar cells.

15. A new dynamic passivation called HUBLA

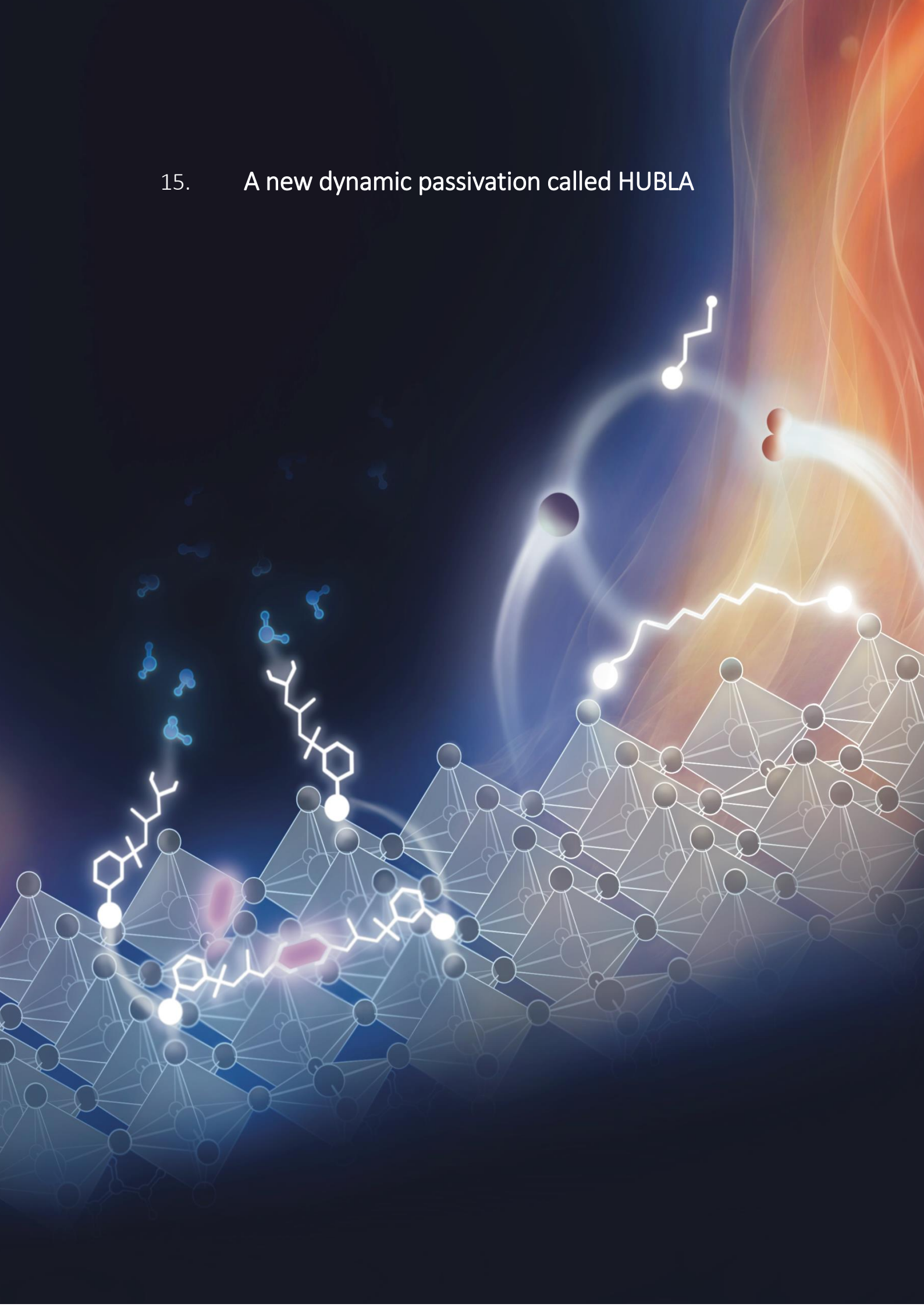

The work in this chapter has been adapted and reproduced in part from Wei-Ting Wang †, Philippe Holzhey †, Ning Zhou †, Qiang Zhang †, Suer Zhou, Elisabeth A. Duijnstee, Kevin J. Rietwyk, Jeng-Yu Lin, Yijie Mu, Yanfeng Zhang, Udo Bach, Chun-Guey Wu, Hin-Lap Yip, Henry J. Snaith, Shien-Ping Feng, Water- and heat-activated dynamic passivation for perovskite photovoltaics, Nature. †contributed equally. The artwork on page 141 was made by Veronika Grader.

15.1. Introduction

Various passivation strategies like ionic liquids[112], lead oxysalt[180] and 2D perovskite layers[30] have been developed to improve the performance and reliability of perovskite solar cells. These passivators heal defects during the manufacturing stage and might improve the resilience towards forming new defects. But so far, the perovskite lattice is still susceptible to the formation of new defects afterwards. Ideally, defects could also be healed during the operation. Similar to plants or living beings, which constantly heal and replace damaged cells and, through that, can live for decades under various weather conditions.

Inspired by that, a new passivation was developed, activated by environmental stress factors, to heal the perovskite dynamically during manufacturing and operation. For the first time a "living passivator" containing dynamic covalent bonds (DCBs) is reported, which can be triggered by water and heat to release additional Lewis bases, thereby healing newly generated traps. Adapted from the concept of living polymerization in polymer chemistry[181], the capability of a living passivation requires a protecting group or a ligand to quench the high reactivity of functional groups temporarily. In contact with water, the highly reactive electrophiles accept electrons and release new passivators to interact with the perovskite. Moreover, heating will accelerate the dynamic reaction of Electrophile-Nucleophile[118,182]

leading to a continuous release of passivators until HUBLA (hindered urea/thiocarbamate bond Lewis acid-base) is depleted.

15.2. Design and dynamic reactions of HUBLA

Compared with most DCBs that rely on catalysts[183–188], a hindered urea bond (HUB) as a partial structure of the living passivator is chosen. In particular, the dynamic behaviour of HUB originates from the non-coplanarity of the amide bond (-N(R)C(O)-, **Figure A 21**), whose conjugation is disturbed by the introduction of the bulky *tert*-butyl structure (-$C(CH_3)_3$)[118,189] to enable intrinsic dissociation-association reaction at room temperature. To demonstrate the dynamic behaviour of HUB (-$N(C(CH_3)_3)C(O)$-), a HUB-based poly(urethane-urea) elastomer is prepared and cut into sixteen small cubes. The elastomer cubes can be reconnected again to build a Rubik's Cube-like structure, as seen in **Figure 51**; the bond between the cubes is formed through the dissociation-association reaction of HUBs (the equilibrium reaction between HUB, isocyanate, and hindered amine) at the interface.[118,184] Based on the mechanism that the conjugation of the amide bond (-N(R)C(O)-) could be disturbed by the introduction of steric hindrance, sulfur was also inserted into the proposed chemical structure to form the thiocarbamate bond (-SC(O)NH-) with the dynamic behaviour at elevated temperature.[190] Both HUB and thiocarbamate bond-based dynamic reactions are necessary to satisfy forward and reverse reaction rates (k_1 and k_{-1}) sufficiently fast. Note that the equilibrium favours the formation of the product (k_1/k_{-1} is large). Otherwise, the HUB and thiocarbamate bond would not exhibit dynamic behaviour, or these bonds could not be formed. The association-dissociation reaction of the two bonds can be expressed as follows.

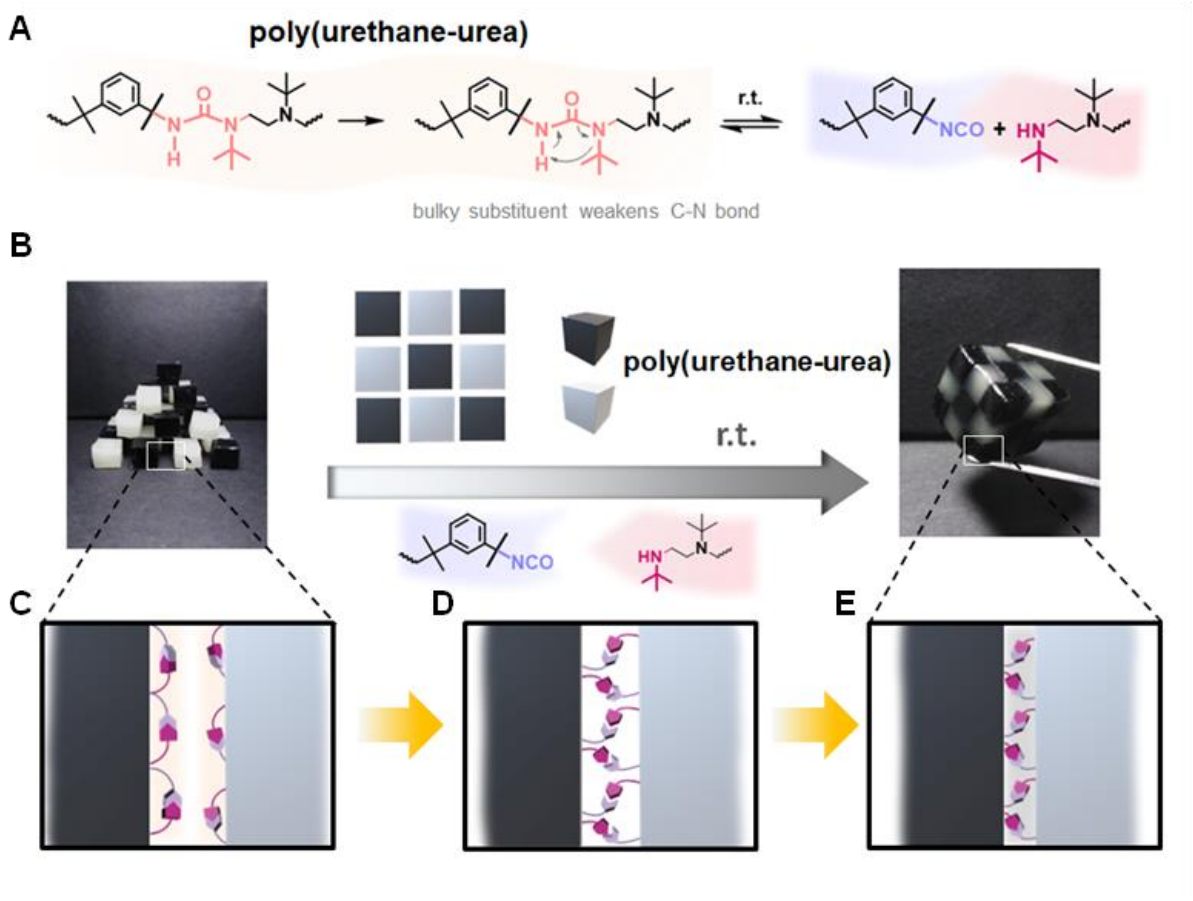

Figure 51 Dynamic reaction of HUB (hindered urea bond) and self-healing of Rubik's cube. (A) Chemical structures of HUB and its dynamic reaction. To demonstrate the dynamic bonds of the HUB a HUB-based poly(urethane-urea) elastomer is produced and cut into smaller cubes. The cubes are shown in (B). Upon holding the small cubes together, the Rubik's cube like structure forms simply by bringing them together. (C)-(E) A schematic illustration of the HUB-based cross-linked poly(urethane-urea) self-healing mechanism between the different cubes.

Dynamic reaction of HUB at room temperature[118]:

$$(Equation\ 1)\ \mathrm{R_1NCO} + ((\mathrm{CH_3})_3\mathrm{C})\mathrm{NHR_2} \underset{k_{-1}}{\overset{k_1}{\rightleftarrows}} \mathrm{R_1N(H)C(O)N(C(CH_3)_3)R_2}$$

Dynamic reaction of thiocarbamate bond at elevated temperature[190]:

$$(Equation\ 2)\ \mathrm{R_1NCO} + \mathrm{HSR_2} \underset{k_{-1}}{\overset{k_1}{\rightleftarrows}} \mathrm{R_1H(N)C(O)SR_2}$$

Further information is shown in **Figure 52A,** and a corresponding schematic is shown in **Figure 53**. HUBLA was further characterised by NMR, attenuated total reflection fourier transform infrared spectroscopy (ATR-IR) and electrospray ionization mass spectrometry (ESI-MS) (**Figure A 22**).

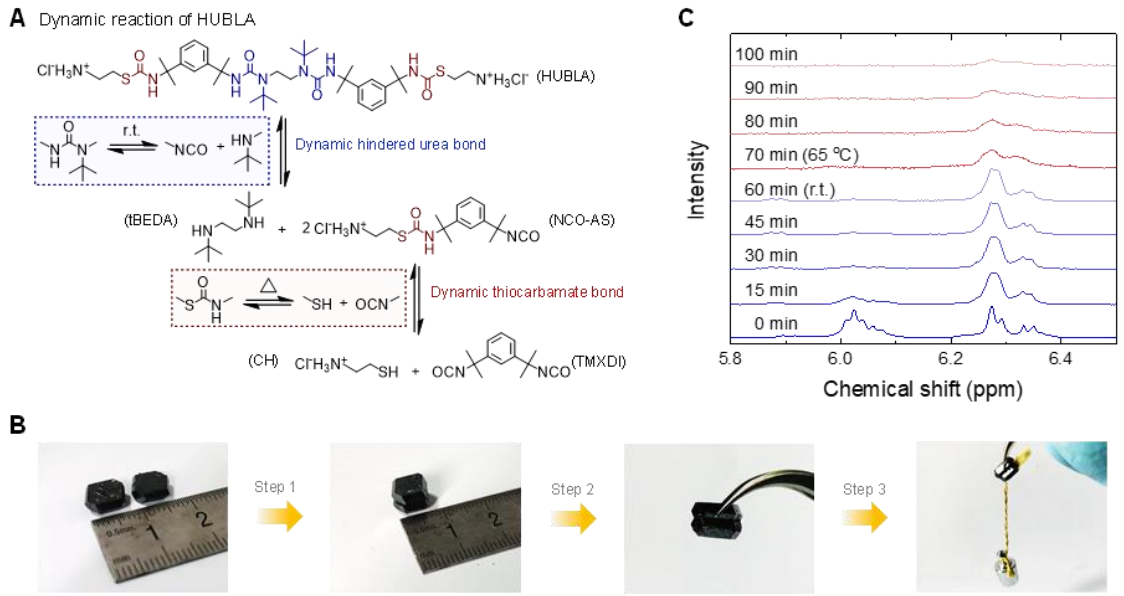

Figure 52 Dynamic reaction, hydrolysis, and redox shuttle of HUBLA. (A) Dynamic reactions of HUBLA. (B) Photographs showing the connection of two $FAPbI_3$ crystals using HUBLA. HUBLA in IPA (10 mg/mL) was drop coated on one side of the $FAPbI_3$ crystal, and another $FAPbI_3$ crystal was placed on top of it for 24 hours at room temperature. The two crystals exhibited a strong adhesion and can lift 5 grams of weight. (C) ^{1}H NMR characterizations of HUBLA in DMSO-d_6 and D_2O during 100 min. 15% D_2O was added immediately after ^{1}H NMR test; the temperature was then raised to 65 ℃ after 60 min.

The dynamic behaviour of HUBLA is also shown in **Figure 52B** by sticking two $FAPbI_3$ crystals together with HUBLA. HUBLA is coated on one side of a $FAPbI_3$ crystal, and another $FAPbI_3$ crystal was placed on top of it. After 24 hours at room temperature, the two crystals exhibited a strong adhesion and could lift 5 grams of weight (the mounting of the weight is shown in **Figure A 23**). Based on that I believe that HUBLA can interact with the perovskite surface due to the association-dissociation reaction and form a cross-linked structure at the interface between the two crystals. A detailed schematic is shown in **Figure A 24**. Such strong ionic interactions of HUBLA could fill and protect, for example, the grain boundaries of the perovskite layer against water penetration.

As I show in equation (1) and **Figure 52A**, the dynamic association-dissociation reaction mechanism HUBLA can reversibly dissociate into NCO-terminated ammonium salt (NCO-AS) and *tert*-butylethylenediamine (tBEDA) at room temperature.[118] In addition, NCO-AS can further undergo association-dissociation reaction to generate cysteamine hydrochloride (CH) and 1,3-bis(2-isocyanato-2-propyl)benzene (TMXDI) at elevated temperatures (equation 2).[190] In contact with water molecules, NCO-AS and TMXDI decompose into NH_2-terminated ammonium salt (NH-AS) and TMXDI hydrolysis, respectively, which accelerates the dissociations of HUB and thiocarbamate bond in HUBLA.[189] To show the processes, ^{1}H NMR is conducted to verify that HUB and the thiocarbamate bond of HUBLA dissociate. 15% (v%) deuterium oxide (D_2O) is added into the HUBLA/DMSO-d_6 solution (20 mg/mL) and the changes of HUBLA are measured at room temperature and 65 °C (**Figure 52C**). D_2O can react with the water-sensitive NCO groups and decompose into amines,[189] preventing the association reaction. Therefore, I expect the peak areas of the HUB and thiocarbamate bond to decrease. At room temperature, the peak area of HUB (in blue), around 6.02 ppm, drops rapidly to 27.5% after 15 min and to 5.5% within one hour, which I attribute to the hydrolysis

of HUB. Subsequently, heating the solution to 65 °C, the peak area of the thiocarbamate bond (in red) around 6.28 ppm drops to 50.0% within 10 min and 19.2% within 40 min, indicating the hydrolysis of the thiocarbamate bond. That shows that the highly reactive isocyanate group (-NCO) can be temporarily quenched by incorporating HUB and thiocarbamate bonds. In **Figure 53**, I show a schematic of how possible passivation pathways for HUBLA under different stress factors could work out. I show all relevant chemical structures and detailed reactions for HUBLA in **Figure A 25**. In the next part, I will try to verify the dynamic passivation behaviour of HUBLA. First, perovskite thin films during aging are characterised with XPS to

show the chemical interaction of HUBLA over time. Secondly, I measure PL maps of HUBLA and control films during aging to show the dynamic passivation of defects.

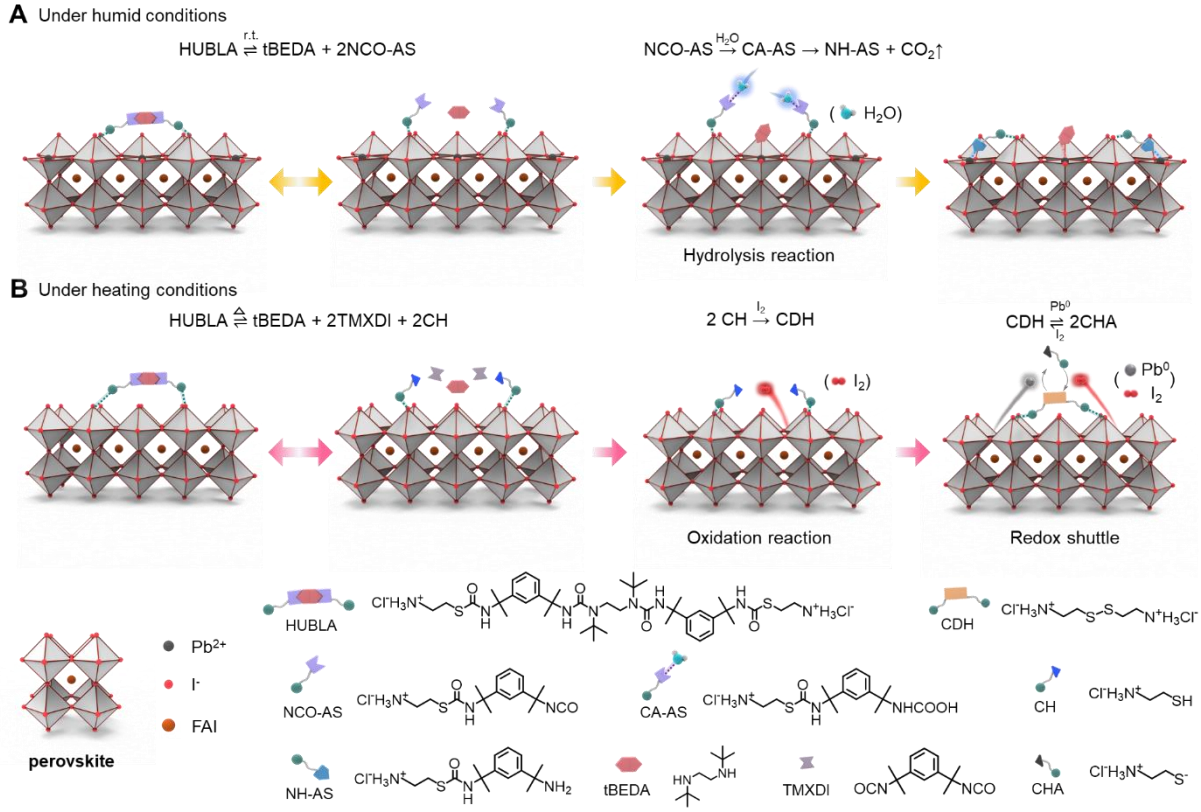

Figure 53 (**A**) Dynamic and hydrolysis reactions of HUBLA coated on perovskite film under humid conditions. (**B**) Dynamic and redox reactions of HUBLA coated on perovskite film under heating conditions.

15.3. Dynamic passivation behaviour of HUBLA

First, I study the dynamic passivation ability of HUBLA under relative humidity exposure. HUBLA can undergo water-activated passivation under moisture exposure. HUBLA reversibly dissociate into tBEDA and NCO-AS at room temperature; the generated NCO-AS can react with the water molecules and then hydrolyze to NH-AS (**Figure 53** and **Figure A 25**).[189] Both -NH- (secondary amine group from tBEDA) and -NH_2 (primary amine group from NH-AS) have the capability to heal the ionic vacancies of the perovskite film.[191] By binding to the

undercoordinated species and with that effectively filling the ionic vacancy. The Pb 4*f* XPS spectrum of $FAPbI_3$/HUBLA films is measured at 25 ℃ and 65% RH. As shown in **Figure 54A**, the Pb^{2+} peaks shift toward higher binding energy during aging, suggesting that more negative charges interact with the Pb^{2+} ions.[192–194] Considering that HUBLA reacts with water to generate tBEDA and NH-AS, the lone pair of electrons in the primary amine (NH-AS) and secondary amine (tBEDA) provide more negative charge to the Pb^{2+}. To further show the primary amines and secondary amines passivation capability, TMXDI hydrolysate and tBEDA are coated onto the $FAPbI_3$ films and their Pb 4*f* XPS spectra (**Figure A 27**) are tested. The results show that the peaks of $FAPbI_3$/TMXDI hydrolysate and $FAPbI_3$/tBEDA shifted toward higher binding energy, indicating that primary amine and secondary amine can interact with Pb^{2+}.

In addition to the water-activated dynamic behaviour, I investigated the changes in the surface chemistry of HUBLA coated on perovskite films during thermal aging. Lead iodide-based perovskites generally degrade into PbI_2 and generate I_2 and Pb^0 under thermal stress or light soaking.[112,195,196] The thiol group (-SH) in CH, dissociated from the thiocarbamate bond at elevated temperature, can be oxidized by I_2 and produce disulfide-containing (-S-S-) cystamine dihydrochloride (CDH). The disulfide bond can be further reduced by Pb^0, producing sulfur anion ($-S^-$)-containing cysteamine hydrochloride anion (CHA). Here, CDH and CHA can act as redox shuttles to selectively and cyclically oxidize Pb^0 and reduce I_2 (see detailed reactions in **Figure A 25**). To verify the hypothesis, $FAPbI_3$/HUBLA films are aged at 85 ℃ in N_2 and the S

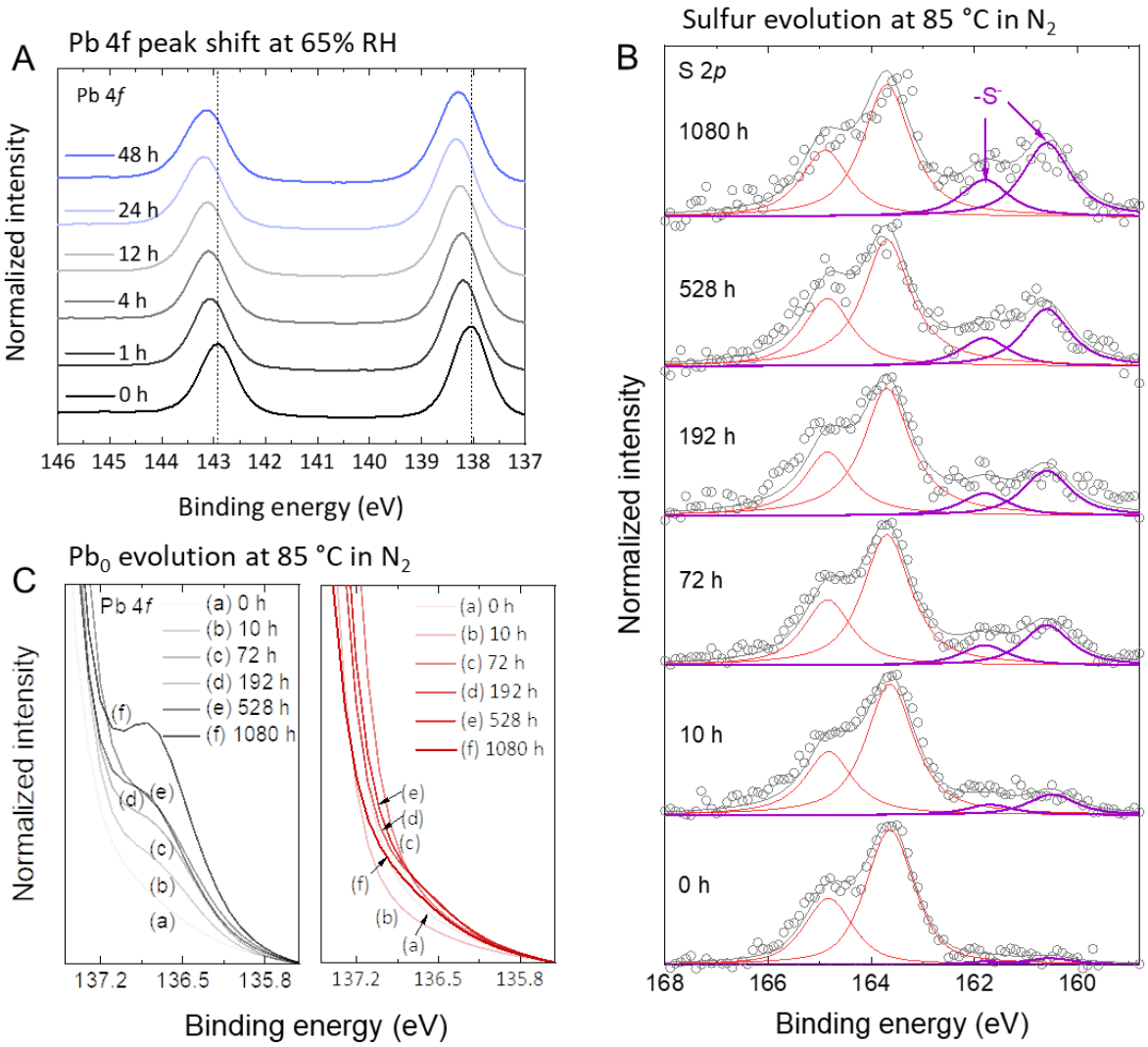

Figure 54 Chemical proof of the dynamic passivation. XPS measurements for (**A**) Pb 4f, (**B**) S 2p and (C) enlarged Pb 4f regions. For the hydrolysis aging test in (**A**), $FAPbI_3$/HUBLA films were aged in an environmental chamber (25 °C, 65% RH). For the thermal aging test in (**B**) and (**C**), $FAPbI_3$ films with and without HUBLA were aged in N_2 at 85 °C. For (**B**) the grey circles and curves represent the raw data and peak sum, respectively. The red and purple curves represent S 2p spectra of the thiocarbamate bond (-SC(O)NH-; also include the -S-S-) and -S-, respectively. The left and right figures in (**C**) are Pb 4f XPS of $FAPbI_3$ (grey curves) and $FAPbI_3$/HUBLA (red curves) films, respectively. The full XPS spectra for (**C**) are shown in **Figure A 26**.

2*p* core level spectra are measured. To identify the binding energy of each component coated on perovskite film, the S 2*p* XPS spectra of pristine HUBLA, $FAPbI_3$/CH, and $FAPbI_3$/CDH films is measured, as shown in **Figure A 28**. In all S 2*p* regions, each component exhibits a characteristic doublet with peaks separated about 1.2 eV apart and with an amplitude ratio of 2:1.[197] In particular, pristine HUBLA has the S 2*p* components at ~164.9 and ~163.7 eV (**Figure A 28A**), corresponding to -SC(O)NH-. CH has the S 2*p* components at ~164.7 and ~163.5 eV (**Figure A 28B**), corresponding to -SH. CDH has two S 2*p* components (**Figure A 28C**); one is at ~164.9 and ~163.7 eV, assigned to -S-S-, and the other one is at ~161.8 and 160.6 eV, which is $-S^-$.[198]

Having identified the relevant peaks for the S 2p XPS spectrum one can now analyse the S 2*p* spectra of $FAPbI_3$/HUBLA aged under 85 ℃ in N_2. Note that the S 2*p* component of -SH maintained a low intensity, and thus, was not fitted; in addition, the S 2*p* components of -S-S- are close to that of -SC(O)NH- in HUBLA and thus is assigned to the thiocarbamate bond. The S 2*p* region of $FAPbI_3$/HUBLA films (**Figure 54B**) shows two components, assigned to the thiocarbamate bond (-SC(O)NH-) in HUBLA (red curve) and the sulfur anion ($-S^-$) in CHA (purple curve). The S 2*p* components of CHA (purple peaks) increased with thermal aging from 0 to 1080 hours, indicating the continuous dissociation of HUBLA and the reduction reaction of CDH. To understand the capability of the redox shuttles (CDH and CHA) for perovskite passivation under heating conditions, the Pb 4*f* XPS spectra of $FAPbI_3$ and $FAPbI_3$/HUBLA films aged at 85 ℃ in N_2 was measured, as shown in **Figure A 26**. The Pb^{2+} shows two peaks at ~138.3 and ~143.2 eV, and Pb^0 shows two peaks at ~136.7 and ~141.6 eV. As shown in **Figure 54C**, the ratio of $Pb^0/(Pb^0+Pb^{2+})$ in the $FAPbI_3$ film increases from 0.2% to 3.7% after heating for 1080 hours, while the ratio in the $FAPbI_3$/HUBLA film remained relatively low (from <0.001% to 0.3%) under the same conditions, which can be attributed to the redox reactions

of -SH (from CH), -S-S- (from CDH) and $-S^-$ (form CHA). In addition, a solution experiment was performed to observe the redox reaction directly (**Figure 55**). HUBLA was added into 85 ℃ iodine solution, and the solution turned from dark brown to colourless due to the oxidation of CH by I_2 and the production of CDH. Lead pellets were then added into the solutions; the lead pellets were slowly dissolved only in the solution containing HUBLA, suggesting that CDH can oxidize Pb^0 and generate Pb^{2+}.

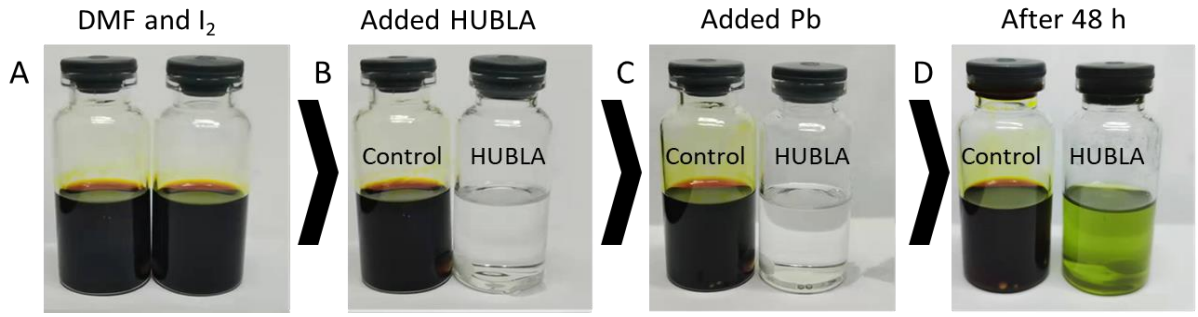

Figure 55 Redox reaction of HUBLA. (A) Two sample bottles were filled with 10 mL DMF and 0.25 g I_2, and stirred at 85 ℃. (B) 1 g HUBLA was added in the right bottle and the solution becomes colourless. (C) Two lead pellets were added into both bottles. (D) The lead pellets in the right bottle were completely dissolved in the solution after stirring for 48 hours, and the lead pellets in the left bottle remained the same.

To evaluate the dynamic passivation of HUBLA, the photoluminescence spectroscopy (PL) maps of the perovskite films were measured during aging. I fabricated $FAPbI_3$ thin films and coated some of them with HUBLA. I then exposed a small area of the film to intense light (96.5 suns equivalent) for two hours. After aging, I left the samples for 10 mins in the dark and measured a PL map with half of the area aged and the other half not exposed to light during the aging, which I refer to as pristine. This allows me to quantify the aging-induced changes in PL. I observed a slight improvement in PL intensity in the aged control area compared to the

pristine area. This photo brightening is a relatively well-described phenomenon in lead halide perovskites and has been previously studied.[199] Compared to the control, all HUBLA films show substantially stronger improvements in PL, around one order of magnitude in counts/s. I show an example of two films (HUBLA and control) in **Figure 56A** and **Figure 56B** with their corresponding histograms provided in **Figure 56C** and **D** while a statistical analysis of all the samples is shown in **Figure 56E**. Given that PL is a direct measure of the amount of radiative

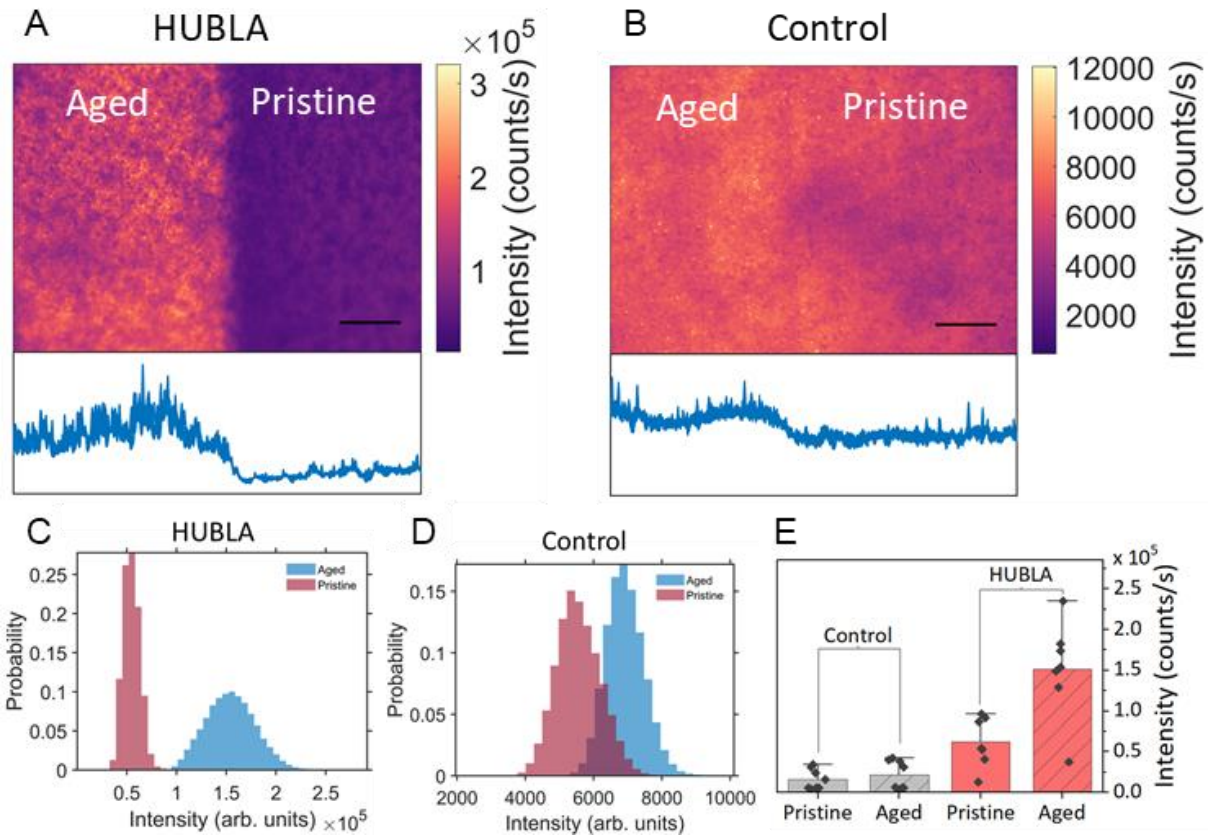

Figure 56 PL map of $FAPbI_3$ films coated with HUBLA (A) and without HUBLA (B). Scale bar is 50 µm. I exposed one site of the $FAPbI_3$ perovskite film to 96.5 suns for 120 mins at ~30% RH (aged) and covered the other side of the film (pristine). The PL map is directly measured after the aging. The inset below shows a horizontal cross section of the middle of the PL map. (C and D) Histograms of the PL intensity for HUBLA and the control maps, respectively. (E) Statistical difference in PL for aged and pristine samples. Each point is an individually measured PL map, as shown in (A) and (B), aged in the same way.

recombination, the ability of HUBLA to increase PL over the control film during aging indicates that HUBLA is dynamically passivating defects or traps in the photo absorber and healing the perovskite film. Please note that I didn't find any changes on the surface with top-view SEM images (**Figure 57A** and **B**) and no detectable changes in the crystallinity (**Figure 57C**) after spin-coating HUBLA onto the perovskite film.

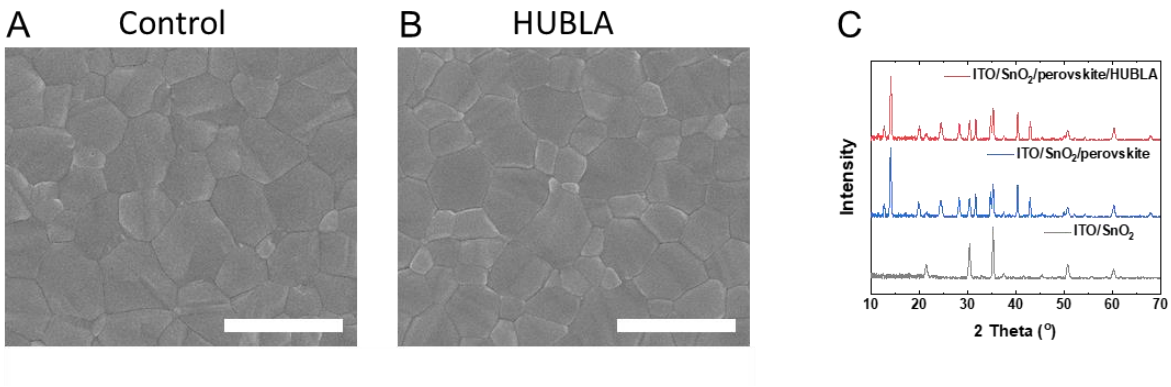

Figure 57 Top-view SEM images of perovskite films. (A) Pristine perovskite. (B) Perovskite with HUBLA. The scale bar is 1 µm. (C) XRD patterns of SnO_2, perovskite and perovskite/HUBLA films.

15.4. Stability of HUBLA-coated perovskite

The operational stability in PSCs is strongly interrelated with the defect density of the halide perovskite. Ion migration, phase segregation, and traps, which cause non-radiative recombination, lead to irreversible device degradation.[200] Accordingly, I first investigated the trap density of HUBLA-coated perovskite and its stability. PL and time-resolved photoluminescence spectroscopy (TRPL) were measured for the pristine and HUBLA-coated $FAPbI_3$ crystals. In **Figure A 29A**, the PL and TRPL spectra show that the HUBLA-coated crystal has a higher PL intensity and a longer lifetime.

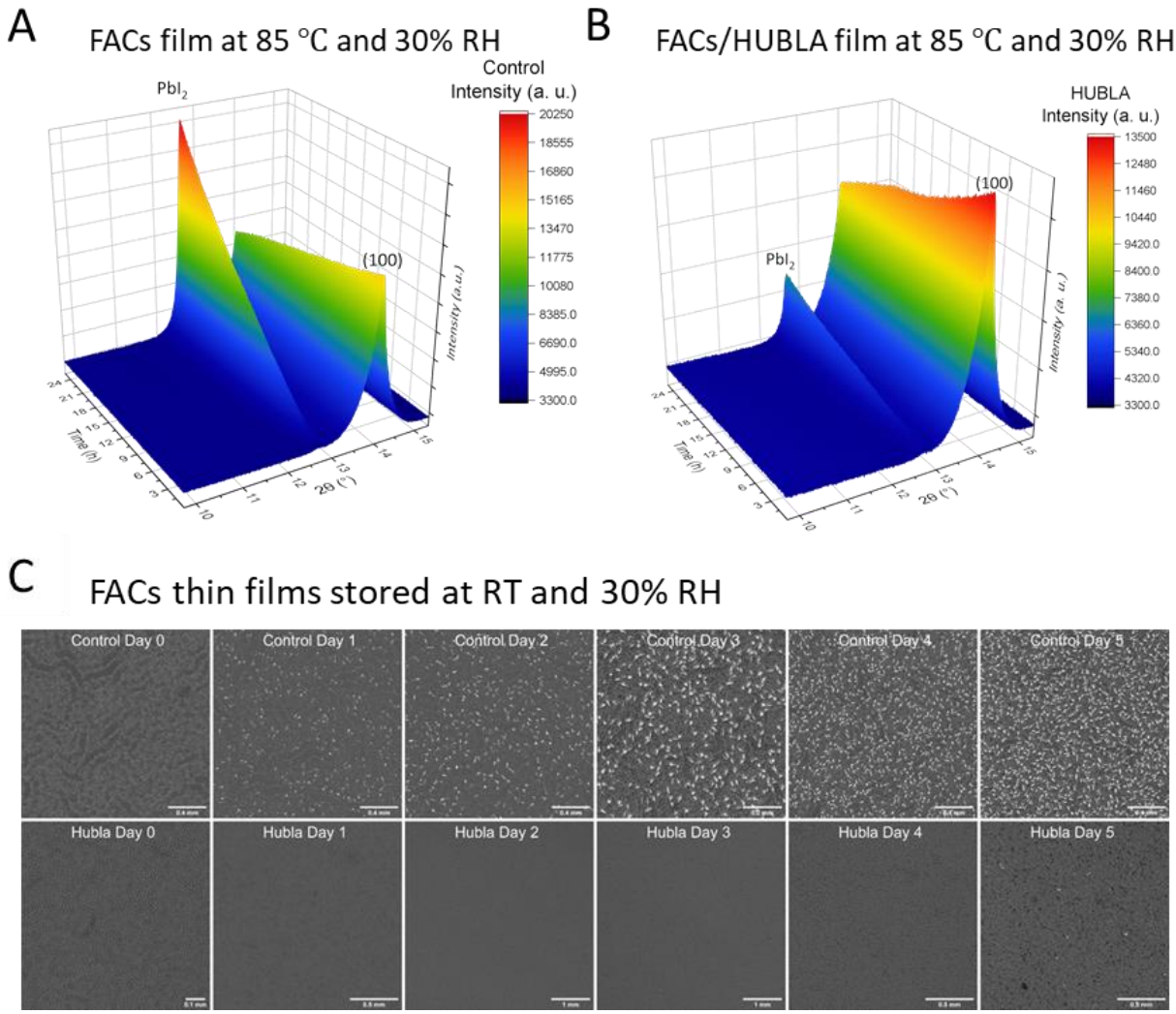

Figure 58 In-situ XRD[2] pattern of $FA_{0.83}Cs_{0.17}Pb(I_{0.9}Br_{0.1})_3$ films (**A**) without and (**B**) with HUBLA heated at 85 °C and 30% RH. Initial and final XRD[2] measurements are shown in **Figure A 30** and the change along the azimuthal angle χ for the PbI_2 peaks is shown in **Figure A 31**. The ratio of the peak area of *(100)* and PbI_2 peak over time is shown in **Figure A 31**. (**C**) Optical microscope images (illuminated from the bottom) of $FA_{0.83}Cs_{0.17}Pb(I_{0.9}Br_{0.1})_3$ perovskite thin films stored under ambient conditions for 5 days.

In the next part, I investigated the stability of HUBLA under different environments. To test the thermal stability, I use a $FA_{0.83}Cs_{0.17}Pb(I_{0.9}Br_{0.1})_3$ perovskite as they have been shown to

have superior stability under light and heat than MA-containing perovskites.[201,202] For the commercialization of PSCs, it is necessary to pass the IEC 61215, the international standard for PSCs.[39] The highest used temperature in the IEC 61215 is 85 ℃. Therefore, I measured in-situ XRD[2] of two $FA_{0.83}Cs_{0.17}Pb(I_{0.9}Br_{0.1})_3$ thin films by heating them at 85 ℃ under 30% RH ambient condition for more than 24 hours (**Figure 58A** and **B**, **Figure A 30** and **Figure A 31**). The pristine $FA_{0.83}Cs_{0.17}Pb(I_{0.9}Br_{0.1})_3$ shows a significant increase in PbI_2 (the degradation product of $FA_{0.83}Cs_{0.17}Pb(I_{0.9}Br_{0.1})_3$) throughout aging.[203,204] In comparison, the thin film treated with HUBLA develops roughly 2/3 less PbI_2 (**Figure A 31**). Here, please note that the degradation of the $FA_{0.83}Cs_{0.17}Pb(I_{0.9}Br_{0.1})_3$ thin films was likely accelerated by the presence of water and oxygen. Therefore, it is not comparable to other published studies on the stability of $FA_{0.83}Cs_{0.17}Pb(I_{0.9}Br_{0.1})_3$ perovskites, which are heated in N_2.[202,205] To decouple the influence of moisture from heat, I characterized another pair of thin films stored in ambient at 30% RH and room temperature. A series of optical microscope images with illumination from below are shown in **Figure 58C**; the corresponding ultraviolet-visible spectroscopy (UV-Vis) and XRD for each day of the same films are shown in **Figure 59** and **Figure 60**.

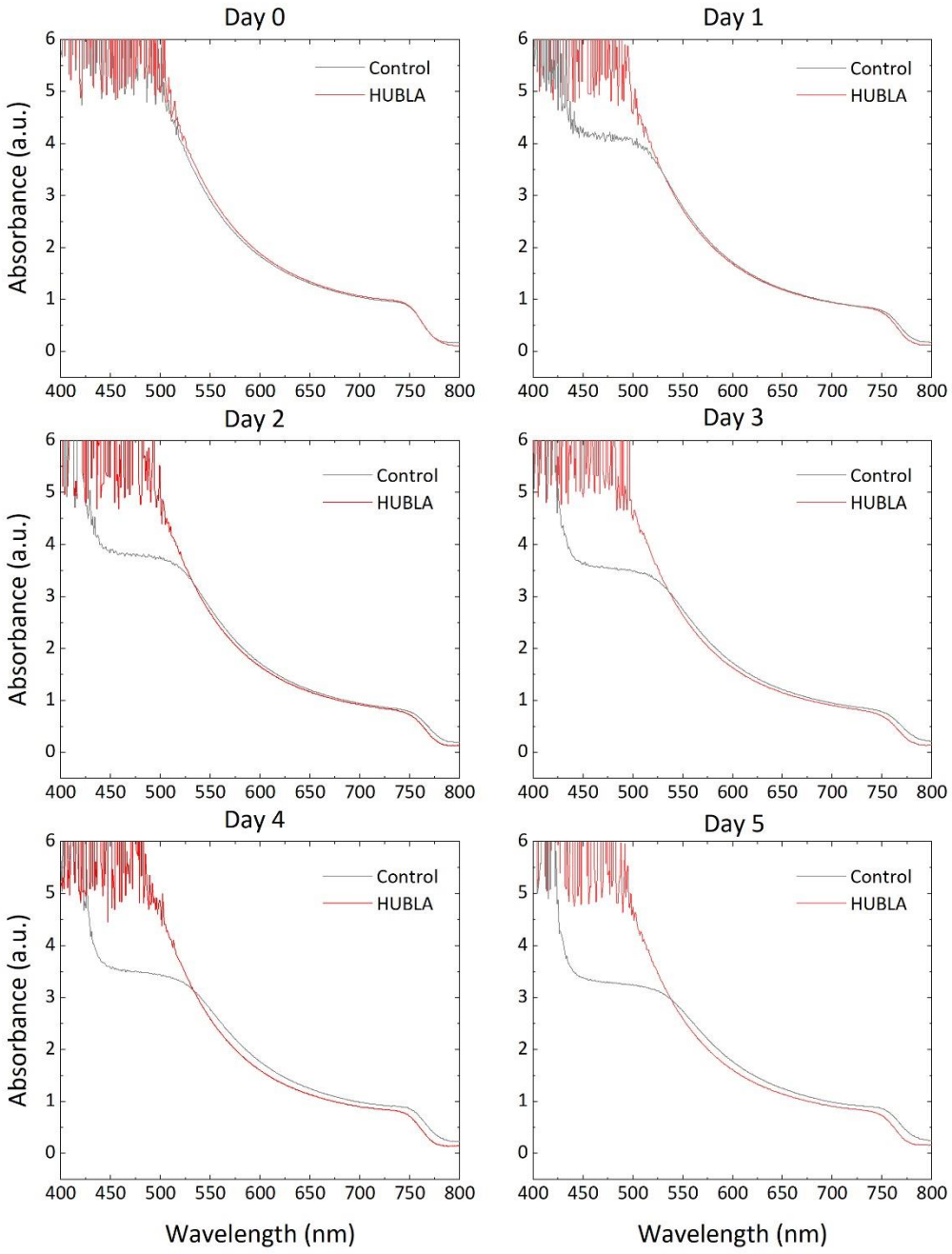

Figure 59 Corresponding UV-Vis of the optical microscope images in **Figure 58C** $FA_{0.83}Cs_{0.17}Pb(I_{0.9}Br_{0.1})_3$ thin films are stored at 30% RH. The loss in absorbance from 450 to 500 nm likely is a feature of the bright spots forming in **Figure 58C** for the control films. The shift in absorbance onset can be interpreted as a sign of a smaller bandgap material forming like an FA^+-richer perovskite. That would also be consistent with the shift in *(100)* I observe in the XRD in **Figure 60**.

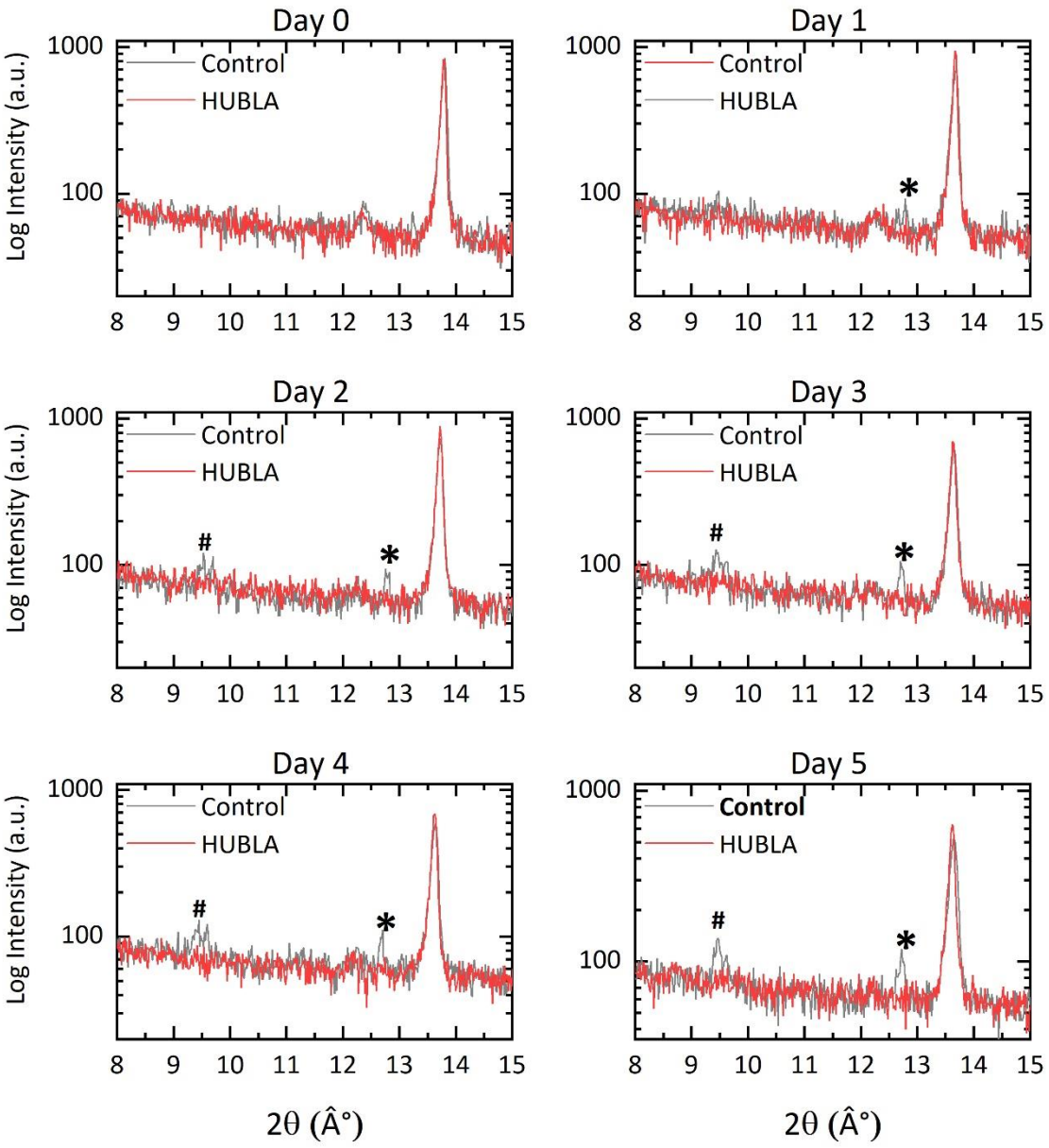

Figure 60 Corresponding XRD of the optical microscope images in **Figure 58C**. $FA_{0.83}Cs_{0.17}Pb(I_{0.9}Br_{0.1})_3$ thin films are stored at 30% RH. The XRD peaks likely correspond to the δ-$CsPbI_3$ (# symbol) and PbI_2 (* symbol) are marked in the XRD.

The $FA_{0.83}Cs_{0.17}Pb(I_{0.9}Br_{0.1})_3$ pristine thin-film showed first signs of degradation after 1 day stored at 30% RH, visible as bright spots in the microscope images and a loss in absorption intensity around 450 to 525 nm. After 2 days, new peaks appeared around 9.5° and 12.7° in

XRD. Likely, the δ-phase of $CsPbI_3$ and PbI_2. Furthermore, I can see a slight peak shift of the *(100)* diffraction and red-shift in absorbance onset for the pristine films, similar to Marchezi *et al*.[47] That is likely correlated with the segregation of FA^+ and Cs^+ cations as I also showed via TOF-SIMS 2D measurements in **Figure 26**, additional FA^+ is decomposing and leaving as gaseous product and PbI_2 forms. In comparison, the $FA_{0.83}Cs_{0.17}Pb(I_{0.9}Br_{0.1})_3$ thin film treated with HUBLA stayed the same until day 5, when the first bright spots appeared. Accordingly, I believe HUBLA can suppress the degradation of perovskite under humidity and thermal aging.

To understand more in detail at what conditions HUBLA is activated, further XPS under different humidity and heat levels was performed. To determine the thresholds for the heat-activated passivation, a 1000-hour thermal aging test of HUBLA in N_2 was conducted, as shown in **Figure 61**. The results reveal that no significant formation of $-S^-$ occurs below 55 ℃. During the 55 ℃ aging test, a small amount of $-S^-$ is observed and increases significantly with further temperature increase. This indicates an enhancement in the thermal activation process above this temperature. So, the heat-activated threshold for HUBLA is above 55 ℃. To determine the thresholds for water-activated passivation, a 48 hours hydrolysis test of HUBLA using XPS at room temperature (25 ℃), and the relative humidity (RH) ranged from 20% to 90% RH was conducted. To clarify the binding energy of each component on perovskite film, the N 1*s* XPS spectra of each monomer on the perovskite film are assigned, as shown in **Figure A 32**, and used TMXDI hydrolysate to evaluate the N 1*s* component of the primary amine group ($-NH_2$). TMXDI and TMXDI hydrolysate show the N 1*s* components at ~400.0 and ~399.7 eV, assigned to isocyanate group (-NCO) and primary amine group ($-NH_2$), respectively. tBEDA shows the N 1*s* components at ~401.8 and ~399.4 eV, assigned to ammonia and secondary amine group (-NH-), respectively. With that I can analyse the XPS spectra shown in **Figure 61**. The results

indicate that HUBLA can undergo hydrolysis under humid condition at 20% RH, which represents the lowest RH within the humidity chamber. This showcases its ability to trigger a passivation process even when exposed to minimal environmental moisture.

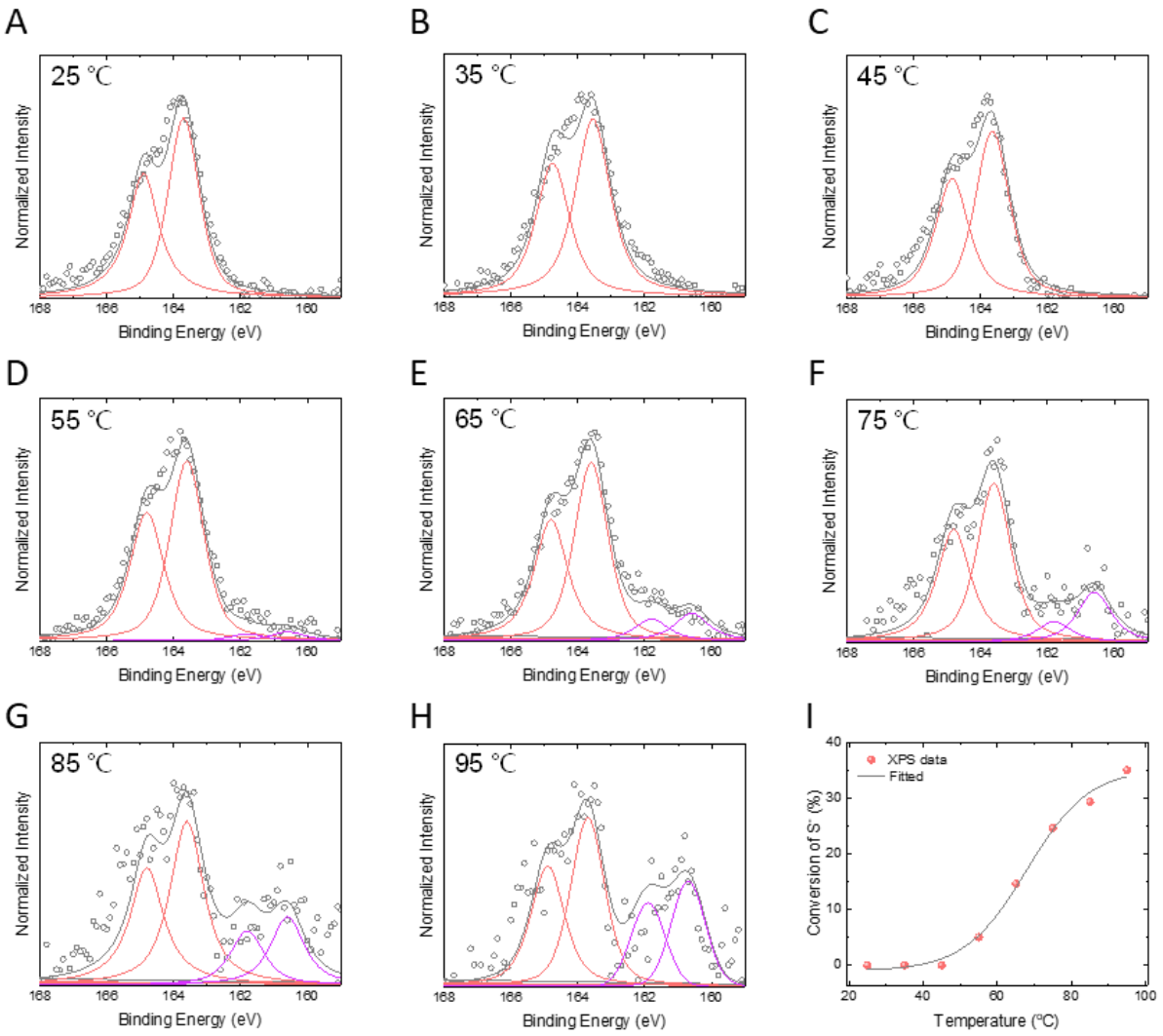

Figure 61 The thresholds of heat-activated characteristics. (**A-H**) S 2p regions of perovskite/HUBLA films aged under 25 to 95 ℃ for 1000 hours, respectively. (**I**) Summary of the conversion of -S- (%). The grey circles and curves represent the raw data and peak sum, respectively. The red and purple curves represent the S 2p spectra of the thiocarbamate bond (-SC(O)NH-; also include the -S-S-) and -S-, respectively.

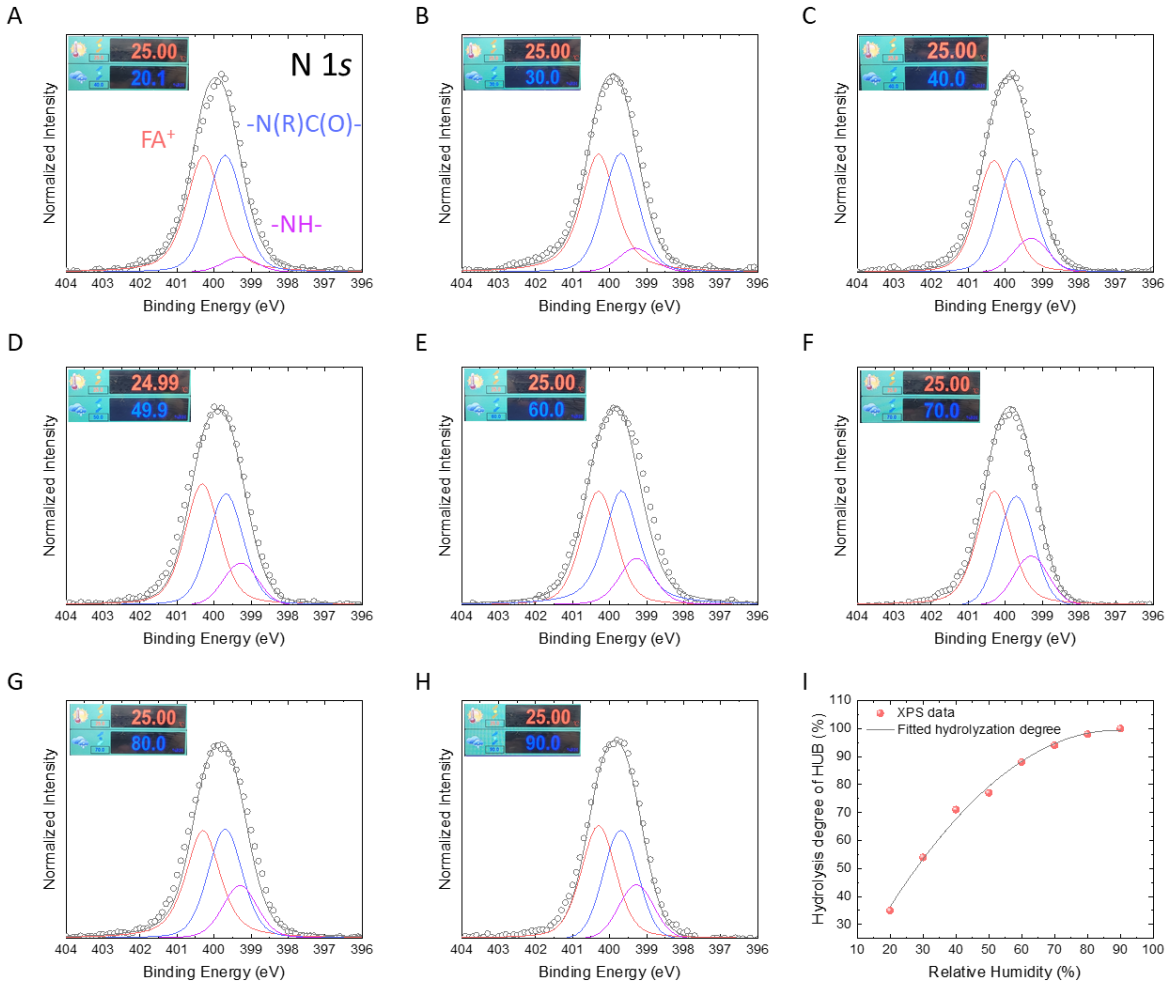

Figure 62 The thresholds of water-activated characteristics. (**A-H**), N 1*s* regions of perovskite/HUBLA films aged under 20% to 90% RH for 48 h, respectively. (**I**), Summary of the conversion of HUB (%) under different humid conditions. The grey circles and curves represent the raw data and peak sum, respectively. The red, blue, green and purple curves represent N 1*s* components of FA^+, the amide bond (-N(R)C(O)-; also include the $-NH_2$), ammonia and -NH-, respectively.

15.5. Device performance and stability

First n-i-p devices with HUBLA are fabricated. A stack of ITO/SnO_2/$FA_{0.72}MA_{0.28}PbI_3$/(wo/w) HUBLA/spiro-OMeTAD/MoO_3/Ag was used. The highest achieved PCE for HUBLA devices is 24.7%, with a J_{SC} of 25.6 mA cm^{-2}, a V_{OC} of 1.16 V, and a FF of 0.83. For the control device, 21.7% with a J_{SC} of 25.6 mA cm^{-2}, a V_{OC} of 1.10 V, and a FF of 0.77 (**Figure 63A**) was reached. HUBLA caused an increase by 60 mV and improved the FF by from 0.77 to 0.83. Please note, that this increase in V_{OC} correlates well with the increase in the PL maps I measured. As seen in the inset, the HUBLA device reached a stabilized power output (SPO) of 24.5% after 30 s, while that of the control device is 21.3%. The increase of performance especially in V_{OC} likely comes from the passivation of defects and the resulting reduction in non-radiative recombination at the interface. The EQE of the HUBLA device exhibits an integrated current density of 24.4 mA cm^{-2} (**Figure A 33**)[206], and the total absorbance spectrum of glass/ITO/perovskite is shown in **Figure A 34**. Please note, that it is commonly observed that there is a difference between EQE and measured J_{SC}.[206] In **Figure 63B**, the stability of the n-i-p devices under ambient conditions with 25 ℃ and 30% RH is measured. The normalized PCE shows that the HUBLA devices retained nearly 87% of the original performance, while that of the control devices dropped to 43% after 3600 hours. Note that the PCE of the HUBLA devices only slightly decreased before 768 hours, while that of the control devices decreased significantly after 336 hours. To study the correlation between HUBLA hydrolysis and device performance, N 1*s* XPS spectra of $FAPbI_3$/HUBLA film aged at 25 ℃ under 30% RH for 480 hours is measured, as shown in **Figure A 32**. During 480 hours, the characteristic component of secondary amine (-NH- from tBEDA, purple curves) continuously increased. After 480 hours, the area of tBEDA was almost half of the HUBLA peak, indicating that HUB has almost dissociated and transformed to tBEDA and NH-AS. I, therefore, believe that HUBLA can

continuously absorb water and release new passivation agents for at least 480 hours under 25 ℃ and 30% RH. The N 1*s* XPS spectra and the PCE result can be mutually verified under the same experimental conditions.

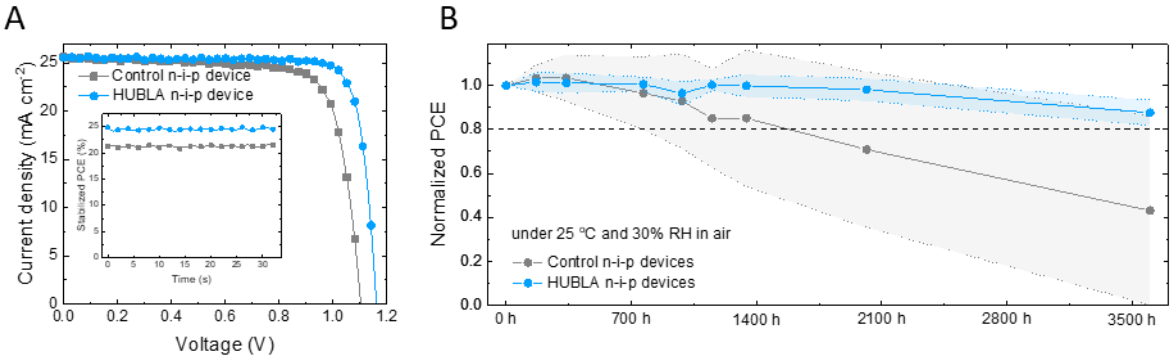

Figure 63 Performance and stability of perovskite photovoltaics. (A), Best J-V curves with SPO and (B) stability of unencapsulated n-i-p devices (Glass/ITO/SnO_2/perovskite/(wo/w) HUBLA/Spiro-OMeTAD/MoO_3/Ag) stored in air at 25 ℃ and 30% RH).

Commonly p-i-n devices show better thermal stability in comparison to n-i-p devices.[93] Consequently, p-i-n devices were fabricated with the device architecture of ITO/SAM/$FA_{0.72}MA_{0.18}Cs_{0.1}PbI_3$/(wo/w) HUBLA/$C_{60}$/BCP/Au), demonstrating a best PCE of 25.1% for the HUBLA device with a V_{OC} of 1.17 V, a J_{SC} of 25.4 mA cm^{-2} and a FF of 0.84. On the other hand, the control device shows a PCE of 22.7% with a V_{OC} of 1.13 V, a J_{SC} of 25.2 mA cm^{-2} and a FF of 0.79 (**Figure 64A**). As seen in the inset the SPO tracking for 30 seconds shows that the HUBLA cell has a steady-state efficiency of 24.9%, while that of the control cell is 22.5%. I believe the enhanced performance comes from the better charge extraction and the lower non-radiative recombination. In addition, p-i-n device with an effective area of 1 cm^2 were fabricated and achieved up to 23.5% for the HUBLA devices (**Figure 64B**), while that of the control device is 22.2%. To assess the capability of HUBLA in enhancing device stability under

thermal and humid conditions, maximum power point tracking (MPPT) of encapsulated control and HUBLA devices was performed under 85 ℃ and ~30% RH in air (ISOS-L-2) (**Figure 64C**). It was observed that the control device rapidly declined to below 50% after 431 hours, while the HUBLA device retained 88% of its initial value after 1000 hours. MPPT of $FA_{0.92}Cs_{0.08}PbI_3$ p-i-n device was also measured at 85 ℃ in N_2 without encapsulation under light (ISOS-L-2) (**Figure 64D**). The T_{80} of the control device was recorded to be 866 hours. The HUBLA device maintained 94% of the initial PCE after aging for nearly 1500 hours.

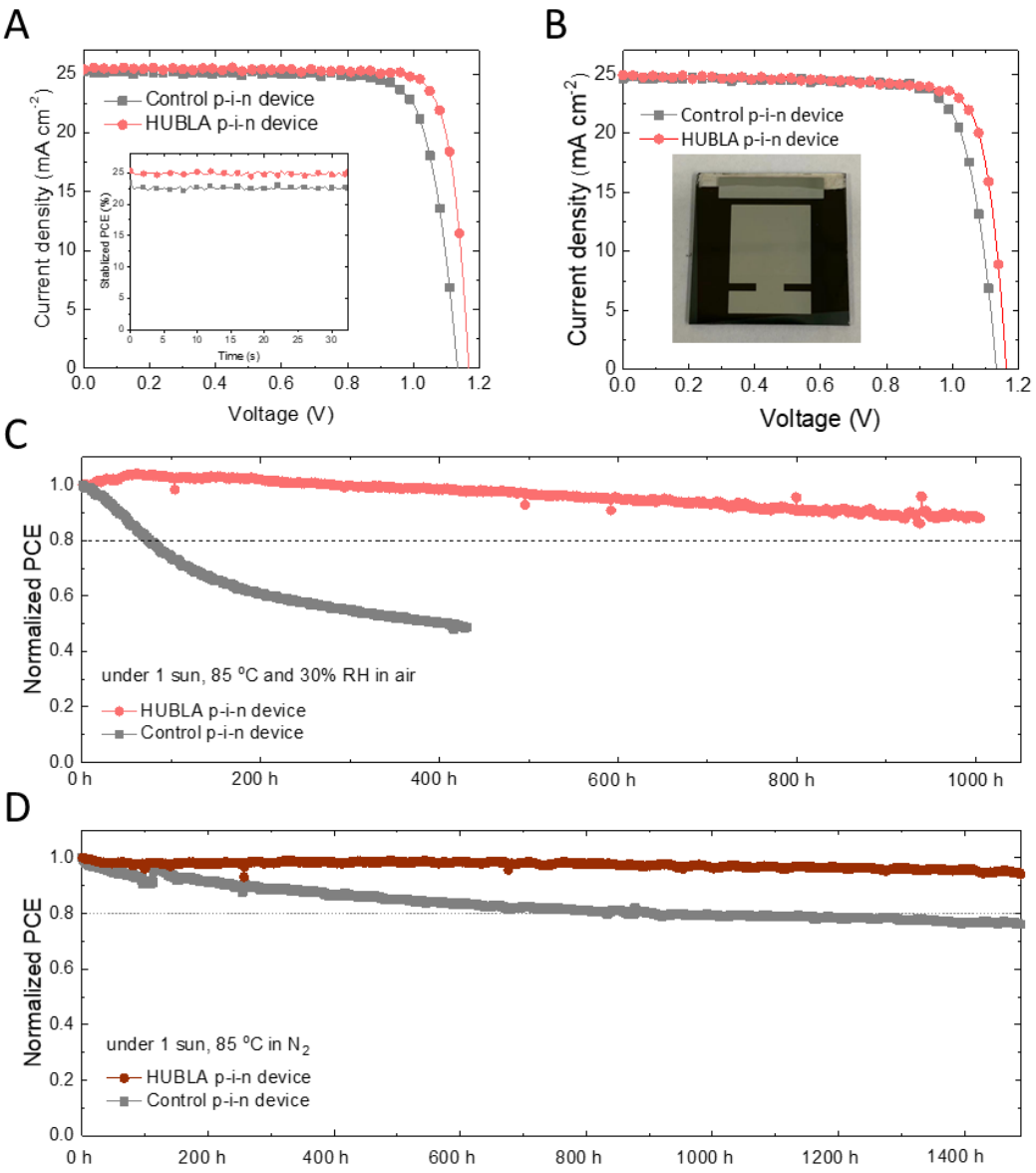

Figure 64 Performance and stability of perovskite photovoltaics. (**A**) Best J-V curves with SPO of p-i-n devices. (**B**) Best J-V curves of 1 cm^2 p-i-n devices. (**C**) The MPPT tests of encapsulated p-i-n devices (same device structure as in (**A**)) aged at 85 ℃ and 30% RH in air under 1 sun. The initial PCE of the control and HUBLA device were 20.9% and 23.0%, respectively. (**D**) The MPPT tests of unencapsulated p-i-n devices aged at 85 ℃ in N_2 under 1 sun. The initial PCEs of the control and HUBLA devices were 20.8% and 23.3%, respectively.

Considering the S 2*p* XPS spectra (**Figure 54B**), which demonstrate the dissociation of the thiocarbamate bond in HUBLA and the formation of a redox shuttle to reduce I_2 and oxidize Pb^0 (**Figure 54C**), it can be inferred that the enhanced thermal stability is attributed to HUBLA's ability to inhibit perovskite degradation and extend operational and storage stability.

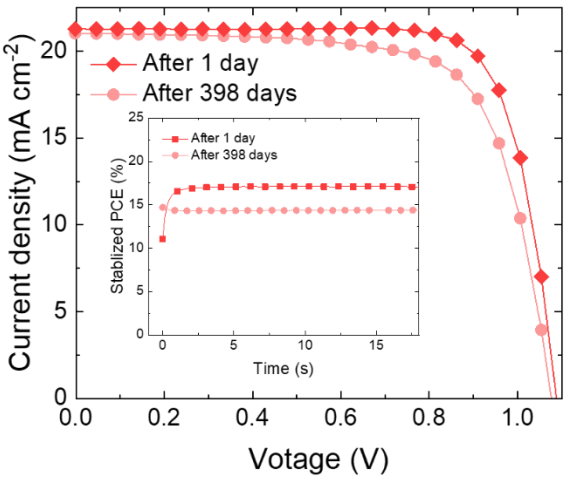

Figure 65 J-V curve of the most stable FACs p-i-n device with HUBLA at 85 °C in N_2.

The most commonly used p-i-n device at the time in the laboratories in Oxford were p-i-n devices with $FA_{0.83}Cs_{0.17}Pb(I_{0.9}Br_{0.1})_3$ as composition with poly(4-butylphenyl-diphenylamine) (polyTPD) as a p-type layer and [6,6]-phenyl-C61-butyric acid methyl ester (PCBM)/BCP as n-type layer[15,16] and Au as an electrode. Therefore, I measured the stability of the p-i-n devices at 85 °C in N_2 in the dark and choose to compare device performance to the most efficient HUBLA device after 1 day of aging as it induces the most significant increase in performance. As shown in **Figure 65**, the HUBLA device has a J-V scan of 17.5% (stabilized PCE of 16.8%) after 1 day, while it maintained a J-V scan of 16.1% after 398 days of aging at 85 °C in N_2 (stabilized PCE of 14.4%, 86% of its stabilized PCE after 1 day). All devices improved initially but then diverged during aging. The control devices reached their peak median performance at 240 hours (**Figure 66B**), and the HUBLA devices peaked at 768 hours (**Figure 66A**). I note that this initial improvement of p-i-n devices has already been studied in literature[15,17]. Given that the stability data is nonmonotonic, the consensus on stability data[18] suggests reporting the time till the devices reach 80% of their maximum PCEs (T_{S80}). The T_{S80} for the HUBLA devices was 11535.65 h, and the retained initial fraction is 0.9048 after 21864 h. In

comparison, the twelve control devices have a T_{S80} of 2965 hours. The corresponding PV parameters for the HUBLA and the control devices are shown in **Figure A 35**. The control devices show a linear decay of the PV parameters after an initial increase; the initial increase in PCE of the HUBLA devices is more significant and over a longer timeframe. This different aging behaviour could arise from the redox shuttle reactions of HUBLA.

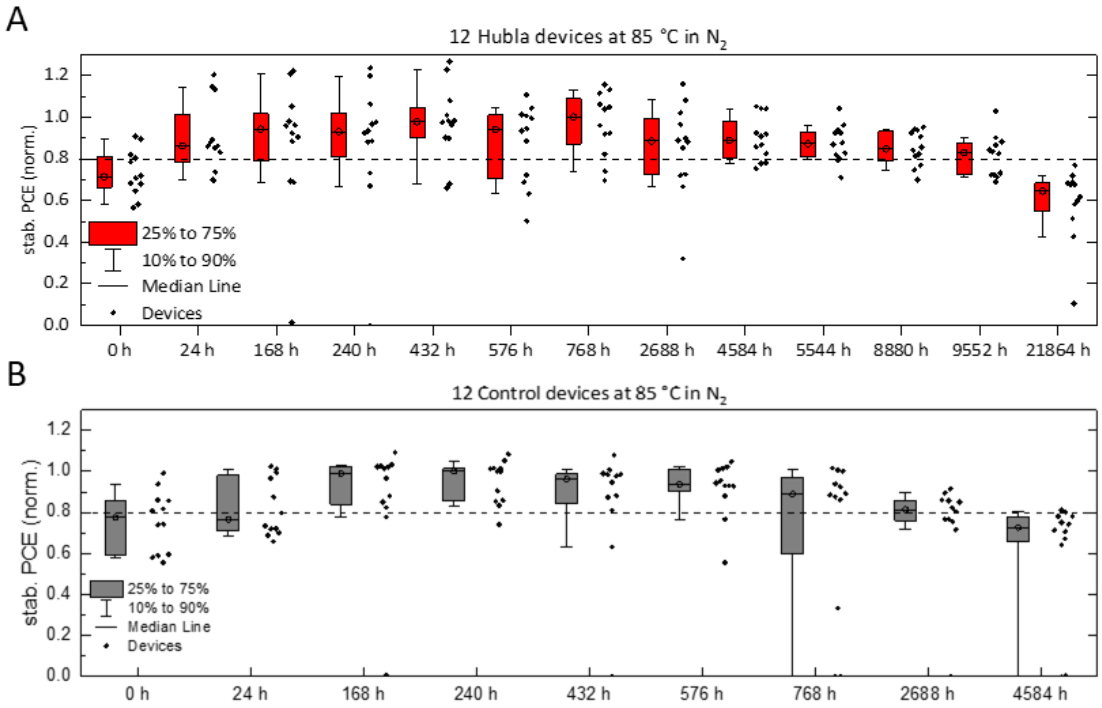

Figure 66 Stability of 12 control and HUBLA devices aged at 85 °C in N_2. (A) Stability of twelve HUBLA p-i-n devices aged at 85 °C in N_2 normalized to the peak median efficiency of 14.0% at 768 hours. They reach their T_{S80} at 11535.65 hours. (B) Stability of twelve control p-i-n devices. The devices were normalized to the peak efficiency at 240 hours of 16.0%. They reach their T_{S80} at 2965 hours.

15.6. Discussion and summary

HUBLA is a new dynamic passivation strategy for perovskites with DCBs, which can passivate as-deposited perovskite films not only during the fabrication process but also afterward. By releasing additional Lewis bases, HUBLA heals defects during the device's operation and storage. Through XPS, UV-Vis, XRD, optical microscope images, in-situ XRD, and in-situ PL studies, I showed that HUBLA-coated perovskites become more resistant to water and heat. With HUBLA and its evolving products, enhanced device performance and improved operational stability at elevated temperatures and under humid conditions were achieved.

Looking at the task ahead for perovskite solar cells the challenge of reaching decade long lifetimes seems daunting. Lead halide perovskites easily develop defects and the harsh environmental conditions further facilitate that. So new ways of tackling defects are needed. A dynamic passivation seems perfectly suited for that.

I hope that HUBLA can inspire other researchers to think about dynamic passivation and design novels ones. I believe that it is an exciting and inspiring new way of going about passivations especially for organic semiconductors. In that sense I also believe that trying HUBLA or other dynamic passivations in other related fields like perovskite LEDs, organic electronics or organic solar cells would be intriguing.

16. Outlook

The impacts of climate change are getting worse, and human activities are still driving up greenhouse gas emissions. A shift away from fossil fuels towards renewable energies is needed. Photovoltaics are ideal for that. A way of improving them is with perovskite solar cells. They allow for an even lower environmental footprint and can improve the efficiency in a tandem. But for that, perovskites have to be stable for decades. As already for Vanguard I, the operational stability of solar cells is the key to their success.

In this thesis, I presented a new fabrication method, the DMA route. It further improves the operational study of perovskite solar cells without using DMSO. By changing the intermediate phases during the crystallisation, I found that the final perovskite layer is significantly more crystalline and orientated. Further, I found that removing DMSO is necessary to achieve stable devices. The residual solvents significantly accelerated the decomposition. That highlights that the departure from strongly coordinating solvents is needed for stable perovskite solar cells. Further improvements of the DMA route should be feasible by creating a more homogenous perovskite film and applying a top-contact passivation. Likely the DMA^+ is not incorporated homogenously throughout the film but only in some regions. That is likely connected to the precursor solution and the formation of specific coordination complexes in the solution. Changing these coordination complexes might be the key to reaching even more stable DMA^+ devices. The usage of the DMA route was already extended to the Pb-Sn perovskites and larger bandgaps of 2eV for the lead halide perovskite. It is a generally applicable route that will help the perovskite community make more stable devices.

While one might wonder what is so special about DMA^+, it does have a unique beneficial effect on the lead halide perovskites. A recent comparison study found that DMA^+ is the best cation

to suppress halide segregation.[207] It also does have a dipole moment and has been used, for example, in azide hybrid organic, inorganic halide perovskites to increase the dielectric permittivity.[208] Another prominent cation for lead halide perovskites with a dipole moment is MA^-. While it has been clear for a while that replacing MA^- is needed to increase the stability, it turned out that replacing MA^- is surprisingly difficult. Often, high efficiencies in perovskite solar cells are only reached if small amounts of MA^- are used.[38] I believe that is because one of the critical properties of MA^- besides its ideal effective radius is its dipole moment. So, the dipole moment of DMA^+ is likely a crucial factor for its success. Further, the effective radius of DMA^+ is close to being suited to incorporate in the 3D $APbI_3$ perovskite. The biggest drawback of DMA^+ seems to be the initial heterogeneity in photocurrent, which has not only been observed by me but also for stoichiometrically used DMA^+ in lead halide perovskites.[209] If the challenge of the initial heterogeneity can be overcome, DMA^+ will be the perfect choice for a cation to reach a stable mixed lead halide perovskite.

I also developed a new passivation called HUBLA. Inspired by the ability of living beings to heal continuously, this passivation allows for the healing of defects after the manufacturing stage. During the operation, newly formed defects are healed. The concept presents an entirely new type of passivation – a dynamic one.

I believe it is imperative to develop new ways of tackling the stability in perovskite solar cells like the here developed dynamic passivation. It is inevitable that a perovskite solar cell will evolve new defects during its operation. From those defects the degradation will start. While the time until these defects will evolve might differ depending on the fabrication and optimisation, but the low activation energy of defects for perovskites makes it unlikely that no defects will evolve at all. Having passivating agents then stored up to heal newly evolving

defects is ideal to prevent further degradation originating from the defects. The stored passivating agents might run out at some point but the ability of the redox shuttle to reduce Iodine and to oxidise Pb^0 is not limited.

Besides perovskite solar cells many organic or hybrid materials suffer from newly evolving defects during operation. Perovskite light emitting diodes (LED), organic electronics and organic solar cells are only some of the many other devices in which a dynamic passivation will improve not only the performance but also the durability.

17. Appendix for 13. Intermediate phase engineering with DMAX

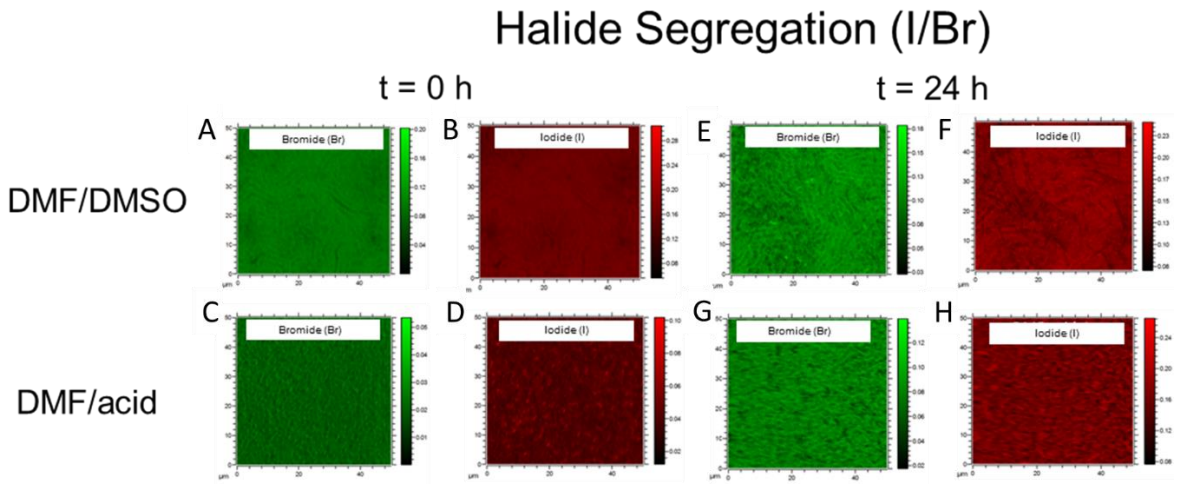

Figure A 1 Light stability of individual halides measured using TOF-SIMS mapping. TOF-SIMS 2D mapping of (**A**) Br and (**B**) I for the DMF/DMSO devices at t = 0 h. TOF-SIMS 2D mapping of (**C**) Br and (**D**) I for the DMF/DMSO devices at t = 24 h. TOF-SIMS 2D mapping of (**E**) Br and (**F**) I for the DMF/acid devices at t = 0 h. TOF-SIMS 2D mapping of (**G**) Br and (**H**) I for the DMF/acid devices at t = 24 h. The devices were aged under AM 1.5G sunlight at maximum power point (MPP) in ambient air for 24 hours without encapsulation. All devices were fabricated with a n-i-p FTO/SnO_2/$PC_{61}BM$/$FA_{0.83}Cs_{0.17}Pb(I_{0.6}Br_{0.4})_3$/spiro-OMeTAD/Au architecture. The data was reconstructed to include data only from the perovskite absorber layer from a 3-D tomography dataset of the entire device stack. All the image sizes are 50 µm × 50 µm. The data were normalized to the total intensity measured at every pixel to minimize topographic effects on the image. Thus the scale at the right of each image is the normalized intensity (I(pixel x) /Itotal at pixel x)). Adapted from [105].

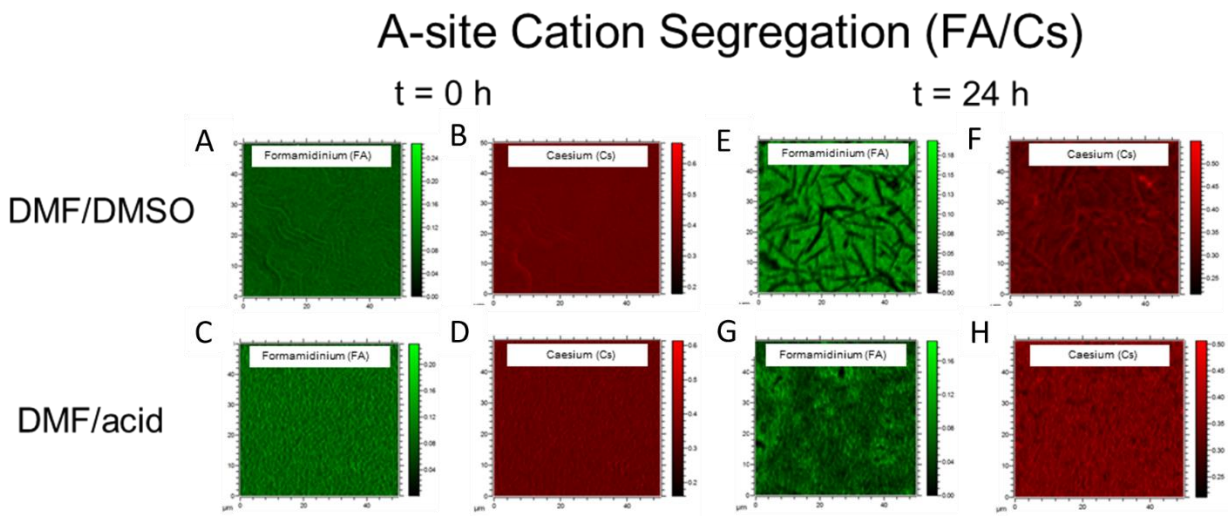

Figure A 2 Light stability of individual A-site cation measured using TOF-SIMS mapping. TOF-SIMS 2D mapping of (**A**) FA and (**B**) Cs for the DMF/DMSO devices at t = 0 h. TOF-SIMS 2D mapping of (**C**) FA and (**D**) Cs for the DMF/DMSO devices at t = 24 h. TOF-SIMS 2D mapping of (**E**) FA and (**F**) Cs for the DMF/acid devices at t = 0 h. TOF-SIMS 2D mapping of (**G**) FA and (**H**) Cs for the DMF/acid devices at t = 24 h. The devices were aged under AM 1.5G sunlight at maximum power point (MPP) in ambient air for 24 hours without encapsulation. All devices were fabricated with a n-i-p FTO/SnO_2/$PC_{61}BM$/$FA_{0.83}Cs_{0.17}Pb(I_{0.6}Br_{0.4})_3$/spiro-OMeTAD/Au architecture. The data was reconstructed to include data only from the perovskite absorber layer from a 3-D tomography dataset of the entire device stack. All the image sizes are 50 µm × 50 µm. The data were normalized to the total intensity measured at every pixel to minimize topographic effects on the image. Thus the scale at the right of each image is the normalized intensity ($I_{(pixel\ x)}$ /$I_{total\ at\ pixel\ x)}$). Adapted from [105].

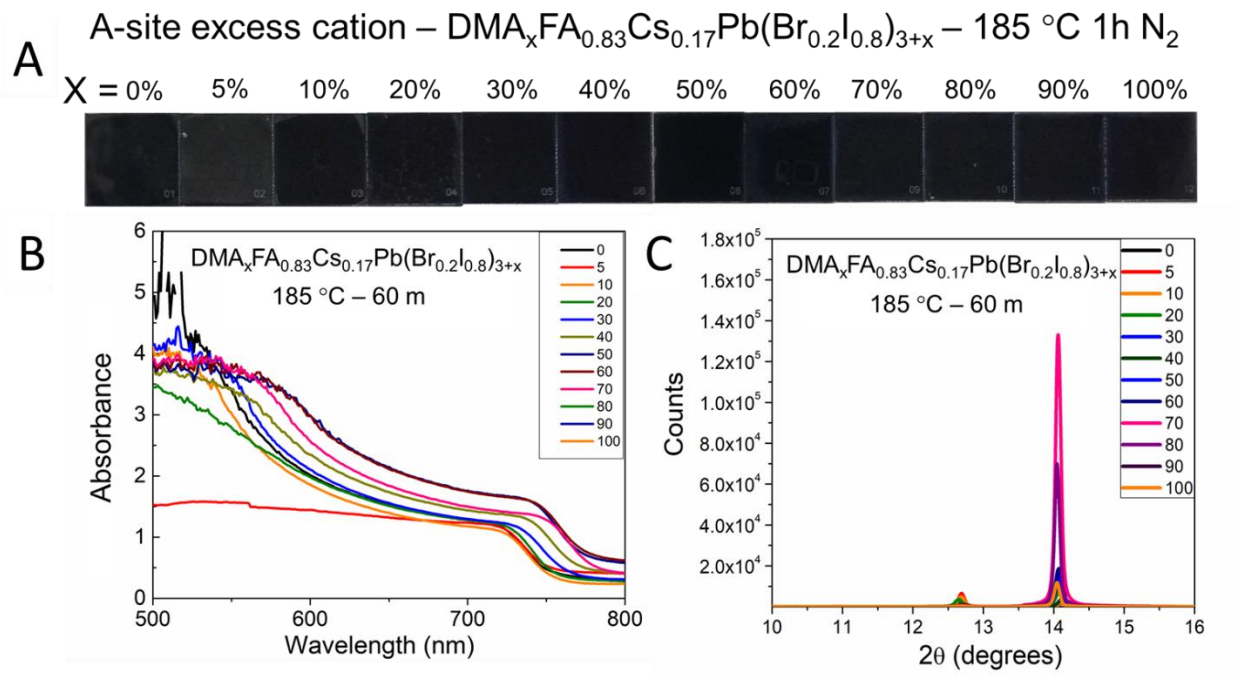

Figure A 3 A-site excess cation of the $DMA_xFA_{0.83}Cs_{0.17}Pb(Br_{0.2}I_{0.8})_{3+x}$ perovskite system after a 60 mins anneal at 185 °C. (**A**) A series of photographs (**B**) XRD patterns (**C**) UV-Vis absorbance spectra of corresponding thin films. Adapted from [105]. The series shows that for all excess concentrations, the perovskite film turns black and into the perovskite phase, meaning that most of the excess material leaves the material and the perovskite phase can form. It is essential that the hexagonal intermediate phases disappear entirely.

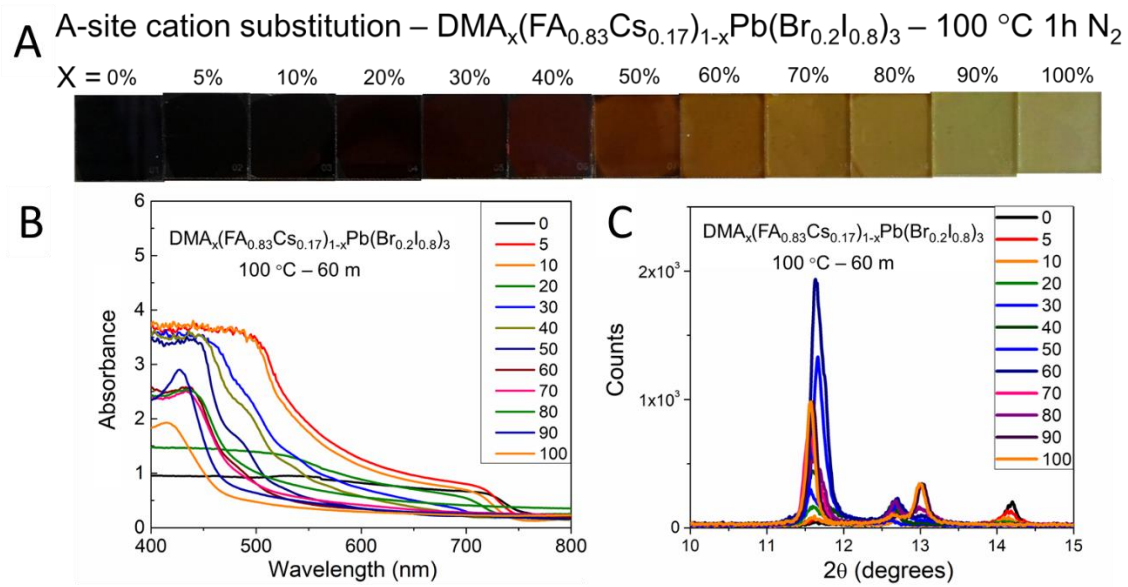

Figure A 4 A-site cation substitution of the $DMA_x(FA_{0.83}Cs_{0.17})_{1-x}Pb(Br_{0.2}I_{0.8})_3$ perovskite system after 60 mins anneal at 100 °C. (**A**) A series of photographs (**B**) XRD patterns (**C**) UV-Vis absorbance spectra of corresponding thin films. Adapted from [105]. While I only add DMA^+ as excess in literature, the stoichiometric use of DMA^+ is commonly used. Here, I compare how this method works when equal amounts of DMA^+ as in the previous figure (**Figure A 3**) are added and annealed. As one can see, only small amounts of DMA^+ still lead to the formation of the perovskite phase, and also hexagonal polytypes and the δ-$FAPbI_3$ phase are forming. That shows that the addition of DMA^+ along with the replacement of the other A-site cations does not work as well as the addition in excess. In the following figure, I show how a longer and higher temperature annealing impacts the same perovskite where DMA^+ replaces other A-site cations.

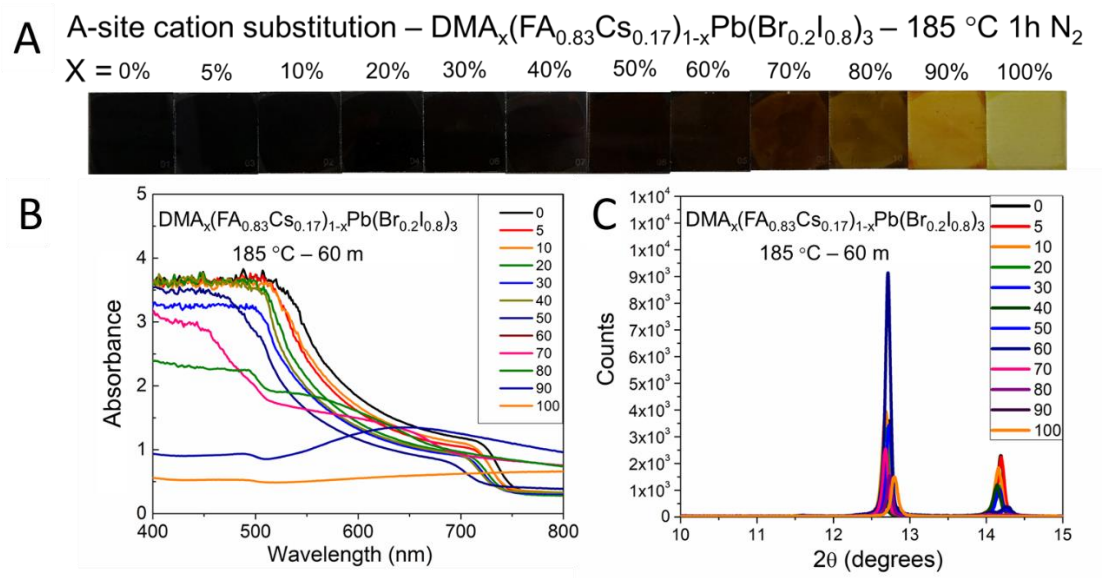

Figure A 5 A-site cation substitution of the $DMA_x(FA_{0.83}Cs_{0.17})_{1-x}Pb(Br_{0.2}I_{0.8})_3$ perovskite system after a 60 m anneal at 185 °C. (**A**) A series of photographs (**B**) X-Ray diffraction patterns (**C**) UV-Vis absorbance spectra of corresponding thin films. Adapted from [105]. This figure shows the same method used as in **Figure A 4** but with a higher annealing temperature. The hexagonal polytypes are removed, but large amounts of residual PbI_2 form instead.

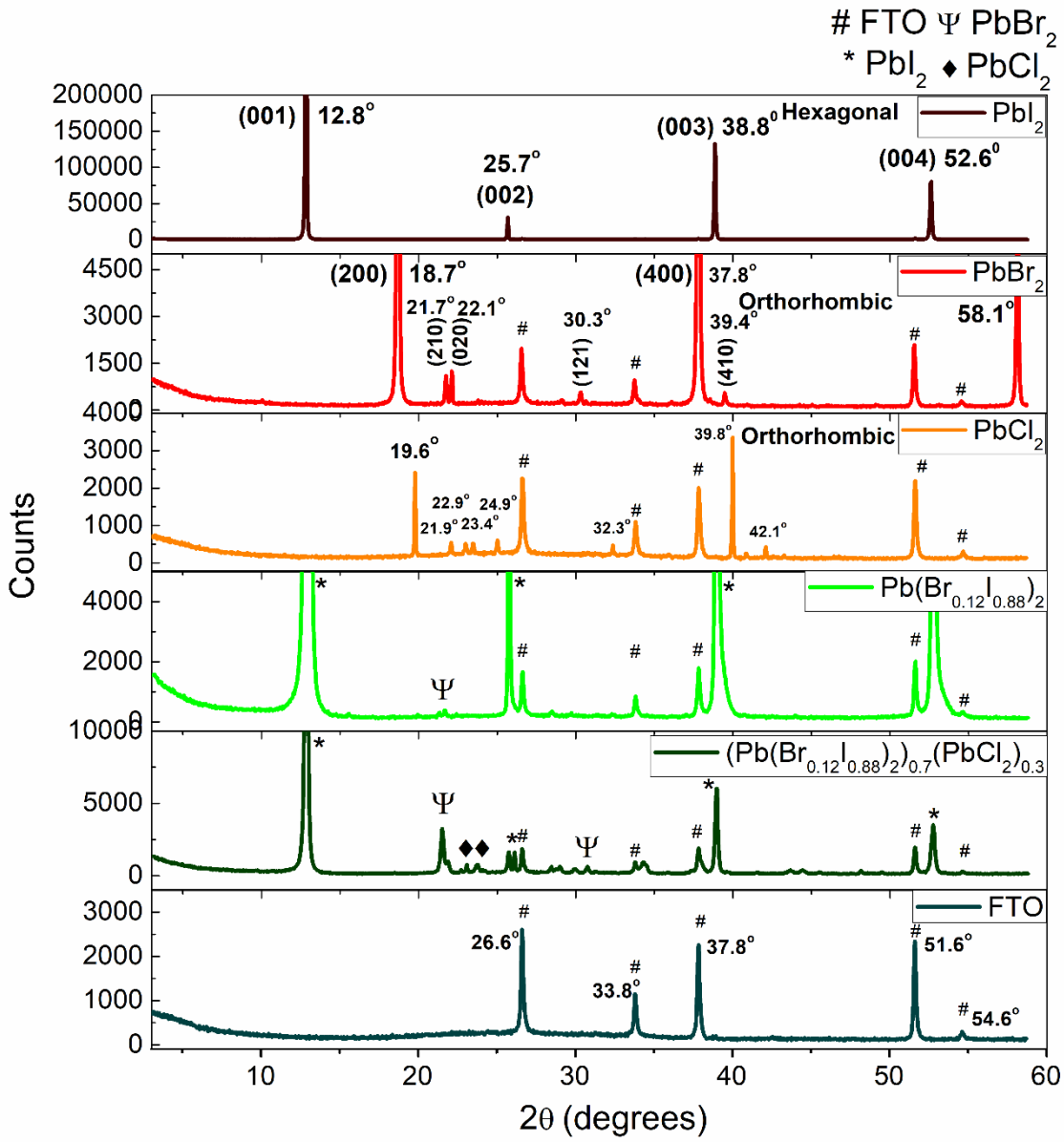

Figure A 6 XRD for several PbX_2 (with X being I^-, Br^- or Cl^-) compositions formed on FTO coated glass substrates when annealed at 100 °C for 5 m. Adapted from [105]. This figure is used to identify the lead halide peaks in the XRD pattern, as in **Figure 33**.

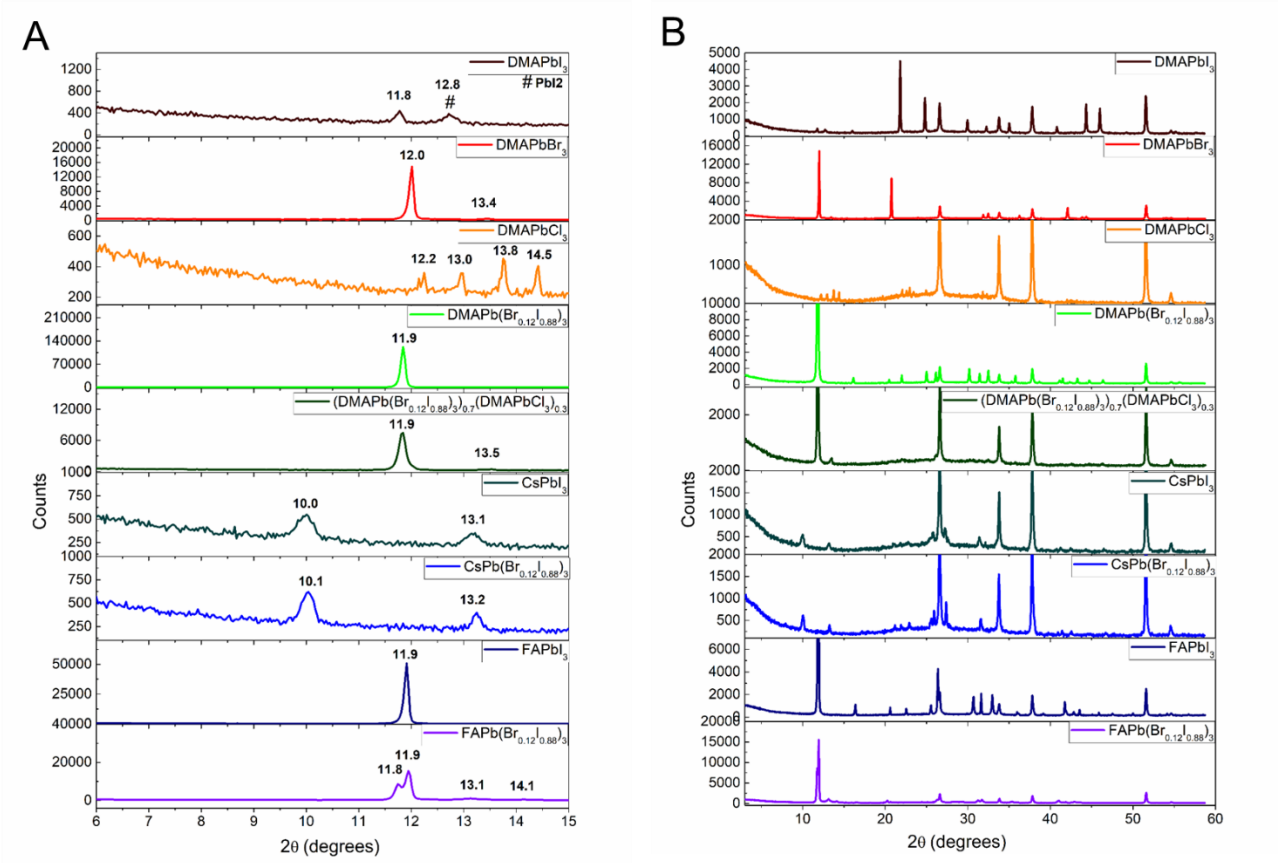

Figure A 7 XRD for $DMAPbI_3$, $DMAPbBr_3$, $DMAPbCl_3$, $DMAPb(Br_{0.12}I_{0.88})_3$, $(DMAPb(Br_{0.12}I_{0.88})_3)_{0.7}$ $DMAPbCl_3)_{0.3}$, $CsPbI_3$, $CsPb(Br_{0.12}I_{0.88})_3$, $FAPbI_3$, $FAPb(Br_{0.12}I_{0.88})_3$ compositions formed on FTO coated glass substrates when annealed at 100 °C for 5 m. I show the XRD for these perovskite compounds from (**A**) 2θ 6 to 15° and (**B**) 2θ 3 to 60°. Adapted from [105]. This is used to identify the DMA^+, FA^+ and Cs^+ lead halide perovskite peaks in the XRD pattern, as shown in **Figure 33**.

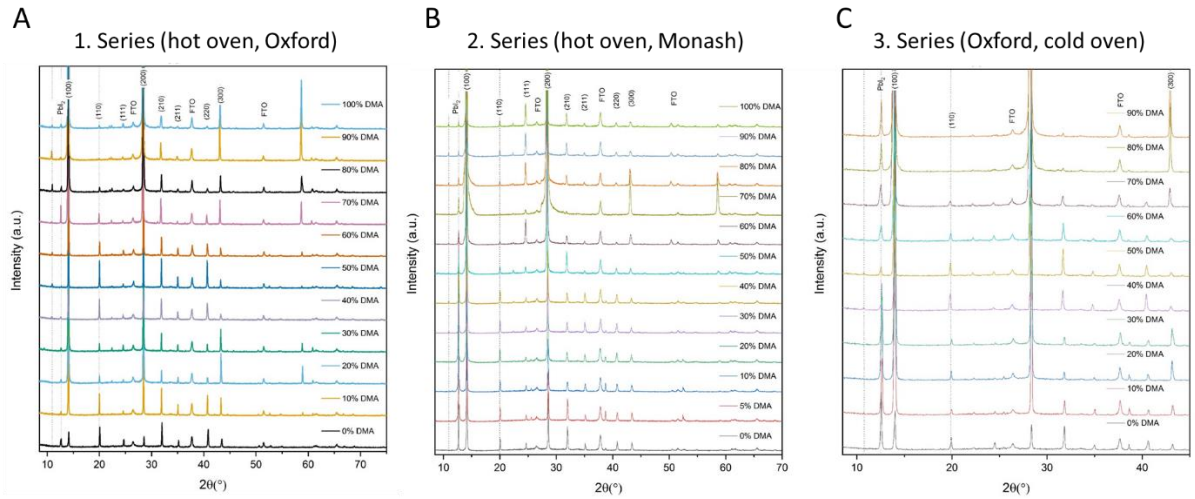

Figure A 8 $DMACl_{excess}$ (X mol%) : $(FA_{0.83}Cs_{0.17})Pb(Br_{0.15}I_{0.85})_3$ perovskite films spin-coated with various amounts of DMACl additive, where percentages are expressed in excess amounts with respect to lead. (**A**) The first series was fabricated in Oxford by heating first in a glovebox and consequently further annealing in an already annealed oven in air at ~180 °C. (**B**) The second series was fabricated in Monash, Melbourne, with the same heating protocol. (**C**) The third series fabricated in Oxford was first heated in a glovebox and then annealed in a cold oven, which was ramped up afterwards. A detailed analysis of all three series is shown in **Figure A 9** and **Figure A 10**. I repeated the series to triple-check the overall trend with DMACl addition to the mixed cation and mixed halide perovskite. The new peak forming around 10.9° was especially relevant since it decided which concentration of DMACl I would use.

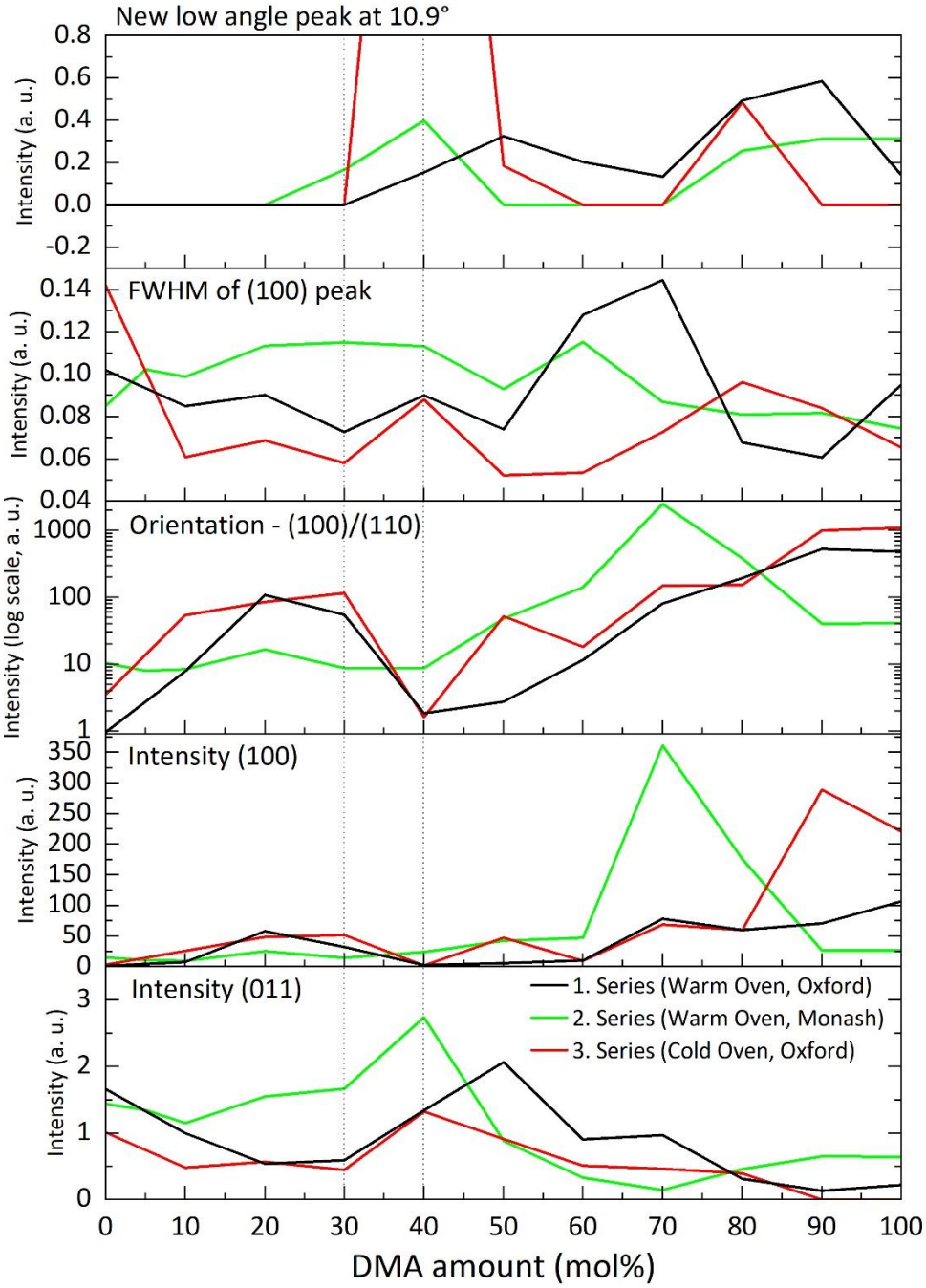

Figure A 9 XRD analysis of three series of $DMA_x(FA_{0.83}Cs_{0.17})_{1-x}Pb(Br_{0.15}I_{0.85})_3Cl_x$ perovskite films spin-coated with various amounts of DMACl additive. All peak areas besides the orientation were divided by the peak area of the FTO peak. The full low-angle peak graph is shown in **Figure A 10**. I decided to use 30 mol% as the standard for the DMA route since, with 40 mol%, the new peak appears, and 30 mol% has the most orientated perovskite phase (see also **Figure A 11**).

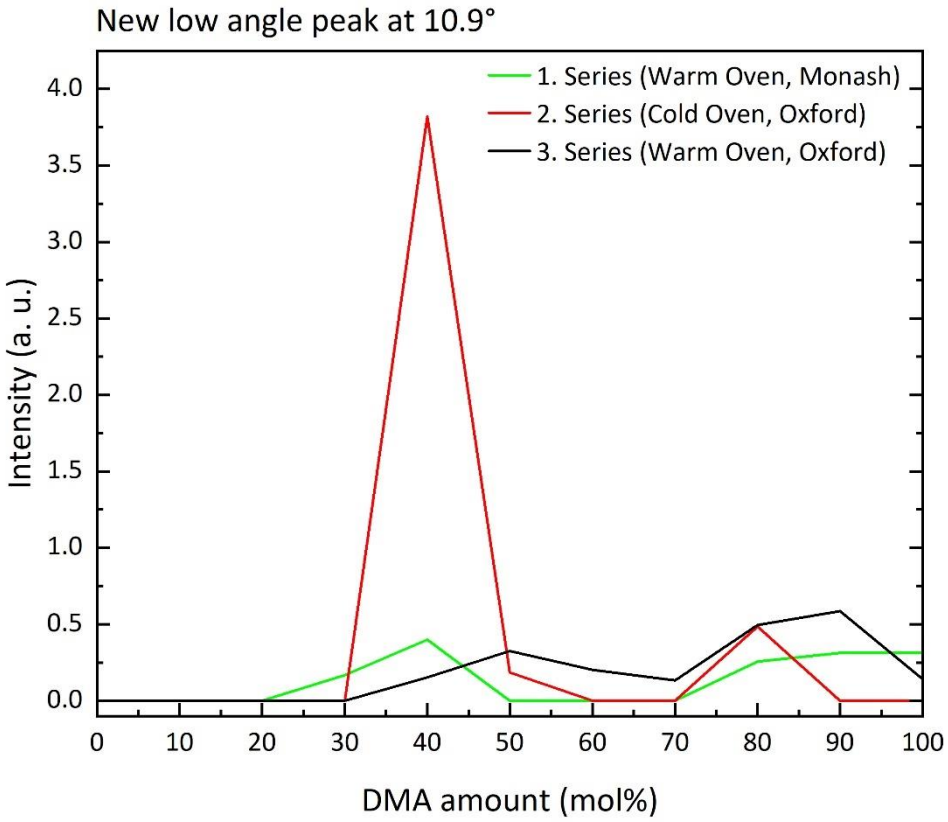

Figure A 10 XRD analysis of three series of $DMA_x(FA_{0.83}Cs_{0.17})_{1-x}Pb(Br_{0.15}I_{0.85})_3Cl_x$ perovskite films spin-coated with various amounts of DMACl additive. All peak areas were divided by the peak area of the FTO peak. This figure shows the trend for the new peak appearing in the 3 different series I measured with XRD. Surprisingly, it is not linear with the used excess DMA^+ amount and even disappears again for some higher concentrations than 40 mol%. As I also explained in the main text, I am not sure what this peak is. The best fit is to a hydrated perovskite phase, but that seems implausible given that the films are annealed at 180 °C for 1 hour, and it seems unlikely that any water is residual in the film afterwards.

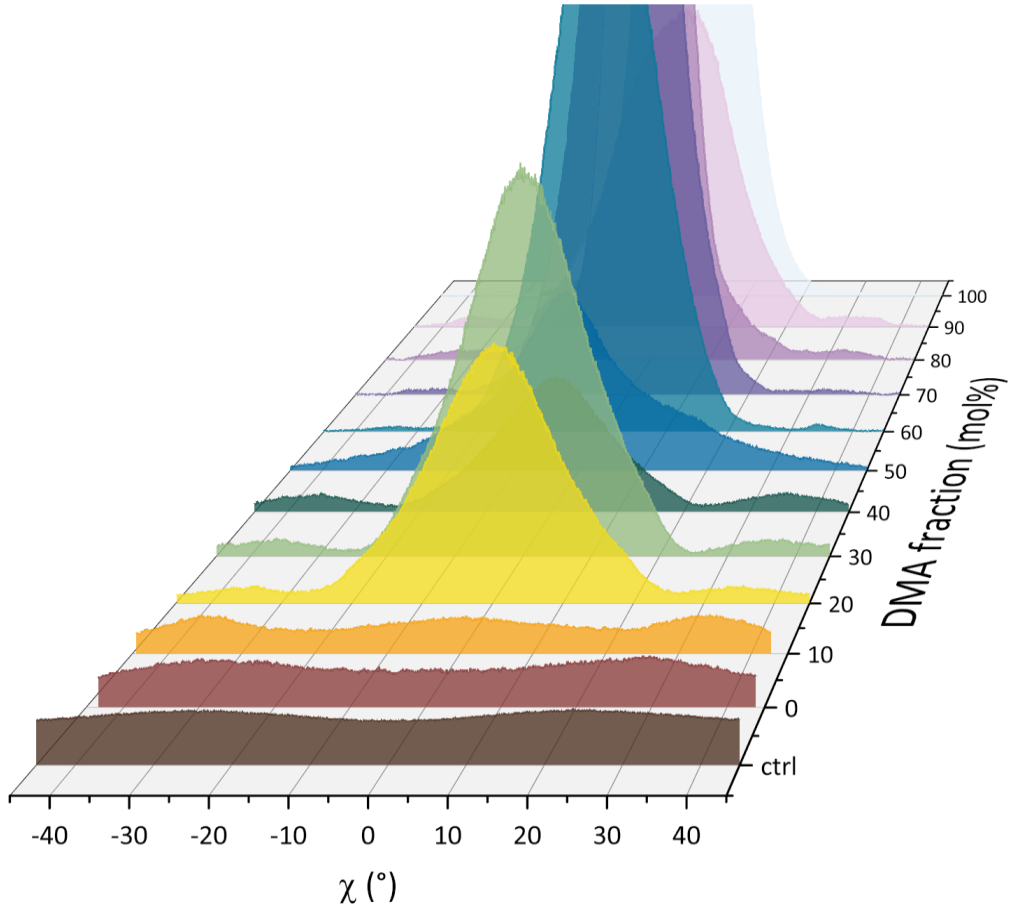

Figure A 11 A 2D XRD beta peak analysis, showing the *(100)* peak intensity as a function of the azimuth angle (χ) for a series $DMACl_x(FA_{0.83}Cs_{0.17})Pb(I_{0.8}Br_{0.2})_3$ perovskite film as shown also in **Figure 35** and **Figure 36**. Adapted from [105]. It shows that with ≥20 mol% excess DMACl the films start to become orientated and significantly increase in intensity. Especially relevant is the increased orientation with 30 mol% and that with the appearance of the new peak at 40 mol% a sudden change in orientation also happens. For 50 mol%, for example, even a new shoulder appears.

18. Appendix for 14. Stability and performance of the DMA route

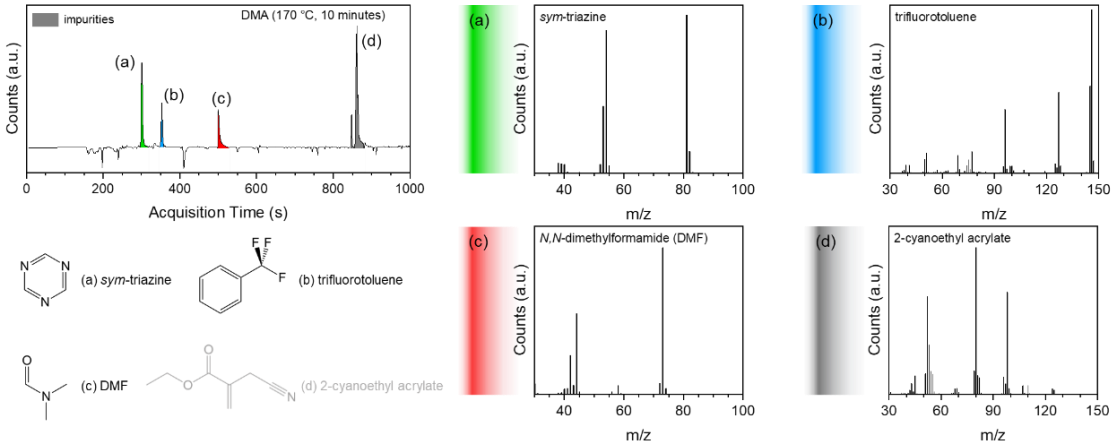

Figure A 12 TD-GC-MS for a $DMA_{0.3}FA_{0.83}Cs_{0.17}Pb(I_{0.9}Br_{0.1})_3Cl_{0.3}$ perovskite thin film annealed for 100 °C in a glovebox and 170 °C in air. 2-cyanoethyl acrylate is a common component of glues and likely a contaminant coming from the sample holders in which the samples were transported. The measured sample was less annealed than the sample in **Figure 40**, and the same residual solvents were still present. Besides the residual DMSO, identified in **Figure 39**, I find that all other solvents, DMF and the antisolvent, here TFT, are residual in the films. So even though the perovskite films were annealed at temperatures above the boiling point of DMF at 153 °C and TFT at ~102 °C, it was not possible to remove those solvents either. These results are consistent with the results from Benjamin Gallant and me[115], where we found that all perovskite films with Cs^+, Br^-, or both contain residual solvents. Even harsher annealing (up to 180 °C for one hour) did not remove the residual solvents.

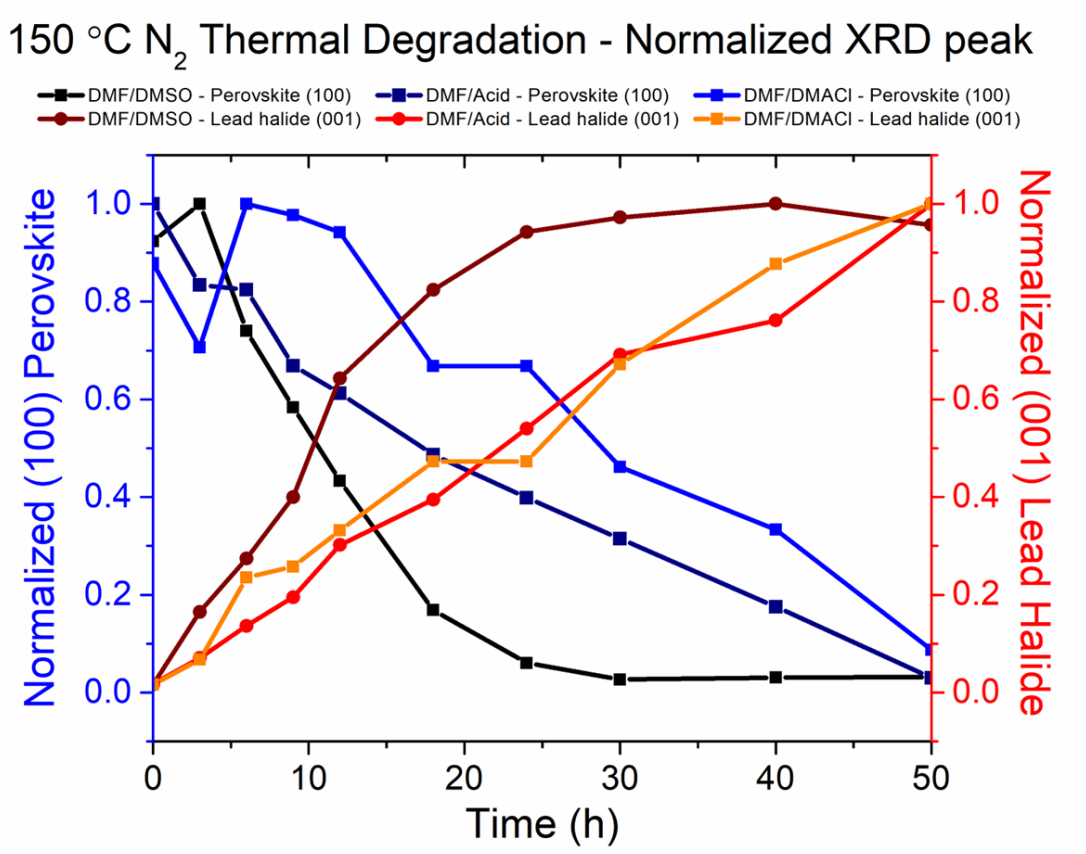

Figure A 13 Evolution of normalised intensity ratio between lead halide and perovskite XRD peak versus thermal aging time. All perovskite films were deposited on an FTO substrate and heated for up to 50 hours on a 150 °C hotplate in an N_2-filled glovebox. The three films were prepared with three different preparation methods: DMF/DMSO, DMF/acid, and DMF/DMACl. Data is taken from Figure 42 and adapted from [105]. The plot shows a detailed analysis of the stability of all three fabrication methods. Shown is the intensity of the (100) peak of the perovskite and lead halide phase as a function of aging time. This figure shows well how the newly developed DMA route improves the thermal stability of the resulting lead halide perovskite.

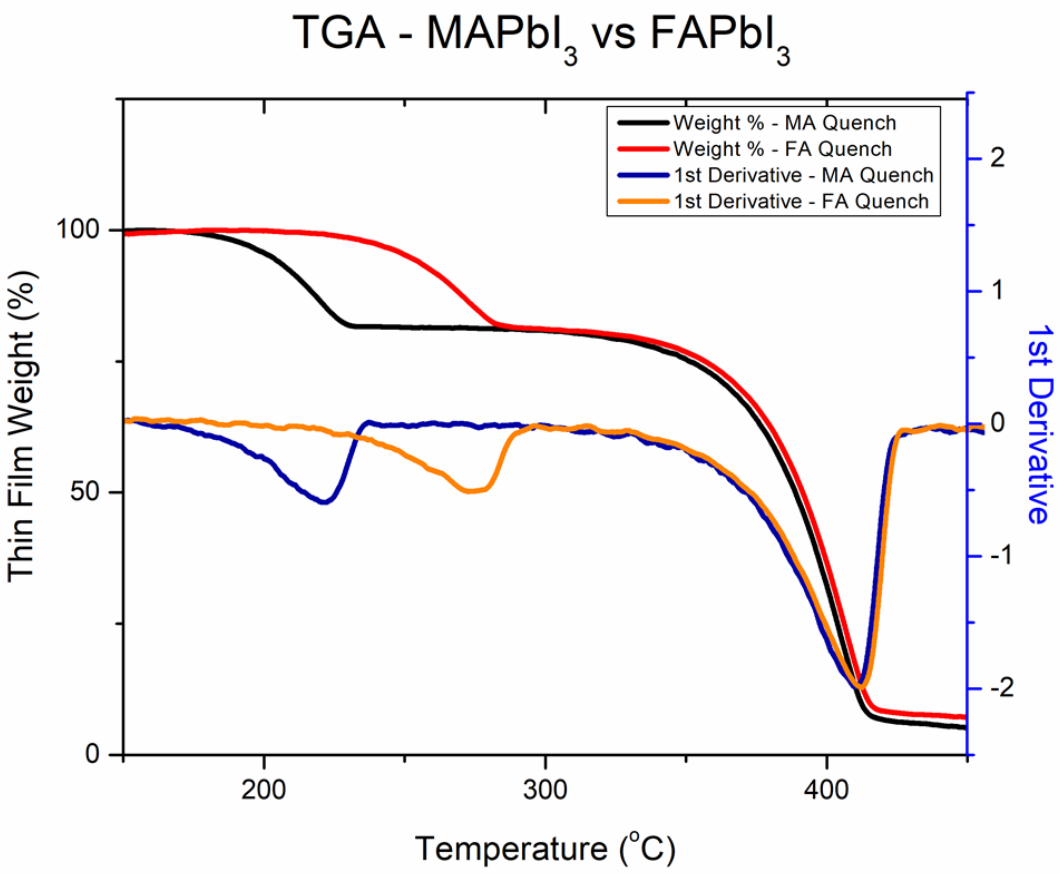

Figure A 14 TGA data of the $MAPbI_3$ compared to the $FAPbI_3$ perovskite films. TGA heating curves and the corresponding first derivative of the $MAPbI_3$ and $FAPbI_3$ perovskite films were prepared using the DMF/DMSO anti-solvent method and adapted from [105]. This figure shows the difference in thermal stability coming from different A-site cations, MA^+ and FA^+. I show this to give an estimate about what the difference we see in **Figure 43** means. Here, we see that the difference between $MAPbI_3$ and $FAPbI_3$ is 50 °C. The difference we see in **Figure 43** is 15 °C.

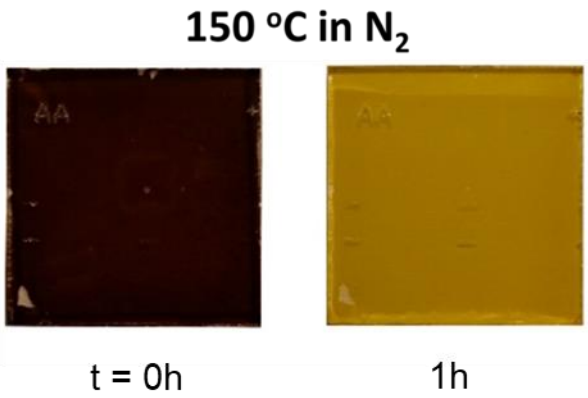

Figure A 15 Thermal stability of a $MAPb(I_{0.6}Br_{0.4})_3$ film using the DMF/DMSO anti-solvent quenching method, stressed at 150 °C in a nitrogen atmosphere. Photographs of films measured before and after thermal stressing. Adapted from [105]. This figure shows how quickly an MA-containing film degrades under heat. An examples of the stability of $MAPbI_3$ is shown in my previous publication from my master thesis.[38]

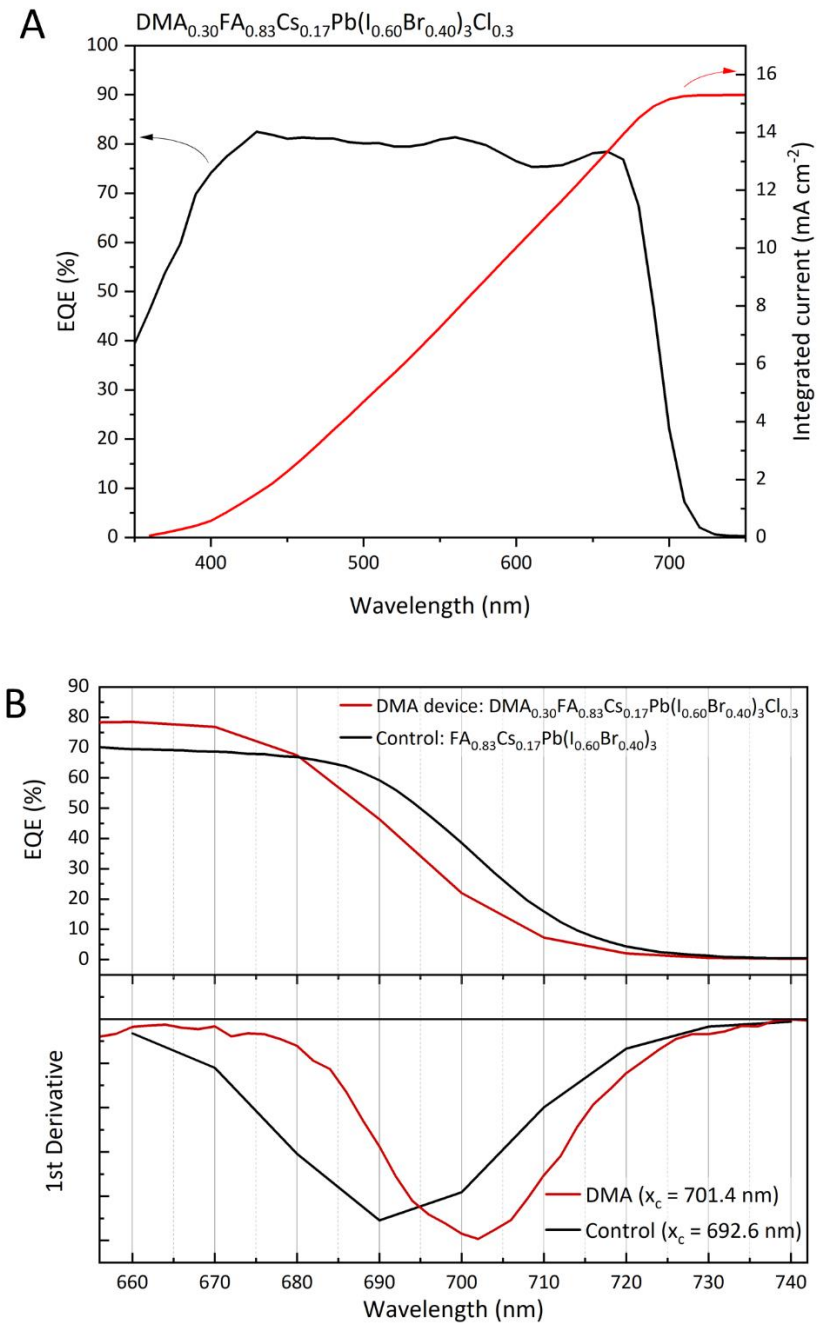

Figure A 16 (**A**) EQE of DMF/DMACl device with 40% Br and (**B**) the corresponding derivative of the EQE onset. The DMF/DMACl and DMF/DMSO device have slightly different bandgaps. The fitted peak minimum (x_c) for the derivative is 701.4 nm for the DMF/DMACl device and for the control 692.6 nm. The DMF/DMACl devices had a V_{OC} of 1.28 V, a J_{SC} of 15.51 mA cm^{-2} and a FF of 0.67. The steady-state efficiency is 13.34%. The integrated current from the EQE is 15.29 mA cm^{-2}.

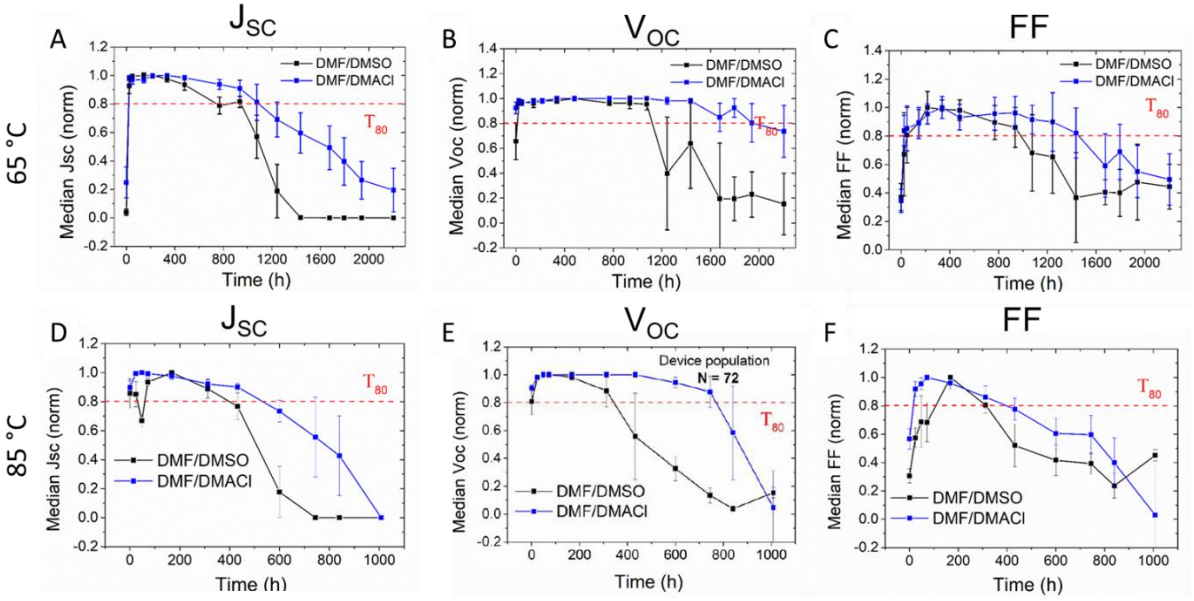

Figure A 17 Evolution of the J-V performances between DMF/DMSO and DMF/DMACl fabrication methods under full spectrum simulated AM 1.5, 76 $mWcm^{-2}$ average irradiance at V_{OC} in air without a UV filter at 85 ° C, using a Suntest XLS $^{+}$ aging box which irradiates pulsed light. All devices are encapsulated p-i-n devices comprised of an FTO/PTAA/Al_2O_3 NPs/perovskite/LiBr/C_{70}/Zr(Acac)/PEIE/Au structure. I show the J-V characteristics for 65 °C in (**A**) J_{SC}, (**B**) V_{OC} and (**C**) FF and for 85 °C in (**D**) J_{SC}, (**E**) V_{OC} and (**F**) FF. The error bars were calculated using the median absolute deviation as a measure of statistical dispersion. The Figure is adapted from [105]. The figure shows the median J-V parameter evolution of the major stability tests for the DMA route (called DMF/DMACl) and the control (DMF/DMSO) devices at 65 and 85 °C under full spectrum illumination.

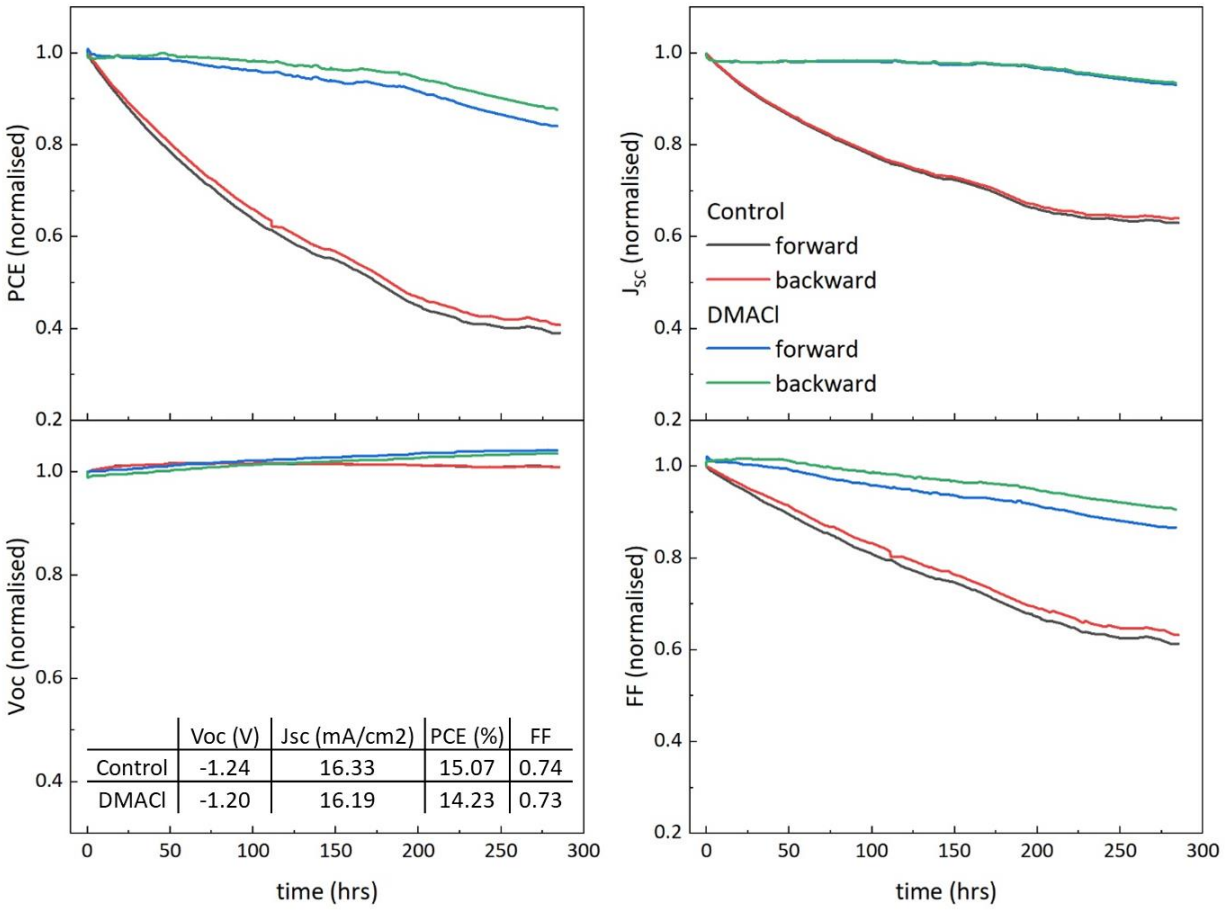

Figure A 18 Normalised J-V parameters of the DMSO and DMACl devices during aging (sequentially) in ambient (~50% RH) under light without encapsulation. Note the DC lamp was approx. ~0.75 SUN. The corresponding photocurrent maps are shown in **Figure 49** and **Figure 50**. The table shows the initial J-V parameters measured in Oxford at a calibrated sun simulator before the devices were shipped to Melbourne for the IMPS measurements. The compositions were $FA_{0.83}Cs_{0.17}Pb(I_{0.6}Br_{0.4})_3$ for the control, and for the DMACl device, it was 30mol% DMACl: $FA_{0.83}Cs_{0.17}Pb(I_{0.63}Br_{0.37})_3$. We adjusted the Br-ratio slightly to account for the slightly different bandgap of the DMF/DMACl device.

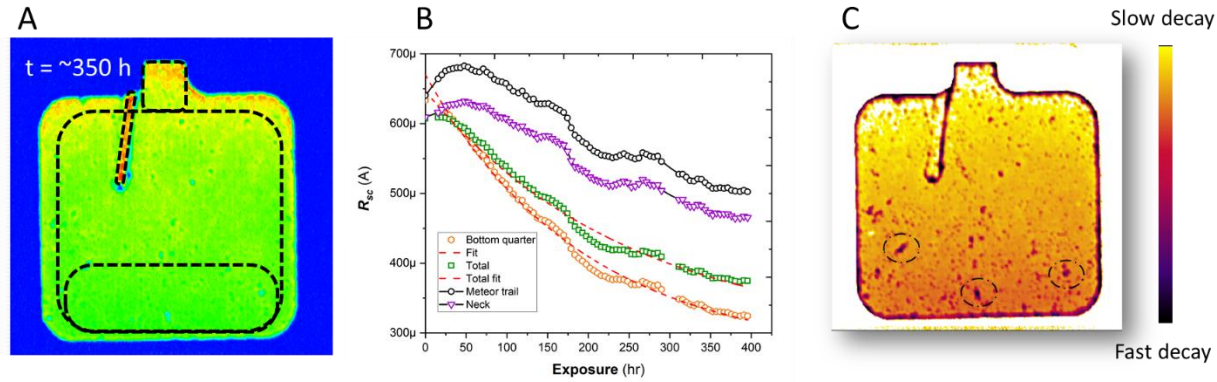

Figure A 19 IMPS mapping analysis. (**A**) A photocurrent map of the $FA_{0.83}Cs_{0.17}Pb(I_{0.6}Br_{0.4})_3$ device during the aging at around 350 h showing four different regions with striped marks. The aging was done in ambient (~50% RH) under light without encapsulation. Note that the DC lamp was approx. ~0.75 SUN. For the same regions marked in (**A**), the photocurrent decay curves are shown in (**B**). All points show an exponential decay. The exponential decay was used to fit each pixel and reconstruct a map of the pixel, indicating areas of fast and slow decay, as shown in (**C**).

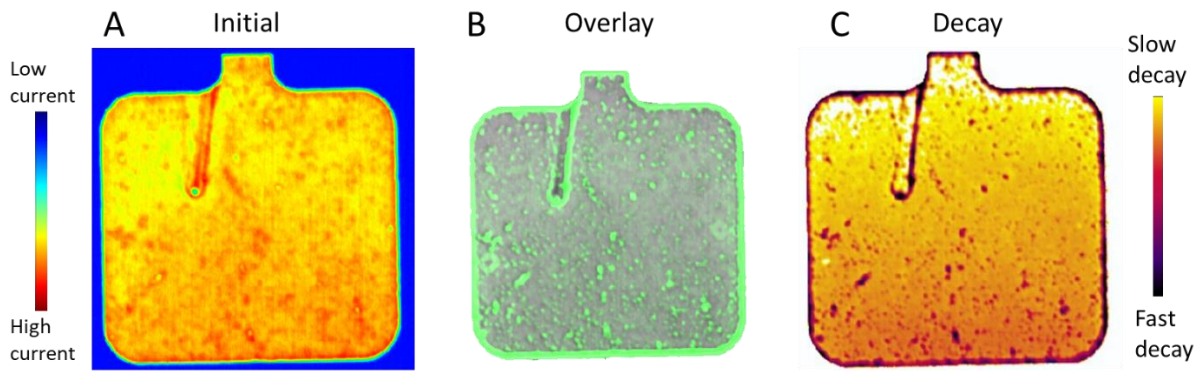

Figure A 20 IMPS maps of the control $FA_{0.83}Cs_{0.17}Pb(I_{0.6}Br_{0.4})_3$ at the beginning of the aging (t=0) (**A**) and overlay (**B**) of the initial (in grey) and the decay curves (in green) which is also shown in (**C**) as a comparison (see for further explanation **Figure A 20**). The figure shows that areas of initial photocurrent heterogeneity correlate with regions which degrade faster than homogenous regions.

19. Appendix for 15. A new dynamic passivation called HUBLA

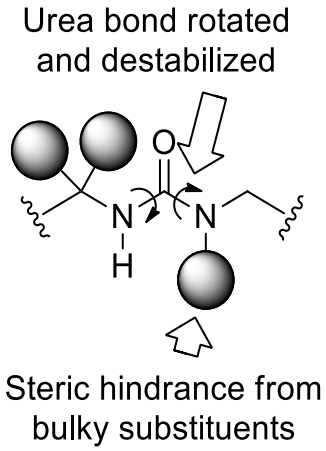

Figure A 21 Hindered urea/thiocarbamate bond (HUB) is destabilized by bulky substituents, which induces bond rotation and a decrease in the conjugation effect. The amide bond (-N(R)C(O)-) is generally very stable because of its conjugation between the long electron pair on the nitrogen atom and the π-electrons on the carbonyl p-orbital. The steric hindrance by adding bulky groups can disturb orbital co-planarity and diminish conjugation effect, thus weakening carbonyl-amine interaction.[118] Hence, the HUB can dissociate into amine and isocyanate.

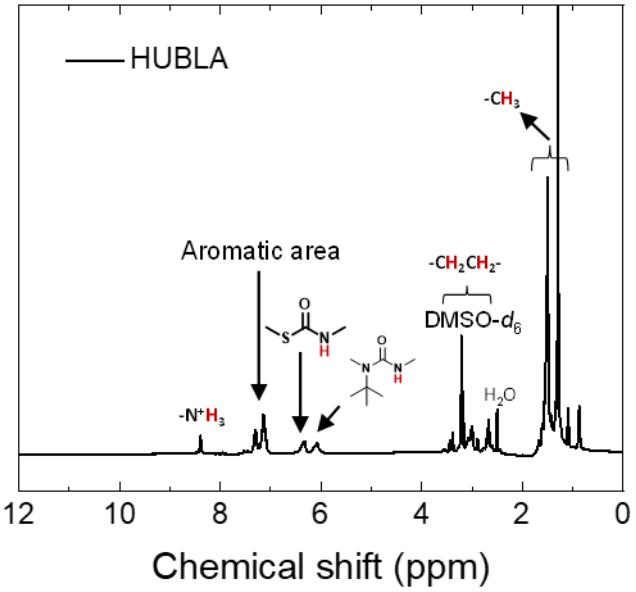

Figure A 22 Characterization of HUBLA. ^{1}H NMR (400MHz, DMSO-d_6): δ (ppm) = 8.39 (s, -N^{+}H$_3$), 7.31 and 7.14 (m, benzene ring), 6.33 (s, -SC(O)NH-), 6.07 (s, -((CH$_3$)C)NC(O)NH-), 2.4-3.4 (m, -CH$_2$CH$_2$-), 1.50 and 1.30 (s, -CH$_3$). The ^{1}H NMR verifies the HUBLA structure. **ATR-IR**: 3285 and 1555 cm^{-1} (N-H); 2979 and 2868 cm^{-1} (C-H); 1649 cm^{-1} (C=O); 1487 cm^{-1} (C-N); 900 cm^{-1} (C-S). **ESI-TOF MS**: m/z = 851.41, calcd. 851.48 [M^{+}] for $C_{42}H_{72}ClN_8O_4S_2$.

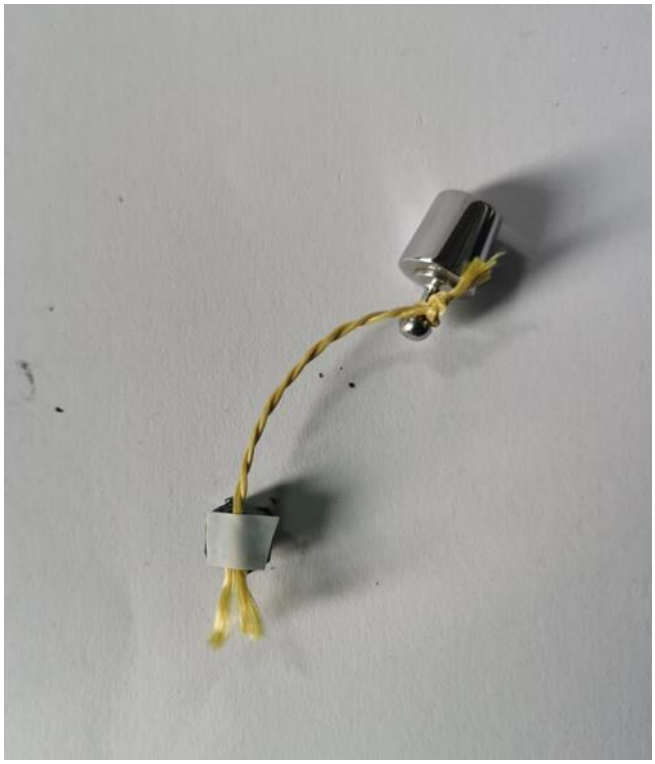

Figure A 23 Five-gram weight was tied with yellow rope and stuck at the bottom of bonded crystals using white tap. This picture shows how the weight was mounted onto the single crystals.

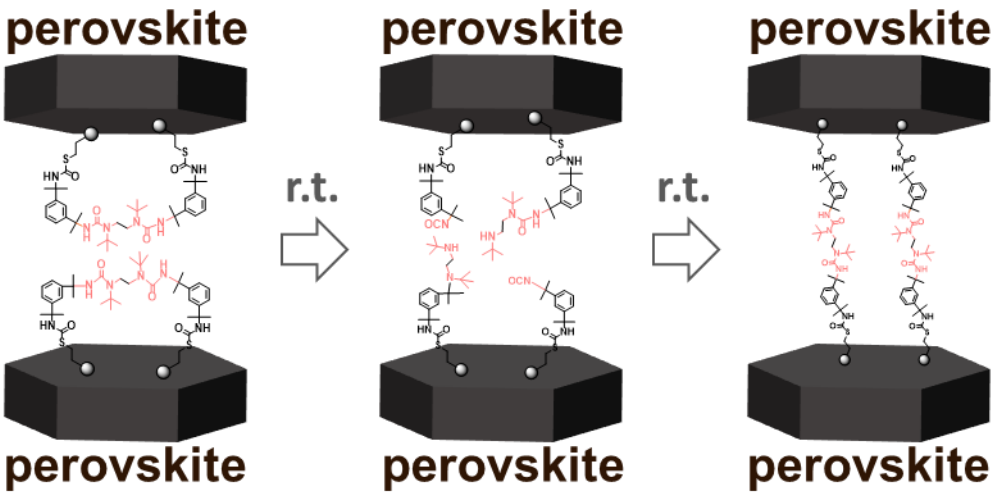

Figure A 24 Graphical explanation of how the cross-link mechanism of HUBLA between two $FAPbI_3$ crystals works. Generally, two crystals could not be bonded together because there is no interaction or bonds at the interface. In contrast, if the surfaces of perovskite crystals are coated with HUBLA, the HUB can dissociate and associate at the interface, part of the HUBs can induce the interface cross-link between two crystals (the white ball represents $-N^+H_3$).

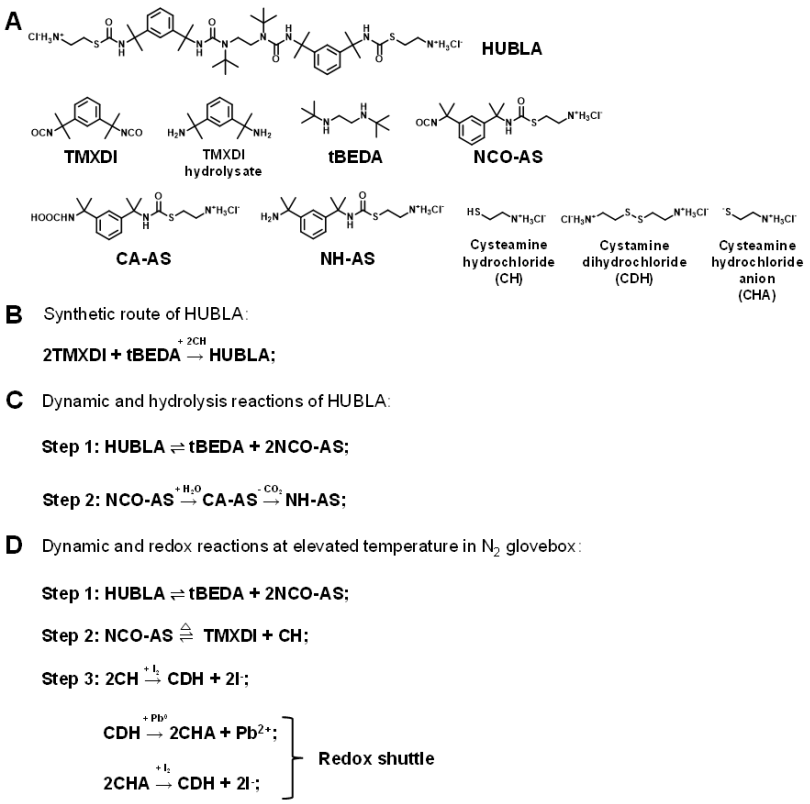

Figure A 25 Chemicals and reactions that are mentioned in this study. (A) All the chemical structures including HUBLA, TMXDI, TMXDI hydrolysate, tBEDA, NCO-terminated ammonium salt (NCO-AS), carbamic acid group (-N(H)C(O)OH in NHCOOH-terminated ammonium salt (CA-AS)), NH_2-terminated ammonium salt (NH-AS), cysteamine hydrochloride (CH), cystamine dihydrochloride (CDH), and cysteamine hydrochloride anion (CHA). (B) Synthetic route of HUBLA. (C) Dynamic and hydrolysis reactions of HUBLA at room temperature. In the step 1, HUBLA reversibly dissociates into tBEDA and NCO-AS. In the step 2, NCO-AS reacts with H_2O to produce CA-AS, and quickly decomposes to NH-AS and releases CO_2. (D) Dynamic and redox reactions at elevated temperature in N_2. In the step 1, HUBLA reversibly dissociates into tBEDA and NCO-AS. In the step 2, NCO-AS reversibly dissociates into TMXDI and CH at elevated temperature. In the step 3, CH reacts with I_2 to produce CDH and I^-. CDH reacts with Pb^0 to produce CHA and Pb^{2+}. CHA reacts with I_2 to produce CDH and I^-. CDH and CHA form redox shuttle reaction.

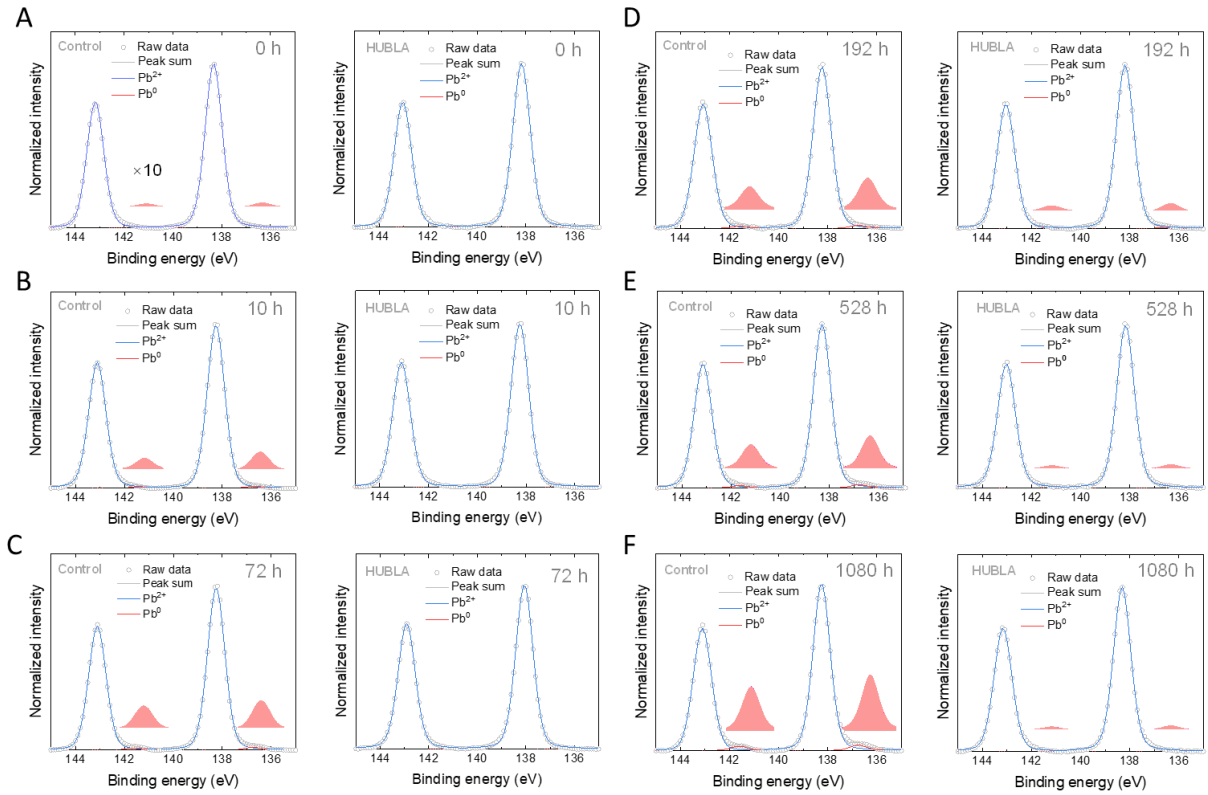

Figure A 26 Pb 4f XPS spectra of $FAPbI_3$ film and perovskite/HUBLA film aged at 85 ℃ in N_2 after (**A**) 0, (**B**) 10, (**C**) 72, (**D**) 192, (**E**) 528, and (**F**) 1080 hours, respectively. The intensity of the Pb^0 components is enlarged for the red peaks by 10 times. The purpose of this figure is to show the dynamic passivation ability of HUBLA and how it prevents the formation of Pb^0.

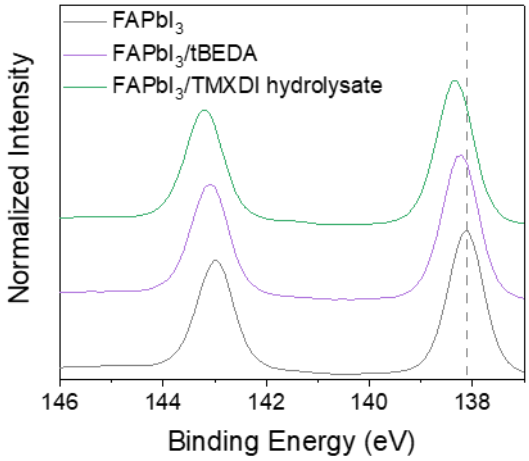

Figure A 27 Pb 4*f* XPS spectra of perovskite, perovskite/TMXDI hydrolysate, and perovskite/ tBEDA films. Identification of the expected shift of the Pb 4f XPS peaks with the different components of HUBLA. It is used to interpret the aging data.

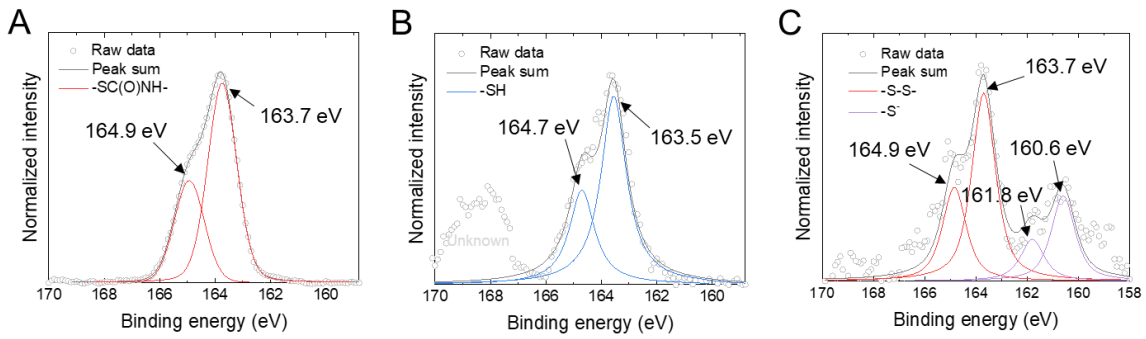

Figure A 28 S 2*p* XPS of (**A**) pristine HUBLA, (**B**) $FAPbI_3$/CH and (**C**) $FAPbI_3$/CDH films. This figure is used for the identification of the S 2p XPS spectrum.

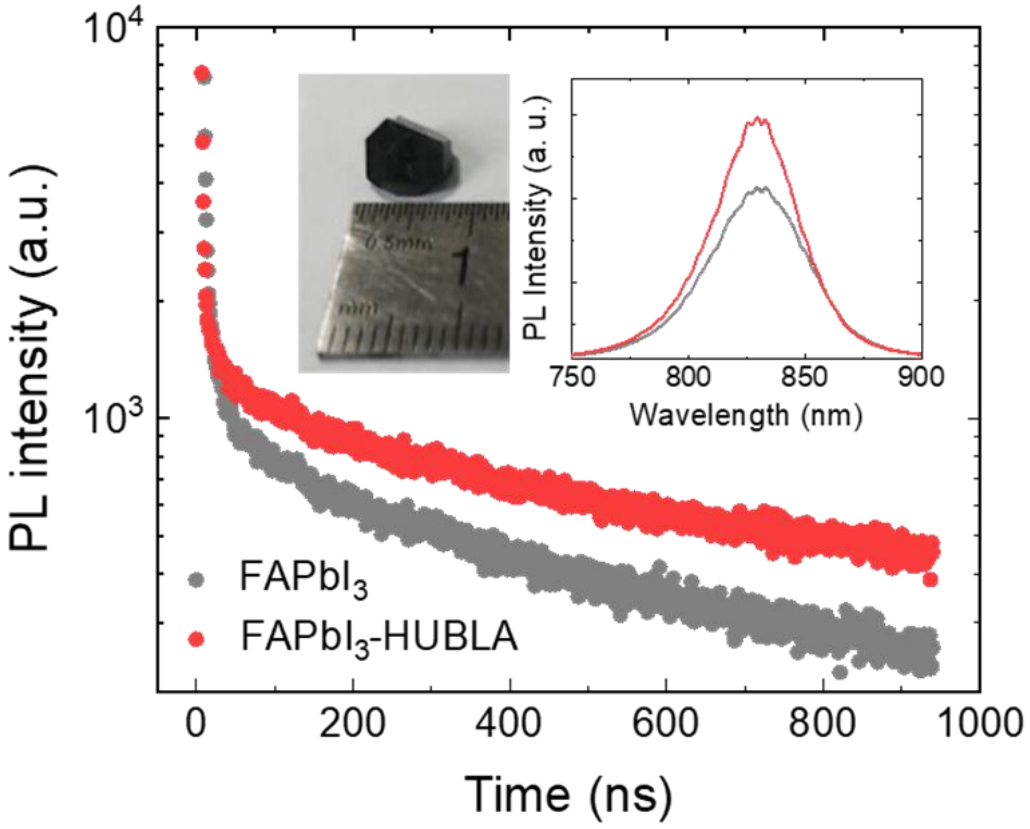

Figure A 29 Steady-state PL and TRPL of pristine and HUBLA-coated perovskite crystals. Insert figure is the steady-state PL and photograph of the $FAPbI_3$ crystal. Improved optoelectronic properties of the single crystals coated with HUBLA.

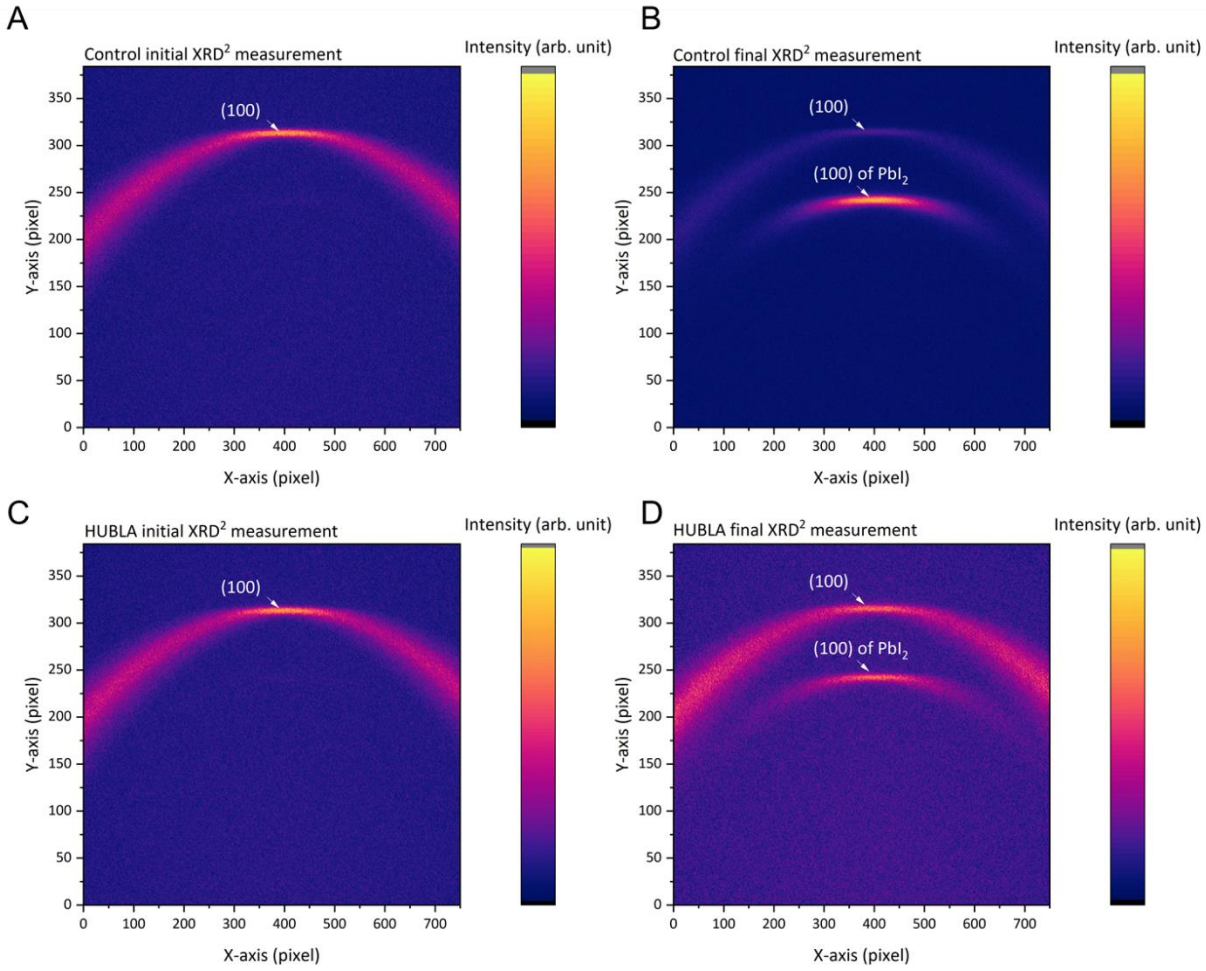

Figure A 30 XRD^2 measurements of the control and HUBLA films before and after 25.5 hours of aging at 85 °C in ambient air (~30% RH). (**A**, **B**) A $FA_{0.83}Cs_{0.17}Pb(I_{0.9}Br_{0.1})_3$ control film and (**C**, **D**) one treated with HUBLA. For **Figure 58A** and **B**, I measured roughly every minute an XRD^2 measurement and sum along the conic section of each peak to obtain a 1D XRD for each minute. **Figure A 31** shows the change of the conic section for the PbX_2 peak and the change in the ratio of the *(100)* and PbX_2 peak.

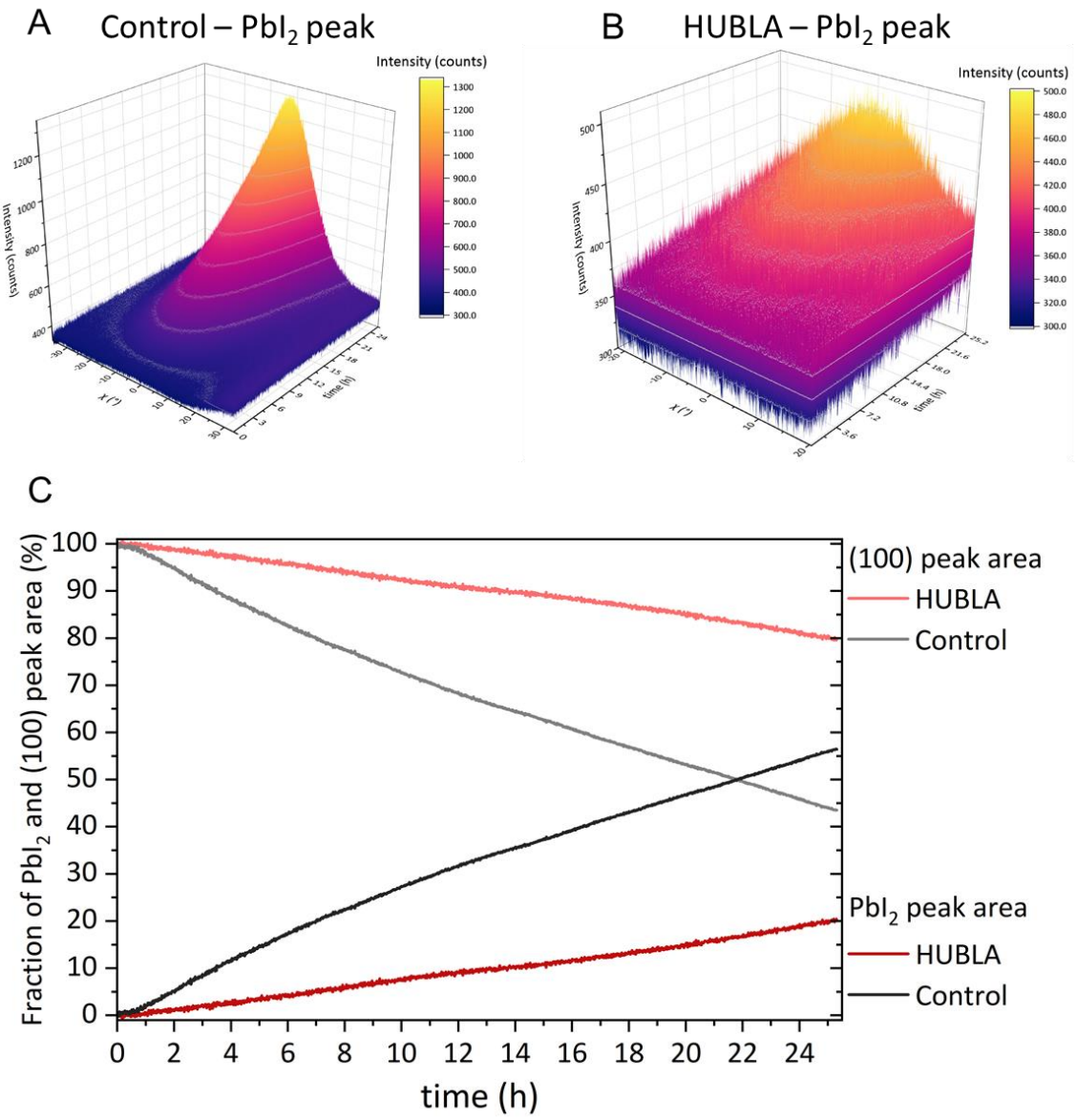

Figure A 31 Change of the PbI_2 peak along the azimuthal angle χ for (**A**) the control and (**B**) HUBLA films throughout the aging at 85 °C in ambient air (~30% RH). (**C**) I show the ratio of the integrated peak area of the *(100)* and PbI_2 peak after I subtracted the background of each peak. The measurements correspond to **Figure 58A** and **B** and **Figure A 30**.

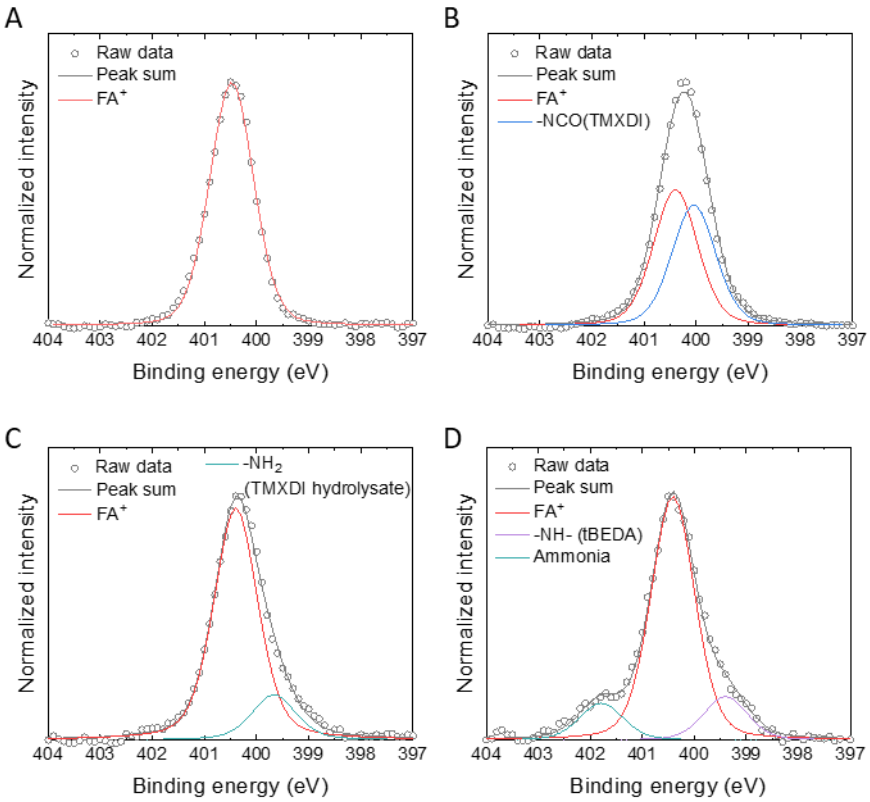

Figure A 32 N 1*s* XPS spectra of (**A**), perovskite film showing a N 1*s* component at ~400.5 eV. (**B**) Perovskite /TMXDI film showing two N 1*s* components at ~400.4 and ~400.0 eV that could be attributed to FA^+ and isocyanate (-NCO)[210], respectively. (**C**) Perovskite/TMXDI hydrolysate showing two N 1*s* components at ~400.4 and ~399.7 eV that could be attributed to FA^+ and primary amine ($-NH_2$)[211], respectively. (**D**) Perovskite/tBEDA films showing three N 1*s* components at ~401.8, ~400.4 and ~399.4 eV that could be attributed to ammonia, FA^+, and secondary amine (-NH-)[211], respectively.

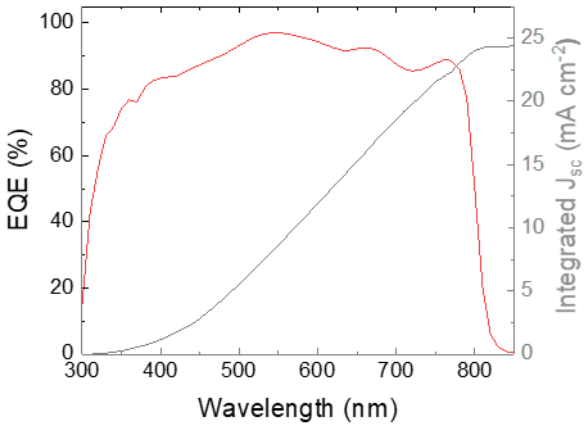

Figure A 33 EQE and integrated current of an n-i-p device with HUBLA.

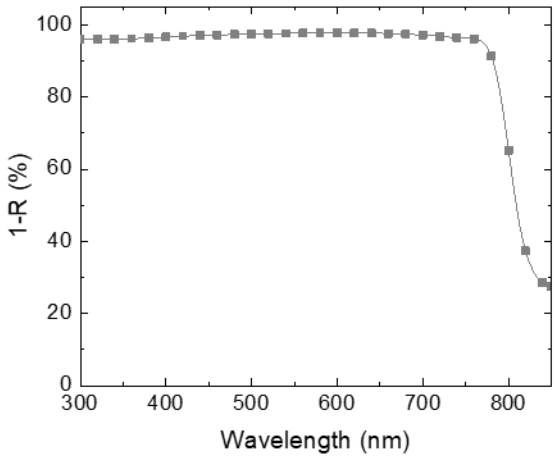

Figure A 34 Total absorbance of Glass/ITO/perovskite.

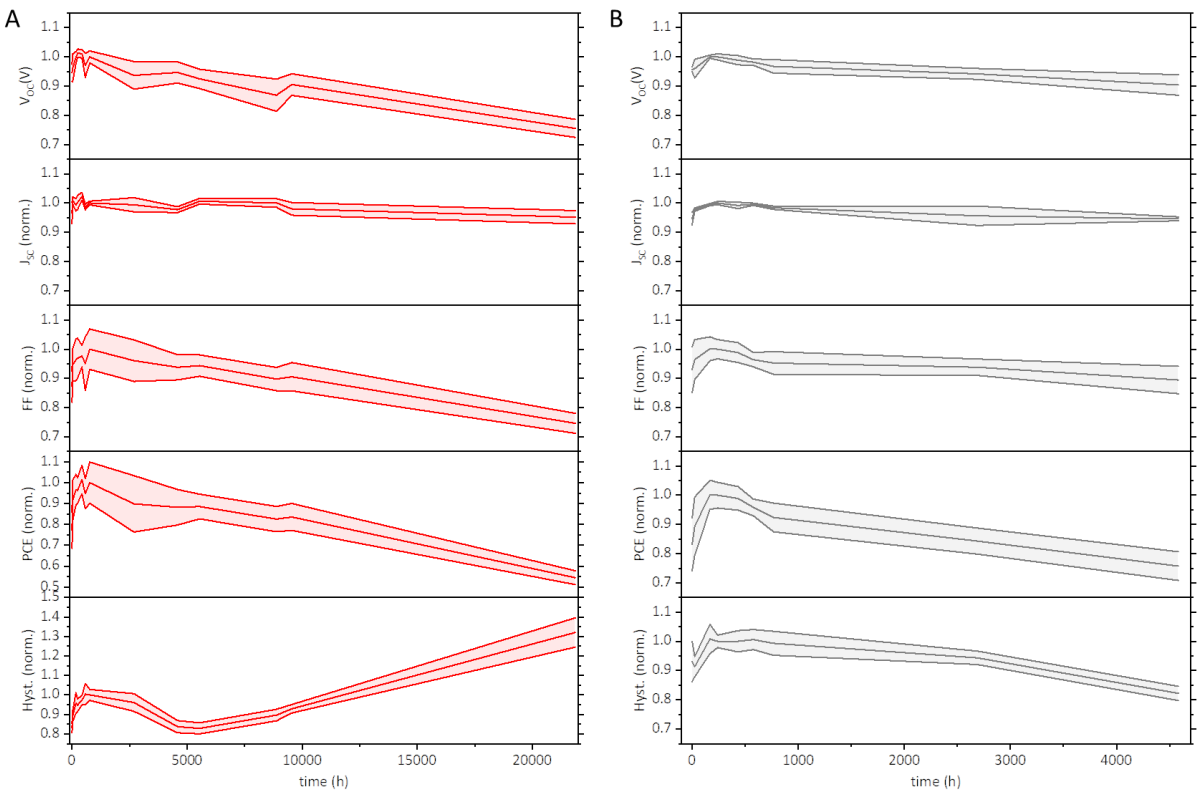

Figure A 35 Median PV parameters of (**A**) HUBLA and (**B**) Control device from **Figure 66.** The upper and lower limit are the median absolute deviation (MAD). The PCE is from the J-V scan from short-circuit to open-circuit. FF, J_{SC} and V_{OC} are from the same J-V scan. This is the corresponding J-V data for the devices which are aged at 85 °C in N_2, as shown in **Figure 66**.

20. References

(1) Lee, H.; Calvin, K.; Dasgupta, D.; Krinner, G.; Mukherji, A.; Thorne, P.; Trisos, C.; Romero, J.; Aldunce, P.; Barret, K. IPCC, 2023: Climate Change 2023: Synthesis Report, Summary for Policymakers. Contribution of Working Groups I, II and III to the Sixth Assessment Report of the Intergovernmental Panel on Climate Change [Core Writing Team, H. Lee and J. Romero (Eds.)]. IPC. **2023**.

(2) Goldschmidt, J. C.; Wagner, L.; Pietzcker, R.; Friedrich, L. Technological Learning for Resource Efficient Terawatt Scale Photovoltaics. *Energy Environ. Sci.* **2021**, *14* (10), 5147–5160. https://doi.org/10.1039/D1EE02497C.

(3) Tian, X.; Stranks, S. D.; You, F. Life Cycle Assessment of Recycling Strategies for Perovskite Photovoltaic Modules. *Nat. Sustain.* **2021**, *4* (9), 821–829. https://doi.org/10.1038/s41893-021-00737-z.

(4) Philippe Holzhey, Michael Prettl, Silvia Collavini, Nathan L. Chang, M. S. Towards Commercialisation with Lightweight, Flexible Perovskite Solar Cells for Residential Photovoltaics. *Joule* **2023**.

(5) Nelson, J. The Phisics of Solar Cells. *Prop. Semicond. Mater.* **2003**, 384. https://doi.org/10.1142/9781848161269_0001.

(6) Lafontaine, M. de; Forcade, G.; Wilson, P.; Patel, J.; Ellis, B.; Fritzsche, H.; Suppiah, S.; Cook, J. P. D.; Valdivia, C. E.; Hinzer, K. GaAs Betavoltaic Cell Modeling for Light to Medium Element Radiation Conversion into Electrical Power. In *2023 IEEE 50th Photovoltaic Specialists Conference (PVSC)*; 2023; p 1. https://doi.org/10.1109/PVSC48320.2023.10359702.

(7) Chapin, D. M.; Fuller, C. S.; Pearson, G. L. A New Silicon P-n Junction Photocell for Converting Solar Radiation into Electrical Power. *J. Appl. Phys.* **2004**, *25* (5), 676–677. https://doi.org/10.1063/1.1721711.

(8) Robert A. Rohde. *Solar spectrum from Wikipedia*. https://commons.wikimedia.org/wiki/File:Solar_spectrum_en.svg.

(9) Bailey, S. G.; Raffaelle, R.; Emery, K. Space and Terrestrial Photovoltaics: Synergy and Diversity. *Prog. Photovoltaics Res. Appl.* **2002**, *10* (6), 399–406. https://doi.org/doi:10.1002/pip.446.

(10) NASA. *International Space Station*. https://www.nasa.gov/international-space-station/space-station-gallery/.

(11) Sandberg, O. J.; Kurpiers, J.; Stolterfoht, M.; Neher, D.; Meredith, P.; Shoaee, S.; Armin, A. On the Question of the Need for a Built-In Potential in Perovskite Solar Cells. *Adv. Mater. Interfaces* **2020**, *7* (10), 2000041. https://doi.org/https://doi.org/10.1002/admi.202000041.

(12) Stranks, S. D.; Eperon, G. E.; Grancini, G.; Menelaou, C.; Alcocer, M. J. P.; Leijtens, T.; Herz, L. M.; Petrozza, A.; Snaith, H. J. Electron-Hole Diffusion Lengths Exceeding 1 Micrometer in an Organometal Trihalide Perovskite Absorber. *Science (80-.).* **2013**. https://doi.org/10.1126/science.1243982.

(13) Kirchartz, T.; Bisquert, J.; Mora-Sero, I.; Garcia-Belmonte, G. Classification of Solar Cells

According to Mechanisms of Charge Separation and Charge Collection. *Phys. Chem. Chem. Phys.* **2015**, *17* (6), 4007–4014. https://doi.org/10.1039/C4CP05174B.

(14) *https://www.pveducation.org/, accessed 09.01.2024*.

(15) Zhou, Y.; Fei, C.; Uddin, M. A.; Zhao, L.; Ni, Z.; Huang, J. Self-Powered Perovskite Photon-Counting Detectors. *Nature* **2023**, *616* (7958), 712–718. https://doi.org/10.1038/s41586-023-05847-6.

(16) Tan, Z.-K.; Moghaddam, R. S.; Lai, M. L.; Docampo, P.; Higler, R.; Deschler, F.; Price, M.; Sadhanala, A.; Pazos, L. M.; Credgington, D.; Hanusch, F.; Bein, T.; Snaith, H. J.; Friend, R. H. Bright Light-Emitting Diodes Based on Organometal Halide Perovskite. *Nat Nano* **2014**, *9* (9), 687–692. https://doi.org/10.1038/nnano.2014.149.

(17) Lee, M. M.; Teuscher, J.; Miyasaka, T.; Murakami, T. N.; Snaith, H. J. Efficient Hybrid Solar Cells Based on Meso-Superstructured Organometal Halide Perovskites. *Science (80-.).* **2012**. https://doi.org/10.1126/science.1228604.

(18) Kim, H.-S.; Lee, C.-R.; Im, J.-H.; Lee, K.-B.; Moehl, T.; Marchioro, A.; Moon, S.-J.; Humphry-Baker, R.; Yum, J.-H.; Moser, J. E.; Grätzel, M.; Park, N.-G. Lead Iodide Perovskite Sensitized All-Solid-State Submicron Thin Film Mesoscopic Solar Cell with Efficiency Exceeding 9%. *Sci. Rep.* **2012**, *2*. https://doi.org/10.1038/srep00591.

(19) Kojima, A.; Teshima, K.; Miyasaka, T.; Shirai, Y. Novel Photoelectrochemical Cell with Mesoscopic Electrodes Sensitized by Lead-Halide Compounds (2). In *ECS Meeting Abstracts*; IOP Publishing, 2006; p 397.

(20) Kojima, A.; Teshima, K.; Shirai, Y.; Miyasaka, T. Organometal Halide Perovskites as Visible-Light Sensitizers for Photovoltaic Cells. *J. Am. Chem. Soc.* **2009**, *131* (17), 6050–6051. https://doi.org/10.1021/ja809598r.

(21) Webb, T.; Sweeney, S. J.; Zhang, W. Device Architecture Engineering: Progress toward Next Generation Perovskite Solar Cells. *Adv. Funct. Mater.* **2021**, *31* (35), 2103121. https://doi.org/https://doi.org/10.1002/adfm.202103121.

(22) Kim, H. S.; Lee, C. R.; Im, J. H.; Lee, K. B.; Moehl, T.; Marchioro, A.; Moon, S. J.; Humphry-Baker, R.; Yum, J. H.; Moser, J. E.; Grätzel, M.; Park, N. G. Lead Iodide Perovskite Sensitized All-Solid-State Submicron Thin Film Mesoscopic Solar Cell with Efficiency Exceeding 9%. *Sci. Rep.* **2012**, *2* (1), 1–7. https://doi.org/10.1038/srep00591.

(23) Chung, I.; Lee, B.; He, J.; Chang, R. P. H.; Kanatzidis, M. G. All-Solid-State Dye-Sensitized Solar Cells with High Efficiency. *Nature* **2012**, *485*, 486.

(24) Frost, J. M.; Butler, K. T.; Brivio, F.; Hendon, C. H.; Schilfgaarde, M. Van; Walsh, A.; Van Schilfgaarde, M.; Walsh, A. Atomistic Origins of High-Performance in Hybrid Halide Perovskite Solar Cells. *Nano Lett.* **2014**, *14* (5), 2584–2590. https://doi.org/10.1021/nl500390f.

(25) NREL National Renewable Energy Laboratory. *Best Research-Cell Efficiency Chart | Photovoltaic Research | NREL*.

(26) Xiao, M.; Huang, F.; Huang, W.; Dkhissi, Y.; Zhu, Y.; Etheridge, J.; Gray-Weale, A.; Bach, U.; Cheng, Y.-B.; Spiccia, L. A Fast Deposition-Crystallization Procedure for Highly Efficient Lead Iodide Perovskite Thin-Film Solar Cells. *Angew. Chemie Int. Ed.* **2014**, *53* (37), 9898–9903. https://doi.org/https://doi.org/10.1002/anie.201405334.

(27) Jeon, N. J.; Noh, J. H.; Kim, Y. C.; Yang, W. S.; Ryu, S.; Seok, S. Il. Solvent Engineering for High-Performance Inorganic-Organic Hybrid Perovskite Solar Cells. *Nat. Mater.* **2014**, *13* (9), 897–903. https://doi.org/10.1038/nmat4014.

(28) Jeon, N. J.; Noh, J. H.; Yang, W. S.; Kim, Y. C.; Ryu, S.; Seo, J.; Seok, S. Il. Compositional Engineering of Perovskite Materials for High-Performance Solar Cells. *Nature* **2015**, *517* (7535), 476–480. https://doi.org/10.1038/nature14133.

(29) Saliba, M.; Matsui, T.; Seo, J.-Y.; Domanski, K.; Correa-Baena, J.-P.; Nazeeruddin, M. K.; Zakeeruddin, S. M.; Tress, W.; Abate, A.; Hagfeldt, A.; Grätzel, M. Cesium-Containing Triple Cation Perovskite Solar Cells: Improved Stability, Reproducibility and High Efficiency. *Energy Environ. Sci.* **2016**, *9* (6), 1989–1997. https://doi.org/10.1039/C5EE03874J.

(30) Jiang, Q.; Zhao, Y.; Zhang, X.; Yang, X.; Chen, Y.; Chu, Z.; Ye, Q.; Li, X.; Yin, Z.; You, J. Surface Passivation of Perovskite Film for Efficient Solar Cells. *Nat. Photonics* **2019**. https://doi.org/10.1038/s41566-019-0398-2.

(31) Yoo, J. J.; Seo, G.; Chua, M. R.; Park, T. G.; Lu, Y.; Rotermund, F.; Kim, Y.-K.; Moon, C. S.; Jeon, N. J.; Correa-Baena, J.-P.; Bulović, V.; Shin, S. S.; Bawendi, M. G.; Seo, J. Efficient Perovskite Solar Cells via Improved Carrier Management. *Nature* **2021**, *590* (7847), 587–593. https://doi.org/10.1038/s41586-021-03285-w.

(32) Al-Ashouri, A.; Köhnen, E.; Li, B.; Magomedov, A.; Hempel, H.; Caprioglio, P.; Márquez, J. A.; Morales Vilches, A. B.; Kasparavicius, E.; Smith, J. A.; Phung, N.; Menzel, D.; Grischek, M.; Kegelmann, L.; Skroblin, D.; Gollwitzer, C.; Malinauskas, T.; Jošt, M.; Matič, G.; Rech, B.; Schlatmann, R.; Topič, M.; Korte, L.; Abate, A.; Stannowski, B.; Neher, D.; Stolterfoht, M.; Unold, T.; Getautis, V.; Albrecht, S. Monolithic Perovskite/Silicon Tandem Solar Cell with >29% Efficiency by Enhanced Hole Extraction. *Science (80-.).* **2020**, *370* (6522), 1300 LP – 1309. https://doi.org/10.1126/science.abd4016.

(33) Meng, L.; You, J.; Yang, Y. Addressing the Stability Issue of Perovskite Solar Cells for Commercial Applications. *Nature Communications*. 2018. https://doi.org/10.1038/s41467-018-07255-1.

(34) Feldman, D.; Ramasamy, V.; Fu, R.; Ramdas, A.; Desai, J.; Margolis, R. *US Solar Photovoltaic System and Energy Storage Cost Benchmark: Q1 2020 (Preprint July 2020)*; National Renewable Energy Lab.(NREL), Golden, CO (United States), 2021.

(35) Song, Z.; McElvany, C. L.; Phillips, A. B.; Celik, I.; Krantz, P. W.; Watthage, S. C.; Liyanage, G. K.; Apul, D.; Heben, M. J. A Technoeconomic Analysis of Perovskite Solar Module Manufacturing with Low-Cost Materials and Techniques. *Energy Environ. Sci.* **2017**, *10* (6), 1297–1305. https://doi.org/10.1039/C7EE00757D.

(36) Chang, N. L.; Zheng, J.; Wu, Y.; Shen, H.; Qi, F.; Catchpole, K.; Ho-Baillie, A.; Egan, R. J. A Bottom-up Cost Analysis of Silicon–Perovskite Tandem Photovoltaics. *Prog. Photovoltaics Res. Appl.* **2021**, *29* (3), 401–413. https://doi.org/https://doi.org/10.1002/pip.3354.

(37) Li, Z.; Zhao, Y.; Wang, X.; Sun, Y.; Zhao, Z.; Li, Y.; Zhou, H.; Chen, Q. Cost Analysis of Perovskite Tandem Photovoltaics. *Joule*. 2018. https://doi.org/10.1016/j.joule.2018.05.001.

(38) Holzhey, P.; Yadav, P.; Turren-Cruz, S. H.; Ummadisingu, A.; Grätzel, M.; Hagfeldt, A.;

Saliba, M. A Chain Is as Strong as Its Weakest Link – Stability Study of MAPbI3 under Light and Temperature. *Mater. Today* **2019**. https://doi.org/10.1016/j.mattod.2018.10.017.

(39) Holzhey, P.; Saliba, M. A Full Overview of International Standards Assessing the Long-Term Stability of Perovskite Solar Cells. *J. Mater. Chem. A* **2018**, *6* (44), 21794–21808. https://doi.org/10.1039/C8TA06950F.

(40) Wang, Z.; Shi, Z.; Li, T.; Chen, Y.; Huang, W. Stability of Perovskite Solar Cells: A Prospective on the Substitution of the A Cation and X Anion. *Angew. Chemie Int. Ed.* **2016**, 2–25. https://doi.org/10.1002/anie.201603694.

(41) Turren-Cruz, S. H.; Hagfeldt, A.; Saliba, M. Methylammonium-Free, High-Performance, and Stable Perovskite Solar Cells on a Planar Architecture. *Science (80-.).* **2018**. https://doi.org/10.1126/science.aat3583.

(42) Schutt, K.; Nayak, P. K.; Ramadan, A. J.; Wenger, B.; Lin, Y.-H.; Snaith, H. J. Overcoming Zinc Oxide Interface Instability with a Methylammonium-Free Perovskite for High-Performance Solar Cells. *Adv. Funct. Mater.* **2019**, *29* (47), 1900466. https://doi.org/10.1002/adfm.201900466.

(43) Wang, S.; Jiang, Y.; Juarez-Perez, E. J.; Ono, L. K.; Qi, Y. Accelerated Degradation of Methylammonium Lead Iodide Perovskites Induced by Exposure to Iodine Vapour. *Nat. Energy* **2017**, *2* (1). https://doi.org/10.1038/nenergy.2016.195.

(44) Domanski, K.; Roose, B.; Matsui, T.; Saliba, M.; Turren-Cruz, S.-H.; Correa-Baena, J.-P.; Roldán Carmona, C.; Richardson, G.; Foster, J.; De Angelis, F.; Ball, J.; petrozza, annamaria; Mine, N.; Nazeeruddin, M. K.; Tress, W.; Grätzel, M.; Steiner, U.; Hagfeldt, A.; Abate, A. Migration of Cations Induces Reversible Performance Losses over Day/Night Cycling in Perovskite Solar Cells. *Energy Environ. Sci.* **2017**, *10*, 604–613. https://doi.org/10.1039/C6EE03352K.

(45) Domanski, K.; Correa-Baena, J.-P. P.; Mine, N.; Nazeeruddin, M. K.; Abate, A.; Saliba, M.; Tress, W.; Hagfeldt, A.; Grätzel, M. Not All That Glitters Is Gold: Metal-Migration-Induced Degradation in Perovskite Solar Cells. *ACS Nano* **2016**, *10* (6), 6306–6314. https://doi.org/10.1021/acsnano.6b02613.

(46) Zhao, L.; Kerner, R. A.; Xiao, Z.; Lin, Y. L.; Lee, K. M.; Schwartz, J.; Rand, B. P. Redox Chemistry Dominates the Degradation and Decomposition of Metal Halide Perovskite Optoelectronic Devices. *ACS Energy Lett.* **2016**, *1* (3), 595–602. https://doi.org/10.1021/acsenergylett.6b00320.

(47) Marchezi, P. E.; Therézio, E. M.; Szostak, R.; Loureiro, H. C.; Bruening, K.; Gold-Parker, A.; Melo, M. A.; Tassone, C. J.; Tolentino, H. C. N.; Toney, M. F.; Nogueira, A. F. Degradation Mechanisms in Mixed-Cation and Mixed-Halide CsxFA1−xPb(BryI1−y)3 Perovskite Films under Ambient Conditions. *J. Mater. Chem. A* **2020**, *8* (18), 9302–9312. https://doi.org/10.1039/D0TA01201G.

(48) Dai, Z.; Yadavalli, S. K.; Chen, M.; Abbaspourtamijani, A.; Qi, Y.; Padture, N. P. Interfacial Toughening with Self-Assembled Monolayers Enhances Perovskite Solar Cell Reliability. *Science (80-.).* **2021**, *372* (6542), 618–622. https://doi.org/10.1126/science.abf5602.

(49) Zhu, H.; Teale, S.; Lintangpradipto, M. N.; Mahesh, S.; Chen, B.; McGehee, M. D.; Sargent, E. H.; Bakr, O. M. Long-Term Operating Stability in Perovskite Photovoltaics.

Nat. Rev. Mater. **2023**, *8* (9), 569–586. https://doi.org/10.1038/s41578-023-00582-w.

(50) Conings, B.; Drijkoningen, J.; Gauquelin, N.; Babayigit, A.; D'Haen, J.; D'Olieslaeger, L.; Ethirajan, A.; Verbeeck, J.; Manca, J.; Mosconi, E.; De Angelis, F.; Boyen, H. G.; Angelis, F. De; Boyen, H. G.; Haen, J. D.; Olieslaeger, L. D.; D'Haen, J.; D'Olieslaeger, L.; Ethirajan, A.; Verbeeck, J.; Manca, J.; Mosconi, E.; Angelis, F. De; Boyen, H. G. Intrinsic Thermal Instability of Methylammonium Lead Trihalide Perovskite. *Adv. Energy Mater.* **2015**, *5* (15), 0–6. https://doi.org/10.1002/aenm.20150.

(51) Saliba, M.; Matsui, T.; Domanski, K.; Seo, J. Y.; Ummadisingu, A.; Zakeeruddin, S. M.; Correa-Baena, J. P.; Tress, W. R.; Abate, A.; Hagfeldt, A.; Grätzel, M. Incorporation of Rubidium Cations into Perovskite Solar Cells Improves Photovoltaic Performance. *Science (80-.).* **2016**. https://doi.org/10.1126/science.aah5557.

(52) Cheacharoen, R.; Rolston, N.; Harwood, D.; Bush, K. A.; Dauskardt, R. H.; McGehee, M. D. Design and Understanding of Encapsulated Perovskite Solar Cells to Withstand Temperature Cycling. *Energy Environ. Sci.* **2018**, *11* (1), 144–150. https://doi.org/10.1039/C7EE02564E.

(53) Tsai, H.; Nie, W.; Blancon, J. C.; Stoumpos, C. C.; Asadpour, R.; Harutyunyan, B.; Neukirch, A. J.; Verduzco, R.; Crochet, J. J.; Tretiak, S.; Pedesseau, L.; Even, J.; Alam, M. A.; Gupta, G.; Lou, J.; Ajayan, P. M.; Bedzyk, M. J.; Kanatzidis, M. G.; Mohite, A. D. High-Efficiency Two-Dimensional Ruddlesden-Popper Perovskite Solar Cells. *Nature* **2016**, *536* (7616), 312–317. https://doi.org/10.1038/nature18306.

(54) Holzhey, P.; Saliba, M. A Full Overview of International Standards Assessing the Long-Term Stability of Perovskite Solar Cells. *J. Mater. Chem. A* **2018**. https://doi.org/10.1039/C8TA06950F.

(55) Wu, S.; Li, Z.; Li, M.-Q.; Diao, Y.; Lin, F.; Liu, T.; Zhang, J.; Tieu, P.; Gao, W.; Qi, F.; Pan, X.; Xu, Z.; Zhu, Z.; Jen, A. K.-Y. 2D Metal–Organic Framework for Stable Perovskite Solar Cells with Minimized Lead Leakage. *Nat. Nanotechnol.* **2020**, *15* (11), 934–940. https://doi.org/10.1038/s41565-020-0765-7.

(56) Li, C.; Wang, X.; Bi, E.; Jiang, F.; Park, S. M.; Li, Y.; Chen, L.; Wang, Z.; Zeng, L.; Chen, H.; Liu, Y.; Grice, C. R.; Abudulimu, A.; Chung, J.; Xian, Y.; Zhu, T.; Lai, H.; Chen, B.; Ellingson, R. J.; Fu, F.; Ginger, D. S.; Song, Z.; Sargent, E. H.; Yan, Y. Rational Design of Lewis Base Molecules for Stable and Efficient Inverted Perovskite Solar Cells. *Science (80-.).* **2023**, *379* (6633), 690–694. https://doi.org/10.1126/science.ade3970.

(57) Zhang, Z.; Wang, H.; Jacobsson, T. J.; Luo, J. Big Data Driven Perovskite Solar Cell Stability Analysis. *Nat. Commun.* **2022**, *13* (1), 7639. https://doi.org/10.1038/s41467-022-35400-4.

(58) Grancini, G.; Roldán-Carmona, C.; Zimmermann, I.; Mosconi, E.; Lee, X.; Martineau, D.; Narbey, S.; Oswald, F.; De Angelis, F.; Graetzel, M.; Nazeeruddin, M. K. One-Year Stable Perovskite Solar Cells by 2D/3D Interface Engineering. *Nat. Commun.* **2017**. https://doi.org/10.1038/ncomms15684.

(59) Mei, A.; Li, X.; Liu, L.; Ku, Z.; Liu, T.; Rong, Y.; Xu, M.; Hu, M.; Chen, J.; Yang, Y.; Grätzel, M.; Han, H. A Hole-Conductor–Free, Fully Printable Mesoscopic Perovskite Solar Cell with High Stability. *Science (80-.).* **2014**, *345* (6194), 295. https://doi.org/10.1126/science.1254763.

(60) Lin, X.; Su, H.; He, S.; Song, Y.; Wang, Y.; Qin, Z.; Wu, Y.; Yang, X.; Han, Q.; Fang, J.; Zhang, Y.; Segawa, H.; Grätzel, M.; Han, L. In Situ Growth of Graphene on Both Sides of a Cu–Ni Alloy Electrode for Perovskite Solar Cells with Improved Stability. *Nat. Energy* **2022**, *7* (6), 520–527. https://doi.org/10.1038/s41560-022-01038-1.

(61) Kerner, R. A.; Schulz, P.; Christians, J. A.; Dunfield, S. P.; Dou, B.; Zhao, L.; Teeter, G.; Berry, J. J.; Rand, B. P. Reactions at Noble Metal Contacts with Methylammonium Lead Triiodide Perovskites: Role of Underpotential Deposition and Electrochemistry. *APL Mater.* **2019**, *7* (4), 41103. https://doi.org/10.1063/1.5083812.

(62) Boyd, C. C.; Cheacharoen, R.; Bush, K. A.; Prasanna, R.; Leijtens, T.; McGehee, M. D. Barrier Design to Prevent Metal-Induced Degradation and Improve Thermal Stability in Perovskite Solar Cells. *ACS Energy Lett.* **2018**, *3* (7), 1772–1778. https://doi.org/10.1021/acsenergylett.8b00926.

(63) Zhao, X.; Liu, T.; Burlingame, Q. C.; Liu, T.; Holley, R.; Cheng, G.; Yao, N.; Gao, F.; Loo, Y.-L. Accelerated Aging of All-Inorganic, Interface-Stabilized Perovskite Solar Cells. *Science (80-.).* **2022**, *377* (6603), 307–310. https://doi.org/10.1126/science.abn5679.

(64) Goldschmidt, V. M. Die Gesetze Der Krystallochemie. *Naturwissenschaften* **1926**, *14* (21), 477–485. https://doi.org/10.1007/BF01507527.

(65) Straus, D. B.; Guo, S.; Abeykoon, A. M. M.; Cava, R. J. Understanding the Instability of the Halide Perovskite CsPbI3 through Temperature-Dependent Structural Analysis. *Adv. Mater.* **2020**, *32* (32), 2001069.

(66) Filip, M. R.; Giustino, F. The Geometric Blueprint of Perovskites. *Proc. Natl. Acad. Sci.* **2018**, *115* (21), 5397–5402. https://doi.org/10.1073/pnas.1719179115.

(67) Shannon, R. D. Revised Effective Ionic Radii and Systematic Studies of Interatomic Distances in Halides and Chalcogenides. *Acta Crystallogr. Sect. A Cryst. physics, diffraction, Theor. Gen. Crystallogr.* **1976**, *32* (5), 751–767.

(68) Kieslich, G.; Sun, S.; Cheetham, A. K. Solid-State Principles Applied to Organic–Inorganic Perovskites: New Tricks for an Old Dog. *Chem. Sci.* **2014**, *5* (12), 4712–4715. https://doi.org/10.1039/C4SC02211D.

(69) Duijnstee, E. A.; Gallant, B. M.; Holzhey, P.; Kubicki, D. J.; Collavini, S.; Sturdza, B. K.; Sansom, H. C.; Smith, J.; Gutmann, M. J.; Saha, S.; Gedda, M.; Nugraha, M. I.; Kober-Czerny, M.; Xia, C.; Wright, A. D.; Lin, Y.-H.; Ramadan, A. J.; Matzen, A.; Hung, E. Y.-H.; Seo, S.; Zhou, S.; Lim, J.; Anthopoulos, T. D.; Filip, M. R.; Johnston, M. B.; Nicholas, R. J.; Delgado, J. L.; Snaith, H. J. Understanding the Degradation of Methylenediammonium and Its Role in Phase-Stabilizing Formamidinium Lead Triiodide. *J. Am. Chem. Soc.* **2023**. https://doi.org/10.1021/jacs.3c01531.

(70) Travis, W.; Glover, E. N. K.; Bronstein, H.; Scanlon, D. O.; Palgrave, R. G. On the Application of the Tolerance Factor to Inorganic and Hybrid Halide Perovskites: A Revised System. *Chem. Sci.* **2016**, *7* (7), 4548–4556. https://doi.org/10.1039/C5SC04845A.

(71) Kubicki, D. J.; Prochowicz, D.; Hofstetter, A.; Saski, M.; Yadav, P.; Bi, D.; Pellet, N.; Lewiński, J.; Zakeeruddin, S. M.; Grätzel, M.; Emsley, L. Formation of Stable Mixed Guanidinium–Methylammonium Phases with Exceptionally Long Carrier Lifetimes for High-Efficiency Lead Iodide-Based Perovskite Photovoltaics. *J. Am. Chem. Soc.* **2018**,

140 (9), 3345–3351. https://doi.org/10.1021/jacs.7b12860.

(72) Doherty, T. A. S.; Nagane, S.; Kubicki, D. J.; Jung, Y.-K.; Johnstone, D. N.; Iqbal, A. N.; Guo, D.; Frohna, K.; Danaie, M.; Tennyson, E. M.; Macpherson, S.; Abfalterer, A.; Anaya, M.; Chiang, Y.-H.; Crout, P.; Ruggeri, F. S.; Collins, S.; Grey, C. P.; Walsh, A.; Midgley, P. A.; Stranks, S. D. Stabilized Tilted-Octahedra Halide Perovskites Inhibit Local Formation of Performance-Limiting Phases. *Science (80-.).* **2021**, *374* (6575), 1598–1605. https://doi.org/10.1126/science.abl4890.

(73) Gholipour, S.; Ali, A. M.; Tajabadi, F.; Tress, W.; Taghavinia, N.; Grätzel, M.; Abate, A.; Angelis, F. De; Gaggioli, C. A.; Mosconi, E.; Hagfeldt, A.; Saliba, M.; Si, S. I. Globularity-Selected Large Molecules for a New Generation of Multication Perovskites. **2017**, *1702005*, 1–9. https://doi.org/10.1002/adma.201702005.

(74) Sun, S.; Deng, Z.; Wu, Y.; Wei, F.; Halis Isikgor, F.; Brivio, F.; Gaultois, M. W.; Ouyang, J.; Bristowe, P. D.; Cheetham, A. K.; Kieslich, G. Variable Temperature and High-Pressure Crystal Chemistry of Perovskite Formamidinium Lead Iodide: A Single Crystal X-Ray Diffraction and Computational Study. *Chem. Commun.* **2017**, *53* (54), 7537–7540. https://doi.org/10.1039/C7CC00995J.

(75) Liu, X.; Luo, D.; Lu, Z.-H.; Yun, J. S.; Saliba, M.; Seok, S. Il; Zhang, W. Stabilization of Photoactive Phases for Perovskite Photovoltaics. *Nat. Rev. Chem.* **2023**. https://doi.org/10.1038/s41570-023-00492-z.

(76) Chen, T.; Foley, B. J.; Park, C.; Brown, C. M.; Harriger, L. W.; Lee, J.; Ruff, J.; Yoon, M.; Choi, J. J.; Lee, S. H. Entropy-Driven Structural Transition and Kinetic Trapping in Formamidinium Lead Iodide Perovskite. *Sci. Adv.* **2016**. https://doi.org/10.1126/sciadv.1601650.

(77) Stoumpos, C. C.; Malliakas, C. D.; Kanatzidis, M. G. Semiconducting Tin and Lead Iodide Perovskites with Organic Cations: Phase Transitions, High Mobilities, and near-Infrared Photoluminescent Properties. *Inorg. Chem.* **2013**, *52* (15), 9019–9038. https://doi.org/10.1021/ic401215x.

(78) Weller, M. T.; Weber, O. J.; Frost, J. M.; Walsh, A. Cubic Perovskite Structure of Black Formamidinium Lead Iodide, α-[HC(NH2)2]PbI3, at 298 K. *J. Phys. Chem. Lett.* **2015**, *6* (16), 3209–3212. https://doi.org/10.1021/acs.jpclett.5b01432.

(79) Weber, O. J.; Ghosh, D.; Gaines, S.; Henry, P. F.; Walker, A. B.; Islam, M. S.; Weller, M. T. Phase Behavior and Polymorphism of Formamidinium Lead Iodide. *Chem. Mater.* **2018**, *30* (11), 3768–3778. https://doi.org/10.1021/acs.chemmater.8b00862.

(80) Fabini, D. H.; Stoumpos, C. C.; Laurita, G.; Kaltzoglou, A.; Kontos, A. G.; Falaras, P.; Kanatzidis, M. G.; Seshadri, R. Reentrant Structural and Optical Properties and Large Positive Thermal Expansion in Perovskite Formamidinium Lead Iodide. *Angew. Chemie - Int. Ed.* **2016**. https://doi.org/10.1002/anie.201609538.

(81) Franz, A.; Tobbens, D. M.; Lehmann, F.; Kargell, M.; Schorr, S. The Influence of Deuteration on the Crystal Structure of Hybrid Halide Perovskites: A Temperature-Dependent Neutron Diffraction Study of FAPbBr3. *Acta Crystallogr. Sect. B* **2020**, *76* (2), 267–274.

(82) Šimėnas, M.; Balčiūnas, S.; Mączka, M.; Banys, J. Phase Transition Model of FA Cation Ordering in FAPbX3 (X = Br, I) Hybrid Perovskites. *J. Mater. Chem. C* **2022**, *10* (13), 5210–

5217. https://doi.org/10.1039/D2TC00559J.

(83) Yarbrough, W. A. Vapor-Phase-Deposited Diamond—Problems and Potential. *J. Am. Ceram. Soc.* **1992**, *75* (12), 3179–3200.

(84) Lee, J.-W.; Tan, S.; Han, T.-H.; Wang, R.; Zhang, L.; Park, C.; Yoon, M.; Choi, C.; Xu, M.; Liao, M. E.; Lee, S.-J.; Nuryyeva, S.; Zhu, C.; Huynh, K.; Goorsky, M. S.; Huang, Y.; Pan, X.; Yang, Y. Solid-Phase Hetero Epitaxial Growth of α-Phase Formamidinium Perovskite. *Nat. Commun.* **2020**, *11* (1), 5514. https://doi.org/10.1038/s41467-020-19237-3.

(85) Chen, L.; Yoo, J. W.; Hu, M.; Lee, S.-U.; Seok, S. Il. Intrinsic Phase Stability and Inherent Bandgap of Formamidinium Lead Triiodide Perovskite Single Crystals. *Angew. Chemie Int. Ed.* **2022**, *61* (50), e202212700. https://doi.org/https://doi.org/10.1002/anie.202212700.

(86) Saidaminov, M. I.; Abdelhady, A. L.; Murali, B.; Alarousu, E.; Burlakov, V. M.; Peng, W.; Dursun, I.; Wang, L.; He, Y.; Maculan, G.; Goriely, A.; Wu, T.; Mohammed, O. F.; Bakr, O. M. High-Quality Bulk Hybrid Perovskite Single Crystals within Minutes by Inverse Temperature Crystallization. *Nat. Commun.* **2015**, *6* (1), 7586. https://doi.org/10.1038/ncomms8586.

(87) Holzhey, P.; Prettl, M.; Collavini, S.; Mortan, C.; Saliba, M. Understanding the Impact of Surface Roughness: Changing from FTO to ITO to PEN/ITO for Flexible Perovskite Solar Cells. *Sci. Rep.* **2023**, *13* (1), 6375. https://doi.org/10.1038/s41598-023-33147-6.

(88) Saliba, M.; Correa-Baena, J.-P.; Wolff, C. M.; Stolterfoht, M.; Phung, N.; Albrecht, S.; Neher, D.; Abate, A. How to Make over 20% Efficient Perovskite Solar Cells in Regular (n–i–p) and Inverted (p–i–n) Architectures. *Chem. Mater.* **2018**, *30* (13), 4193–4201. https://doi.org/10.1021/acs.chemmater.8b00136.

(89) Min, H.; Ji, S.-G.; Seok, S. Il. Relaxation of Externally Strained Halide Perovskite Thin Layers with Neutral Ligands. *Joule* **2022**, *6* (9), 2175–2185. https://doi.org/https://doi.org/10.1016/j.joule.2022.06.031.

(90) Park, J.; Kim, J.; Yun, H.-S.; Paik, M. J.; Noh, E.; Mun, H. J.; Kim, M. G.; Shin, T. J.; Seok, S. Il. Controlled Growth of Perovskite Layers with Volatile Alkylammonium Chlorides. *Nature* **2023**. https://doi.org/10.1038/s41586-023-05825-y.

(91) Bu, T.; Li, J.; Zheng, F.; Chen, W.; Wen, X.; Ku, Z.; Peng, Y.; Zhong, J.; Cheng, Y.-B.; Huang, F. Universal Passivation Strategy to Slot-Die Printed SnO2 for Hysteresis-Free Efficient Flexible Perovskite Solar Module. *Nat. Commun.* **2018**, *9* (1), 4609. https://doi.org/10.1038/s41467-018-07099-9.

(92) Al-Ashouri, A.; Magomedov, A.; Roß, M.; Jošt, M.; Talaikis, M.; Chistiakova, G.; Bertram, T.; Márquez, J. A.; Köhnen, E.; Kasparavičius, E.; Levcenco, S.; Gil-Escrig, L.; Hages, C. J.; Schlatmann, R.; Rech, B.; Malinauskas, T.; Unold, T.; Kaufmann, C. A.; Korte, L.; Niaura, G.; Getautis, V.; Albrecht, S. Conformal Monolayer Contacts with Lossless Interfaces for Perovskite Single Junction and Monolithic Tandem Solar Cells. *Energy Environ. Sci.* **2019**, *12* (11), 3356–3369. https://doi.org/10.1039/c9ee02268f.

(93) Zhou, S.; Daskeviciene, M.; Steponaitis, M.; Bubniene, G.; Jankauskas, V.; Schutt, K.; Holzhey, P.; Marshall, A. R.; Caprioglio, P.; Christoforo, G.; Ball, J. M.; Malinauskas, T.; Getautis, V.; Snaith, H. J. Low-Cost Dopant-Free Carbazole Enamine Hole-Transporting Materials for Thermally Stable Perovskite Solar Cells. *Sol. RRL* **2022**, *6* (1), 2100984.

https://doi.org/https://doi.org/10.1002/solr.202100984.

(94) Boyd, C. C.; Cheacharoen, R.; Leijtens, T.; McGehee, M. D. Understanding Degradation Mechanisms and Improving Stability of Perovskite Photovoltaics. *Chem. Rev.* **2019**, *119* (5), 3418–3451. https://doi.org/10.1021/acs.chemrev.8b00336.

(95) Saliba, M.; Correa-Baena, J.-P.; Grätzel, M.; Hagfeldt, A.; Abate, A. Perovskite Solar Cells from the Atomic to the Film Level. *Angew. Chemie* **2017**. https://doi.org/10.1002/ange.201703226.

(96) Taylor, A. D.; Sun, Q.; Goetz, K. P.; An, Q.; Schramm, T.; Hofstetter, Y.; Litterst, M.; Paulus, F.; Vaynzof, Y. A General Approach to High-Efficiency Perovskite Solar Cells by Any Antisolvent. *Nat. Commun.* **2021**, *12* (1), 1878. https://doi.org/10.1038/s41467-021-22049-8.

(97) Park, N.-G.; Zhu, K. Scalable Fabrication and Coating Methods for Perovskite Solar Cells and Solar Modules. *Nat. Rev. Mater.* **2020**, *5* (5), 333–350. https://doi.org/10.1038/s41578-019-0176-2.

(98) Mahesh, S.; Ball, J. M.; Oliver, R. D. J.; McMeekin, D. P.; Nayak, P. K.; Johnston, M. B.; Snaith, H. J. Revealing the Origin of Voltage Loss in Mixed-Halide Perovskite Solar Cells. *Energy Environ. Sci.* **2020**, *13* (1), 258–267. https://doi.org/10.1039/C9EE02162K.

(99) Shen, X.; Gallant, B. M.; Holzhey, P.; Smith, J. A.; Elmestekawy, K. A.; Yuan, Z.; Rathnayake, P. V. G. M.; Bernardi, S.; Dasgupta, A.; Kasparavicius, E.; Malinauskas, T.; Caprioglio, P.; Shargaieva, O.; Lin, Y.-H.; McCarthy, M. M.; Unger, E.; Getautis, V.; Widmer-Cooper, A.; Herz, L. M.; Snaith, H. J. Chloride-Based Additive Engineering for Efficient and Stable Wide-Bandgap Perovskite Solar Cells. *Adv. Mater.* **2023**, *35* (30), 2211742. https://doi.org/https://doi.org/10.1002/adma.202211742.

(100) Huang, T.; Tan, S.; Nuryyeva, S.; Yavuz, I.; Babbe, F.; Zhao, Y.; Abdelsamie, M.; Weber, M. H.; Wang, R.; Houk, K. N.; Sutter-Fella, C. M.; Yang, Y. Performance-Limiting Formation Dynamics in Mixed-Halide Perovskites. *Sci. Adv.* **2024**, *7* (46), eabj1799. https://doi.org/10.1126/sciadv.abj1799.

(101) Guaita, M. G. D.; Szostak, R.; da Silva, F. M. C.; de Morais, A.; Moral, R. F.; Kodalle, T.; Teixeira, V. C.; Sutter-Fella, C. M.; Tolentino, H. C. N.; Nogueira, A. F. Influence of Methylammonium Chloride on Wide-Bandgap Halide Perovskites Films for Solar Cells. *Adv. Funct. Mater.* **2023**, *n/a* (n/a), 2307104. https://doi.org/https://doi.org/10.1002/adfm.202307104.

(102) Liu, Y.; Yang, Z.; Cui, D.; Ren, X.; Sun, J.; Liu, X.; Zhang, J.; Wei, Q.; Fan, H.; Yu, F.; Zhang, X.; Zhao, C.; Liu, S. (Frank). Two-Inch-Sized Perovskite CH3NH3PbX3 (X = Cl, Br, I) Crystals: Growth and Characterization. *Adv. Mater.* **2015**, *27* (35), 5176–5183. https://doi.org/https://doi.org/10.1002/adma.201502597.

(103) Nagabhushana, G. P.; Shivaramaiah, R.; Navrotsky, A. Direct Calorimetric Verification of Thermodynamic Instability of Lead Halide Hybrid Perovskites. *Proc. Natl. Acad. Sci.* **2016**, *113* (28), 7717–7721.

(104) Ivanov, I. L.; Steparuk, A. S.; Bolyachkina, M. S.; Tsvetkov, D. S.; Safronov, A. P.; Zuev, A. Y. Thermodynamics of Formation of Hybrid Perovskite-Type Methylammonium Lead Halides. *J. Chem. Thermodyn.* **2018**, *116*, 253–258.

(105) McMeekin, D. P.; Holzhey, P.; Fürer, S. O.; Harvey, S. P.; Schelhas, L. T.; Ball, J. M.;

Mahesh, S.; Seo, S.; Hawkins, N.; Lu, J.; Johnston, M. B.; Berry, J. J.; Bach, U.; Snaith, H. J. Intermediate-Phase Engineering via Dimethylammonium Cation Additive for Stable Perovskite Solar Cells. *Nat. Mater.* **2023**, *22* (1), 73–83. https://doi.org/10.1038/s41563-022-01399-8.

(106) Wei-Ting Wang, Philippe Holzhey, Qiang Zhang, Ning Zhou, Suer Zhou, Elisabeth A. Duijnstee, Kevin J. Rietwyk, Chien-Hung Chiang, Yanfeng Zhang, Udo Bach, Chun-Guey Wu, Hin-Lap Yip, Henry J. Snaith, S.-P. F. Water- and Heat-Activated Dynamically Evolving Passivation for Perovskite Photovoltaics. *Submitted*.

(107) Jiang, W.; Li, F.; Li, M.; Qi, F.; Lin, F. R.; Jen, A. K.-Y. π-Expanded Carbazoles as Hole-Selective Self-Assembled Monolayers for High-Performance Perovskite Solar Cells. *Angew. Chemie Int. Ed.* **2022**, *61* (51), e202213560. https://doi.org/https://doi.org/10.1002/anie.202213560.

(108) Wang, W.-T.; Chen, P.; Chiang, C.-H.; Guo, T.-F.; Wu, C.-G.; Feng, S.-P. Synergistic Reinforcement of Built-In Electric Fields for Highly Efficient and Stable Perovskite Photovoltaics. *Adv. Funct. Mater.* **2020**, *30* (19), 1909755. https://doi.org/https://doi.org/10.1002/adfm.201909755.

(109) Toby, B. H.; Von Dreele, R. B. GSAS-II: The Genesis of a Modern Open-Source All Purpose Crystallography Software Package. *J. Appl. Crystallogr.* **2013**, *46* (2), 544–549. https://doi.org/10.1107/S0021889813003531.

(110) He, B. B. Introduction to Two-Dimensional X-Ray Diffraction. *Powder Diffr.* **2003**, *18* (2), 71–85.

(111) Braunger, S.; Mundt, L. E.; Wolff, C. M.; Mews, M.; Rehermann, C.; Jost, M.; ESTEVES, A. T.; Eisenhauer, D.; Becker, C.; Torres, J. A. G.; Unger, E.; Korte, L.; Neher, D.; Schubert, M. C.; Rech, B.; Albrecht, S. On the Appearance of Wrinkled Morphology for Cs x FA 1-x Pb(I 1-y Br y) 3 Perovskite Compositions and the Impact on Solar Cell Performance. *J. Phys. Chem. C* **2018**, *122*, 17123–17135. https://doi.org/10.1021/acs.jpcc.8b06459.

(112) Lin, Y. H.; Sakai, N.; Da, P.; Wu, J.; Sansom, H. C.; Ramadan, A. J.; Mahesh, S.; Liu, J.; Oliver, R. D. J.; Lim, J.; Aspitarte, L.; Sharma, K.; Madhu, P. K.; Morales-Vilches, A. B.; Nayak, P. K.; Bai, S.; Gao, F.; Grovenor, C. R. M.; Johnston, M. B.; Labram, J. G.; Durrant, J. R.; Ball, J. M.; Wenger, B.; Stannowski, B.; Snaith, H. J. A Piperidinium Salt Stabilizes Efficient Metal-Halide Perovskite Solar Cells. *Science (80-.).* **2020**. https://doi.org/10.1126/science.aba1628.

(113) Ravishankar, S.; Riquelme, A.; Sarkar, S. K.; Garcia-Batlle, M.; Garcia-Belmonte, G.; Bisquert, J. Intensity-Modulated Photocurrent Spectroscopy and Its Application to Perovskite Solar Cells. *J. Phys. Chem. C* **2019**, *123* (41), 24995–25014. https://doi.org/10.1021/acs.jpcc.9b07434.

(114) Laird, J. S.; Ravishankar, S.; Rietwyk, K. J.; Mao, W.; Bach, U.; Smith, T. A. Intensity Modulated Photocurrent Microspectrosopy for Next Generation Photovoltaics. *Small Methods* **2022**, *6* (9), 2200493. https://doi.org/https://doi.org/10.1002/smtd.202200493.

(115) Benjamin M. Gallant, Philippe Holzhey, Saqlain Choudhary, Joel A. Smith, Karim A. Elmestekawy, Pietro Caprioglio, Igal Levine, James M. Ball, M. Greyson Christoforo, Laura M. Herz, H. J. S. A Green Solvent System for Precursor Phase-Engineered Sequential Deposition of Stable Formamidinium Lead Triiodide for Perovskite Solar

Cells. *arXiv:2406.08441*.

(116) Nayak, P. K.; Moore, D. T.; Wenger, B.; Nayak, S.; Haghighirad, A. A.; Fineberg, A.; Noel, N. K.; Reid, O. G.; Rumbles, G.; Kukura, P.; Vincent, K. A.; Snaith, H. J. Mechanism for Rapid Growth of Organic–Inorganic Halide Perovskite Crystals. *Nat. Commun.* **2016**, *7* (1), 13303. https://doi.org/10.1038/ncomms13303.

(117) Wenger, B.; Nayak, P. K.; Wen, X.; Kesava, S. V; Noel, N. K.; Snaith, H. J. Consolidation of the Optoelectronic Properties of CH3NH3PbBr3 Perovskite Single Crystals. *Nat. Commun.* **2017**, *8* (1), 590. https://doi.org/10.1038/s41467-017-00567-8.

(118) Ying, H.; Zhang, Y.; Cheng, J. Dynamic Urea Bond for the Design of Reversible and Self-Healing Polymers. *Nat. Commun.* **2014**, *5* (1), 3218. https://doi.org/10.1038/ncomms4218.

(119) Jeon, N. J.; Noh, J. H.; Kim, Y. C.; Yang, W. S.; Ryu, S.; Seok, S. Il. Solvent Engineering for High-Performance Inorganic–Organic Hybrid Perovskite Solar Cells. *Nat. Mater.* **2014**, *13* (9), 897–903. https://doi.org/10.1038/nmat4014.

(120) Rong, Y.; Venkatesan, S.; Guo, R.; Wang, Y.; Bao, J.; Li, W.; Fan, Z.; Yao, Y. Critical Kinetic Control of Non-Stoichiometric Intermediate Phase Transformation for Efficient Perovskite Solar Cells. *Nanoscale* **2016**, *8* (26), 12892–12899. https://doi.org/10.1039/c6nr00488a.

(121) Yang, W. S.; Noh, J. H.; Jeon, N. J.; Kim, Y. C.; Ryu, S.; Seo, J.; Seok, S. I. High-Performance Photovoltaic Perovskite Layers Fabricated through Intramolecular Exchange. *Science (80-.).* **2015**, *348* (6240), 1234–1237. https://doi.org/10.1126/science.aaa9272.

(122) Lee, J.; Baik, S. Enhanced Crystallinity of CH3NH3PbI3 by the Pre-Coordination of PbI2-DMSO Powders for Highly Reproducible and Efficient Planar Heterojunction Perovskite Solar Cells. *RSC Adv.* **2018**, *8* (2), 1005–1013. https://doi.org/10.1039/c7ra12304c.

(123) Lee, S. J.; Heo, J. H.; Im, S. H. Large-Scale Synthesis of Uniform PbI2(DMSO) Complex Powder by Solvent Extraction Method for Efficient Metal Halide Perovskite Solar Cells. *ACS Appl. Mater. Interfaces* **2020**, *12* (7), 8233–8239. https://doi.org/10.1021/acsami.9b20493.

(124) Mutlu, A.; Yeşil, T.; Kiymaz, D.; Zafer, C. Approach to Enhance the Stability and Efficiency of Triple-Cation Perovskite Solar Cells by Reactive Antisolvents. *ACS Appl. Energy Mater.* **2021**, *4* (1), 47–60. https://doi.org/10.1021/ACSAEM.0C00849/SUPPL_FILE/AE0C00849_SI_001.PDF.

(125) Shi, D.; Adinolfi, V.; Comin, R.; Yuan, M.; Alarousu, E.; Buin, A.; Chen, Y.; Hoogland, S.; Rothenberger, A.; Katsiev, K.; Losovyj, Y.; Zhang, X.; Dowben, P. A.; Mohammed, O. F.; Sargent, E. H.; Bakr, O. M. Low Trap-State Density and Long Carrier Diffusion in Organolead Trihalide Perovskite Single Crystals. **2015**, *347* (6221), 519–522.

(126) Dong, Q.; Fang, Y.; Shao, Y.; Mulligan, P.; Qiu, J.; Cao, L.; Huang, J. Electron-Hole Diffusion Lengths > 175 m in Solution-Grown CH3NH3PbI3 Single Crystals. *Science (80-.).* **2015**, *347* (6225), 967–970. https://doi.org/10.1126/science.aaa5760.

(127) Saidaminov, M. I.; Adinolfi, V.; Comin, R.; Abdelhady, A. L.; Peng, W.; Dursun, I.; Yuan, M.; Hoogland, S.; Sargent, E. H.; Bakr, O. M. Planar-Integrated Single-Crystalline Perovskite Photodetectors. *Nat. Commun.* **2015**, *6* (1), 8724. https://doi.org/10.1038/ncomms9724.

(128) Wang, Q.; Chen, B.; Liu, Y.; Deng, Y.; Bai, Y.; Dong, Q.; Huang, J. Scaling Behavior of Moisture-Induced Grain Degradation in Polycrystalline Hybrid Perovskite Thin Films. *Energy Environ. Sci.* **2017**, *10* (2), 516–522. https://doi.org/10.1039/C6EE02941H.

(129) Sakai, N.; Warren, R.; Zhang, F.; Nayak, S.; Liu, J.; Kesava, S. V; Lin, Y.-H.; Biswal, H. S.; Lin, X.; Grovenor, C.; Malinauskas, T.; Basu, A.; Anthopoulos, T. D.; Getautis, V.; Kahn, A.; Riede, M.; Nayak, P. K.; Snaith, H. J. Adduct-Based p-Doping of Organic Semiconductors. *Nat. Mater.* **2021**, *20* (9), 1248–1254. https://doi.org/10.1038/s41563-021-00980-x.

(130) McMeekin, D. P.; Wang, Z.; Rehman, W.; Pulvirenti, F.; Patel, J. B.; Noel, N. K.; Johnston, M. B.; Marder, S. R.; Herz, L. M.; Snaith, H. J. Crystallization Kinetics and Morphology Control of Formamidinium–Cesium Mixed-Cation Lead Mixed-Halide Perovskite via Tunability of the Colloidal Precursor Solution. *Adv. Mater.* **2017**. https://doi.org/10.1002/adma.201607039.

(131) McMeekin, D. P.; Wang, Z.; Rehman, W.; Pulvirenti, F.; Patel, J. B.; Noel, N. K.; Johnston, M. B.; Marder, S. R.; Herz, L. M.; Snaith, H. J. Crystallization Kinetics and Morphology Control of Formamidinium–Cesium Mixed-Cation Lead Mixed-Halide Perovskite via Tunability of the Colloidal Precursor Solution. *Adv. Mater.* **2017**, *29* (29). https://doi.org/10.1002/adma.201607039.

(132) Barker, A. J.; Sadhanala, A.; Deschler, F.; Gandini, M.; Senanayak, S. P.; Pearce, P. M.; Mosconi, E.; Pearson, A.; Wu, Y.; Srimath Kandada, A. R.; Leitjens, T.; De Angelis, F.; Dutton, S. E.; Petrozza, A.; Friend, R. H. Defect-Assisted Photoinduced Halide Segregation in Mixed-Halide Perovskite Thin Films. *ACS Energy Lett.* **2017**, *2* (6), 1416–1424. https://doi.org/10.1021/acsenergylett.7b00282.

(133) Hoke, E. T.; Slotcavage, D. J.; Dohner, E. R.; Bowring, A. R.; Karunadasa, H. I.; McGehee, M. D. Reversible Photo-Induced Trap Formation in Mixed-Halide Hybrid Perovskites for Photovoltaics. *Chem. Sci.* **2014**, *6* (1), 613–617. https://doi.org/10.1039/C4SC03141E.

(134) Penã-Camargo, F.; Caprioglio, P.; Zu, F.; Gutierrez-Partida, E.; Wolff, C. M.; Brinkmann, K.; Albrecht, S.; Riedl, T.; Koch, N.; Neher, D.; Stolterfoht, M. Halide Segregation versus Interfacial Recombination in Bromide-Rich Wide-Gap Perovskite Solar Cells. *ACS Energy Lett.* **2020**. https://doi.org/10.1021/acsenergylett.0c01104.

(135) Knight, A. J.; Borchert, J.; Oliver, R. D. J.; Patel, J. B.; Radaelli, P. G.; Snaith, H. J.; Johnston, M. B.; Herz, L. M. Halide Segregation in Mixed-Halide Perovskites: Influence of A-Site Cations. *ACS Energy Lett.* **2021**, *6* (2), 799–808. https://doi.org/10.1021/acsenergylett.0c02475.

(136) Noel, N. K.; Congiu, M.; Ramadan, A. J.; Fearn, S.; McMeekin, D. P.; Patel, J. B.; Johnston, M. B.; Wenger, B.; Snaith, H. J. Unveiling the Influence of PH on the Crystallization of Hybrid Perovskites, Delivering Low Voltage Loss Photovoltaics. *Joule* **2017**, *1* (2), 328–343. https://doi.org/10.1016/J.JOULE.2017.09.009.

(137) Dou, B.; Wheeler, L. M.; Christians, J. A.; Moore, D. T.; Harvey, S. P.; Berry, J. J.; Barnes, F. S.; Shaheen, S. E.; van Hest, M. F. A. M. Degradation of Highly Alloyed Metal Halide Perovskite Precursor Inks: Mechanism and Storage Solutions. *ACS Energy Lett.* **2018**, *3* (4), 979–985. https://doi.org/10.1021/acsenergylett.8b00305.

(138) Magtaan, J. K.; Devocelle, M.; Kelleher, F. Regeneration of Aged DMF for Use in Solid-Phase Peptide Synthesis. *J. Pept. Sci.* **2019**, *25* (1), e3139.

https://doi.org/10.1002/psc.3139.

(139) Kim, M.; Kim, G. H.; Lee, T. K.; Choi, I. W.; Choi, H. W.; Jo, Y.; Yoon, Y. J.; Kim, J. W.; Lee, J.; Huh, D.; Lee, H.; Kwak, S. K.; Kim, J. Y.; Kim, D. S. Methylammonium Chloride Induces Intermediate Phase Stabilization for Efficient Perovskite Solar Cells. *Joule* **2019**. https://doi.org/10.1016/j.joule.2019.06.014.

(140) Stoumpos, C. C.; Mao, L.; Malliakas, C. D.; Kanatzidis, M. G. Structure–Band Gap Relationships in Hexagonal Polytypes and Low-Dimensional Structures of Hybrid Tin Iodide Perovskites. *Inorg. Chem.* **2017**, *56* (1), 56–73. https://doi.org/10.1021/acs.inorgchem.6b02764.

(141) Tarakina, N. V.; Tyutyunnik, A. P.; Bazuev, G. V.; Vasilev, A. D.; Gould, C.; Nikolaenko, I. V.; Berger, I. F. Synthesis and Crystal Structure of a New Hexagonal Perovskite 7H-Ba7Li1.75Mn3.5O15.75 with Mn4+/Mn5+ Charge Distribution. *Dalt. Trans.* **2015**, *44* (42), 18527–18535. https://doi.org/10.1039/c5dt01528f.

(142) Gratia, P.; Zimmermann, I.; Schouwink, P.; Yum, J. H.; Audinot, J. N.; Sivula, K.; Wirtz, T.; Nazeeruddin, M. K. The Many Faces of Mixed Ion Perovskites: Unraveling and Understanding the Crystallization Process. *ACS Energy Lett.* **2017**, *2* (12), 2686–2693. https://doi.org/10.1021/acsenergylett.7b00981.

(143) Tian, J.; Cordes, D. B.; Quarti, C.; Beljonne, D.; Slawin, A. M. Z.; Zysman-Colman, E.; Morrison, F. D. Stable 6H Organic-Inorganic Hybrid Lead Perovskite and Competitive Formation of 6H and 3C Perovskite Structure with Mixed A Cations. *ACS Appl. Energy Mater.* **2019**, *2* (8), 5427–5437. https://doi.org/10.1021/acsaem.9b00419.

(144) Mancini, A.; Quadrelli, P.; Amoroso, G.; Milanese, C.; Boiocchi, M.; Sironi, A.; Patrini, M.; Guizzetti, G.; Malavasi, L. Synthesis, Structural and Optical Characterization of APbX3 (A=methylammonium, Dimethylammonium, Trimethylammonium; X=I, Br, Cl) Hybrid Organic-Inorganic Materials. *J. Solid State Chem.* **2016**, *240*, 55–60.

(145) García-Fernández, A.; Juarez-Perez, E. J.; Bermúdez-García, J. M.; Llamas-Saiz, A. L.; Artiaga, R.; López-Beceiro, J. J.; Señarís-Rodríguez, M. A.; Sánchez-Andújar, M.; Castro-García, S. Hybrid Lead Halide $[(CH_3)_2NH_2]PbX_3$ ($X = Cl^-$ and Br^-) Hexagonal Perovskites with Multiple Functional Properties. *J. Mater. Chem. C* **2019**, *7* (32), 10008–10018. https://doi.org/10.1039/C9TC03543E.

(146) García-Fernández, A.; Bermúdez-García, J. M.; Castro-García, S.; Llamas-Saiz, A. L.; Artiaga, R.; López-Beceiro, J.; Hu, S.; Ren, W.; Stroppa, A.; Sánchez-Andújar, M.; Señarís-Rodríguez, M. A. Phase Transition, Dielectric Properties, and Ionic Transport in the $[(CH_3)_2NH_2]PbI_3$ Organic–Inorganic Hybrid with 2H-Hexagonal Perovskite Structure. *Inorg. Chem.* **2017**, *56* (9), 4918–4927. https://doi.org/10.1021/acs.inorgchem.6b03095.

(147) Moore, D. T.; Sai, H.; Tan, K. W.; Smilgies, D. M.; Zhang, W.; Snaith, H. J.; Wiesner, U.; Estroff, L. A. Crystallization Kinetics of Organic-Inorganic Trihalide Perovskites and the Role of the Lead Anion in Crystal Growth. *J. Am. Chem. Soc.* **2015**, *137* (6), 2350–2358. https://doi.org/10.1021/ja512117e.

(148) Eperon, G. E.; Stone, K. H.; Mundt, L. E.; Schloemer, T. H.; Habisreutinger, S. N.; Dunfield, S. P.; Schelhas, L. T.; Berry, J. J.; Moore, D. T.; Eperon, G. E.; Moore, D. T. The Role of Dimethylammonium in Bandgap Modulation for Stable Halide Perovskites. *ACS Energy Lett.* **2020**, *5* (6), 1856–1864. https://doi.org/10.1021/acsenergylett.0c00872.

(149) Gehrmann, C.; Egger, D. A. Dynamic Shortening of Disorder Potentials in Anharmonic Halide Perovskites. *Nat. Commun.* **2019**, *10* (1), 1–9. https://doi.org/10.1038/s41467-019-11087-y.

(150) Ke, W.; Spanopoulos, I.; Stoumpos, C. C.; Kanatzidis, M. G. Myths and Reality of HPbI3 in Halide Perovskite Solar Cells. *Nat. Commun.* **2018**, *9* (1), 4785. https://doi.org/10.1038/s41467-018-07204-y.

(151) Marshall, A. R.; Sansom, H. C.; McCarthy, M. M.; Warby, J. H.; Ashton, O. J.; Wenger, B.; Snaith, H. J. Dimethylammonium: An A-Site Cation for Modifying $CsPbI_3$. *Sol. RRL* **2021**, *5* (1), 2000599. https://doi.org/10.1002/solr.202000599.

(152) Michael D Farrar. Improving the Performance and Reproducibility of Lead-Tin Perovskite Absorbers toward All-Perovskite Tandem Solar Cells. University of Oxford 2022.

(153) Ju, D.; Zhao, T.; Yangyang, D.; Zhang, G.; Hu, X.; Cui, D.; Tao, X. Gas Induced Conversion of Hybrid Perovskite Single Crystal to Single Crystal for Great Enhancement of Their Photoelectric Properties. *J. Mater. Chem. A* **2017**, *5* (41), 21919–21925. https://doi.org/10.1039/C7TA07413A.

(154) Oesinghaus, L.; Schlipf, J.; Giesbrecht, N.; Song, L.; Hu, Y.; Bein, T.; Docampo, P.; Müller-Buschbaum, P. Toward Tailored Film Morphologies: The Origin of Crystal Orientation in Hybrid Perovskite Thin Films. *Adv. Mater. Interfaces* **2016**, *3* (19), 1600403. https://doi.org/doi:10.1002/admi.201600403.

(155) Palmstrom, A. F.; Eperon, G. E.; Leijtens, T.; Prasanna, R.; Habisreutinger, S. N.; Nemeth, W.; Gaulding, E. A.; Dunfield, S. P.; Reese, M.; Nanayakkara, S.; Moot, T.; Werner, J.; Liu, J.; To, B.; Christensen, S. T.; McGehee, M. D.; van Hest, M. F. A. M.; Luther, J. M.; Berry, J. J.; Moore, D. T. Enabling Flexible All-Perovskite Tandem Solar Cells. *Joule* **2019**, *3* (9), 2193–2204. https://doi.org/https://doi.org/10.1016/j.joule.2019.05.009.

(156) Chen, H.; Ding, X.; Xu, P.; Hayat, T.; Alsaedi, A.; Yao, J.; Ding, Y.; Dai, S. Forming Intermediate Phase on the Surface of PbI2 Precursor Films by Short-Time DMSO Treatment for High-Efficiency Planar Perovskite Solar Cells via Vapor-Assisted Solution Process. *ACS Appl. Mater. Interfaces* **2018**, *10* (2), 1781–1791. https://doi.org/10.1021/acsami.7b17781.

(157) Ahn, N.; Son, D. Y.; Jang, I. H.; Kang, S. M.; Choi, M.; Park, N. G. Highly Reproducible Perovskite Solar Cells with Average Efficiency of 18.3% and Best Efficiency of 19.7% Fabricated via Lewis Base Adduct of Lead(II) Iodide. *J. Am. Chem. Soc.* **2015**, *137* (27), 8696–8699. https://doi.org/10.1021/jacs.5b04930.

(158) Rong, Y.; Tang, Z.; Zhao, Y.; Zhong, X.; Venkatesan, S.; Graham, H.; Patton, M.; Jing, Y.; Guloy, A. M.; Yao, Y. Solvent Engineering towards Controlled Grain Growth in Perovskite Planar Heterojunction Solar Cells. *Nanoscale* **2015**, *7* (24), 10595–10599. https://doi.org/10.1039/c5nr02866c.

(159) Fulmer, G. R.; Miller, A. J. M.; Sherden, N. H.; Gottlieb, H. E.; Nudelman, A.; Stoltz, B. M.; Bercaw, J. E.; Goldberg, K. I. NMR Chemical Shifts of Trace Impurities: Common Laboratory Solvents, Organics, and Gases in Deuterated Solvents Relevant to the Organometallic Chemist. *Organometallics* **2010**, *29* (9), 2176–2179. https://doi.org/10.1021/om100106e.

(160) Chen, S.; Dai, X.; Xu, S.; Jiao, H.; Zhao, L.; Huang, J. Stabilizing Perovskite-Substrate Interfaces for High-Performance Perovskite Modules. *Science (80-.).* **2021**, *373* (6557), 902–907. https://doi.org/10.1126/science.abi6323.

(161) Alberti, A.; Bongiorno, C.; Smecca, E.; Deretzis, I.; La Magna, A.; Spinella, C. Pb Clustering and PbI2 Nanofragmentation during Methylammonium Lead Iodide Perovskite Degradation. *Nat. Commun.* **2019**, *10* (1), 2196. https://doi.org/10.1038/s41467-019-09909-0.

(162) Chiang, C.-H.; Wu, C.-G. Film Grain-Size Related Long-Term Stability of Inverted Perovskite Solar Cells. *ChemSusChem* **2016**, *9* (18), 2666–2672. https://doi.org/10.1002/cssc.201600887.

(163) Eperon, G. E.; Paternò, G. M.; Sutton, R. J.; Zampetti, A.; Haghighirad, A. A.; Cacialli, F.; Snaith, H. J. Inorganic Caesium Lead Iodide Perovskite Solar Cells. *J. Mater. Chem. A* **2015**, *3* (39), 19688–19695. https://doi.org/10.1039/C5TA06398A.

(164) Sutton, R. J.; Filip, M. R.; Haghighirad, A. A.; Sakai, N.; Wenger, B.; Giustino, F.; Snaith, H. J. Cubic or Orthorhombic? Revealing the Crystal Structure of Metastable Black-Phase CsPbI3 by Theory and Experiment. *ACS Energy Lett.* **2018**, *3* (8), 1787–1794. https://doi.org/10.1021/acsenergylett.8b00672.

(165) Stoumpos, C. C.; Mao, L.; Malliakas, C. D.; Kanatzidis, M. G. Structure-Band Gap Relationships in Hexagonal Polytypes and Low-Dimensional Structures of Hybrid Tin Iodide Perovskites. *Inorganic Chemistry*. American Chemical Society January 2017, pp 56–73. https://doi.org/10.1021/acs.inorgchem.6b02764.

(166) Straus, D. B.; Guo, S.; Cava, R. J. Kinetically Stable Single Crystals of Perovskite-Phase CsPbI 3. **2019**. https://doi.org/10.1021/jacs.9b06055.

(167) Widmann, G. Interpreting TGA Curves.

(168) Thass. *Buoyancy Phenomenon in TGA Systems*.

(169) Tan, B.; Raga, S. R.; Chesman, A. S. R.; Fürer, S. O.; Zheng, F.; McMeekin, D. P.; Jiang, L.; Mao, W.; Lin, X.; Wen, X.; Lu, J.; Cheng, Y.; Bach, U. LiTFSI-Free Spiro-OMeTAD-Based Perovskite Solar Cells with Power Conversion Efficiencies Exceeding 19%. *Adv. Energy Mater.* **2019**, 1901519. https://doi.org/10.1002/aenm.201901519.

(170) Hu, M.; Wu, X.; Tan, W. L.; Tan, B.; Scully, A. D.; Ding, L.; Zhou, C.; Xiong, Y.; Huang, F.; Simonov, A. N.; Bach, U.; Cheng, Y. B.; Wang, S.; Lu, J. Solvent Engineering of a Dopant-Free Spiro-OMeTAD Hole-Transport Layer for Centimeter-Scale Perovskite Solar Cells with High Efficiency and Thermal Stability. *ACS Appl. Mater. Interfaces* **2020**, *12* (7), 8260–8270. https://doi.org/10.1021/acsami.9b21177.

(171) Schloemer, T. H.; Christians, J. A.; Luther, J. M.; Sellinger, A. Doping Strategies for Small Molecule Organic Hole-Transport Materials: Impacts on Perovskite Solar Cell Performance and Stability. *Chem. Sci.* **2019**, *10* (7), 1904–1935. https://doi.org/10.1039/C8SC05284K.

(172) Pellaroque, A.; Noel, N. K.; Habisreutinger, S. N.; Zhang, Y.; Barlow, S.; Marder, S. R.; Snaith, H. J. Efficient and Stable Perovskite Solar Cells Using Molybdenum Tris(Dithiolene)s as p-Dopants for Spiro-OMeTAD. *ACS Energy Lett.* **2017**, *2* (9), 2044–2050. https://doi.org/10.1021/acsenergylett.7b00614.

(173) Habisreutinger, S. N.; Leijtens, T.; Eperon, G. E.; Stranks, S. D.; Nicholas, R. J.; Snaith, H.

J. Carbon Nanotube/Polymer Composites as a Highly Stable Hole Collection Layer in Perovskite Solar Cells. *Nano Lett.* **2014**, *14* (10), 5561–5568. https://doi.org/10.1021/nl501982b.

(174) Nguyen, W. H.; Bailie, C. D.; Unger, E. L.; McGehee, M. D. Enhancing the Hole-Conductivity of Spiro-OMeTAD without Oxygen or Lithium Salts by Using Spiro(TFSI) $_2$ in Perovskite and Dye-Sensitized Solar Cells. *J. Am. Chem. Soc.* **2014**, *136* (31), 10996–11001. https://doi.org/10.1021/ja504539w.

(175) Jena, A. K.; Ikegami, M.; Miyasaka, T. Severe Morphological Deformation of Spiro-OMeTAD in (CH3NH3)PbI3 Solar Cells at High Temperature. *ACS Energy Letters*. American Chemical Society August 2017, pp 1760–1761. https://doi.org/10.1021/acsenergylett.7b00582.

(176) Wang, S.; Sina, M.; Parikh, P.; Uekert, T.; Shahbazian, B.; Devaraj, A.; Meng, Y. S. Role of 4-Tert-Butylpyridine as a Hole Transport Layer Morphological Controller in Perovskite Solar Cells. *Nano Lett.* **2016**. https://doi.org/10.1021/acs.nanolett.6b02158.

(177) Khenkin, M. V.; Katz, E. A.; Abate, A.; Bardizza, G.; Berry, J. J.; Brabec, C.; Brunetti, F.; Bulović, V.; Burlingame, Q.; Di Carlo, A.; Cheacharoen, R.; Cheng, Y. B.; Colsmann, A.; Cros, S.; Domanski, K.; Dusza, M.; Fell, C. J.; Forrest, S. R.; Galagan, Y.; Di Girolamo, D.; Grätzel, M.; Hagfeldt, A.; von Hauff, E.; Hoppe, H.; Kettle, J.; Köbler, H.; Leite, M. S.; Liu, S. (Frank); Loo, Y. L.; Luther, J. M.; Ma, C. Q.; Madsen, M.; Manceau, M.; Matheron, M.; McGehee, M.; Meitzner, R.; Nazeeruddin, M. K.; Nogueira, A. F.; Odabaşı, Ç.; Osherov, A.; Park, N. G.; Reese, M. O.; De Rossi, F.; Saliba, M.; Schubert, U. S.; Snaith, H. J.; Stranks, S. D.; Tress, W.; Troshin, P. A.; Turkovic, V.; Veenstra, S.; Visoly-Fisher, I.; Walsh, A.; Watson, T.; Xie, H.; Yıldırım, R.; Zakeeruddin, S. M.; Zhu, K.; Lira-Cantu, M. Consensus Statement for Stability Assessment and Reporting for Perovskite Photovoltaics Based on ISOS Procedures. *Nat. Energy* **2020**. https://doi.org/10.1038/s41560-019-0529-5.

(178) Snaith, H. J.; Hacke, P. Enabling Reliability Assessments of Pre-Commercial Perovskite Photovoltaics with Lessons Learned from Industrial Standards. *Nat. Energy* **2018**. https://doi.org/10.1038/s41560-018-0174-4.

(179) Dasgupta, A.; Mahesh, S.; Caprioglio, P.; Lin, Y.-H.; Zaininger, K.-A.; Oliver, R. D. J.; Holzhey, P.; Zhou, S.; McCarthy, M. M.; Smith, J. A.; Frenzel, M.; Christoforo, M. G.; Ball, J. M.; Wenger, B.; Snaith, H. J. Visualizing Macroscopic Inhomogeneities in Perovskite Solar Cells. *ACS Energy Lett.* **2022**, *7* (7), 2311–2322. https://doi.org/10.1021/acsenergylett.2c01094.

(180) Yang, S.; Chen, S.; Mosconi, E.; Fang, Y.; Xiao, X.; Wang, C.; Zhou, Y.; Yu, Z.; Zhao, J.; Gao, Y.; De Angelis, F.; Huang, J. Stabilizing Halide Perovskite Surfaces for Solar Cell Operation with Wide-Bandgap Lead Oxysalts. *Science (80-.).* **2019**, *365* (6452), 473–478. https://doi.org/10.1126/science.aax3294.

(181) Goethals, E. J.; Du Prez, F. Carbocationic Polymerizations. *Prog. Polym. Sci.* **2007**, *32* (2), 220–246. https://doi.org/https://doi.org/10.1016/j.progpolymsci.2007.01.001.

(182) Van Lijsebetten, F.; Spiesschaert, Y.; Winne, J. M.; Du Prez, F. E. Reprocessing of Covalent Adaptable Polyamide Networks through Internal Catalysis and Ring-Size Effects. *J. Am. Chem. Soc.* **2021**, *143* (38), 15834–15844. https://doi.org/10.1021/jacs.1c07360.

(183) Montarnal, D.; Capelot, M.; Tournilhac, F.; Leibler, L. Silica-Like Malleable Materials

from Permanent Organic Networks. *Science (80-.).* **2011**, *334* (6058), 965–968. https://doi.org/10.1126/science.1212648.

(184) Zheng, N.; Xu, Y.; Zhao, Q.; Xie, T. Dynamic Covalent Polymer Networks: A Molecular Platform for Designing Functions beyond Chemical Recycling and Self-Healing. *Chem. Rev.* **2021**, *121* (3), 1716–1745. https://doi.org/10.1021/acs.chemrev.0c00938.

(185) Lu, Y.-X.; Tournilhac, F.; Leibler, L.; Guan, Z. Making Insoluble Polymer Networks Malleable via Olefin Metathesis. *J. Am. Chem. Soc.* **2012**, *134* (20), 8424–8427.

(186) Lu, Y.-X.; Guan, Z. Olefin Metathesis for Effective Polymer Healing via Dynamic Exchange of Strong Carbon–Carbon Double Bonds. *J. Am. Chem. Soc.* **2012**, *134* (34), 14226–14231.

(187) Neal, J. A.; Mozhdehi, D.; Guan, Z. Enhancing Mechanical Performance of a Covalent Self-Healing Material by Sacrificial Noncovalent Bonds. *J. Am. Chem. Soc.* **2015**, *137* (14), 4846–4850.

(188) Zhao, J.; Zhang, Z.; Cheng, L.; Bai, R.; Zhao, D.; Wang, Y.; Yu, W.; Yan, X. Mechanically Interlocked Vitrimers. *J. Am. Chem. Soc.* **2021**, *144* (2), 872–882.

(189) Ying, H.; Cheng, J. Hydrolyzable Polyureas Bearing Hindered Urea Bonds. *J. Am. Chem. Soc.* **2014**, *136* (49), 16974–16977.

(190) Cui, C.; Chen, X.; Ma, L.; Zhong, Q.; Li, Z.; Mariappan, A.; Zhang, Q.; Cheng, Y.; He, G.; Chen, X.; Dong, Z.; An, L.; Zhang, Y. Polythiourethane Covalent Adaptable Networks for Strong and Reworkable Adhesives and Fully Recyclable Carbon Fiber-Reinforced Composites. *ACS Appl. Mater. Interfaces* **2020**, *12* (42), 47975–47983. https://doi.org/10.1021/acsami.0c14189.

(191) Wu, W.-Q.; Yang, Z.; Rudd, P. N.; Shao, Y.; Dai, X.; Wei, H.; Zhao, J.; Fang, Y.; Wang, Q.; Liu, Y.; Deng, Y.; Xiao, X.; Feng, Y.; Huang, J. Bilateral Alkylamine for Suppressing Charge Recombination and Improving Stability in Blade-Coated Perovskite Solar Cells. *Sci. Adv.* **2019**, *5* (3). https://doi.org/10.1126/sciadv.aav8925.

(192) Chang, J.; Wang, Y.-C.; Song, C.; Zhu, L.; Guo, Q.; Fang, J. Carboxylic Ester-Terminated Fulleropyrrolidine as an Efficient Electron Transport Material for Inverted Perovskite Solar Cells. *J. Mater. Chem. C* **2018**, *6* (26), 6982–6987. https://doi.org/10.1039/C8TC01955J.

(193) Wang, R.; Xue, J.; Wang, K.-L.; Wang, Z.-K.; Luo, Y.; Fenning, D.; Xu, G.; Nuryyeva, S.; Huang, T.; Zhao, Y.; Yang, J. L.; Zhu, J.; Wang, M.; Tan, S.; Yavuz, I.; Houk, K. N.; Yang, Y. Constructive Molecular Configurations for Surface-Defect Passivation of Perovskite Photovoltaics. *Science (80-.).* **2019**, *366* (6472), 1509–1513. https://doi.org/10.1126/science.aay9698.

(194) Xiong, H.; DeLuca, G.; Rui, Y.; Zhang, B.; Li, Y.; Zhang, Q.; Wang, H.; Reichmanis, E. Modifying Perovskite Films with Polyvinylpyrrolidone for Ambient-Air-Stable Highly Bendable Solar Cells. *ACS Appl. Mater. Interfaces* **2018**, *10* (41), 35385–35394.

(195) Wang, L.; Zhou, H.; Hu, J.; Huang, B.; Sun, M.; Dong, B.; Zheng, G.; Huang, Y.; Chen, Y.; Li, L. A Eu3+-Eu2+ Ion Redox Shuttle Imparts Operational Durability to Pb-I Perovskite Solar Cells. *Science (80-.).* **2019**, *363* (6424), 265–270.

(196) Tang, X.; Brandl, M.; May, B.; Levchuk, I.; Hou, Y.; Richter, M.; Chen, H.; Chen, S.; Kahmann, S.; Osvet, A.; Maier, F.; Steinrück, H.-P.; Hock, R.; Matt, G. J.; Brabec, C. J.

Photoinduced Degradation of Methylammonium Lead Triiodide Perovskite Semiconductors. *J. Mater. Chem. A* **2016**, *4* (41), 15896–15903. https://doi.org/10.1039/C6TA06497C.

(197) Kolesov, V. A.; Fuentes-Hernandez, C.; Chou, W.-F.; Aizawa, N.; Larrain, F. A.; Wang, M.; Perrotta, A.; Choi, S.; Graham, S.; Bazan, G. C.; Nguyen, T.-Q.; Marder, S. R.; Kippelen, B. Solution-Based Electrical Doping of Semiconducting Polymer Films over a Limited Depth. *Nat. Mater.* **2017**, *16* (4), 474–480. https://doi.org/10.1038/nmat4818.

(198) Chu, H.; Noh, H.; Kim, Y.-J.; Yuk, S.; Lee, J.-H.; Lee, J.; Kwack, H.; Kim, Y.; Yang, D.-K.; Kim, H.-T. Achieving Three-Dimensional Lithium Sulfide Growth in Lithium-Sulfur Batteries Using High-Donor-Number Anions. *Nat. Commun.* **2019**, *10* (1), 188. https://doi.org/10.1038/s41467-018-07975-4.

(199) Andaji-Garmaroudi, Z.; Anaya, M.; Pearson, A. J.; Stranks, S. D. Photobrightening in Lead Halide Perovskites: Observations, Mechanisms, and Future Potential. *Adv. Energy Mater.* **2020**, *10* (13), 1903109.

(200) Xie, H.; Wang, Z.; Chen, Z.; Pereyra, C.; Pols, M.; Gałkowski, K.; Anaya, M.; Fu, S.; Jia, X.; Tang, P. Decoupling the Effects of Defects on Efficiency and Stability through Phosphonates in Stable Halide Perovskite Solar Cells. *Joule* **2021**, *5* (5), 1246–1266.

(201) Conings, B.; Drijkoningen, J.; Gauquelin, N.; Babayigit, A.; D'Haen, J.; D'Olieslaeger, L.; Ethirajan, A.; Verbeeck, J.; Manca, J.; Mosconi, E.; Angelis, F. De; Boyen, H. Intrinsic Thermal Instability of Methylammonium Lead Trihalide Perovskite. *Adv. Energy Mater.* **2015**.

(202) Turren-Cruz, S.-H.; Hagfeldt, A.; Saliba, M. Methylammonium-Free, High-Performance and Stable Perovskite Solar Cells on a Planar Architecture. *Science (80-.).* **2018**.

(203) Ho, K.; Wei, M.; Sargent, E. H.; Walker, G. C. Grain Transformation and Degradation Mechanism of Formamidinium and Cesium Lead Iodide Perovskite under Humidity and Light. *ACS Energy Lett.* **2021**, *6* (3), 934–940. https://doi.org/10.1021/acsenergylett.0c02247.

(204) Li, N.; Luo, Y.; Chen, Z.; Niu, X.; Zhang, X.; Lu, J.; Kumar, R.; Jiang, J.; Liu, H.; Guo, X.; Lai, B.; Brocks, G.; Chen, Q.; Tao, S.; Fenning, D. P.; Zhou, H. Microscopic Degradation in Formamidinium-Cesium Lead Iodide Perovskite Solar Cells under Operational Stressors. *Joule* **2020**, *4* (8), 1743–1758. https://doi.org/https://doi.org/10.1016/j.joule.2020.06.005.

(205) Schwenzer, J. A.; Hellmann, T.; Nejand, B. A.; Hu, H.; Abzieher, T.; Schackmar, F.; Hossain, I. M.; Fassl, P.; Mayer, T.; Jaegermann, W.; Lemmer, U.; Paetzold, U. W. Thermal Stability and Cation Composition of Hybrid Organic–Inorganic Perovskites. *ACS Appl. Mater. Interfaces* **2021**, *13* (13), 15292–15304. https://doi.org/10.1021/acsami.1c01547.

(206) Saliba, M.; Unger, E.; Etgar, L.; Luo, J.; Jacobsson, T. J. A Systematic Discrepancy between the Short Circuit Current and the Integrated Quantum Efficiency in Perovskite Solar Cells. *Nat. Commun.* **2023**, *14* (1), 5445. https://doi.org/10.1038/s41467-023-41263-0.

(207) Safdari, M.; Kim, D.; Balvanz, A.; Kanatzidis, M. G. Mitigation of Halide Segregation by Cation Composition Management in Wide Bandgap Perovskites. *ACS Energy Lett.* **2024**,

3400–3408. https://doi.org/10.1021/acsenergylett.4c01281.

(208) Li, W.; Wang, Z.; Deschler, F.; Gao, S.; Friend, R. H.; Cheetham, A. K. Chemically Diverse and Multifunctional Hybrid Organic–Inorganic Perovskites. *Nat. Rev. Mater.* **2017**, *2* (3), 16099. https://doi.org/10.1038/natrevmats.2016.99.

(209) Jariwala, S.; Kumar, R. E.; Eperon, G. E.; Shi, Y.; Fenning, D. P.; Ginger, D. S. Dimethylammonium Addition to Halide Perovskite Precursor Increases Vertical and Lateral Heterogeneity. *ACS Energy Lett.* **2022**, *7* (1), 204–210. https://doi.org/10.1021/acsenergylett.1c02302.

(210) Tardio, S.; Abel, M.-L.; Carr, R. H.; Watts, J. F. The Interfacial Interaction between Isocyanate and Stainless Steel. *Int. J. Adhes. Adhes.* **2019**, *88*, 1–10.

(211) Oh, D. X.; Shin, S.; Lim, C.; Hwang, D. S. Dopamine-Mediated Sclerotization of Regenerated Chitin in Ionic Liquid. *Materials (Basel).* **2013**, *6* (9), 3826–3839.